Chemical and physical behaviour of the trace elements in the silicate melts of the Earth's mantle

Alexandra Catalina Seclaman

N° d'ordre NNT : N004

THESE de DOCTORAT DE L'UNIVERSITE DE LYON

opérée au sein de

Ecole normale supérieure de Lyon

Ecole Doctorale N° 34

Ecole Doctorale Matériaux de Lyon

Spécialité de doctorat :

Sciences de la terre

Soutenue publiquement le 01/04/2016, par :

Alexandra Catalina SECLAMAN

Chemical and physical behaviour of the trace elements in the silicate melts of the Earth's mantle

Devant le jury composé de :

M. Bernard BOURDON, ENS de Lyon, LGL-TPE, Examinateur

M. Razvan CARACAS, ENS de LYON, LGL-TPE, Directeur

M. Guillaume FIQUET, UPMC, IMPMC, Examinateur

M. Dan J. FROST, BGI, Rapporteur

M. Stephané LABROSSE, ENS de Lyon, LGL-TPE Examinateur

Mme Lidunka VOCADLO, UCL, Rapporteur [absente]

Contents

1. Introduction

The Apollo Program provided humanity with the first rock samples collected from another planetary body. This tremendous technological achievement brought back more than samples, it brought back the idea that would revolutionize the way we think about planetary differentiation. In the soil samples collected by Apollo 11, Na poor-feldspars rocks, anorthosites (An_{93}-An_{98}), were the most surprising find (Wood et al.,1970). These rocks present a random orientation of the crystals, with a texture described by Wood et al., 1970 as 'polyhedral-granular'. The bulk composition of the anorthosites alongside the texture was interpreted by Wood et al., 1970, as indicating an igneous cumulate origin of the samples. Most samples present signs of shock metamorphism, suggesting that they are debris resulting from cratering events in the Lunar Highlands. The Highlands origin is supported by similar chemistry between the lunar samples collected by Apollo 11 in Mare Tranquillitatis and the chemical analysis made by Surveyor VII of the ejecta from crater Tycho. Wood et al., 1970 make this comparison and argue that the Highlands must be high because they are less dense. In their paper, Wood et al., 1970, draw attention to the low density of the anorthosite rocks several times, and compare their light colour to that of the Highlands. All these observations and the interpretation that the ejecta from the Tycho crater is representative of the bulk composition of the Highlands, lead Wood et al.,1970 and Smith et al.,1970 to create a model which implied that a large portion of the Moon was molten in its early days. The Moon's crust was the result of the fractional crystallization and gravitational separation of anorthosite from the magma (Figure 1). In this model, Wood et al. proposed a Moon core that was a solid mixture of silicates. Nonetheless, the idea of an almost molten Moon proposed by Wood et al.,1970 and Smith et al.,1970 came to be known as the Magma Ocean model/hypothesis and it retains its appeal to this day.

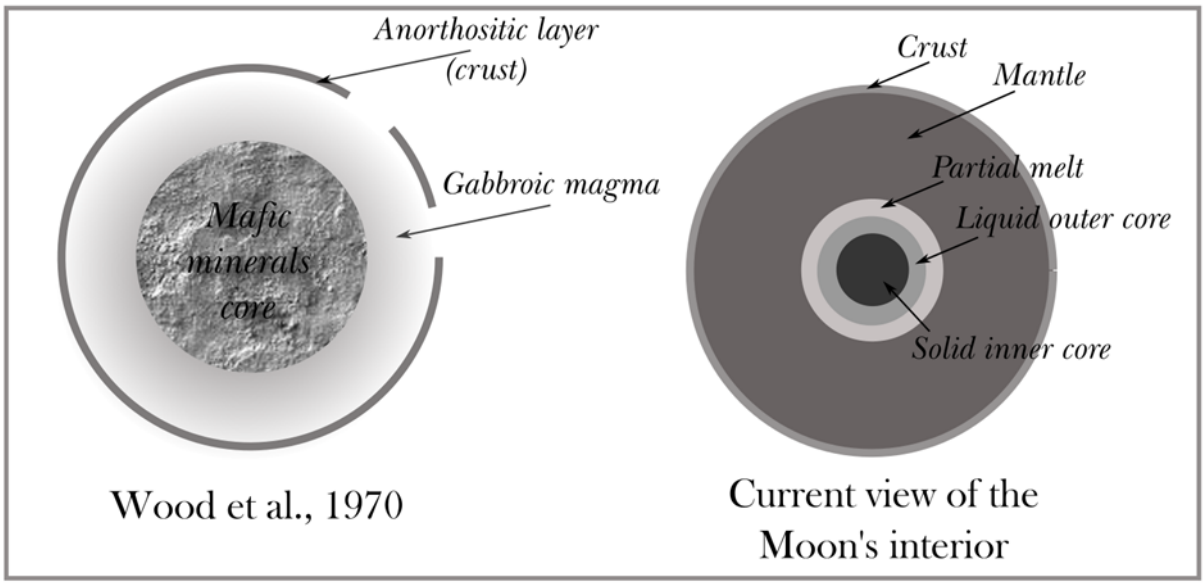

Figure 1 Wood et al., 1970 model for the interior of the Moon compared to the model resulted from the seismic data gathered by Apollo Passive Seismic experiment.

Perhaps the most famous geochemical evidence supporting the Lunar Magma Ocean hypothesis is the Eu anomaly. In the lunar Highlands, Eu shows a positive anomaly while in the Mare basalts Eu is depleted (Grove & Krawczynski, 2009). Eu was preferentially partitioned in the anorthite during its fractional crystallization leaving the source magmas for the basalts depleted. This explains why Wood et al., 1970, didn't find any intermediary compositions linking the basalts and the anorthosite and supports their idea that if the two rocks types are indeed related the evidence of their relationship to one-another was hidden by a large scale event.

More geochemical evidence for a Lunar Magma Ocean lay in the unusual chemistry of the Mare lavas brought by Apollo 12 and Highlands samples taken by Apollo 14 (Taylor & Jakes,1974). The compositions of these samples can be explained only by extensive fractional crystallization and the creation of large scale cumulates, anorthositic ones that would lead to the formation of the highlands, and olivine-rich cumulates that helped create the Mare basalts (Taylor & Jakes,1974). None of the large-scale processes that can explain the anorthositic samples, or the Mare basalts could have taken place without the existence of a magma ocean in the early history of the Moon.

The idea that maybe Earth and other planets have been molten in their early histories came in the early '80 (Hostetler & Drake,1980). By investigating possible heating sources, tidal heating of the Moon, ^{26}Al decay, the enhanced luminosity of the early sun, accretion, and other mechanisms, Hostetler & Drake reach the conclusion that large scale melting events as those recorded by the Lunar samples, are possible even in the case of larger planets such as Earth.

The key to the Terrestrial Magma Ocean hypothesis lies in the origin of the Moon. By mid '90 it was clear that a giant impact could explain successfully the origin of the Moon (Canup & Esposito,1996; Ida et al.,1997). The unresolved problem at the time was that all simulations didn't manage to create one Moon, appropriate in mass, or condense the ejecta beyond the Roche limit (Cameron,1997). In the early '00, impact simulation have shown that one impact involving a Mars-sized body taking place at the late stage of Earth's accretion can produce a realistic Earth-Moon system, with a Fe-poor Moon (Canup & Asphaug,2001). Through their work, Canup & Asphaug show that one impact, with a smaller than previously expected planetary body, the Moon can be formed. Smaller planetary bodies have a higher chance of existence and thus the probability of an impact happening increases.

Subsequent studies have shown that the temperatures resulted from the impact can reach values of 10^4K (Canup, 2004). These suggests that the energy produced by a large impact at the near-end stage of Earth's accretion can generate sufficient thermal energy to melt at least a portion of the proto-Earth.

Simulations involving a differentiated impactor have managed to create a Moon formed predominantly from impactor material with an Earth-like composition (Canup, 2008).

The need for an impactor of similar composition with the proto-Earth is removed in the simulations of Canup (2012) by using a more massive disk and a larger impactor. They successfully produce a planet-disk system in terms of composition but with a higher angular momentum than the present day Earth-Moon

system. Canup (2012) states that a reduction in angular momentum can be achieved by evection resonance with the sun in accordance with results from Cuk & Stewart (2012). Cuk and Stewart also show that a Moon-forming disk can be produced by a fast spinning target hit by a small planetesimal.

There are three main scenarios for the origin of the Moon material: most of the material came from Earth, the impactor was the main source, or a mixture of Earth and impactor material. If the source material for the Moon was predominantly the proto-Earth, then no significant deviation from Earth isotopic values is expected. O, Ti, and W isotopic signatures of Moon samples appear to be similar to Earth values (Wiechert et al.,2001; Zhang et al.,2012; Touboul et al.,2007; Touboul et al.,2009). Moon samples are enriched in heavy Zn isotopes, suggesting a mass fractionation during condensation from a vapour originating from Earth (Paniello et al.,2012). More precise O isotopic measurements show small deviation in Moon samples from Earth values (Herwartz et al.,2014). This suggests that some small degree of mixing between the impactor and the proto-Earth took place.

The major and minor elements concentration of the Moon's mantle, Fe (Jones & Delano,1989), Ni, Co, and W (Ringwood,1986; Delano,1986), are higher than Earth values from a few orders of magnitude for the moderately siderophyle elements, to a few tens of wt% in the case of Fe (Table 1).

Table 1 Fe, Ni, and Co comparison between the bulk mantles of Earth and Moon. Fe data for the Moon mantle is from Jones & Delano,1989*, Ni and Co from* Delano,1986.

	Fe %	***Co ppm***	***Ni ppm***
Earth's mantle	6.35	102	1860
Moon's mantle	10.1	90	470

This difference in composition has been interpreted as the result of mixing between the impactor material and proto-Earth material, with a substantial contribution from the impactor (Rubie et al.,2011).

The existence of a larger quantity of melt in the proto-Earth such as a Magma Ocean, must have left some evidences in the major and minor composition of the

Earth's mantle. If a Terrestrial Magma Ocean has indeed existed, some form of fractional crystallization is expected to occur and leave some geochemical evidences as in the case of the Moon. As early as 1985 it has been observed that the Mg/Si ratio of the upper mantle is higher than expected and can only be explained by fractional crystallization of bridgmanite (Ohtani,1985). Such a fractional crystallization of bridgmanite would explain the Si enrichment of the upper mantle but it might produce unrealistic signatures in trace elements (Hirose et al.,2004).

The concentration of moderately siderophile elements, for example Ni and Co, in the Earth's mantle has been explained by equilibration of small metallic droplets with a Magma Ocean (Rubie et al.,2003). No matter what was the degree of equilibration, the concentration of moderately siderophile elements in the present-day bulk mantle reflects the complex core formation processes which most likely occurred through a series of impacts and differentiations (Wade & Wood,2005; Rubie et al.,2015; Nakajima & Stevenson,2015), indicating the possibility of more than, one magma ocean.

Isotopic arguments for the existence of a Terrestrial Magma Ocean come from crustal ages. ^{146}Sm-^{142}Nd and ^{147}Sm-^{143}Nd model ages time the formation of the continental crust at 30-75 million years after accretion (Bennett et al.,2006). The differentiation of the continental crust so early in the Earth's history supports the idea of a Terrestrial Magma Ocean, or at least large molten areas of the Earth's surface. Lu/Hf and Sm/Nd signatures in Archean zircons suggests they crystallized from melts derived from melt extraction from a crystallizing magma ocean (Caro et al.,2005).

Perhaps the strongest argument for the existence of a Terrestrial Magma Ocean comes from the fact that core differentiation happened very early (Yu & Jacobsen,2011), a scenario possible only if the proto-Earth was extensively molten. W-Hf systematics is widely used to date core forming events (Halliday et al.,1996; Yu & Jacobsen,2011). If metal-silicate equilibration is assumed, W-Hf gives a core forming age of 30 million years (Yu & Jacobsen,2011), and slightly younger ages if disequilibrium is assumed (Rudge et al.,2010).

From the cornucopia of isotopes and elements that have recorded events that took place in the Earth's magma ocean, Ni, Co, and W are perhaps the most relevant. Ni, Co, and W show pressure effects when they partition between silicate and metallic melts, making them good indicators of equilibration pressures (Rubie et al.,2011), and thus can be used to evaluate the depth of the magma ocean.

Silicate melts have played an important role in the differentiation of the Earth and the Moon, and they still play an active role in the formation and destruction of the Earth's crust.

Mid-oceanic ridges are vivid examples that silicate melts still exist in the upper-most mantle, but their existence in the lowermost parts of the mantle is dependent on the high pressure melting curves of relevant materials and the temperature profile of the mantle.

Fiquet et al.,2010 performed laser-heated diamond-anvil experiments on natural fertile peridotite up to the Earth's core-mantle boundary (CMB). Their experiments find a solidus line that reaches ≈4000K at the CMB with a liquidus above 5000K. Nomura et al.,2014 did similar experiments but on a different composition, pyrolite. Pyrolite is a theoretical material which aims to represent today's average upper

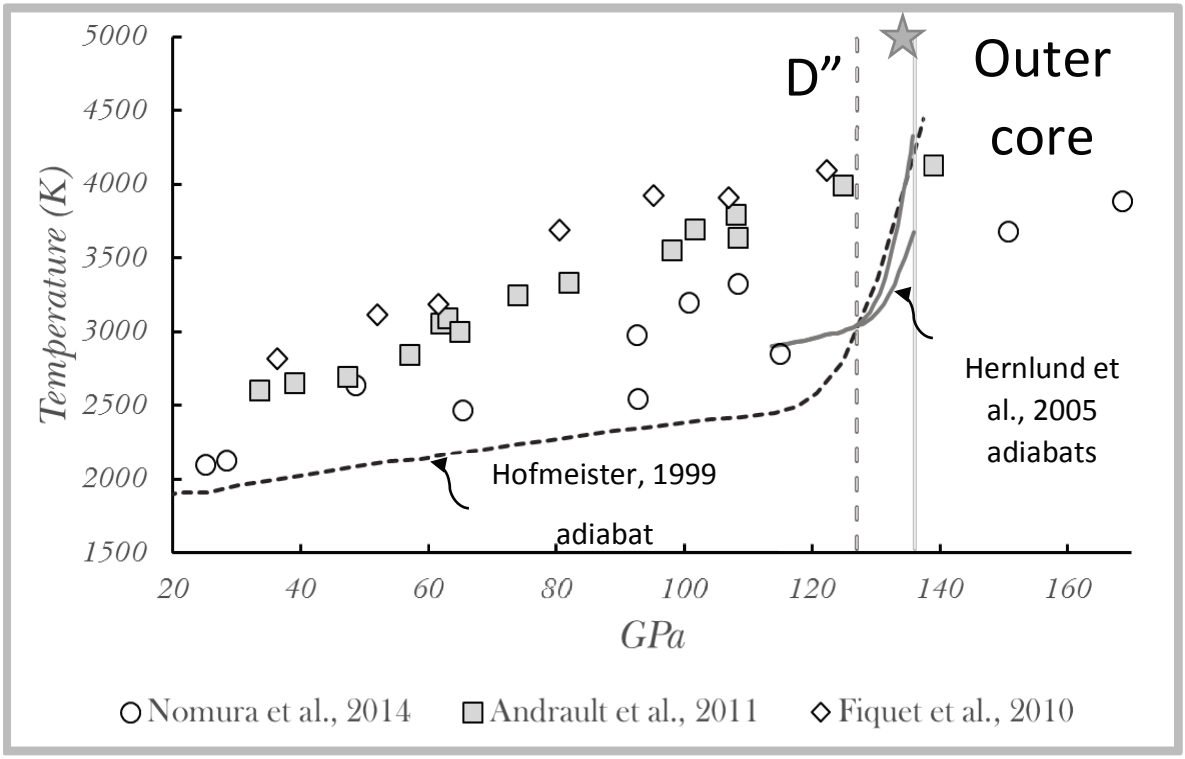

Figure 2 Solidus experimental data points for most recent published works, circles – pyrolite; squares – chondritic mantle; diamonds – fertile peridotite.. The dark grey dotted line is the mantle adiabat of Hofmeister,1999, *the light grey dotted*

mantle composition. Nomura et al.,2014 solidus temperature is 500K lower than that of Fiquet et al.,2010 at the CMB. Andrault et al.,2011 measured the solidus of a 'chondritic mantle' and has similar results to that of Fiquet et al. (Figure 2). These most recent studies open interesting and intriguing questions. Are these materials (peridotite, chondrite, and pyrolite), all evolved from a geochemical perspective, representative for the very early Earth, or for today's lower mantle? And the second, even more tantalizing for the mantle of today, can we quantify the effect of chemistry on such basic physical properties as melting? In all three experiments mentioned above, all starting materials had an FeO content of around 8 wt%.

From the results shown above one can bracket the melting temperature of complex compositions between 3500-4000K at the CMB. Bowen's classical work showed that Fe decreases the melting temperature, this effect has been observed experimentally numerous times since. The decrease in solidus temperature due to Fe-amount present in the material has not yet been constrained. Since in the studies of Nomura, Fiquet, and Andrault the iron content of the samples was constant no inference on the Fe effect on the melting curve can be made.

de Koker et al.,2013 suggest an eutectic temperature between bridgmanite and periclase at ≈5000K and CMB pressure. They also suggest that an increase of 10 mol% of FeO should decrease the eutectic point by 180-320K.

If we assume a rate of decrease of 180K/10 mol% Fe added, then the experimental solidus points would drop under the mantle adiabat close to the CMB for compositions 10 mol% Fe-richer (Figure 3). This exercise shows two important things:

- At Earth's current estimated isotherm, Fe-rich pyrolytic or peridotitic material can be molten inside the D" at relatively low temperatures.
- Fe-rich melt can be preserved in the vicinity of the CMB if its density is greater than that of the lower mantle.

The solidus curve reported by Andrault et al.,2014 for a MORB basalt, with an iron content of 11.29 wt% FeO, reaches a maximum temperature at the CMB and is

substantially lower than the previously mentioned studies. The melting curve of MORB intersects the mantle adiabats (Figure 3) within the D". Even though the

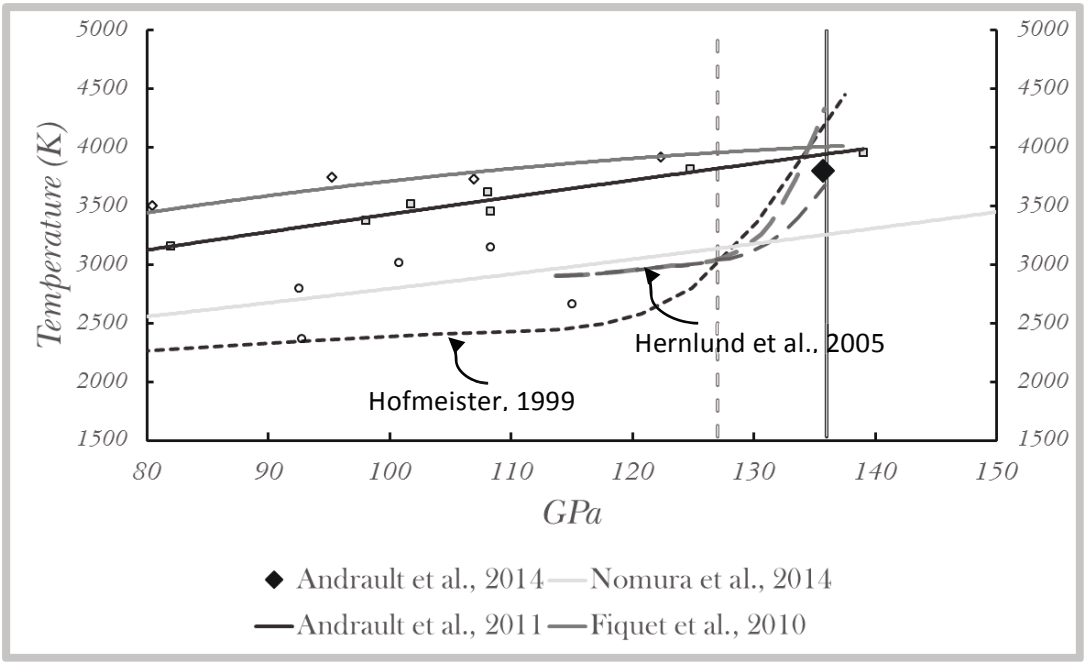

Figure 3 Best fits through the experimental solidus temperature points decreased by 180K . The point of this exercise is to show that it is plausible that a FeO - enrichment of 10% mol can decrease the solidus substantially and intersect it with the mantle isotherm in D". The mantle isotherms are those of Hofmeister,1999; Hernlund et al.,2005. *Dotted vertical line marks the D" and the vertical grey line marks the CMB. The size of the data points have been decreased for clarity. The black diamond shows the temperature of the MORB solidus at the CMB, as reported by* Andrault et al.,2014.

existence of MORB-like material at the CMB is debatable, Figure 3 shows that melt in the D" is possible at relatively low temperatures.

Accurate melting curves for relevant compositions provide constraints not only on the temperature profile of the mantle and Earth's heat budget, but also indirectly constrain the composition (mineralogical and in a lesser manner, chemical) of the lower mantle.

As argued above, melts play a key role in the differentiation of Earth and their existence in today's deep mantle is possible. Remnants of the magma ocean have been proposed to exist in the lowermost mantle (Labrosse et al.,2007), but the melt preservation over geological time-scales is dependent on its geodynamical stability. Buoyant melts will rise and freeze, so they must be denser than the surrounding mantle. Fe is the most abundant heavy element in the Earth's mantle (Palme & O'Neill,2014), and it partitions preferentially into the melt at lower mantle

conditions(Nomura et al.,2011). Therefore Fe facilitates melting at lower temperatures and it increases the density of silicate melts, perhaps stabilizing them in the lower mantle. Equation of state of melt compositions with various Fe contents covering the entire mantle pressure regime can shed light on the density of Fe-bearing silicate melts, and the Fe content required for melts to be neutrally buoyant.

Most density studies of melts at high pressures involved simple compositions (Figure 4). Recently, complex compositions such as basalts have been investigated experimentally and with first principles molecular dynamics (Sanloup et al.,2013;

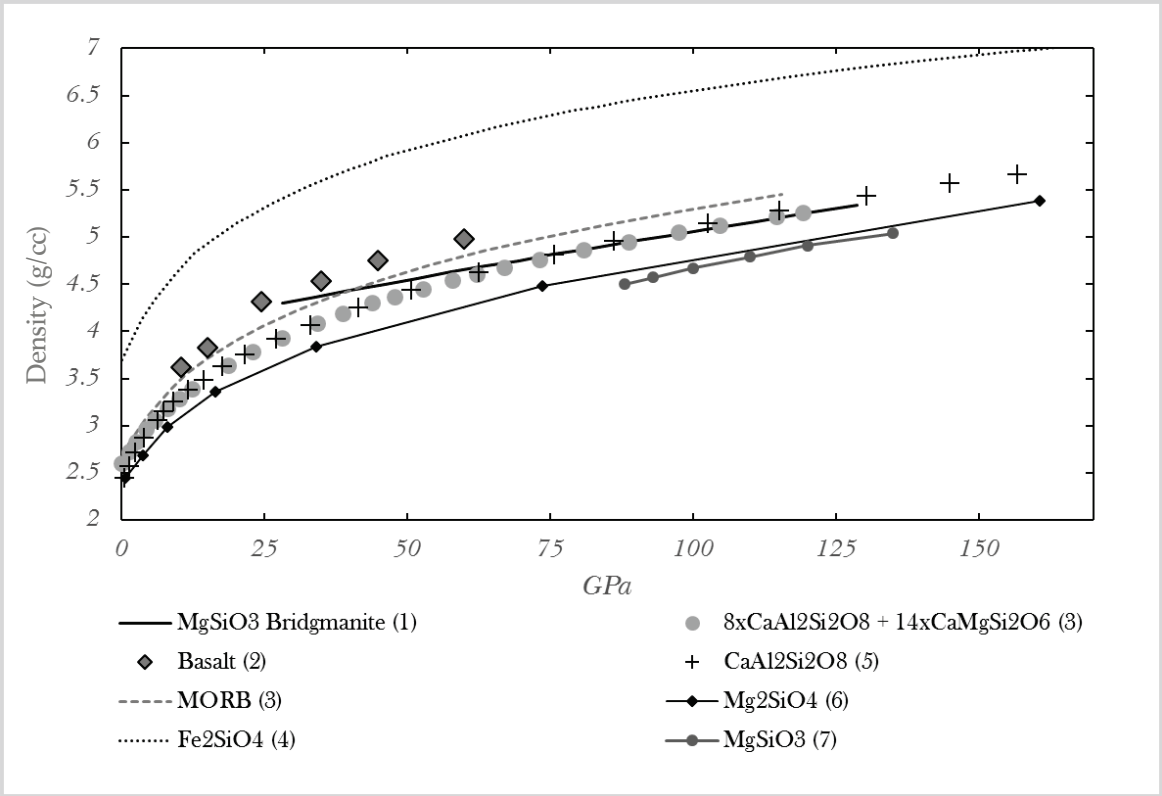

Figure 4 Density versus pressure plot. The legend described the composition of the melt, with the exception of (1) which is solid bridgmanite plotted for comparison. With the exception of (2), (4) and (7) all data is at 3000K. References: (1) : Marton et al.,2000*; (2) :* Sanloup et al.,2013 *temperature is 2200-3273K; (3)* Bajgain et al.,2015*; (4) :* Thomas et al.,2012 *temperature is 1573K ; (5):* Karki et al.,2011*; (6):* de Koker et al.,2008*; (7) :* Wan et al.,2007 *temperature is 3500K.*

Bajgain et al.,2015)(Figure 4).

Figure 4 presents a compilation of published data on the densities of different melts at high pressure and temperature. The effect of Fe content and temperature cannot be assessed properly due to differences in techniques and the errors associated with them. For these reasons we have chosen to investigate the effect of temperature and

Fe content on two compositions representative for the Earth's mantle, and lower mantle in particular, $(Mg,Fe)_2SiO_4$ and $(Mg,Fe)SiO_3$.

Density is not the only physical property responsible for the dynamic equilibrium or melt migration in the mantle, viscosity plays an important part. At 3000K the computed bulk viscosities of Mg_2SiO_4, $MgSiO_3$, and $MgSi_2O_5$ are 0.0047, 0.0062, and 0.014 Pas (de Koker et al.,2013). At higher temperatures (4000K) the difference in viscosity is negligible, 0.0003 Pas. Maybe more importantly the compressional response of the melt with increasing pressure has a greater relevance in the context of the Earth's mantle and magma ocean crystallization. Wan et al.,2007 reports a viscosity of 0.019 Pas at 120 GPa and 4000K, which implies a 67.4% increase in viscosity from 0 GPa data of Karki et al.,2013a.

The compressional response of a silicate melt is dictated by the atomic rearrangements that accommodate pressure increase. At low pressure the changes in Si-O coordination number might be responsible for the abnormal changes in viscosity (Wang et al.,2014; Scarfe et al.,1987). The decreasing viscosity with pressure of polymerized melts (Suzuki et al.,2010) has been explained through the use of classical molecular dynamics as resulting from the tetrahedral packing limit (Wang et al.,2014).

Sanloup et al.,2013 is the first experimental study dealing with the Si-O coordination changes in molten basalt up to mid-lower mantle pressures. They observe an unusually steep increase in Si-O coordination with pressure, a trend closer to that of silica glass than a depolymerized composition (Sanloup et al.,2013). First principles molecular studies show a less steep slope of coordination increase (De Koker,2010; Bajgain et al.,2015) for similar compositions and polymerization degree (Figure 5).

The coordination of other cations by O follows an increasing trend with pressure (Figure 6). Both Mg and Ca have higher coordination numbers than Si at low pressure. Ca has a steeper increase in coordination number with pressure than Mg and Si. At lower mantle pressures Ca is coordinated by 8 oxygens (De Koker,2010).

At the same pressure, Mg is coordinated by 7 oxygens (de Koker et al.,2008; Bajgain et al.,2015). In the lower mantle Ca continues to increase its coordination reaching values close to 10 at 40 GPa, while Mg-O coordination number is still 7.

Melt composition seems to have an effect on the coordination of Mg. In Al and Ca

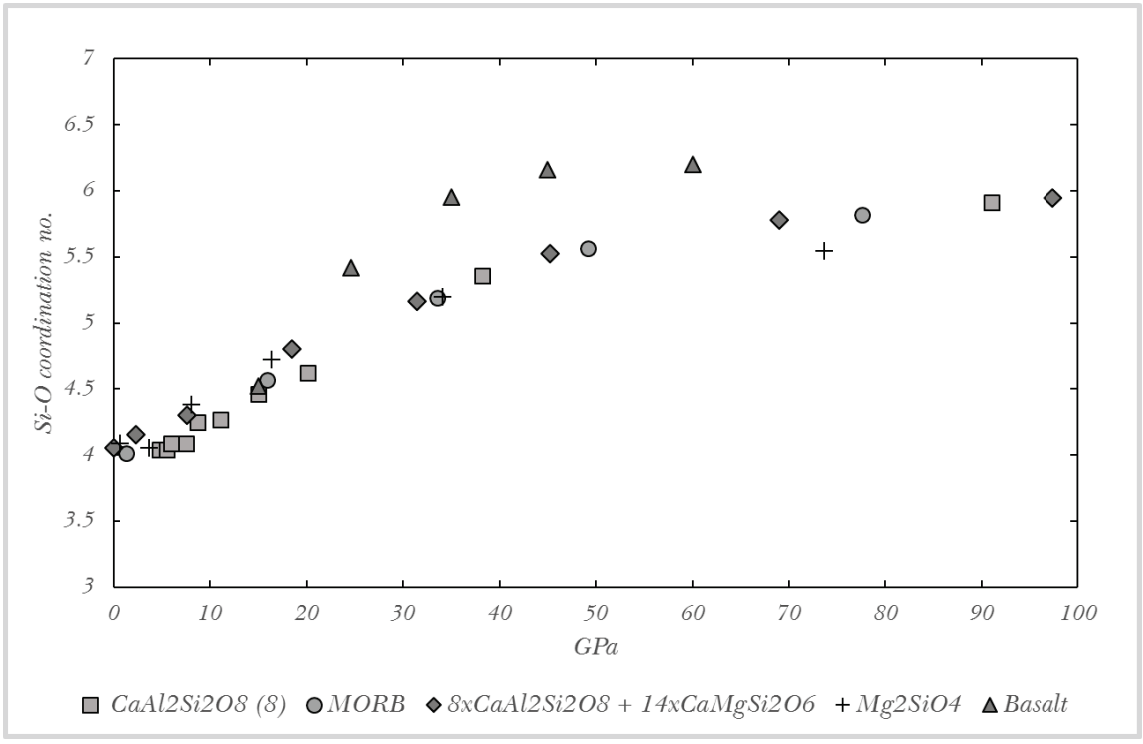

Figure 5 Si-O coordination number increase with pressure. The experimental results reach a Si-O octahedral coordination at substantially lower pressures than equivalent compositions investigated with first principles molecular dynamics. Data has the same source as in figure 4, with the exception of (8) which is from De Koker,2010.

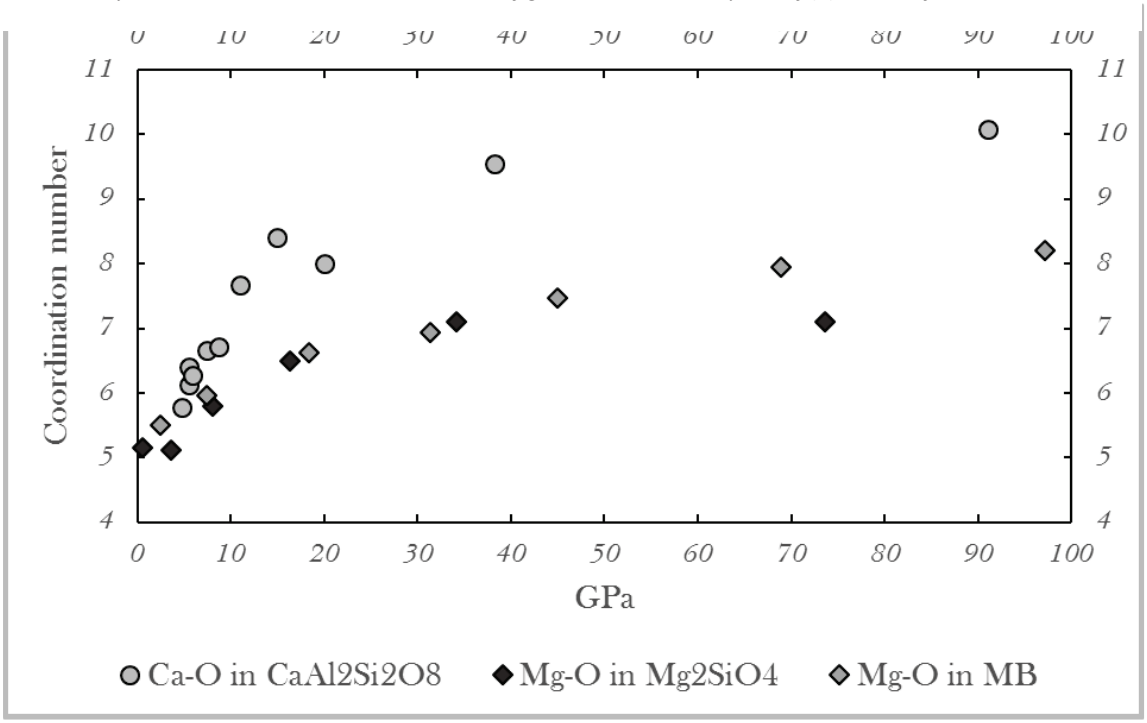

Figure 6 Ca-O and Mg-O coordination change with pressure. The coordination of Ca increases rapidly with pressure up to 20 GPa, and continues to increase after this pressure but at a slower rate. Mg in olivine melt is coordinated by 5 O atoms at low pressures. At 35GPa it reaches a coordination number of 7 and it remains constant throughout the rest of the mantle. Mg-O coordination in Al-bearing melts, shows a similar trend up to 35 GPa but it continues to

bearing melts Mg continues to increase its coordination after 35 GPa.

None of the above mentioned studies have investigated the effects of Fe, Ni, Co, and W on the structural changes with pressure. In this work, a comprehensive discussion on coordination of network forming, network modifying and other cations is presented.

Network-forming cations are the atomic species which bounded by an anion are capable of creating polymer structures, i.e. chains, rings, etc. In the case of silicate melts, the most common network-forming cations are Si and Al. At low pressures, Si and Al are found in tetrahedral coordination by O. The O linking two tetrahedra are called bridging oxygens. O connected to only one Si atom are called non-bridging oxygens.

Network-modifiers are cations that bind to non-bridging oxygens. Usually network-modifiers are cations that form weaker bonds with O, are large, and have a low charge (Wu & Stebbins,2013).

We assess not only the pressure effects, but also compositional effects. We investigate the effect of major elements and trace elements on the Si-O coordination. The structural environment of transitional metals in silicate melts is the direct result of their size (influenced by their spin state), charge, and major chemistry of the melt. Charge as a function of redox state influences the coordination environment by affecting the charge balance and the size of the transitional metal. Spin state, charge, and size effects can be summarized by the field strength, valence over the square of the cation-oxygen bond length (Farnan et al.,1992; Stebbins et al.,1992). We find a steeper increase in coordination numbers of Si by O as the degree of polymerization increases. The Mg-O coordination trend with pressure in depolymerized silicate melts is similar to that of an MgO melt, leading us to the conclusion that Mg-O short range order is independent of the presence of Si-O coordination polyhedra in depolymerized melts.

The interaction of the silicate melts in the magma ocean with the separating metallic melts represents another important part of the scenario. Fe-rich metallic

melts separated due to immiscibility from the silicate magma ocean, and descended gravitationally to form the core. The exact mechanism of descent, the dynamic regime in which it took place, and the size of the metallic drops are still actively researched. No matter the size or mechanism, some equilibration with the mantle must have taken place in order to create the trace element signature of the mantle, as previously argued. Partitioning coefficients of trace elements at mantle relevant pressure and temperature conditions have to be well constrained and the mechanism behind their evolution with pressure must be understood. Numerous studies have dealt with the partitioning of different trace elements between silicate and metallic melts, at various pressures, temperatures, oxygen fugacity, and silicate melts compositions. The most recent and relevant ones are cited throughout this work[1]. From this multitude of data, an interesting picture has emerged. The affinity of Ni, for metallic melts decreases with pressure. Even more interestingly it doesn't present a linear decrease, making the extrapolation from very low pressures tricky at best (Figure 7).

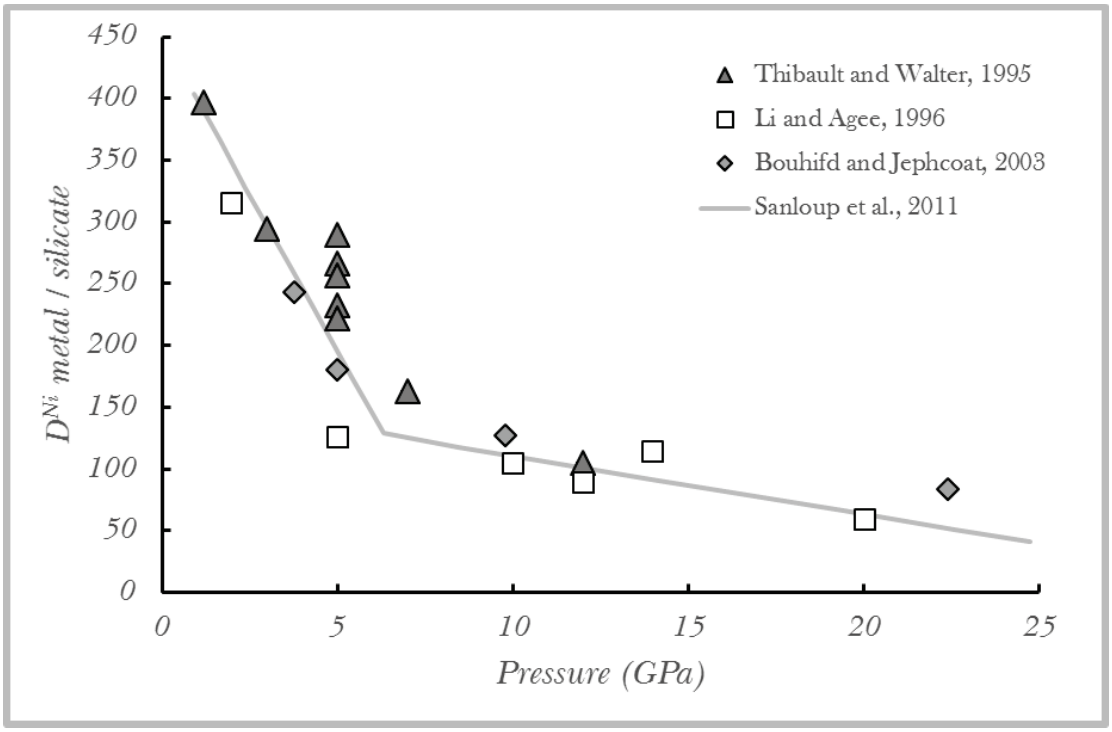

Figure 7 Metal-silicate melt partitioning coefficients of Ni versus pressure. Sanloup et al.,2011 *proposed a kink in the partitioning coefficient of Ni with pressure at around 5 GPa. The grey line marks the kink as proposed by Sanloup et al.,2011. The oxygen fugacity is IW-1.*

[1] ***Most of the discussion on trace element partitioning takes place in Chapter 5.***
[2] ***A more extensive discussion is found in the Introduction to Chapter 4.***

Such a change in affinity with pressure complicates core forming models and raises, yet again, an interesting question. Why would the behaviour of an element be so drastically affected by pressure? Even more tantalizing, if the mechanism responsible for this change in affinity can be determined and understood then models that predict the partitioning of transitional metals can be developed.

Figure 7 shows a "change" in the partitioning with pressure, which was widely interpreted as a kink (Sanloup et al.,2011; Sanloup et al.,2013; Kegler et al.,2008). The exact pressure and the inflection value of D_{Ni} at which the kink happens is dependent mainly on oxygen fugacity. In Figure 7 a grey line is drawn at a kink pressure point close to that proposed by Sanloup et al.,2011 and Kegler et al.,2008.

The partitioning coefficient value can be influenced by oxygen fugacity, melt composition, and temperature. Neither of these parameters are very well constrained for the magma ocean or for the current state of the overall mantle.

Another peculiar partitioning trend is observed in the case of W (Walter & Thibault,1995; Cottrell et al.,2009; Siebert et al.,2011), this time not as a function of pressure but as a function of the degree of polymerization of the silicate melt (Figure 8). W shows an increased lithophile character during partitioning between a metallic melt and a depolymerized silicate melt, by comparison to a polymerized silicate melt. This trend is observed regardless of pressure. W is an important element in the core forming process, as argued previously, for its role in the Hf-W systematics and its moderately siderophyle character. In a crystallizing magma the composition of the liquid and solid phases is ever-changing due to fractional crystallization. Seen from a planetary evolution perspective the increasing affinity of W for lesser polymerized melts (Figure 8) has implications not only for core formation but also for crustal differentiation. Studying the reasons behind tungsten's affinity for depolymerized silicate melts can reveal important information about the nature of partitioning between silicate and metallic melts. The influence of the NBO/T of silicate melts on the partitioning of Ni, Co, and W is explored at isobaric and isothermic conditions through multi-anvil experiments presented in this work. We employ first principles

molecular dynamic simulations to explore the possibility of a structural explanation

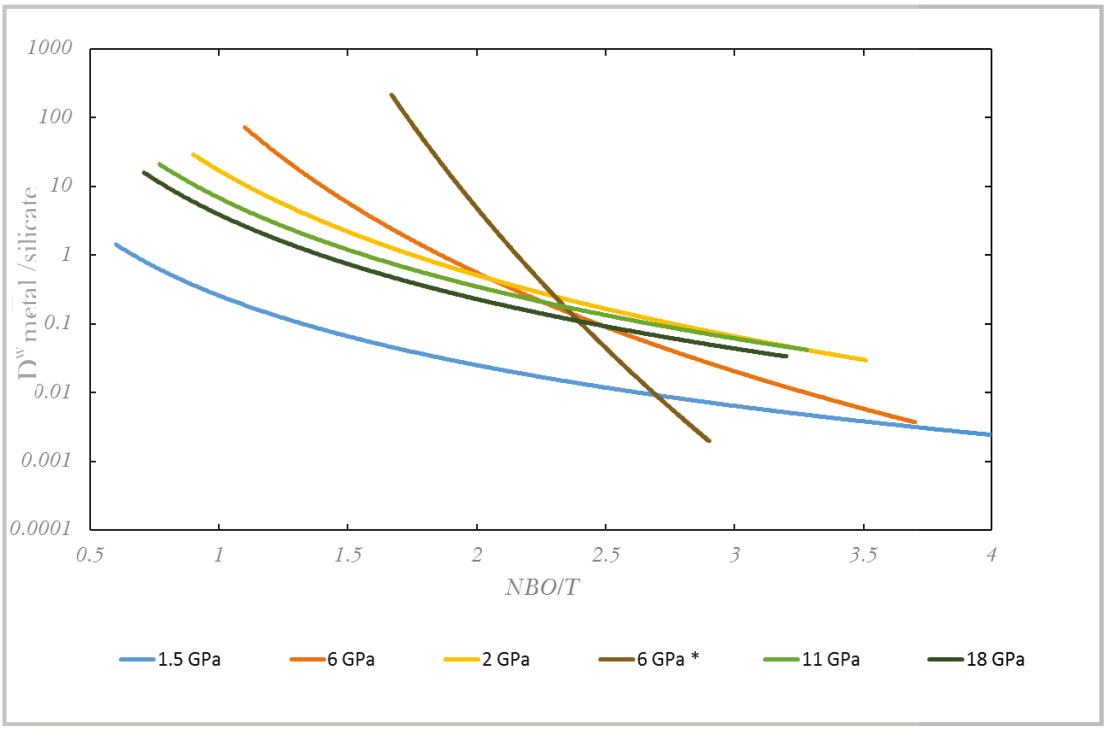

Figure 8 The partitioning coefficient of W show a decreasing trend with the increasing value of NBO/T (0- fully polymerized, 4 fully depolymerized). NBO/T is the ratio of non-bridging oxygens to tetrahedral coordinated cations.The trends represent best fits, the actual datum was omitted for the sake of clarity. 1.5GPa & 6 GPa from Wade et al.,2012*, 6 GPa* and 2 GPa from* Walter & Thibault,1995*, 11GPa and 18 GPa from* Cottrell et al.,2009.

for the dependence of the partitioning of W on the degree of polymerization.

Spin state changes might affect the coordination of elements because of different d-orbitals occupancies. Moreover, the transition of a metal from high-spin to low spin affects its coordination (Zhang et al.,2014) as expected from the change in ionic volume. The intermediate spin states, as the intermediate-spin of Fe for example, or the mechanism of spin crossover has not been investigated in silicate melts. Changes in the atomic volume induced by spin-state changes can, theoretically, facilitate the partitioning of metals in silicate melt. In solids[2], spin crossover of Fe has been predicted by first principles and also observed experimentally (Cohen et al.,1997; McCammon et al.,2008; Umemoto et al.,2008). (Fe,Mg)O presents a Fe spin crossover associated with a change in volume (Crowhurst et al.,2008) whereas in

[2] ***A more extensive discussion is found in the Introduction to Chapter 4.***

bridgmanite it might facilitate the incorporation of Fe^{3+} (Badro et al.,2003a; McCammon et al.,2008; Umemoto et al.,2008; Badro et al.,2004).

For the experimental observations of spin-state changes in solids, electron (XES) and Mossbauer spectroscopies are the tools of choice (McCammon et al.,2008; Prescher et al.,2014; Chen et al.,2012; Badro et al.,2004; Badro et al.,2003a; Badro et al.,2003b; Badro,2014). For amorphous materials the experiments are confined to the use of glasses as proxies. Because of this, first principles molecular dynamics is a tool unrestricted by phase, temperature, and pressure, to study the spin-state behaviour of silicate melts in the Earth's mantle pressure regime. If spin state changes of transitional metals are also observed in silicate melts, the effects they might have on their EOS and their partitioning into other phases can have a tremendous impact on the chemical evolution of Earth and other planetary bodies. For example, Nomura et al.,2011 finds a spin-crossover in Fe at 76GPa, and interprets their findings as the cause for a kink in the partitioning of Fe. They used $(Mg_{0.95}, Fe_{0.05})SiO_3$ glass as a proxy for melt in their X-ray emission spectroscopy experiments. If the spin state of an element in an amorphous solid is influenced by the short range order around it then, glasses cannot be adequate proxies for melts. From a slightly different perspective, temperature can affect the delta splitting energy and it can provide the activation energy required for a spin crossover. Another argument would be that glasses retain the short range order of the stable solid phases of their isobar (Goodman,1975; Ferlat et al.,2012), thus the spin-state change in a glass would be more relevant for their equivalent solids rather than for the melt they are supposed to mimic. Due to these differences between glasses and melts and benefiting from the advantages of first principles molecular dynamics we have chosen to study the spin state of transitional metals in silicate melts.

The existence of silicate melts in the lower mantle has been hypothesized as an explanation for seismic anomalies found in the lowermost regions of D" (Williams & Garnero,1996; Labrosse et al.,2007; Hier-Majumder,2008; Rost et al.,2005). These anomalies are called Ultra-Low Velocity Zones, because of the substantial decrease in the seismic waves velocities (Garnero & Helmberger,1995). The most pronounced

decrease in velocity is seen in the shear-wave velocities (Vs), and it has been estimated between 20-30% lower than PREM (Williams & Garnero,1996; Cottaar & Romanowicz,2012; McNamara et al.,2010; Brown et al.,2015). Because melts lack the shear modulus component, the existence of partial melt inside the Ultra-Low Velocity Zones might be the answer to their origins (Labrosse et al.,2007) and composition (Williams & Garnero,1996; Rost et al.,2005). Besides the low velocities associated with Ultra-Low Velocity Zones, they have been interpreted as having higher densities than the surrounding mantle, and explaining further the decrease in velocity (Williams & Garnero,1996; Garnero & Helmberger,1995). Based on the high density expectations, Fe enrichment in the Ultra-Low Velocity Zones is expected (Williams & Garnero,1996; Rost et al.,2005; Labrosse et al.,2007; Brown et al.,2015). Several explanations for the nature of the Ultra-Low Velocity Zones have been proposed in the past.

A solid state Ultra-Low Velocity Zones has been proposed by Wicks et al.,2010 in which the phase responsible for the high density and low seismic velocities is $(Mg_{0.16},Fe_{0.84})O$. The model created to explain the Ultra-Low Velocity Zones used a Voight-Reuss-Hill mixing of the experimentally measured compressional properties and density of $(Mg_{0.16},Fe_{0.84})O$ with PREM. The most important shortcoming of this study, is the lack of chemical information. Since the model is based on a mixture of $(Mg_{0.16},Fe_{0.84})O$ with PREM the chemical information of the silicate part, which must exist, cannot be quantified.

Another solid state explanation for the Ultra-Low Velocity Zones involves the presence of Fe-rich post-perovskite (Mao et al.,2006). This possible origin of the Ultra-Low Velocity Zones links their location in the D" with the existence of the dense post-perovskite in the lowermost part of the mantle. The $FeSiO_3$ expected in the post-perovskite is less than 40% (Mao et al.,2006). The authors suggest an accumulation mechanism based on the high density of the post-perovskite and the turbulent nature of the lower D", in order to explain the topography of the Ultra-Low Velocity Zones.

In the last chapter of this work, we apply our results and literature data to construct a chemical and mineralogical model of present-day Ultra-Low Velocity Zones (ULVZ) found on top of the Core Mantle Boundary. We find that a mixture of silicate melt and the major mineral phases of the deep mantle can explain the seismic observations of ULVZs. Our model proposes that ULVZs contain Fe-rich melts and solids, thus making them distinct geochemical reservoirs.

In this work, we present results on the effects of pressure, temperature, degree of polymerization, and transitional metals concentrations, on the spin-state of Fe, Ni, and Co. We propose an explanation for the discrepancies between previous works (experimental and simulations) regarding the spin-state of Fe in silicate melts. In the case of Ni and Co we report a decrease of average spin-state with pressure, achieving a spin crossover in the Earth's mantle pressure range. We propose that the spin state change with pressure is the reason for the kink in the partitioning coefficients of Ni and Co with pressure. Moreover, the spin state change is also seen as a perturbation of the Ni-O coordination trend with pressure.

In conclusion, this work aims to provide new results and interpretations that will lead to a better understanding of silicate melts throughout the deep Earth. Comprehensive knowledge of the structure and the behaviour of trace metals in silicate melts can reveal the mechanisms behind their interactions with other phases. A well-known EoS and its variation with compositional changes can answer important dynamical questions regarding the crystallization of the Magma Ocean and the later evolution of the Earth's Mantle.

2. *First principles molecular dynamics:* *Theory and Methods*

2.1. Density Functional Theory Overview

2.1.1. Schrodinger's equation

The Schrodinger equation (eq. 1) represents the quantum mechanical equivalent of Newton's equation of motion. It describes the quantum state of a system as a function of time. At a subatomic scale, particles, such as fermions (e.g. electrons) are subjected to the duality principle and thus can be treated as waves. Wave functions (also known as state functions) describe the quantum state of an isolated particle or many particles.

For a given system containing *n* particles there is only *one* wave function that contains the entire information about that system. Unfortunately natural systems are composed of many atoms, meaning a very large number of nuclei and electrons (*n*), and this turns the Schrodinger equation into a many body problem (Ψ is the many-body wave function) with a very large number of unknowns.

Using the wavefunction, the time-dependent Schrodinger equation is:

$$i\bar{h}\frac{\partial}{\partial t}\Psi = \widehat{H}\Psi \qquad (1)$$

where $\bar{h}$ is the Plank constant divided by 2π; $\frac{\partial}{\partial t}$ is the partial derivative with respect to time, Ψ is the wave function of the quantum state, and $\widehat{H}$ is the Hamiltonian.

The Hamiltonian describes the total energy of a given wave function, and has different forms depending on the system described.

If we consider a system as the one in Figure 9, with a number of atoms and their corresponding electrons, the Hamiltonian of the system would be:

$$\hat{H} = \sum_A -\frac{\bar{h}^2 \nabla^2_{\vec{R}_A}}{2M_A} + \sum_A -\frac{\bar{h}^2 \nabla^2_{\vec{r}_i}}{2m_i} + \frac{1}{2}\frac{1}{4\pi\varepsilon_0}\sum_{A\neq B}\frac{+e^2 Z_A Z_B}{|\vec{R}_A - \vec{R}_B|} + \frac{1}{2}\frac{1}{4\pi\varepsilon_0}\sum_{i\neq j}\frac{-e^2}{|\vec{r}_i - \vec{r}_j|} + \frac{1}{4\pi\varepsilon_0}\sum_{i,A}\frac{-e^2 Z_A}{|\vec{r}_i - \vec{R}_A|} \quad (2)$$

where M is the mass of the nucleus and m is the mass of the electron.

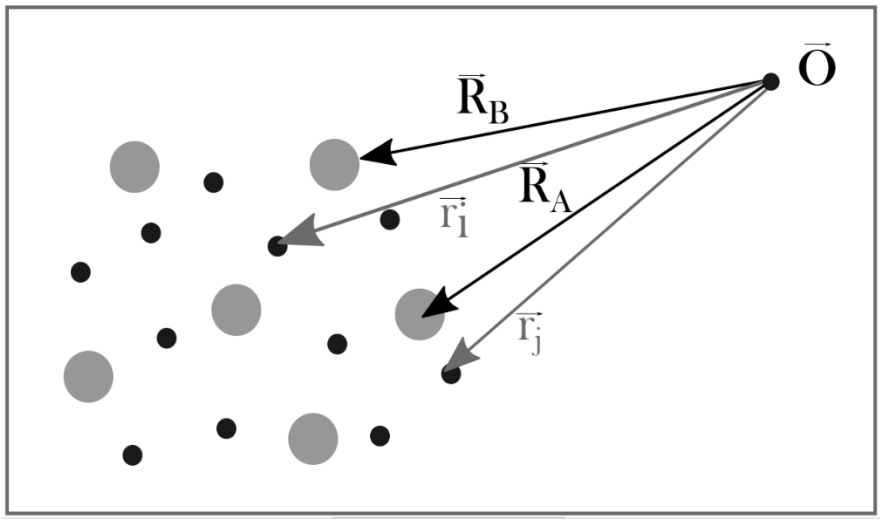

Figure 9 A theoretical system consisting of nuclei and their electrons. Their positions can be described by position vectors.

The first and second terms of eq. 2 correspond to the kinetic energy of the nuclei and the electrons respectively; the third and the forth are the Coulomb interaction between the nuclei and between the electrons, and each other.

If one is able to solve the many body wave function corresponding to a system of particles, as a condensed matter system for example, one can get from the Schrodinger equation the total energy of that system. Knowing the wave function of the system means that one can know everything that it is to know about that system.

$$\hat{H}\Psi = E_{Tot}\Psi \quad (3)$$

Equation 3 represents the time independent Schrodinger equation. In the time-independent Schrodinger equation, Ψ can form stationary states (or i.e. orbitals), knowing these states the time dependant equation is easier to solve. However, this is

not a general statement, equation 3 has physical meaning only when $\widehat{H}$ is time independent which is the case for non-relativistic problems.

Because of the many-body character of the wave function, the resolution of the Schrödinger equation is not analytical, except for the H atom, nor it is tractable computationally for a realistic system. A solution to this problem was proposed in the mid-60s with by Khon and Sham's Density Functional Theory (DFT).

2.1.2. Kohn-Sham ansatz

Kohn-Sham proposed in the mid-1960s (Kohn & Sham,1965) a new set of equations that re-write the Schrodinger equation and make it solvable without any information loss, provided the exact form of the exchange-correlation potential of that system is known.

In the Density Functional Theory the electrons are replaced by non-interacting quasi-electrons in order to reduce the complexity of the problem and make it solvable. These quasi-electrons interact with the nuclei and the interaction between each-other is described by an external exchange-correlation field. This field replaces the actual electron-electron interaction. The mathematical form of this exchange-correlation field is the Exchange-Correlation functional. For each unique system of particles exists a unique exchange-correlation field.

A corner-stone in the Density Functional Theory is represented by the Hohenberg-Kohn theorems (Hohenberg & Kohn,1964).

The electronic density of a system is shown in equation 4.

$$\rho_{(\vec{r}_{i,j})} = \left|\Psi_{(\vec{r}_{i,j})}\right|^2 \tag{4}$$

As it can be observed there is a direct link between the electronic density of a system and its wave function Ψ. In other words, there is no information loss in re-writing the wave function as an electronic density. This is known as the first theorem of Hohenberg and Kohn. Any property of a system at its ground state can be written as a unique functional of the electronic density:

$$E = \langle \Psi \left| \widehat{H} \right| \Psi \rangle = O_{[\rho]} \tag{5}$$

The second theorem of Hohenberg and Kohn states that the ground state energy of a system can be obtained by finding the electronic density that minimizes the total energy. This new density is the electronic density of the ground state.

These two theorems are exploited in the DFT, and are used to help solve the Kohn-Sham equation:

$$\left(-\frac{\bar{h}^2}{2m} \nabla^2 + V_{EXC(\vec{r}_i)} \right) \phi_{i,j(r_{i,j})} \quad = \epsilon_i \phi_i(r) \tag{6}$$

where m is the mass of the electron, V_{EXC} is the exchange-correlation potential, ϵ_i is the Kohn-Sham orbital energy, and ϕ_i is the density of the system.

Since the great ansatz introduced by Kohn and Sham is to assume that a system of non-interacting fermions suspended in an external exchange-correlation potential behaves the same as a natural system, the problem is only reduced to finding the correct Exchange-Correlation potential.

2.1.3. Exchange-correlation functional and pseudopotentials

Kohn & Sham,1965 have envisioned a theoretical system in which the nuclei are smeared across the available space. This non-localization of the nuclei makes the electrons form a homogenous distributed gas (jellium). In such a system, one can calculate the density of the system as a function of spatial position and used it as a first hand approximation to find the form of the Exchange-Correlation functional. This method is known as the Local Density Approximation (LDA) and in spite the predictions of Kohn and Sham that it will not be able to simulate any real system, it works for certain systems.

Since the 1970s more complex and accurate functionals have been developed and used, as the General Gradient Approximation (GGA) or more accurate GGA forms as PBE (Perdew-Burke-Ernzerhof) (Perdew et al.,1996) etc.

The short-coming is that LDA and GGA do not work for every system, and great care should be taken when choosing a functional.

The complexity and accuracy of an exchange-correlation functional can be described in terms of the so called "Jacob's Ladder" (Perdew et al.,2005). In this schematic view the LDA would occupy the first rung of the ladder and GGA the second, building up by keeping what is good in each previous functional and increasing the accuracy. The last rung of the ladder would be the "divine" absolute functional (Mattsson,2002).

In simpler terms, the electrons responsible for the properties of a material are the valence electrons. As such a simplification can be made, the entire electrons of an atom can be split into two parts, the core electrons (electrons that do not participate in bonding) and valence electrons (Figure 10). The complex Coulombic interaction of the core electrons with the nucleus can be replaced by a pseudopotential, a

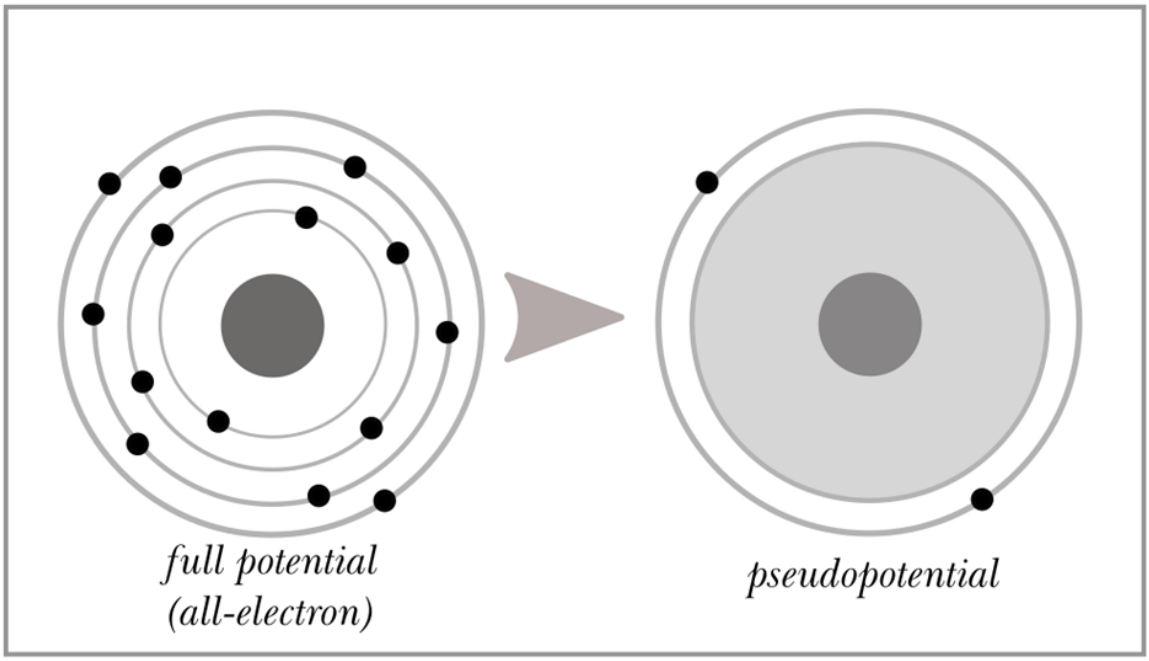

Figure 10 Schematic representation of a pseudopotential for a fictitious atom. The electrons that do not contribute to bonding have been replaced by a functional, represented here schematically as the grey homogenous region in the right-hand sketch.

functional that mimics this complex interaction.

One very important motivation for the use of pseudo-potential is that they reduce the number of basis set size, thus allowing for a significant decrease in

computational resources (see section 2.2). Without this, the computational handling of heavy elements would be impossible.

2.1.4. Born-Oppenheimer approximation

The Born-Oppenheimer approximation assumes that the wave function of a system can be broken down into its electronic and nuclear components. As the name states, this is just an approximation and not the reality of nature but it models the natural system reasonably well.

$$\Psi = \Psi_e \times \Psi_n \tag{7}$$

This splitting of the wave function make the calculation of the total energy more feasible by dividing the calculation in two parts. Due to the important mass difference between the nuclei and the electrons, the nuclei move much more slowly than electrons. As an approximation one can consider the electrons as moving in a field of static nuclei, reducing equation 2 to:

$$\hat{H} = \sum_A -\frac{\bar{h}^2 \nabla_{\vec{r}_i}^2}{2m_i} + \frac{1}{2}\frac{1}{4\pi\varepsilon_0} + \kappa + \frac{1}{2}\frac{1}{4\pi\varepsilon_0}\sum_{i\neq j}\frac{-e^2}{\left|\vec{r}_i - \vec{r}_j\right|} + \frac{1}{4\pi\varepsilon_0}\sum_{i,A}\frac{-e^2 Z_A}{\left|\vec{r}_i - \vec{R}_A\right|} \tag{8}$$

where κ is the Coulomb interaction of the nuclei. Since the nuclei are considered static this interaction is a constant. κ is also known as the static external potential V^{ext}.

The Hamiltonian can be re-written as:

$$\hat{H} = V^{ext} + \hat{F} \tag{9}$$

where $\hat{F}$ is the same for all systems containing the same number of electrons since the uniqueness of the system is given by the positions of the nuclei contained in V^{ext}. Hohenberg & Kohn,1964 state through their first theorem that the external potential (V^{ext}) is uniquely determined by its ground state electronic density to within an

additive constant. In other words there is just one position of the nuclei in the ground state of a system.

2.1.5. Applying the DFT

In order to solve the Kohn-Sham equations for a given system three things need to be implemented:

1. The Exchange Correlation Functional, here we will use the Perdew – Burke – Ernzerhof functional (PBE) (Perdew et al.,1996).
2. The method by which one chooses to solve the Kohn-Sham equations. The method that we choose was the Projector Augmented Wave approach (PAW) (Kresse,1999; Blochl,1994).

The computer code. we used the tools mentioned in 1 & 2 as they are implemented in the VASP code (Kresse,1995; Kresse & Hafner,1994; Kresse & Furthmüller,1996; Kresse,1996).

2.2. *First principles Molecular Dynamics using PAW and PBE as implemented in the VASP code*

2.2.1. *First principles molecular dynamics*

In molecular dynamics (MD) the atoms move according to Newtonian mechanics under the action of interatomic forces. In classical MD the electronic interactions are replaced by simplified interatomic potentials. This short coming, the need to know the exact potentials for any given system limits the method substantially. The replacement of one atom in the system with a new atomic species requires the change in the potentials used.

In ab initio molecular dynamics, also called first principles molecular dynamics, the movement of the nuclei obeys the classical equations of motion under the action of interatomic forces computed in a fully first principles framework (Figure 11).

There are several approaches to first principles molecular dynamics but here the focus will be on Born-Oppenheimer molecular dynamics (Payne et al.,1986; Payne et al.,1992).

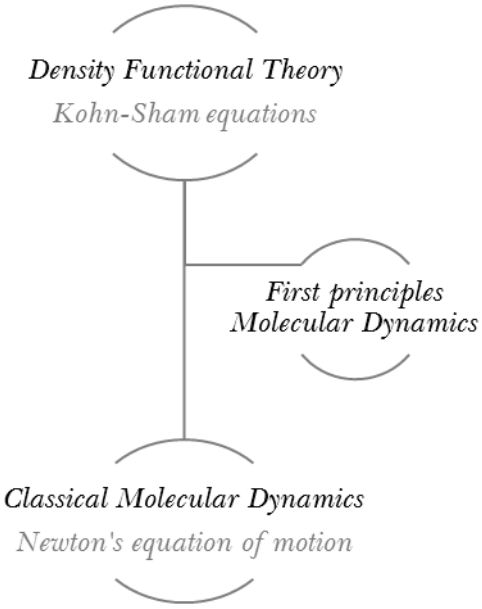

Figure 11 The relationship of ab initio molecular dynamics with the DFT and classical dynamics. The Kohn-Sham equations and Newton's equation of motion are used to describe the electronic and nuclei dynamics, in what is called First Principle Molecular Dinamics.

As it was mentioned in a previous section the Born-Oppenheimer approximation offers a way of decoupling the nuclei contribution and the electronic contribution to the wave function.

For each instance of time the electronic contribution is solved as a static contribution by solving the time-independent Schrodinger equation. This assumption is made based on the idea that the electrons adjust instantaneously in their equilibrium positions after the movement of each atomic nuclei. Nuclei propagation is done concurrently and is solved by classical mechanics means (a Verlet algorithm; Verlet,1967).

Thus one can write the Born-Oppenheimer molecular dynamics as:

$$MR(t) = -\nabla_i min_{\Psi_0}\{\langle\Psi_0|H_e^{KS}|\Psi_0\rangle\} \quad (10)$$

$$E_0\Psi_0 = H_0\Psi_0 \quad (11)$$

where M is the mass of the nucleus, R it's position (as in Figure 9), and t the time, the H_e^{KS} is the Hamiltonian describing the Kohn-Sham electronic contribution.

The minimum of H_e^{KS} has to be reached at each time-step by diagonalizing the Hamiltonian.

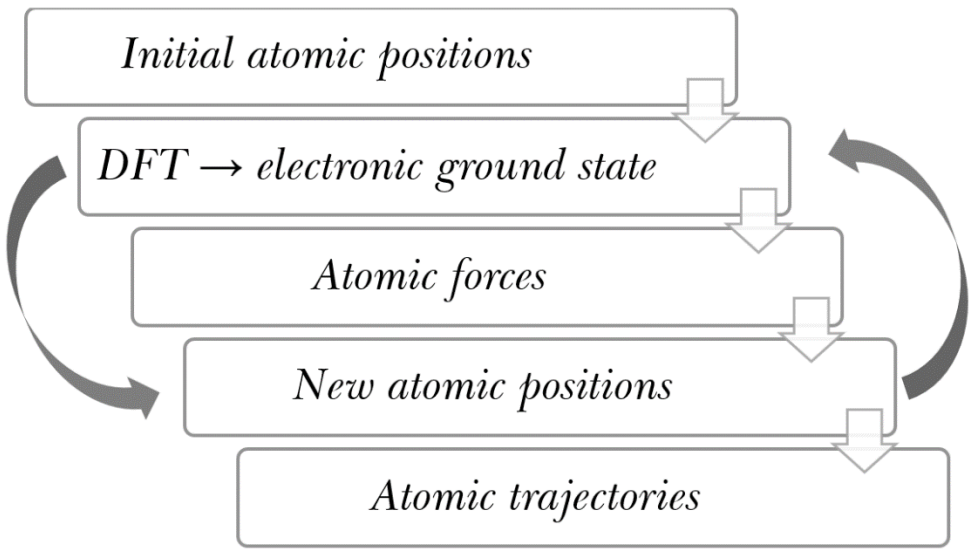

Figure 12 Diagram representation of the Born-Oppenheimer molecular dynamics. The arrows represent the molecular dynamics loop that is repeated n times. Each converged loop equals a time step.

2.2.2. *Perdew-Burke-Ernzerhof approximation (PBE) for the exchange-correlation functional*

An improvement over the LDA is the General Gradient Approximation (GGA) which can be described as:

$$E_{EXC}^{GGA}[n_{\uparrow}, n_{\downarrow}] = \int d^3 r f(n_{\uparrow}, n_{\downarrow}, \nabla_{n_{\uparrow}}, \nabla_{n_{\downarrow}}) \tag{12}$$

as opposed to the LDA where the gradient part is missing and the exchange-correlation energy of a particle in a uniform electron gas replaces the gradient ($\epsilon_{EXC}^{jellium}(n_{\uparrow}, n_{\downarrow})$).

Perdew et al.,1996 propose an improved GGA which fixes the most pronounced caveats of previous GGA derivations paving the way for a simpler and more efficient GGA. Their solution is to replace all parameters with the exception of $\epsilon_{EXC}^{jellium}(n_{\uparrow}, n_{\downarrow})$ with fundamental constants. Their resulting GGA derivative is called PBE.

$$E_{EXC}^{PBE}[n_{\uparrow}, n_{\downarrow}] = \int d^3 r n \, \epsilon_{EXC}^{jellium}(n_{\uparrow}, n_{\downarrow}) F_{EXC}(r_s, \zeta, s) \tag{13}$$

F_{EXC} is an enhancement factor over local exchange; r_s is the local Seitz radius, ζ is the relative spin polarization $= \frac{n_{\uparrow} - n_{\downarrow}}{n}$; s is a dimensionless density gradient.

In this formulation of the GGA, exchange dominates the high density limit as $r_s \to 0$ and correlation dominates the low density limit.

PBE is a very efficient functional, it is versatile and accurate within its limitations. It is superior to previous GGA formulations in accuracy. Being a part of GGA class of functionals, PBE is a better alternative to LDA in the study of metals due to its non-localization.

2.2.3. Projector augmented wave approach (PAW)

After replacing the all-electron potential of an atom with a pseudopotential, due to the orthogonality constraint that must be applied onto the valence wave functions and the core waves, powerful oscillations occur and complicate the calculations. One way of circumventing this problem is to smooth this rapidly oscillating wave functions.

Firstly, the space (Ω) is divided in two distinct regions, the non-overlapping regions around the atoms Ω_a , and the inter-atomic region Ω_i.

$$\Omega = \Omega_i + \bigcup_a \Omega_a \tag{14}$$

The difficulty of using plane waves basis sets in the Ω_i space is resolved by introducing auxiliary wave functions that satisfy two important conditions:

- The auxiliary wave function ($\tilde{\phi}_i(r)$) must be obtained from the all-electron wave function ($\phi_i(r)$) using an irreversible linear transformation.
- $\tilde{\phi}_i(r)$ must be smooth. The smoothness conditions ensures the capacity to use plane wave basis sets in the entire space.

These two conditions imply that the Kohn-Sham equations can be solved in terms of $\tilde{\phi}_i(r)$ using plane waves basis sets, which simplify the calculations substantially.

As mentioned in *Section 1.2*, there is a direct link between the wave function and the electronic density. Thus the new, smooth inter-atomic electronic density is:

$$\tilde{\rho}_r = \sum_i f_i \left|\tilde{\phi}_i(r)\right|^2 \tag{15}$$

And the true all-electronic density can be written as:

$$\rho_r = \tilde{\rho}_r + \sum_a \rho^a(r - R_a) - \sum_a \tilde{\rho}^a(r - R_a) \tag{16}$$

where ρ^a and $\tilde{\rho}^a$ are the normal and smooth atomic centre electronic densities.

This transformation is the PAW method (Blochl,1994).

In recent years the PAW method has been included in many first principles simulation packages. PAW method allows for faster computations (Blochl,1994) , and it is widely used in the study of Earth materials (Pozzo et al.,2012; Karki et al.,2011; Muir & Brodholt,2015; De Koker,2010; Bengtson et al.,2008; Stackhouse et al.,2005; Stackhouse et al.,2006; Bouchet et al.,2013; Journaux et al.,2014 etc.). Its accuracy is well established and is in good agreement with experimental data in the limits of DFT and the functionals being used. For all these reasons we have chosen to use PAW.

2.2.4. Berendsen thermostat as an example of temperature handling

One of the most computationally viable methods of treating temperature is the Berendsen thermostat (Berendsen et al.,1984).

Unlike previous methods, Berendsen et al. propose a non-modifying Hamiltonian approach which they call "weak coupling to an external bath". De facto, they propose the scaling of ionic velocities by coupling them to an external heat bath of a fixed reference temperature (T_0).

$$\frac{dE_k}{dt} = \sum_{i=1}^{3N} v_i F_i + 3N\gamma k(T_0 - T) \tag{17}$$

E_k is the kinetic energy, t is time, N is the number of atoms, v_i is velocity, γ is the damping constant (the coupling between the system and the bath).

The pressure correction due to thermal agitation in the Berendsen formalism is:

$$P = \frac{2}{3V}(E_k - \Xi) \tag{18}$$

$$\Xi = -\frac{1}{2}\sum_{A<B} r_{AB} \cdot F_{AB} \tag{19}$$

F_{AB} is the force on atom A due to atom B. V represents the volume of the simulation cell and it's the determinant of the matrix formed by the three vectors that represent the edges of the cell.

In terms of implementation, Berendsen et al. propose a leap-frog algorithm through the SHAKE procedure (Ryckaert et al.,1977). SHAKE is consistent with the Verlet algorithm. The schematic representation of this algorithm is shown in Figure 13.

All the steps presented in Figure 13 are incorporated in the last 3 steps present in Figure 12.

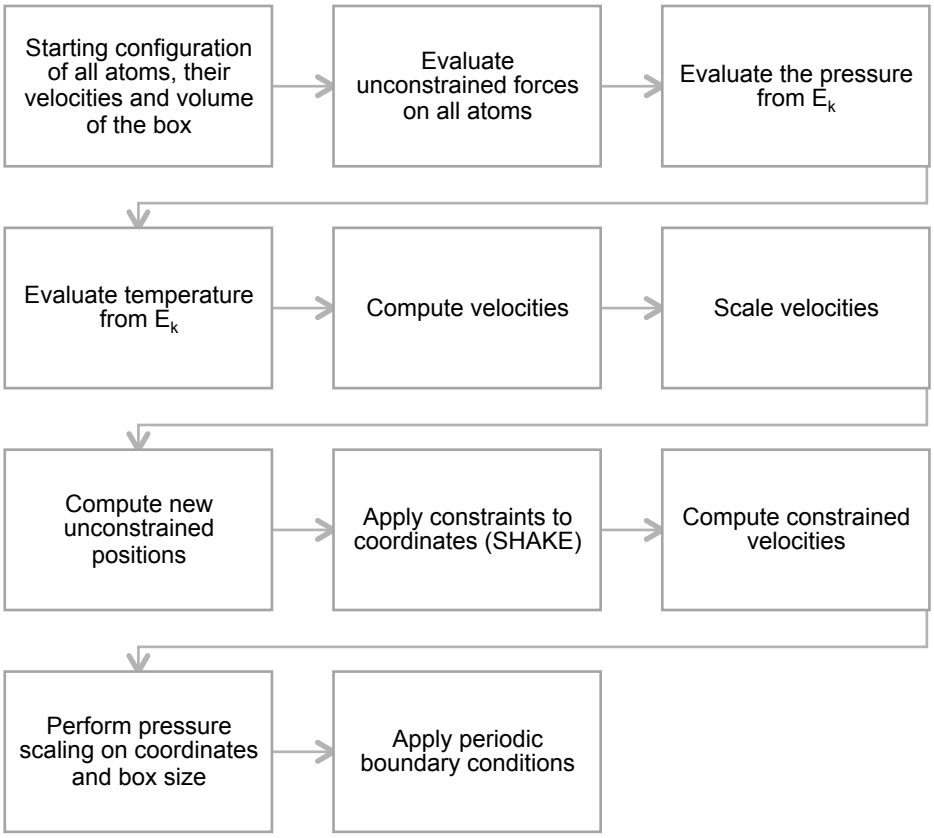

Figure 13 Berendsen et al. algorithm. Periodic boundary condition is the mathematical procedure that moves back inside the simulation cell atoms that have moved outside of it. This is done by replacing their coordinates with their mirror coordinates inside the box.

2.3. *Simulation set-up*

DFT offers the perfect conceptual framework for simulating the behaviour of condensed matter at different thermodynamic conditions. Due to fast and reliable algorithms as the Berendsen thermostat, deep Earth conditions are easily simulated and a wide range of physical and chemical properties can now be calculated.

Advances in computational power in the form of supercomputers with PFLOPS capabilities have made DFT based codes viable and systems containing hundreds of atoms possible. For this work we use JADE and OCCIGEN supercomputers hosted at the CINES computing centre.

The main difference between first principles approach and the experimental one is the size of the "sample", but this deficiency is compensated by the richness of the information that can be obtained from ab initio methods (total energy, heat capacity, structure, free energy, etc).

In this work, we will present results obtained from First Principles Molecular Dynamics performed in the PAW methods with PBE as implemented in the VASP code on silicate melts.

2.3.1. *Computational details*

First principles Molecular Dynamics were performed using VASP (Kresse & Hafner,1994; Kresse & Furthmüller,1996; Kresse,1996; Kresse,1999) code on CINES supercomputers. The simulation details are:

- Cut-off energy of the plane waves: 550 eV
- 1 K-Point, the Gamma point in the Brillouin sampling zone[3]
- Born-Oppenheimer molecular dynamics
- Berendsen et al.,1984 thermostat for temperature control
- Spin polarized calculations for the cells containing Fe, Ni and Co. Non spin polarized calculations for the rest.

[3] The Gamma point is the central sampling point in the irreducible Brillouin zone. It is where the properties are sampled, by integration over the point's zone.

The choice of only 1 K-point, the Gamma provides faster computations. Liquids are disordered phases and the Gamma point provides sufficient sampling. Previous studies have used the Gamma point successfully in computing liquids properties (de Koker et al.,2008; Zhang & Guo,2009; Karki et al.,2013b; Karki et al.,2006).

Supercells of enstatite and forsterite were created and heated at 5000K in order to achieve melting. Afterwards they were cooled at 3000K and 4000K and thermalized for 1ps (the time step of the simulations is 1fs). Fe was added by replacing the desired amount of Mg atoms with Fe ones. Ni, Co and W were added without any replacement by positioning the atoms in available spaces using the *particle in a cell* method. The configurations of these supercells is:

- 4x4 $MgSiO_3$ clino-enstatite supercell containing 160 atoms. Replacing some of the Mg atoms with Fe or just adding Ni we obtained the following compositions:
  - $Mg_{32}Si_{32}O_{96}$
  - $(Fe_1, Mg_{31})Si_{32}O_{96}$
  - $(Fe_3, Mg_{29})Si_{32}O_{96}$
  - $(Fe_6, Mg_{26})Si_{32}O_{96}$
  - $(Fe_{16}, Mg_{16})Si_{32}O_{96}$
  - $Ni_1Mg_{32}Si_{32}O_{96}$
  - $Ni_2Mg_{32}Si_{32}O_{96}$
- 4x4 Mg_2SiO_4 forsterite supercell containing 112 atoms. Replacing some of the Mg atoms with Fe or just adding Ni, Co, and W we obtained the following compositions:
  - $Mg_{32}Si_{16}O_{64}$
  - $(Fe_1, Mg_{31})Si_{16}O_{64}$
  - $(Fe_6, Mg_{26})Si_{16}O_{64}$
  - $Ni_1Mg_{32}Si_{16}O_{64}$
  - $Co_1Mg_{32}Si_{16}O_{64}$
  - $W_1Mg_{32}Si_{16}O_{64}$

- A $CaW_3Mg_{26}Si_{64}O_{161}$ created by making a $Mg_{32}Si_{16}O_{64}$ supercell melt and removing MgO in order to reach the desired NBO/T value of 1. In the resulting melt (a 4x1x1 supercell) CaO and WO_2 were added, the melt was thermalized and 14 ps of run were generated.

Because of the large numbers of atoms present in each of our simulation cells, 100 or more, the finite-size uncertainties for the properties of interest in this study are negligible (Karki,2015; Zhang et al.,2004).

The results from these simulations are detailed in the next chapters.

2.3.2. VASP input files

VASP package requires a minimum of 4 input files. These files consist of command files that detail the type of simulation and the conditions at which it will be performed (INCAR and KPOINTS), an atom position and cell size information file (POSCAR), and a pseudopotential file (POTCAR).

In the INCAR file the details of the simulations are listed and parameters of the parallelization are specified. A typical INCAR file for non-spin-polarized simulation is detailed below:

- ENCUT tag sets the energy cut-off. We chose the value 550 eV, without performing convergence tests. Previous studies used a lower cut-off value for silicate melts while using the same simulation package, 400 eV (Zhang & Guo,2009; Stixrude et al.,2009; de Koker et al.,2008; Karki et al.,2011; Bajgain et al.,2015). Our higher ENCUT ensures an accurate evaluation of properties.
- ENAUG tag defines the kinetic energy cut-off for the augmentation charges. Out value is 1400 eV. This value is responsible for the density of the FFT-grid, a value of >2ENCUT ensures a dense grid which in turn increases the accuracy of the evaluation of properties.
- The above mentioned two tags coupled with PREC (precision) dictate the degree of precision of the simulation. We set PREC=High, meaning that wrap around errors are avoided. The determination of the density of the FFT-grid for this setting is heuristically determined in conjecture with ENCUT.

- The LREAL tag defines the space in which the projection operators are evaluated. We used LREAL=Auto, evaluating the projector operators in real space, i. e. the projection operators are confined to spheres surrounding each atom. This method allows for a reduction of operation necessary to evaluate the projected wave-function character. For this setting the projection operators are evaluated on start-up by VASP, and their evaluation is influenced by ENCUT and PREC. Everything beyond the ENCUT, 500 eV, is removed from the projection operators. For PREC=High, the accuracy is $2 \cdot 10^{-4}$.
- ALGO tag determines the electronic minimisation algorithm. The ALGO=Fast tag was used. This tag is a mixture between blocked Davidson block iteration scheme and RMM-DIIS. The blocked Davidson iteration scheme is employed by VASP in the initial phase and then it switches to RMM-DIIS.
- EDIFF tag defines the accuracy for the electronic minimization. The value we specified is 5.0-E-03.
- BMIX is the cut-off wave vector for the Kerker mixing scheme.
- NELM tag defines the number of electronic steps. For our simulations we used NELM = 100
- NSW is the tag that allows the user to define the number of ionic steps made in the simulation. The number of ionic steps performed in each simulation was a mainly determined by the number of atoms present in the simulation cell (rule of thumb, cells containing a small number of atoms run faster) and the maximum job time allowed for each job on a certain machine (JADE or OCCIGEN). This time varied between 24h maximum time per job or 72h. For non-spin polarized computations a few ps of simulations could be achieved in 24h.
- ISTART tag dictates the way in which simulation are started. We kept this tag at ISTART=1, allowing the continuation of simulations from previously finished ones. For this setting VASP reads the WAVECAR file and continues the simulation with the information provided there.
- IBRION tag allows the user to define the way in which ions are updated and moved. We chose molecular dynamics.

- POTIM is the tag used to define the time step. We set POTIM=1 meaning the step size is 1fs.
- NBLOCK is the frequency of computing the pair correlation function and DOS (density of states) and written in XDATCAR , PCDAT, and DOSCAR. NBLOCK=1 means that at each simulation step the ionic positions and DOS are computed and written.
- MDALGO defines the type of molecular dynamics to be performed. We performed standard molecular dynamics.
- TEBEG and TEEND set the beginning and ending temperature during the simulation. The values are in Kelvin and if TEBEG=TEEND the temperature is maintained constant during the simulation.
- SMASS dictates the treatment of temperature through kinetic energy. For the SMASS=-1 a scaling of the kinetic energy through a velocity quench algorithm is performed.

  Temp=TEBEG+(TEEDND-TEBEG) * NSTEP/NSW

  where NSTEP is the current step.

  Between the simulation steps a micro-canonical ensemble is simulated.
- LASPH =.TRUE. includes the non-spherical contributions to the gradient correction inside PAW.
- NBAND tag allows the user to define the number of electronic bands. In our simulation we have always checked that the number of band were sufficient by verifying the occupancy in the OUTCAR file. Several empty band were allowed for a better parallelization.
- ISMEAR value was set to default, ISMEAR=1, Methfessel-Paxton scheme for distributing the partial occupancies for each wavefunction.
- SIGMA determines the width of the above smearing in eV, and it was set as a default.
- The existence of NPAR tells VASP to switch to parallel computing and parallelize over bands. The value of NPAR is dependent on the system type, i.e. no. of bands, and the architecture of the machine. The number of nodes

working on one band must be an integer number of the *total number of nodes requested/NBAND*.

- NSIM is another tag related to parallelization. It relates the number of bands treated by the blocked algorithm.

For spin-polarized simulations two tags were added in order to compute and write the total magnetization of the simulation cell:

- ISPIN=2 triggers the spin-polarized calculations.
- MAGMOM lets the user to specify the initial magnetic moment for each ion. The values inputted for MAGMOM depend on the system, the number of atoms of interest in the simulation cell (Fe, Ni, and Co) and the total number of atoms in the simulation cell.

The total magnetization of the system is computed as $M^{system} = \mu_B(DoS_{\uparrow} - DoS_{\downarrow})$, i.e. from the total number of states containing spin-up configurations the number of states containing spin-down configurations are subtracted. The unit of measurements for M is the *Bohr magneton* ($\mu_B = \frac{e\bar{h}}{2m_e}$), where e is the elementary charge, the $\bar{h}$ is the reduced Plank constant, and m_e is the electron rest mass.

The POSCAR file contains the cell size (defined by cell vectors), the types of

```
1  Ca+W silicate melt(NBO/T=1)
2       1.000000000000
3      18.310590744019        0.000000000000        0.000000000000
4       0.000000000000       18.310590744019        0.000000000000
5       0.000000000000        0.000000000000        9.155295372009
6  Mg  Si   O   W  Ca
7  26  64  161  3  1
8  Direct
9       0.359225545605        0.119399232169        0.508504562958
10      0.089874843269        0.262121403251        0.482978738697
11      0.911440837173        0.754585483806        0.493018714643
12      0.409618237373        0.670765267958        0.456584479016
13      0.381408096626        0.495411625576        0.846533544763
14      0.343181183003        0.716838126325        0.108905865382
15      0.956623958088        0.717992446476        0.106989509296
```

Figure 14 Example of a POSCAR file. The first line is a comment line. The second line is the scaling factor for the simulation cell vectors. Increasing or decreasing this factor results in a larger or a smaller simulation cell, increasing or decreasing the volume and thus the pressure. Lines 3,4, and 5 define the three cell vectors, in this case the cell is tetragonal in symmetry. The lengths of a,b, and c, can be discerned in this case, and their lengths are in Å. Line 6 specifies the types of atoms present, in the same order as defined in the POSCAR file (the pseudopotentials file). In line

atoms, their numbers, and atomic coordinates in a specified system (Cartesian or Direct). The POSCAR file must be created by the user and it must contain all the above. Figure 14 shows and example of the first few lines of a POSCAR file. A POSCAR file must exist for every molecular dynamics simulation. For continuation of a run, the CONCAR file is transformed into a POSCAR file, thus the last atomic positions of the previous simulation become the initial positions of the next one. In CONCAR velocities are also written so the continuing simulation will have as much information as possible from the previous run. Additionally, the user can define in POSCAR velocities, but they are not mandatory for a successful molecular dynamics simulation.

The POTCAR file contains the pseudopotentials for each atomic species, listed in the order given in the POSCAR file. As stated before, PBE functionals are being used.

The KPOINTS file specifies the k-point position. We used the automated generating method for the gamma points. We specified the gamma point division of the Brillouin zone and the shift from that position. A Monkhorst-Pack generating scheme was selected, meaning that each gamma point was shifted in order to create a symmetric mesh centred around the gamma point of the Brillouin zone.

The INCAR, POTCAR, POSCAR, and KPOINTS files must be provided by the user for each simulation. VASP reads but doesn't overwrite any of these files.

2.3.3. VASP output files

The main output file generated by VASP is the OUTCAR file. In this file all the details of the simulation are written. The file also contains all the energies, forces, stress tensors, pressure, temperature, band occupancies, and the simulation cell volume, just to name the most important information. VASP does not use the OUTCAR file as input for further simulations. At the end of the OUTCAR file the total time of the simulation and the memory used can be found if the total number of simulation steps provided by NSW was achieved in the requested job time. If not,

the OUTCAR file does not contain these computing details but it ends abruptly where the simulation was cut short.

XDATCAR file contains all the atomic positions for all the simulation steps. The file is written using the key provided by the POSCAR file. This file can be used to compute structure dependant properties of the simulated system, such as Radial Pair Distribution function.

CONTCAR file is written also in the format of a POSCAR file but after molecular dynamics simulation it also contains the velocities and the predictor-corrector coordinates. Because of this the CONTCAR file is used as a POSCAR file for continuation runs.

OSZICAR file contains the number of convergence steps, the temperature at each converged step and for spin-polarized simulation it also contains the total magnetic moment of the simulation cell. It also contains energy information for each step.

The DOSCAR contains the densities of states (DOS) and the integrated DOS.

2.3.4. Runs for Bader Analysis

Bader analysis requires knowledge of the charge density in the simulation cell. VASP computes this at each step as part of the DFT component of the ab initio molecular dynamics, but it doesn't write by default the specific files CHG and CHGCAR. This process of writing this information is memory expensive. The INCAR tag that triggers the writing of this information is LCHARG which is set to .FALSE. in our production runs because of the memory requirements. If the setting of the tag is changed to .TRUE. then the CHG and CHGCAR files are written.

The CHG file contains the atomic coordinated, the charge density at each 10^{th} step, and the lattice vectors. The charge density being written is multiplied by the volume of the cell on the FFT grid.

The CHGCAR file contains the same information as CHG plus the PAW one-centre occupancies.

We have employed the *aedens* module of VASP, activated by the INCAR tag LAECHG=.TRUE. in order to write new VASP output files: AECCAR0 and AECCAR2.

The AECCAR0 file contains the core charges, and the AECCAR2 contains the valence charge.

We have performed 'snapshot' simulations (taking the atomic coordinates at a specific time step from a simulation run and performing 1 simulation step) using the input files mentioned in the previous session and the new INCAR tags described here for use in the Bader analysis.

Because of the high memory requirements for the LCHARG=.TRUE. and LAECHG=.TRUE. , we have taken from XDATCAR at equal time intervals the positions of the ions in the simulation cell (snap-shots) and created POSCAR files containing this information. The NSW tag in INCAR was set to 1, one molecular dynamics step, in which VASP has computed and written the charge densities. We have performed such short molecular dynamics runs for several snap-shots from our production runs, at every volume.

2.4. Data processing methods

2.4.1. Bader Analysis

In first principles simulations the electronic charge density is computed as the total charge density of the simulation cell. This becomes problematic when one wants to define the charge of a specific atom. The Bader analysis provides a way of doing this. In the beginning of the 1990's Richard F.W. Bader published a new theory dealing with the extent of atoms in molecules and their charges Bader,1991. His approach was intuitive and simple. The space is described as a continuous electronic charge density and the atoms are divided by what he called ***zero flux surfaces*** (Figure 15).

Zero flux surfaces are surfaces in which no flux in the density gradient vector field exist. The density gradient vector field is created by vectors pointing in the

direction of maximum charge density increase, the nuclei. Once the direction is found, infinitesimal steps towards the gradient maxima are made and at each step the gradient is re-evaluated and a new direction is found. So the zero flux surface is where the following relationship is satisfied:

$$\nabla\rho(r_s) \cdot n(r_s) = 0 \qquad (20)$$

where r_s is a point on the surface and $n(r_s)$ is the vector normal to the surface at that point.

These zero flux surfaces are just three dimensional surfaces where the density of charge is minimum. It is intuitive that the space between atoms is the place where the density of charge would be minimum. The zero flux surfaces delimit the atomic Bader volumes. An inevitable outcome of defining atoms in this way is that the resulting atoms shape is not spherical.

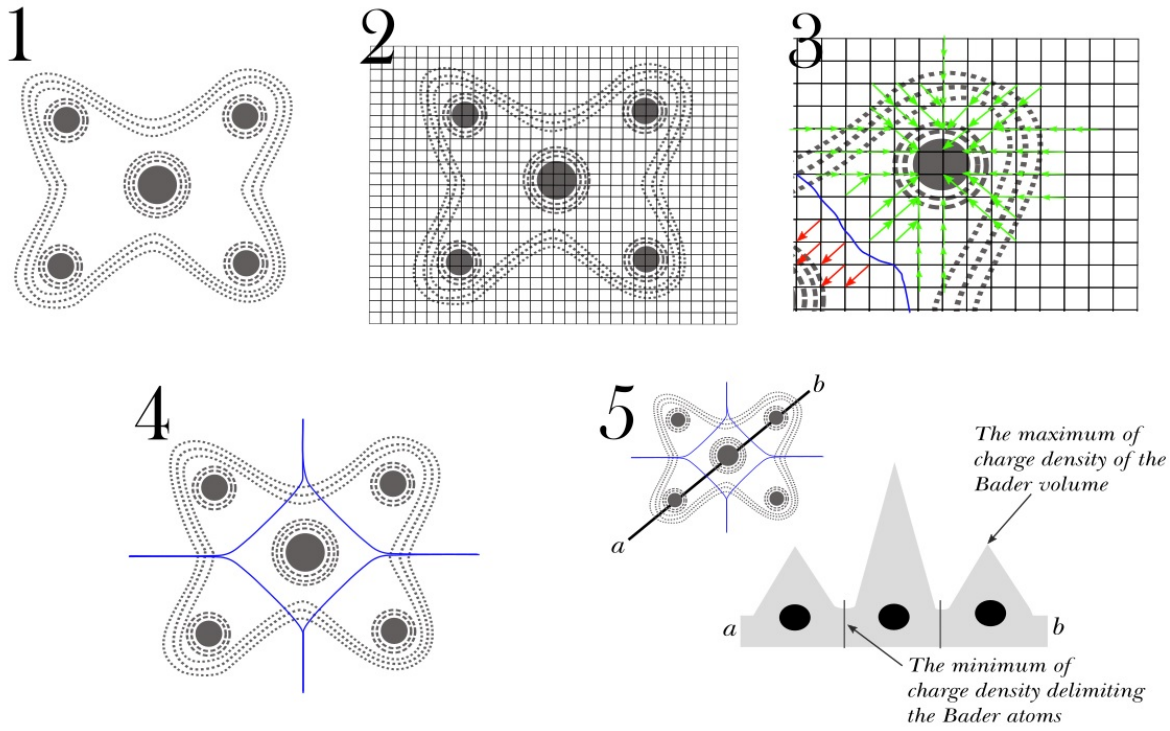

Figure 15 Schematic explanations of the Bader atoms and the algorithms used to compute the Bader charges and volumes. 1) Represents a theoretical molecule. The dashed lines represent core electrons and the dotted lines delimit the valence electrons. 2) A grid is created. 3) The charge density gradient in computed using the steepest ascent method Tang et al.,2009 *and the surface of zero flux are found. 4) The surface is corrected for grid bias. Figure 5 shows the charge density maxima corresponds to the core electrons. For partial charges this contribution must be subtracted.*

The Bader charges are all the charges enclosed in the Bader volume. Subtraction of the contribution of core electrons from the Bader charges gives the partial charge of an atom.

The Bader Charge Analysis program from the Henkelman Group (Tang et al.,2009; Sanville et al.,2010; Henkelman et al.,2006) was used to compute the Bader charges and volumes from VASP output files.

2.4.2. *Radial pair distribution function*

Melts and liquids present a high degree of disorder and a statistical approach to assess the short-range order is required. A distribution function, averaged over the entire length of the simulation, is a suitable choice.

Radial distribution function (RDF) describes the variation of the density in a system of particles from a pre-set reference point. In the case of atoms, it can offer statistical information on the variation of density around a given atomic species.

A simpler form of the RDF is the *radial pair distribution function* (PDF) which only takes into account the variation in density of an atomic species around a given atom. The usefulness of this function, is that it calculates the density by statistical approximation of the numbers of atoms surrounding the given origin point, thus allowing the calculation of the coordination number.

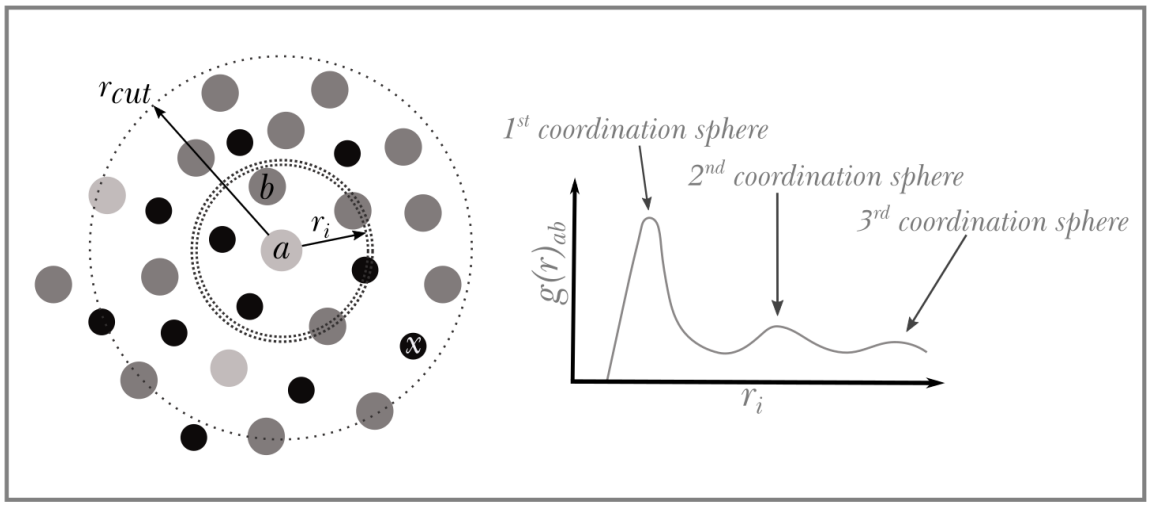

*Figure 16 The PDF of atom **a** with regards to **b** is calculated by counting the interceptions of atom **b** by a sphere centred around **a**. The radius (r_i) of this sphere is increasing in equal steps until it reaches the maximum radius (r_{cut}). This procedure is applied to all atoms of type **a** in the system. Plotting g(r) vs r_i shows the total number of coordination spheres in r_{cut}.*

In order to calculate the coordination number of an atom $\boldsymbol{a}$ by an atom $\boldsymbol{b}$, a sphere of radius r is created around the atom $\boldsymbol{a}$ (Figure 16). The radius of the sphere is increased and the number of b atoms that intersect the sphere is counted. This process is repeated until the cut-off radius is reached. Mathematically this translates as:

$$g(r)_{ab} = \frac{1}{N_a N_b} \sum_{i=1}^{N_a} \sum_{j=1}^{N_b} \langle \delta(|r_{ij}| - r) \rangle \tag{21}$$

Where g(r) is the PDF for the relationship atom a coordination by atom b, N_a and N_b are the numbers of the atoms $\boldsymbol{a}$ and $\boldsymbol{b}$ in the r_{cut} volume.

Plotted, the $g_{(r)}$ looks like in Figure 17, where the first maxima represents the contribution of the first coordination sphere and the 2nd maxima the second coordination and so on. In the case of the Network-forming cations in silicate melts, the first coordination sphere is the most important because it represents the polyhedral coordination of these cations. Si is the most important such cation, and it forms with oxygen tetrahedral configurations at low pressures.

Integration over the first maxima, up the first saddle point, of the $g(r)_{Si-O}$ results in the coordination number of Si by O (Figure 17).

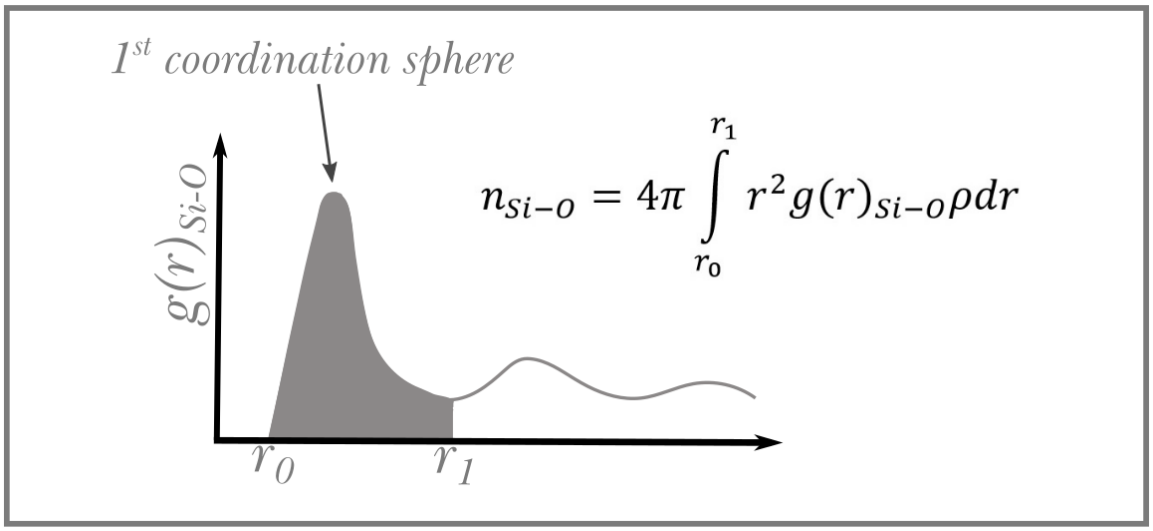

Figure 17 Schematic representation of the integration procedure over the $g(r)_{Si-O}$ of the first coordination sphere. The integration is done between r0 and r1, where r0 is the beginning point of the first maxima and r1 is the first saddle point. The value of the integral given above at the saddle point is the coordination number of Si by O.

In this work, the coordination number of an atomic species by another will represent the average coordination over all the time steps of the simulation for a given, pressure, temperature and composition.

3. The structure of silicate melts up to core-mantle boundary pressure

Unlike crystalline materials, liquids are devoid of long-range order (LO), or translational symmetry. Some liquids may present non-translational short-range order (SO), in the form of small symmetrical units, that repeat unpredictably in the liquid. In the case of silicate melts such units are possible due to the presence of network-forming (or network-modifying) cations. Si and Al are the most important network-forming cations is silicate melts.

Based on the symmetry of these small SO arrangements, they can be described as: monomers, dimers, chains, sheets and three dimensional structures (Mysen et al.,1982).

Melting, the crossing of the melting point with increasing temperature, happens in two main forms: homogenous melting and inhomogeneous melting. In nature, minerals melt inhomogenously with melt progressing from the crystal margins towards the interior, a process mostly driven by the formation of dislocations and their propagation. In the work presented here, FPMD melting was achieved by superheating and thus it is homogenous in nature.

The structure of silicates melts affects their viscosity, density, thermal expansivity (Mysen et al.,1982), diffusivity (De Koker,2010) and the partitioning of elements (Henderson et al.,2006).

The work of de Koker et al.,2008; De Koker,2010 has shown that temperature increase has little to no effect on the coordination changes of Si. Some small temperature dependence might be discerned in the case of Mg between 3000K and 6000K (de Koker et al.,2008).

Here we will present data at 3000K, regarding the structure of silicate melts throughout the Earth's mantle and we will present links to spin behaviour, compressibility, and charge changes.

3.1. Si-O coordination

The Si-O tetrahedron is the building block of all silicates and SiO_2 at low pressures. It is also the structural unit responsible for the density, viscosity, and compressibility of melts due to its crucial role in the polymerization of melts.

Recent experimental studies have shown that the coordination of Si by O changes as a function of pressure in basaltic melts (Sanloup et al.,2013). But the influence of the Si/O ratio on the coordination changes in melts, and the presence of other cations has not been investigated. Here we will present results on two main compositions $MgSiO_3$ and Mg_2SiO_4 with Fe and without, and investigate if other cations (Ni, Co, and W) have an effect on the Si-O coordination.

3.1.1. Si-O coordination in Mg2SiO4 as a function of pressure

PDF was calculated as an average over 4 picoseconds of simulation (4000 steps) using the g(r) plug-in of VMD (Levine et al.,2011). The sphere radius was increased

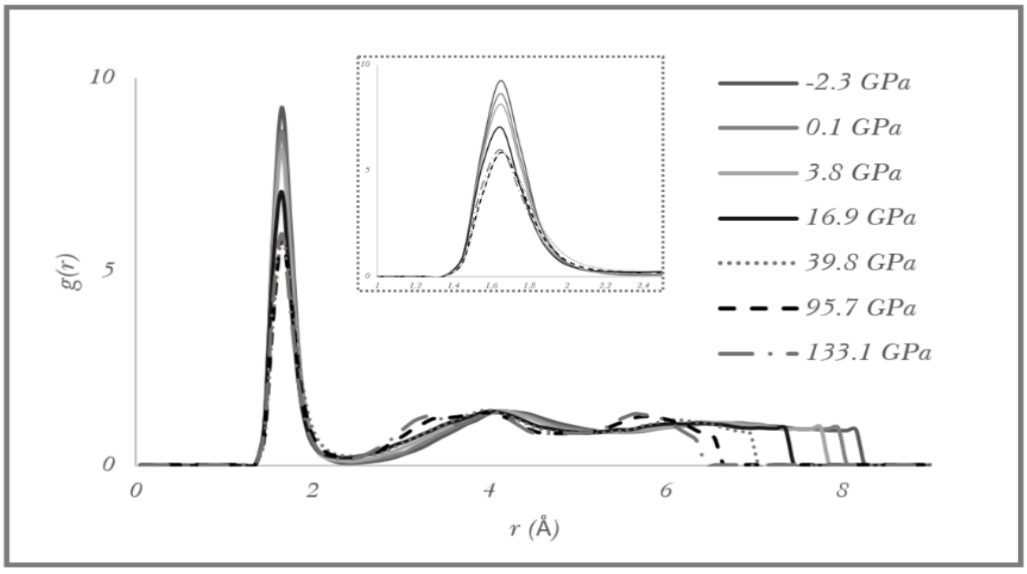

Figure 18 The Si-O pair distribution function g(r) at different pressures in an $Mg2SiO_4$ melts along the 3000K isotherm. Pressure has a substantial effect on the intensity and shape of the coordination spheres as seen in the diminished intensity of the first maximum. The downward shift of the second peak with pressure reflects the compaction of the melt structure under compression. The inset shows in detail the pressure effect on the 1st coordination sphere.

with a step size of 0.10 Å until r_{cut}= 10 Å. The first maximum correlates with the most likely Si-O bond; the first minimum is the radius of the first coordination

sphere. A decrease in intensity with pressure can be observed in the inset in Figure 18. This decrease is continuous with increasing pressure but not linear.

The second coordination sphere is present, and its maxima shift their peak towards lower values of r as the pressure increases (Figure 18). This is the result of increasing compaction to accommodate pressure. The Si-O bond length does not change substantially with pressure as shown by the position of the first maximum (Figure 18).

Integration over the first coordination sphere (Figure 18) yields the coordination numbers of Si-O.

At low pressure the prevalent coordination of Si-O is 4, as the pressure increases the coordination increases as well, and at ≈40 GPa the Si-O coordination number is 5. At this pressure, 4, 5, and 6 Si-O coordination numbers coexist (Figure 19). This is consistent with the findings of Karki & Stixrude,2010 on SiO_2 melt.

Since the PDF is an average over all time steps, the coordination number of Si by O is an average itself, thus even though 5-fold coordinated Si is present, the coordination number represents an average of the three types of coordination

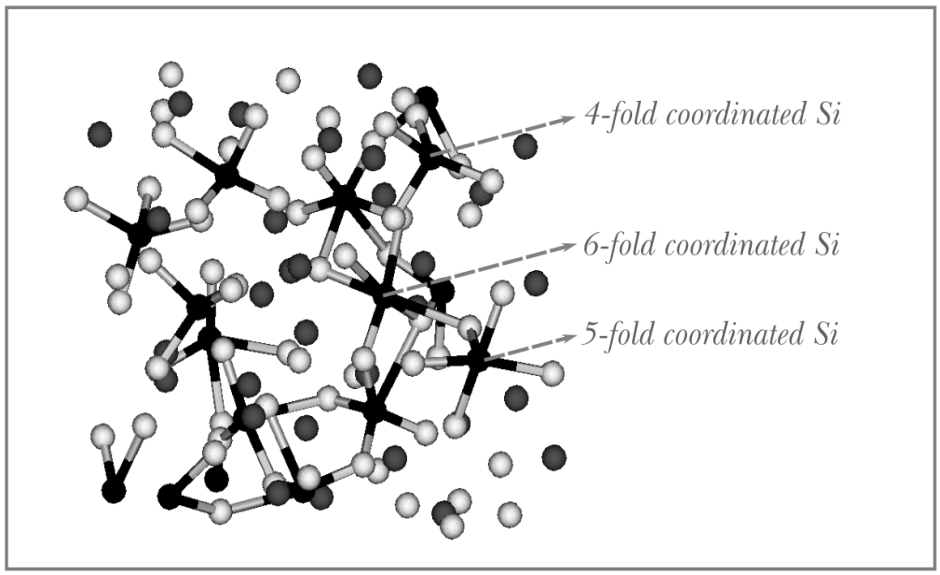

Figure 19 Snapshot from a Mg_2SiO_4 melt, at 39.8 GPa, 3000 K. For clarity only the Si-O bonds are shown. Dark grey atoms are Mg. Three types of Si-O coordination are present.

(Karki,2010) found at ≈40 GPa.

In the second coordination sphere the Si-O coordination is an order of magnitude higher and it holds no physical meaning.

3.1.2. The effect of chemistry on the Si-O coordination

We investigate the possible influence of trace elements (Fe, Ni, Co, and W) on the Si-O coordination at 3000K and the Earth's mantle pressure range.

Co, Ni, and Fe, regardless of their amount do not affect the Si-O coordination

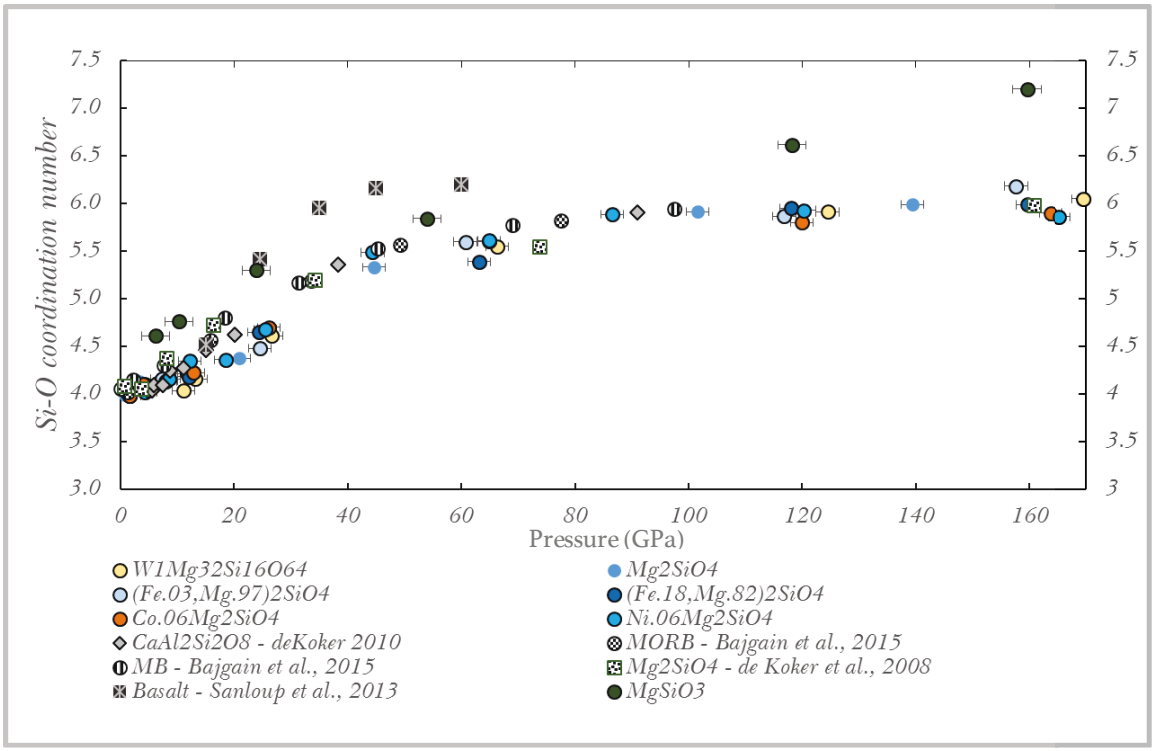

Figure 20 The Si-O coordination number of silicate melts spanning the Earth's mantle pressure range. Small amounts of impurities such as W, Co, or Ni, do not affect the slope of the coordination with pressure. Fe does not affect the Si-O coordination number trend with pressure even at higher concentrations (dark blue circles on the graph, corresponding to an Fe content of ~14wt%). The data presented here is in good agreement with published data for a wide range of compositions, MORB, forsterite melt, anorthite melt, anorthite and diopside mixture (MB). Enstatite melt Si-O coordination is close to experimental data on basalt. The higher coordination numbers in $MgSiO_3$ melt are explained by a tighter packing due to higher polymerization.

due to their small sizes (Figure 20).

Figure 20 shows the variation with pressure of the Si-O coordination in all our olivine stoichiometry FPMD runs, compared with experimental data (Basalt - Sanloup et al.,2013) and other FPMD data, Al-bearing melts (De Koker,2010;

Bajgain et al.,2015) and forsterite melt (de Koker et al.,2008). Al is thought to be a network former due to its substitution in the Si-O tetrahedron at low pressures. Despite this there is no difference in coordination between Al-bearing melt and our data. Si-O coordination numbers from Mg_2SiO_4 melt data (de Koker et al.,2008) at 3000K are in good agreement with our results. The Si-O coordination in olivine-type melts follows the same trend with pressure as the reported values for MORB, anorthite melt, and Fe-free olivine melts. The Si-O coordination numbers in basalt acquired experimentally by Sanloup et al.,2013 seem to achieve higher coordination at lower pressures than the results presented here and the other literature data. W is a large (see Chapter 5) cation and thus it can be considered a network modifier alongside Mg, Ca etc. Unlike Mg and Ca, W is siderophyle[4] and it is found in ppm amounts in silicate melts (König et al.,2011). Despite its large volume, in natural concentrations or even higher as presented here, W does not affect the Si-O coordination change with pressure (Figure 20).

Silicon is in a higher coordination state in enstatite melts than in olivine ones (Figure 20). Our results shown for the Si-O coordination number in enstatite melts, present a trend with pressure that is in good agreement with the reported Si-O coordination changes with pressure in basalt (Sanloup et al.,2013).

In $CaAl_2Si_2O_8$ melts, the Si-O coordination number is closer to olivine melts than enstatite ones, because of the presence of Al. At low pressures in solids, in tetrahedral coordination, Al is larger than Si, a trend maintained in silicate melts (De Koker,2010). The Si-O distance is smaller than the Al-O distance (De Koker,2010). The Al-O-Al angles are smaller and have a lesser degree of freedom than Si-O-Si angles. The aluminium avoidance principles dictates that Al-O polyhedra prefer to link to Si-O polyhedra rather than another Al one. In Al-free polymerized melts the Si polyehdra have more freedom of arrangement, allowing more non-bridging oxygens to enter the coordination sphere. In depolymerized Al-free silicate melts, as olivine melts, the presence of higher numbers of Mg limits the Si-O coordination increase by limiting the polyhedra connectivity through bonding with non-bridging

[4] ***It has a metal/silicate partitioning coefficient larger than 1.***

oxygens. Consequently, the Si-O coordination increase with pressure in olivine melts is close to $CaAl_2Si_2O_8$ melts.

3.2. Cation coordination in silicate melts

Mg occupies the interstitial spaces between the Si-O polyhedra and binds to the available valence of Si bonded O, and the remaining O. As in the case of Si-O, the PDF shows the existence of two coordination spheres up to approximately 40 GPa. After this pressure a third coordination sphere appears. Mg-O bonds are 14% shorter at the CMB pressures than at 1GPa (Figure 21). Unlike the Si-O pair distribution function the intensities of the maxima increase with pressure. The minima also shift towards smaller r values. Due to both of these effects, the decrease in Mg-O bond length is not accompanied by a substantial increase in coordination.

In Annex 4 the integration over the PDF can be found.

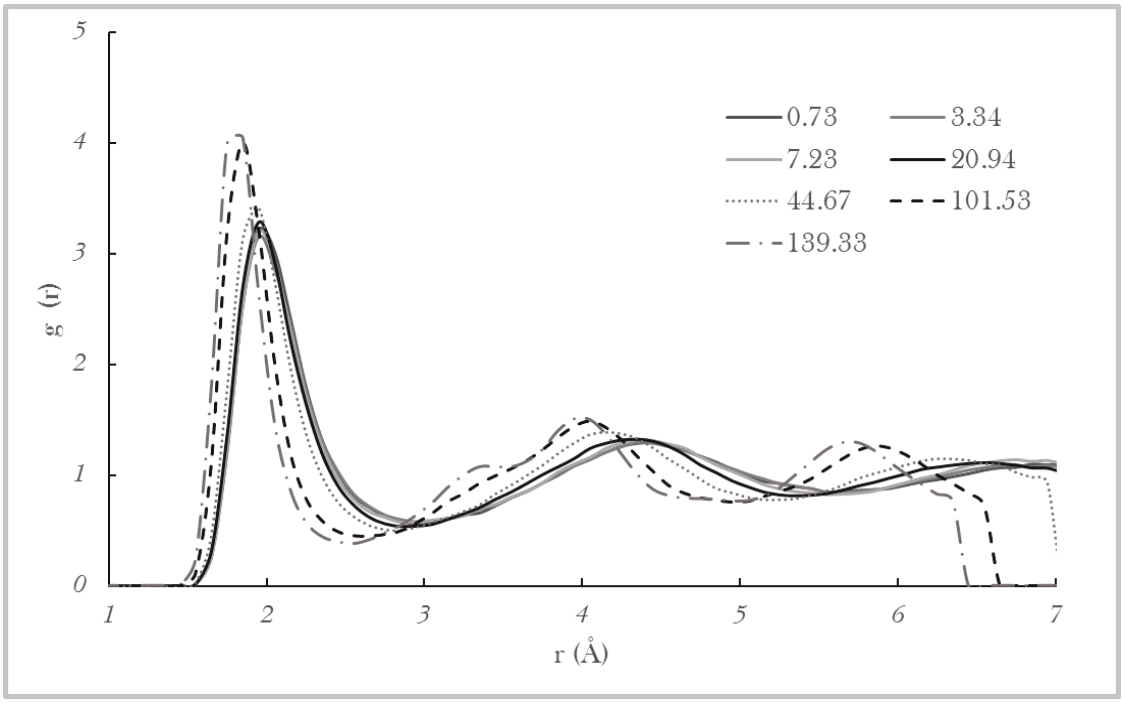

Figure 21 The radial pair distribution function of Mg-O in Mg2SiO4 melt at different pressures along the 3000K isotherm. After 40 GPa the first maximum shifts towards smaller r values. The appearance of a third coordination sphere and the decrease in r values for the first maximum are due to pressure accommodation. The legends gives the pressure for each g (r) curve, in GPa.

The Mg-O coordination number increases rapidly up to 40 GPa after which it maintains an almost constant value of 7 (Figure 22).

The Mg-O coordination change with pressure in olivine melts is similar to the

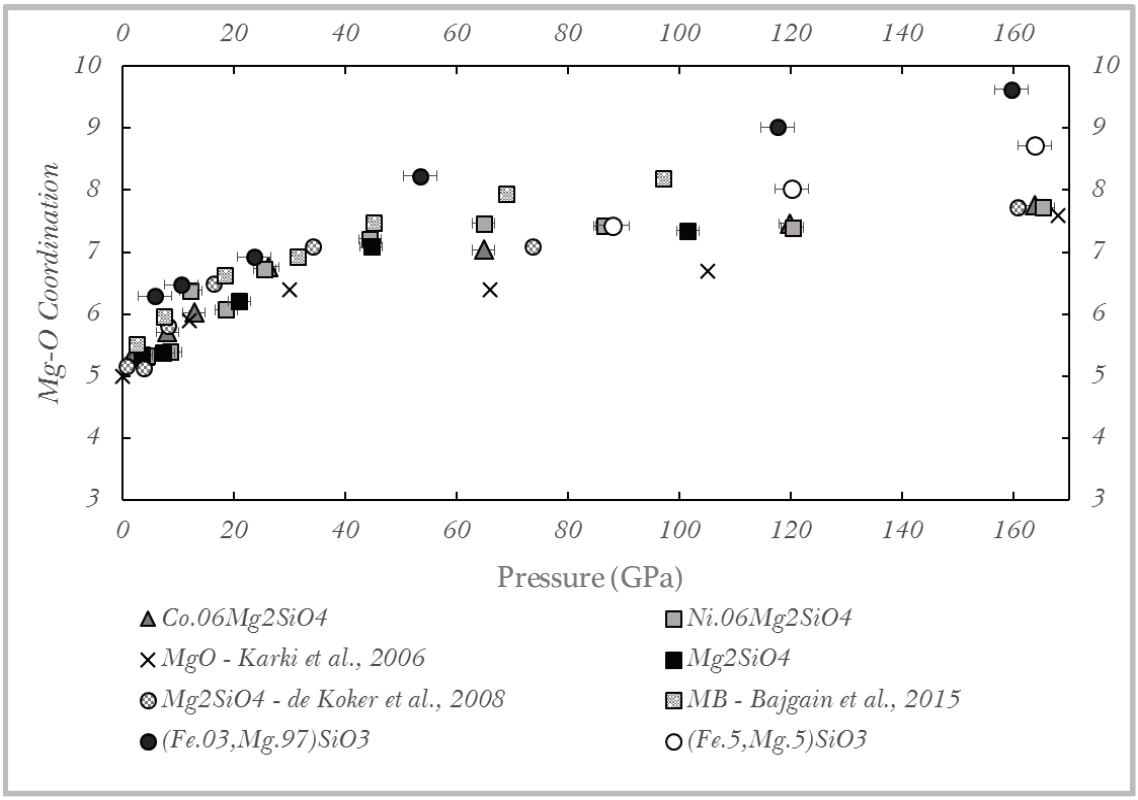

Figure 22 The coordination of Mg by O follows a similar trend as Si-O but with higher coordination numbers. The Mg-O coordination trend with pressure of pure MgO melt is similar to that of Mg-O in the olivine melts studied here and the literature. Melts with higher degree of polymerization as enstatite (this study) and a mix of anorthite and diopside compositions (MB- Bajgain et al.,2015*) have a steeper trend in the Mg-O coordination number increase with pressure.*

one reported in MgO melt by Karki et al.,2006, suggesting that Mg-O coordination in depolymerized silicate melts is independent of the other components. In melts with a higher degree of polymerization the Mg-O coordination trend with pressure departs from the MgO melt, increasing coordination faster with pressure.

$Fe_2SiO_4 - Mg_2SiO_4$ form a solid solution in crystalline form, thus the positions of Mg and Fe are interchangeable. The first maxima values of Fe-O pair distribution function increase with pressure. The Fe-O bond shortening is negligible (Figure 23).

Fe in melts with a Si/O ratio of olivine will always follow the coordination trend of Mg with pressure but with lower values (Figure 24). Fe starts at low pressure with a 3-fold coordination (similar to very recent results of Bajgain et al.,2015) and continues to increase its coordination number as the pressure increases. At CMB, Fe is in an octahedral coordination by O.

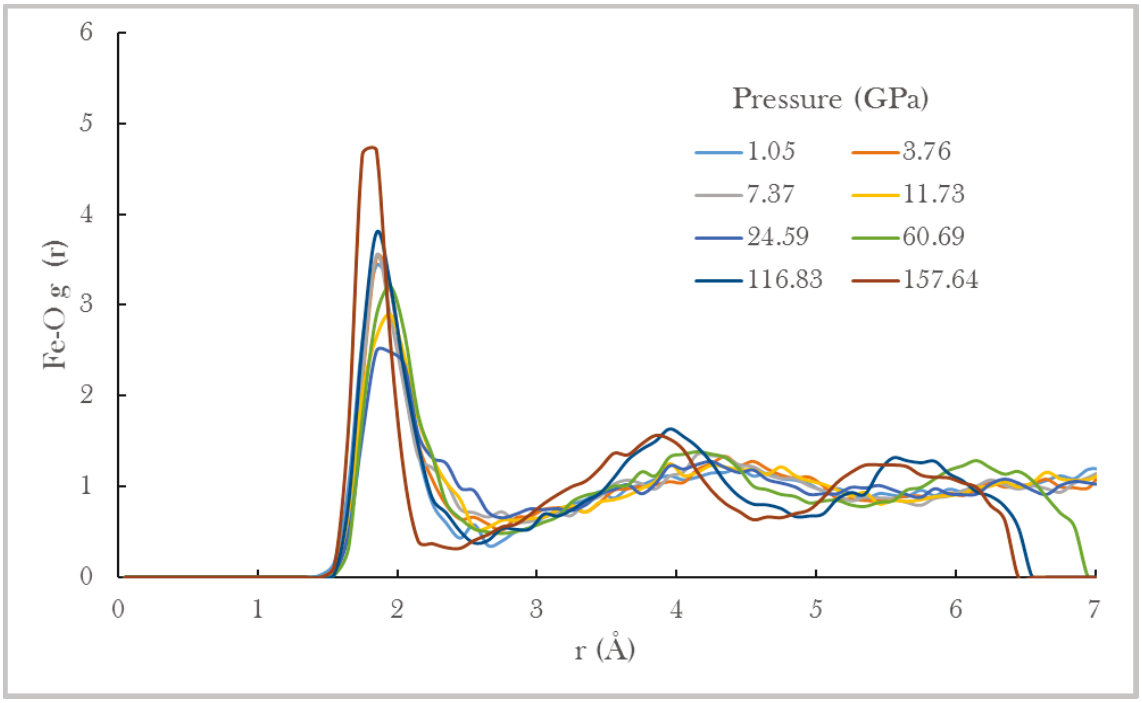

Figure 24 The PDF of Fe-O show a pressure dependence similar to Mg-O. The first coordination peak shift with pressure is less pronounced as in the case of Mg-O. At very high pressures third coordination spheres appear. The ragged aspect of the pair distribution function is due to presence of, only 1 Fe atom in the simulation box.

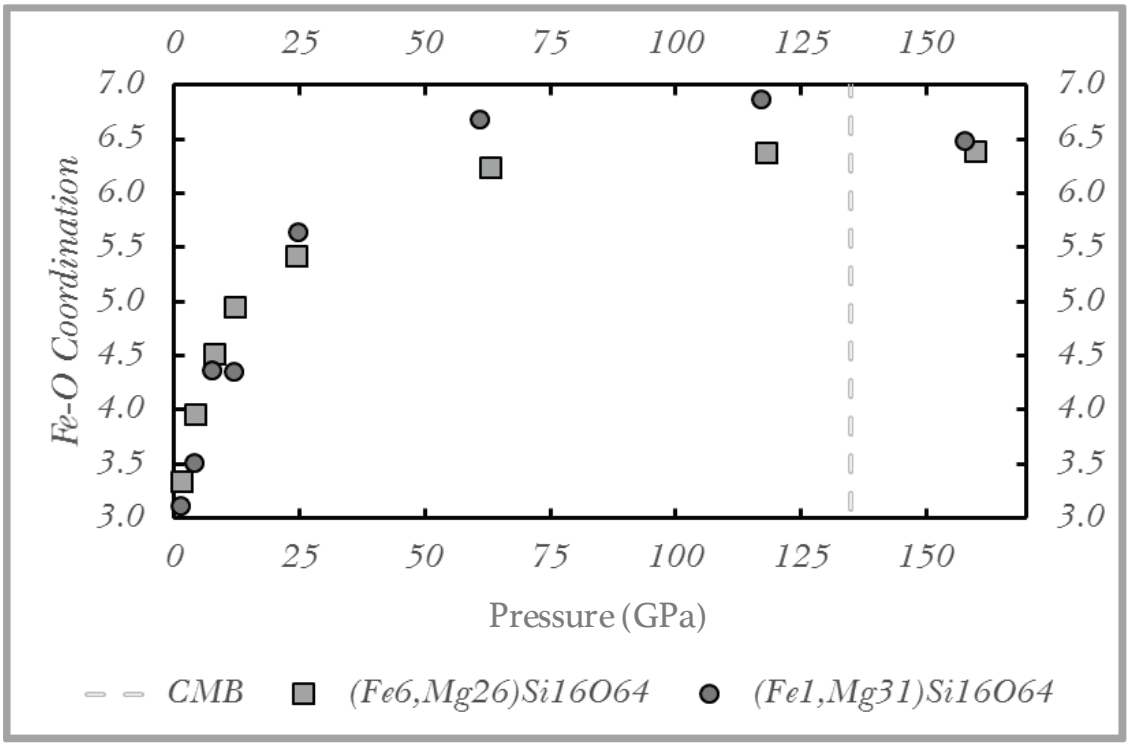

Figure 23 Fe-O coordination for two Fe concentrations showing no dependance on the amount of Fe present in the melt. As is the case for the other cations Fe-O coordination shows a rapid increase in the first 25 GPa of compression. The vertical dotted line marks the CMB.

Ni and Co are found in very low concentrations in natural melts due to their siderophyle character. The coordination of Co increases with pressure from 3 to 5 at the CMB pressure (Figure 25). At 8GPa a decrease of 6% in coordination occurs. Ni presents an interesting coordination trend, it decreases from a coordination number of 4.7 until 18 GPa when it reaches a minimum of 3 (Figures 26). After this pressure the coordination increases reaching the low pressure values at 120GPa.

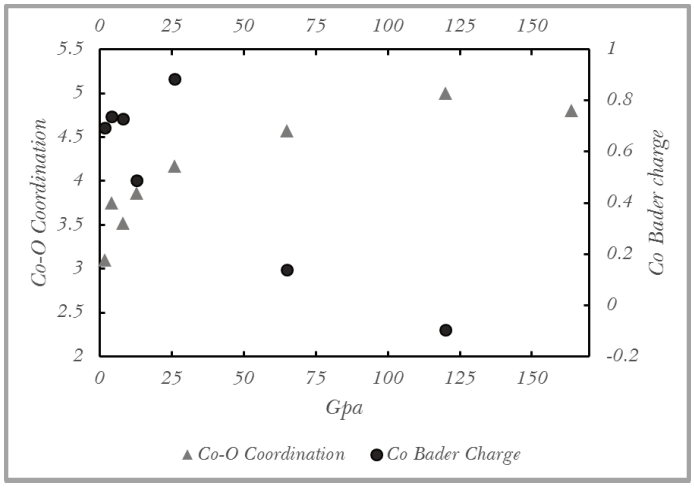

Figure 25 Co-O coordination change with pressure. The dark dots show the Co Bader charge as a function of pressure. An inverse correlation of the two can be observed.

Since the coordination by oxygen of the cations is dictated by charge and volume, but does not contain information about bonding in itself, Bader charges (Bader, 1991) can be used to better understand the structure of silicate melts. As shown in Figures 25 and 26, a decreasing value of the Bader charges associated to Co and Ni as a function of increasing pressure is observed. Co and Ni were introduced in the melt as metals, therefore their charges should be zero. Figures 25 and 26 show that some electronic charge is being redistributed to Co and Ni especially at low pressures. At lower mantle pressures their charge is almost null.

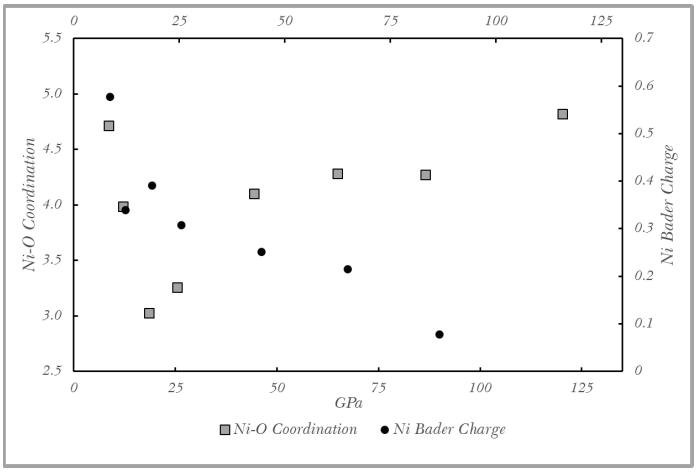

Figure 26 Ni-O coordination fluctuates greatly with pressure. Dark dots show the Ni Bader charge.

The Bader charge behaviour of Fe exhibits a different trend than in the case of Co and Ni, with a constant value of 3 (±0.06) throughout the pressure range investigated. A more detailed discussion about the pressure dependence of the Bader charges and spin behaviour is found in Chapter 4.

3.3. Bader atomic volumes in olivine melt

Atomic coordination is dependent on the charge and volume of ionic species, and for this reason we computed the Bader volumes of several atomic species in olivine melts.

Silicon presents a decreasing trend in volume with pressure (Figure 27), with a

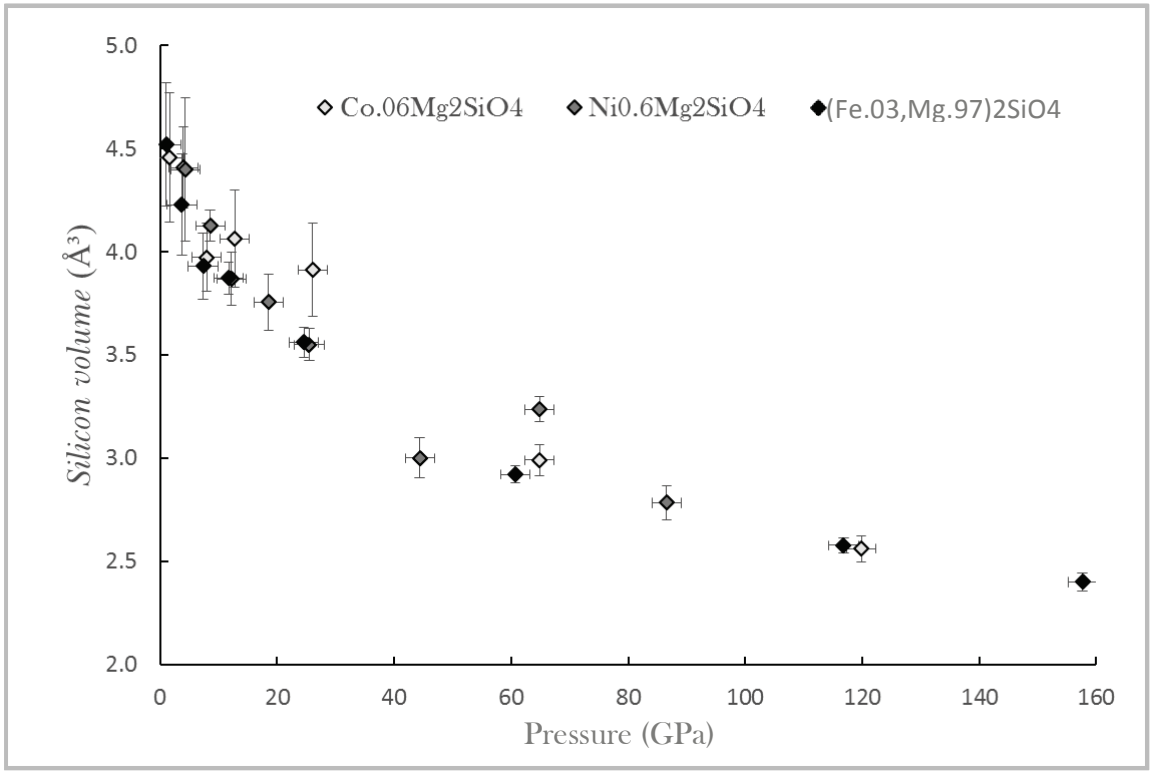

Figure 27 Bader volumes of Si in Ni,Co, and Fe bearing olivine melts. Si presents a major volume decrease in the first 25GPa of compression, which corresponds to the fast increase in Si-O coordination. After this pressure, the Si is less compressible, achieving the same volume decrease in the next 100 GPa. The Y error bars represent the standard deviation between the average Si Bader volumes of each snapshot.

steep decrease between 0 and 25 GPa of 1 Å³. This pressure range coincides with the rapid increase in Si-O coordination. The decrease in volume continues after 25 GPa but with a less steep slope, achieving another 1 Å³ decrease in the next 100 GPa. Beyond the Earth's mantle pressure range we approximate a decrease in volume of 0.1 Å³ /40 GPa. The presence of Co, Ni, or Fe does not affect the average Si Bader volume.

The Bader volume of Mg follows a similar trend with pressure as Si (Figure 28). At low pressures it is 2 Å³ larger than Si. In the first 25 GPa of compression Mg, as Si, shows the most compressible response. The decrease in Bader volume in this

pressure range is greater than in the case of Si, 1.5 Å^3. Mg continues to decrease in

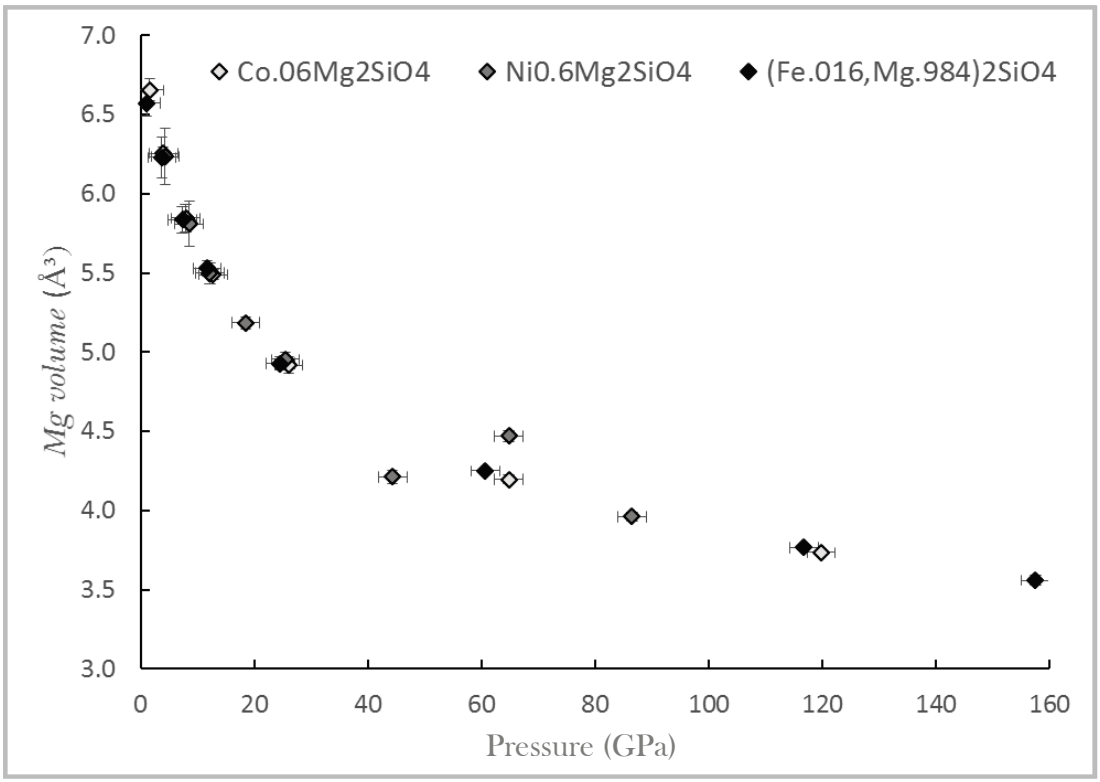

Figure 28 The Bader variation of Mg with pressure in olivine melts. Mg has the same behaviour as Si, with a rapid decrease in volume over the first 25 GPa followed by a slow decrease. The slightly larger volume of Mg in the Ni-bearing olivine melt at ≈60 GPa is perhaps due to the snapshot method of calculating the Bader volumes. The Y error bar represents the standard deviation between the several snapshots, and at higher pressures is smaller than the symbols.

volume throughout the pressure range studied, reaching a Bader volume of 3.6 Å^3 at the CMB pressure, 1.1 Å^3 larger than Si.

Fe, Co, and Ni are the largest cations in olivine melts (Figure 29), 17 Å^3 at low pressures. Overall they present the same pressure trends as Si and Mg, but the most significant decrease in volume happens at lower pressures, up to 12 GPa in the case of Fe and Co, and 8 GPa in the case of Ni. At 8.6 GPa the Bader volume of Ni decreases to 13.5 Å^3. At 12 GPa it increases to 15 Å^3. Fe and Co do not present such a decrease in volume at low pressures. At higher pressures, Ni and Co depart from the compressional trend of Fe. At CMB, Co has a Bader volume of 9.5 Å^3.

The variation of volume with pressure of all cations in olivine melts has a similar trend to the equation of state of the melt (Annex 2).

Ignoring the non-linear behaviour and estimating the volume decrease per pressure unit, Mg and Si accommodate pressure with the same procentual rate per

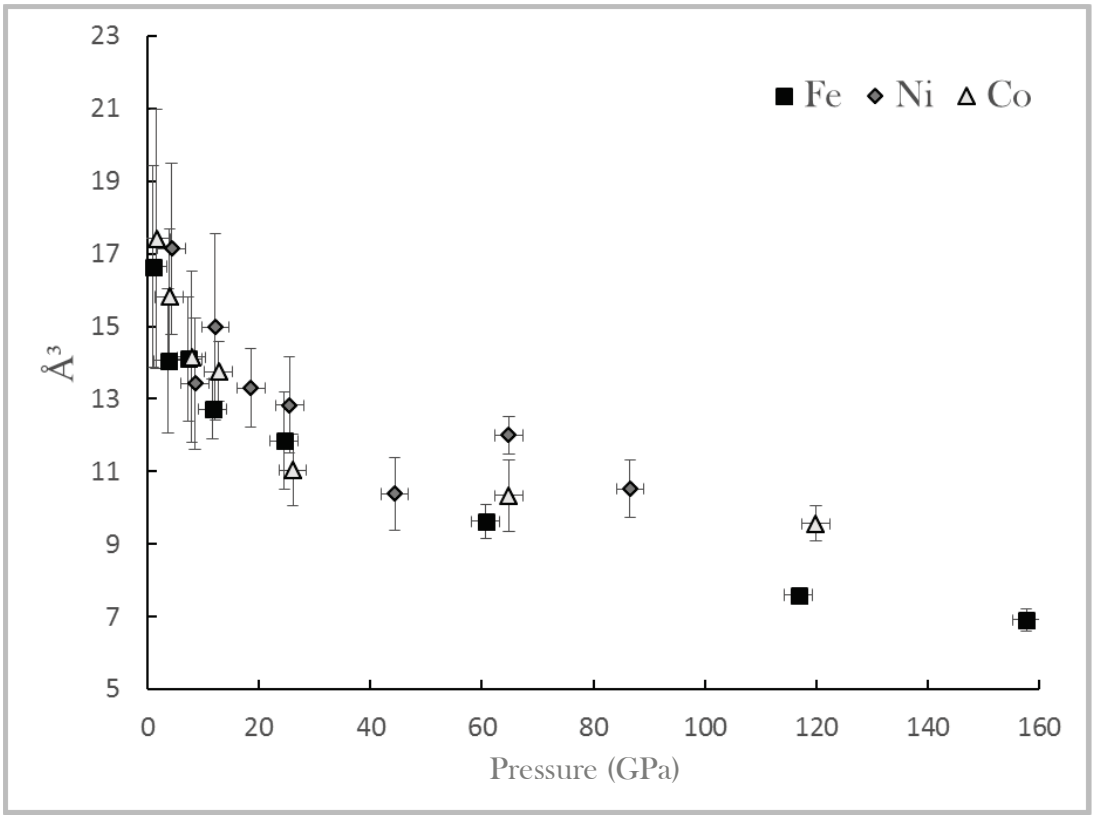

Figure 29 The Bader volumes of Fe, Co, and Ni have similar values and trends at low pressures. After 60 GPa Ni and Co are less compressible as Fe in olivine melts. At the CMB pressure, the Bader volume of Fe is almost 10 Å³ less than at 0 GPa, making it the most compressible cation in olivine melts.

1GPa (Table 2) over the entire pressure range studied. Co and Ni have a volume decrease with pressure slightly larger. Fe is more compressible than all the other cations.

Table 2 Procentual decrease of Bader volumes per GPa, calculated for the entire pressure range studied.

Si	Mg	Fe	Co	Ni
Vol.%/GPa	Vol.%/GPa	Vol.%/GPa	Vol.%/GPa	Vol.%/GPa
0.37	0.37	0.47	0.38	0.38

Oxygen has a Bader volume procentual rate decrease of 0.44 Å³/GPa in olivine melts. This is higher than all cations with the exception of Fe, and thus in Fe-poor olivine melts the bulk of the compressional response is done by O.

Thus, the increase in Fe content in a silicate melt should affect substantially its compressibility, resulting in a more pronounced effect in density increase, more than that provided by the mass difference.

3.4. The inadequacies of NBO/T parameter as a measure of polymerization

The viscosity of silicate melts, at low pressures, is very dependent on the degree of polymerization (Wang et al.,2014). Due to packing limits, the compressibility of silicate melts is also influenced by the degree of polymerization (Wang et al.,2014). Both of these properties are important in understanding silicate melts in Earth's crust and mantle. The ability to quantify some structural characteristics of a melt based solely on its chemistry is thus important, and allows adequate comparison of different properties.

NBO/T ($\frac{O}{Si+Al} = NBO/T$), the ratio of non-bridging oxygens (NBO) to tetrahedral-coordinated cations (T), represents an useful and easy way to quantify the polymerization of a silicate melt based on its composition. And yet, the shortcomings stem from its simplicity.

To exemplify the meaning of NBO/T values, Mg_2SiO_4 melts have a NBO/T of 4, and SiO_2 melts are 0.

As previously shown, Si is tetrahedrally coordinated only at relatively low pressures (below 15GPa), and thus the NBO/T parameter should be of relevance only in this pressure range. For higher pressures, a different expression of a similar ratio should replace the NBO/T following a similar logic as non-bridging oxygens/octahedral coordinated cations (NBO/O). But this approach is useless in the pressure regime of transition from 4-fold to 6-fold coordinated cations since it requires knowledge of the proportions of 4-fold coordinated (if any) cations.

The fundamental issue with NBO/T is that chemistry by itself does not always offer information about the structure of a melt.

The question is: do melts with the same NBO/T value at the same P and T conditions have the same degree of polymerization? Where polymerization is the ability of the predominant polyhedra to link into chains or 3D structures. This definition can be quantified in terms of direct structural factors by the O-Si coordination number.

Figure 30 shows silicate melts at similar P conditions with the same NBO/T values which have different O-Si coordination values, and thus different polymerization degrees. O-Si coordination values of ≈1 mean that in the proximity of each O there is only 1 Si, indicating single, non-polymerized Si-O tetrahedra. Compositions with values of NBO/T of 3.7 which are supposed to be more polymerized than Mg_2SiO_4 have smaller O-Si coordination numbers than olivine melts. Even compositions with a value of 2.5 do not have a significantly higher O-Si coordination numbers. This shows that NBO/T does not directly reflect the

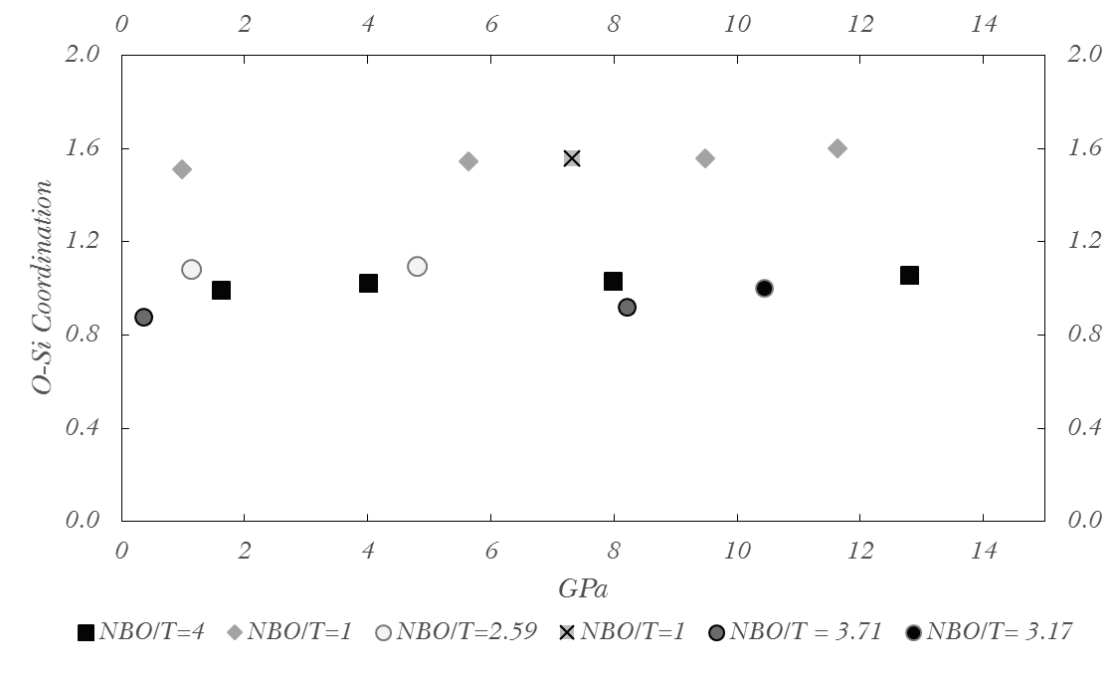

Figure 30 O-Si Coordination number versus pressure for 7 different silicate melts.The circles represent a pyrolytic melt that has a very different NBO/T value than the squares (an Mg_2SiO_4 melt) and yet they have very similar degrees of polymerization. The arrow indicates the increasing polymerization as a function of O-Si coordination number. For composition see table 3.

polymerization degree.

Due to the usefulness of a chemical approach to estimating the degree of polymerization of silicate melts in experiments, additional ratios should be taken into consideration before using the NBO/T systematics.

Table 3 comprises the chemical compositions of the melts whose NBO/T values are shown in Figure 30. Different elemental ratios are considered in the attempt to better constrain the NBO/T relationship to polymerization. Si/Mg ratio has the same value for melts found at the opposite sides of the polymerization scale. The Si/O ratios shows no predictable pattern. O/Mg is an integer for those compositions in which NBO/T link to the degree of polymerization holds true. Mg is a network modifier and in high amounts it disrupts the polymer chains in the melt. This is a well-known fact (Kuryaeva,2009), but it only accentuates the issues with using NBO/T as an indicator of polymerization.

*Table 3 * Indicates the average O-Si coordination value over the pressure range indicated in Figure 20: a – light diamonds, , b – squares, c – white circles, d – dark grey circles,e – black circle, f—crossed square. Complex melts data is from R. Caracas (unpublished) and Anorthite data is from* De Koker,2010.

Composition of the melt	**Simplified compositions**	**NBO/ T**	**Si/Mg**	**O/Mg**	**Si/O**	***O-Si CN**
[a] $Mg_8Si_{16}O_{40}$	$MgSi_2O_5$	1	2	5	0.4	1.54
[b] Forsterite	$Mg2SiO_4$	4	0.5	2	0.25	1.03
Enstatite	$MgSiO_3$	2	1	3	0.33	
[c] Pyrolite 1	$Na_1Ca_2Fe4Mg_{30}Al_3Si_{24}O_{89}$	2.59	0.27	2.96	0.269	1.09
[d] Pyrolite 2	$Na_1Ca_3Fe_7Mg_{30}Al_3Si_{18}O_{81}$	3.71	0.6	2.7	0.222	0.9
[e] Pyrolite 3	$Na_1Ca_2Fe_6Mg_{31}Al_3Si_{21}O_{86}$	3.17	0.68	2.77	0.24	1
[f]Anorthite	$CaAl_2Si_2O_8$	0	0	----	0.25	2
$W_1Ca_1Mg_{32}Si_{64}O_{160}$	$W_1Ca_1Mg_{32}Si_{64}O_{160}$	1	2	5	0.4	1.55

We have shown above that the coordination of Mg by O follows the trend of Si – O coordination with pressure. The coordination change of Mg with pressure might hold information about the change in abundancies of non-bridging oxygens. Higher

coordination number of O surrounding Mg might imply a higher number of NBO due to the transition from a tetrahedral coordinated Si to an octahedral one. Chemistry, despite all the efforts made, offers no information on how many of the total number of O are bridging or not, especially when P and T are variables. Compression might bridge polymers and increasing temperature might break polymer chains apart.

The obvious disadvantage of this observation is the fact that it holds true only for melts containing Mg. Alternatively, we could define another complementary way of expressing polymerization taking the ratio between the total number of oxygens and the non-Network-forming cations. Such a ratio could be expressed as:

$$\alpha = \frac{O}{\sum non\ network\ forming\ cations} \tag{22}$$

The sum of non-network-forming cations is the difference between all cations (C) and the sum of the network-forming cations (N) and the high-field strength network-modifiers (M). For most silicate melts Si and Al are the network formers, so N=Al+Si, and M are large, highly-charged cations as W. With this the alpha can be calculated as:

$$\alpha = \frac{O}{C - (N + M)} \tag{23}$$

In Table 4 a comparison between NBO/T values and α, for several melt compositions, is presented. α is not always an integer. If α is an integer, then NBO/T can be used as an approximation for the degree of polymerization of silicate melts at low pressures (below 15GPa). α becomes a mathematical impossibility for melts where the number of network formers is equal to the total number of cations, but in such cases the NBO/T correlation to polymerization holds well. For more chemically complex melts, the α parameter is a useful tool in assessing the acuracy of NBO/T.

Table 4

Melt	NBO/T	α
$Mg_8Si_{16}O_{40}$	1	5
Forsterite	4	2
Enstatite	2	3
Pyrolite1	2.59	2.40
Pyrolite2	3.71	1.98
Pyrolite3	3.17	2.15
Anorthite	0	4
$W_1Ca_1Mg_{32}Si_{64}O_{160}$	1	5

Table 4 shows the calculated values for different melts, with and without Mg, with Ca and other cations present. Thus, a pyrolite melt and a forsterite melt have similar polymerization degrees as assessed by the O-Si coordination number but NBO/T ratio difference of 35.25%. O-Si coordination numbers are intrinsic structural characteristics, and thus reflect directly structural parameters. NBO/T fails in assessing the correct polymerization degree.

By using the α parameter there is no need to know how many O are NBO, but the total number of O can be used. Thus, α parameter in conjuncture with NBO/T can give an accurate description of the polymerization degree.

3.5. Discussion

Structural changes in silicate melts as a function of pressure are unaffected by the presence of Fe, Co, Ni, and W.

Si-O coordination numbers in the 0-60GPa pressure regime increase rapidly regardless of Si/O ratio. At pressures higher than 60GPa the increase in coordination takes place slowly until it reaches 6-fold or 7-fold (depending on Si/O ratio) at the CMB. The point of slope-change in the Si-O coordination is found at pressures higher than the Transition Zone pressure.

In the lower mantle silicate melts have 6-fold or higher Si-O coordination. Our findings are in good agreement with previously published data (Karki & Stixrude,2010; De Koker,2010). The Bader volume of Si has the same procentual decrease as Mg with pressure (Figure 25). At low pressures they also accommodate compression through rapid coordination increase following the O volume decrease. Down to the lower Transition Zone pressures the Mg-O coordination numbers in pure MgO melts are the same as in silicate melts. After 20 GPa, Mg has a higher coordination in silicate melts than in oxyde melts. In olivine melts the coordination numbers of Mg-O are closer to those found in MgO melts (Karki et al.,2006) and reach the same values at very high pressures. Mg-O retains the same bond-length in depolymerized silicate melts as in MgO ones.

In Fe-free olivine melts, most of the compression is supported by the O atoms, through their significant decrease in volume (Figure 31).

Fe is more compressible, making Fe-rich olivine melts possibly more

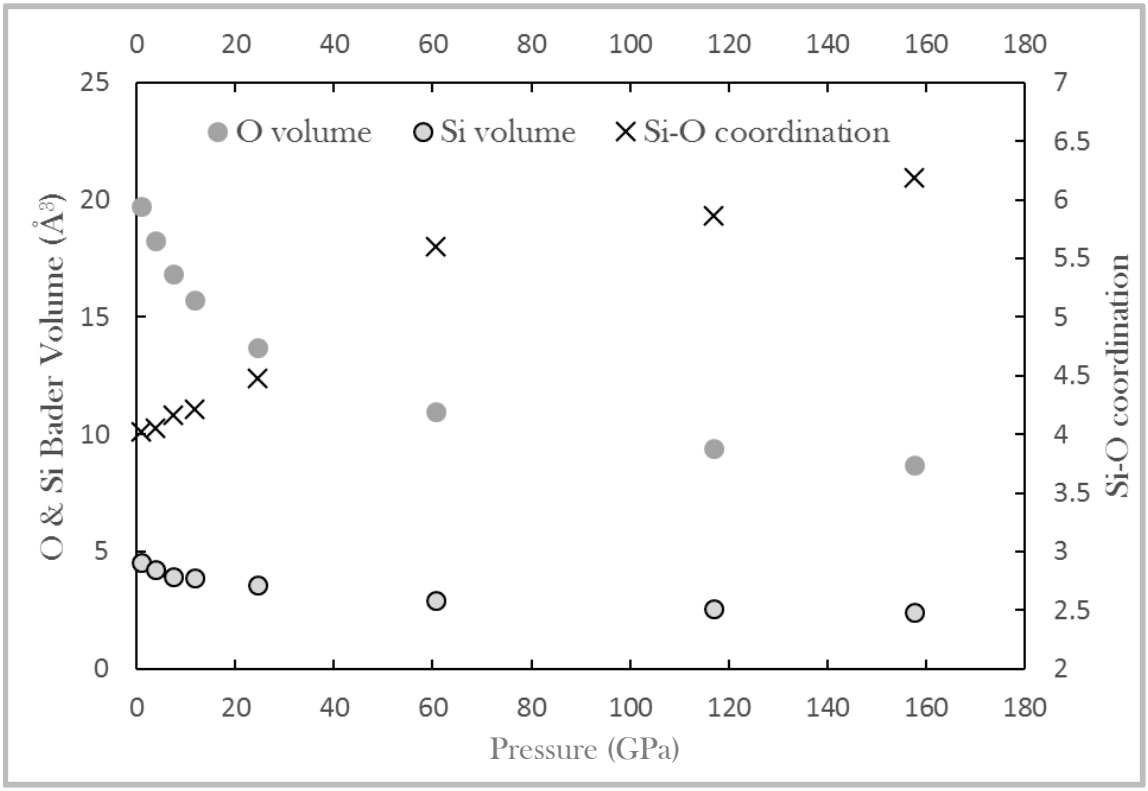

Figure 31 The variation of O and Si Bader volumes with pressure compared to Si-O coordination increase. The rate of compression of O is greater than that of Si. At pressures below the octahedral coordination of Si , the decrease in O and Si Bader volumes is the most rapid. At pressures where the octahedraly coordinated Si is stable, the Si Bader volume stabilizes. The composition is $(Fe_{.03}Mg_{.97})2SiO_4$.

compressible than their Fe-free counterparts.

Fe and Co show changes in their coordination by O from 3 to 7, and 3 to 5 respectively, through the mantle pressure regime. Ni has the same coordination number by O, 5, in the upper mantle as in the D", but between 12 GPa and 30 GPa its coordination number drops to 3. After 30 GPa the coordination number increases gradually until it reaches its initial value at the CMB. Bader charge analysis shows anomalous pressure trends in the same pressure range as the drop in coordination. The Bader volume of Ni fluctuates in the same pressure regime. Even though both Ni and Co have been introduced in the simulation cell as metallic, some ionization occurred in the silicate melt. The Bader charge and volume variations with pressure can be correlated to the spin transition, due to the re-arrangement of d-electrons, from a high-spin state to a low-spin state due to increasing pressure, as described at length in the next chapter.

To conclude, Si-O coordination number increases faster with pressure in $MgSiO_3$ melts than in Mg_2SiO_4. All cation with the exception of Ni, show a rapid increase in coordination numbers at low pressures. Mg in Mg_2SiO_4 melts, Fe and Co show a stabilization in coordination numbers at pressures higher than the Transition Zone.

4. The spin state of Ni, Co, and Fe in silicate melts

Fyfe,1960 suggested that the pressure inside the Earth's mantle, possibly after the newly proposed phase transition of olivine by A.E. Ringwood, was sufficient to generate changes in the electronic arrangement of the d-orbitals in ferric iron in fayalite. His suggestion opened a new way of looking at the deep mantle.

Changes in the spin behaviour of Fe in the most significant mineral phases of the mantle have been fairly well studied in the past two decades. Cohen et al.,1997 predicted the high-spin (HS) to low-spin (LS) transition in transitional metal-bearing oxides using first principles simulations, and proposed that band theory and not crystal-field theory is more suitable to understanding such electronic rearrangements.

Badro et al.,2003a measured a spin transition in ferropericlase at 60 – 70GPa. This change in the electronic arrangement is affecting the partitioning of Fe^{2+} between ferropericlase and bridgmanite (Badro et al.,2003a) and leads to significant changes in volume (Badro et al.,2003a; Crowhurst et al.,2008). The changes in volume translate in changes in the elastic properties of periclase-structure Fe and Mg oxides in the mantle which in turn reflect in the seismic observations of mantle discontinuities. Moreover, the partitioning of heavy isotopes into ferropericlase is strongly dependent on the spin state of Fe (Rustad & Yin,2009). LS Fe in ferropericlase favours the preferential portioning of heavy isotopes of Fe in ferropericlase at the base of the mantle because of the shorter Fe-O bonds than in the case of HS Fe (Rustad & Yin,2009).

Transition in the spin state of bridgmanite have been reported experimentally as well as from first principles simulations by many authors (McCammon et al.,2008; Umemoto et al.,2008; Badro et al.,2004). The complexities of the spin state behaviour in bridgmanite are enhanced by the presence of Fe in two oxidation state, 2+ and 3+, and the presence or absence of Al. Nonetheless, the rearrangement of electrons from HS to LS can have an impact on the processes of the mantle (Badro et al.,2003a; Badro et al.,2004; Vilella et al.,2015; Goncharov et al.,2010). The HS to

LS transition in bridgmanite, coupled with preferred orientation due to mantle convection might be observable in seismic studies (Caracas et al.,2010). Heavy Fe isotopic enrichment due to spin crossover is not observed in bridgmanite (Rustad & Yin,2009). Due to the octahedral site of Fe, and the presence of IS state in Fe in bridgmanite, the Fe-O bonds do not decrease systematically through the Fe spin crossover removing the facilitating factor for heavy Fe preferential partitioning (Rustad & Yin,2009).

In silicate melts, the observation of changes in spin state presents tremendous experimental challenges. Glasses have been used as proxies for silicate melts (Nomura et al.,2011; Gu et al.,2012; Prescher et al.,2014) but the results are conflicting. Nomura et al.,2011 find a sharp spin crossover in $(Mg_{0.95},Fe_{0.05})SiO_3$ glass at 70 GPa and 300K, while Gu et al.,2012 report that some of the Fe^{2+} undergoes a slow transition from HS to either LS or IS. Prescher et al.,2014 found no change from the HS state up to 84GPa (the highest pressure achieved in their experiments) for any of their glasses, Al-bearing and Al-free.

These experimental discrepancies might be attributed to different experimental set-ups, different compositions of the glasses and perhaps, to the slow structural changes that occur in glasses with pressure (Shim & Catalli,2009). Last but not least, temperature is an important factor due to the fact that in a melt, the local environment and ligand of Fe are rapidly changing and oscillating broadly around an equilibrium value.

Considering the challenges of experimentally observing the spin state of Fe at high pressures and temperatures in liquids, and the even more challenging task of investigating other transitional metals, first principles simulations provide the best tool to investigate this important phenomena.

Ramo & Stixrude,2014 used PBE and PBE+U to investigate the spin crossover of Fe in Fe_2SiO_4 melt, and found that the spin transition takes places over a wide range of pressure (≈ 200 GPa). In the case of solids, the Fe amount influences the

spin crossover pressure and temperature . Thus, silicate melts with different Fe contents and Si/O ratios need to be investigated.

Here we will present data on the electronic spin behaviour of Fe, Ni, and Co in silicate melts, as a function of composition, pressure, and temperature.

4.1. Spin transition

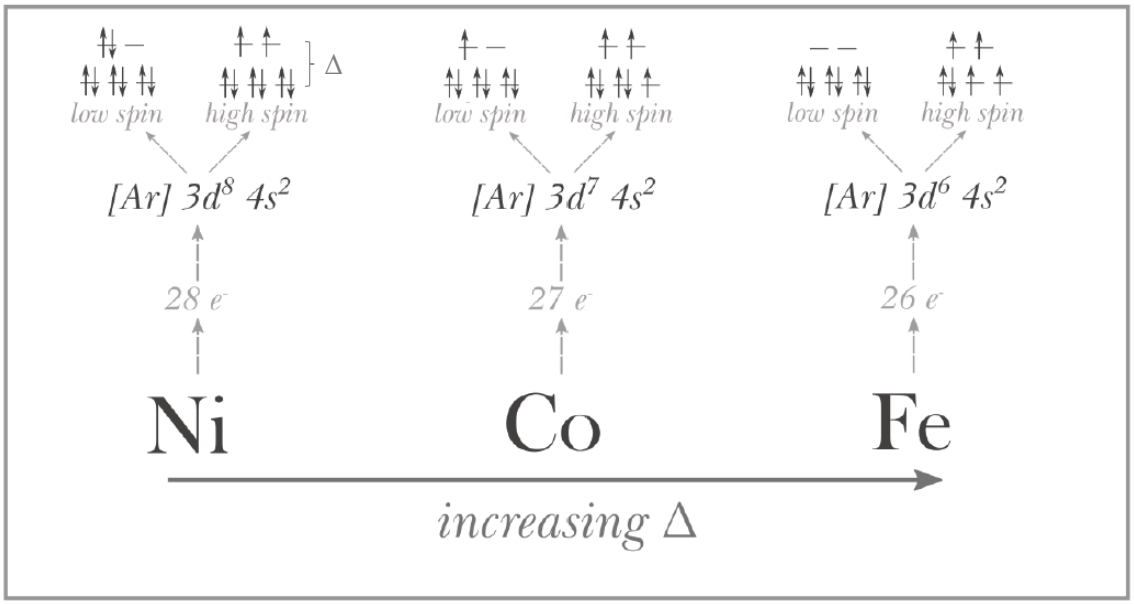

Figure 32 Schematic representation of the Δ (difference in energy between the two types of d orbitals after splitting, 3 t_{2g} and 2 e_g) relationship of Ni, Co and Fe and their high-spin and low-spin electronic arangements. The lower 3 orbitas represented are t_{2g} and the upper two are e_g. The value between t_{2g} and e_g degenerate states is dependent on local symmetry (coordination). Even the existence of these states is geometry-dependent.

For normal pressure and temperature conditions, and in most compounds found at normal pressure and temperature, d-metals are found in a high-spin state. In Crystal Field Theory (CFT) considering an octahedral coordination of the transitional metal two types of orbitals are possible: e_g and t_{2g} . In a High Spin state the d-electrons of the metal occupy both types of split orbitals (eg and t2g). The occupancy of the orbitals can be full or partial depending on the number of electrons present in the d-shell. In Figure 32 the first 3 schematic orbitals in the high spin or low spin configurations represent the t_{2g} orbitals, and the remaining two the e_g.

The Δ splitting of the d-orbitals is the splitting of the d-orbitals in two states, divided by an energy difference Δ (Figure 25). If the energy required to place an electron in an eg (for example) is smaller than the energy required to pair two electrons together then Δ splitting occurs. The splitting energy, Δ, increases with the

oxidation number of the metal and as you go lower in the periodic table. These two dependencies of Δ are not affected by the ligand species or the coordination number (Huheey et al.,1993).

The transition between a HS state to a LS state can sometimes be done through an Intermediate Spin state. In the IS, one electron moves between the e_g and t_{2g} orbitals, sometimes occupying an e_g degenerate doublet.

In the case of solids, CFT is the classical theory employed to explain the spin state. In CFT the geometry and the type of ligand surrounding the metal influence the hybridization of the orbitals and thus influence the spin state. Cohen et al.,1997 employed a more unified approach to understand and predict spin state changes. They used the extended Stoner calculations (Krasko,1987) which take into account localized influences (CFT) and the classical Stoner approach.

In a melt, the coordination number of the metal cation varies widely around an average value, with different configurations possible at a given time, and thus a statistical approach to spin behaviour is necessary.

Most FPMD results presented here, were obtained by placing a single metal cation in the melt and computing the total magnetic moment of the system (M^{system}):

$$M^{system} = \mu_B(DOS_{\uparrow}{}^{system} - DOS_{\downarrow}{}^{system}) \quad (24)$$

where the DOS stands for Density of States, i.e. $DOS_{\uparrow}^{system}$ is the number of electrons in spin up, and $DOS_{\downarrow}^{system}$ is the number of electrons in spin down. As discussed in Chapter 2, the magnetic moment per atom is indicated in the INCAR file. We attributed magnetic moments only to the transitional metals present in the simulation cell. Ideally, a simulation cell containing only one Fe (defined as the only atom carrying magnetic moment) in an HS state will have:

$$M^{system} = \mu_B\,(5 - 1) = 4\,\mu_B \quad (25)$$

The same system in a LS configuration will have two more electrons in spin up, thus:

$$M^{system} = \mu_B\,(3 - 3) = 0\,\mu_B \quad (26)$$

Liquids are disordered, and depending on pressure, temperature, and composition a variety of spin-states can exist between the two extreme values (HS and LS).

The effect of Fe concentration on spin behaviour was also investigated. The M^{system} is the sum of each Fe atom magnetic moment.

4.2. Fe spin state in olivine melts

Fe is the major transitional metal as abundance in the Earth. It is also of great significance since it makes up the bulk of the Earth's core. Because of this, and because its spin states can be studied by Mössbauer spectroscopy and XES, it is the most investigated element in terms of spin behaviour in geosciences. So far, there is only one published work on the spin behaviour of Fe in silicate melts, (Ramo & Stixrude,2014). Because of correlation effects, the value of the magnetic spin in Fe-bearing systems depends on the amount of Fe. Thus, two concentrations will be discussed here. The first, a simulation cell containing 112 atoms, from which 31 are Mg, one Mg atom was replaced by one atom of Fe. The second case, 6 atoms of Mg

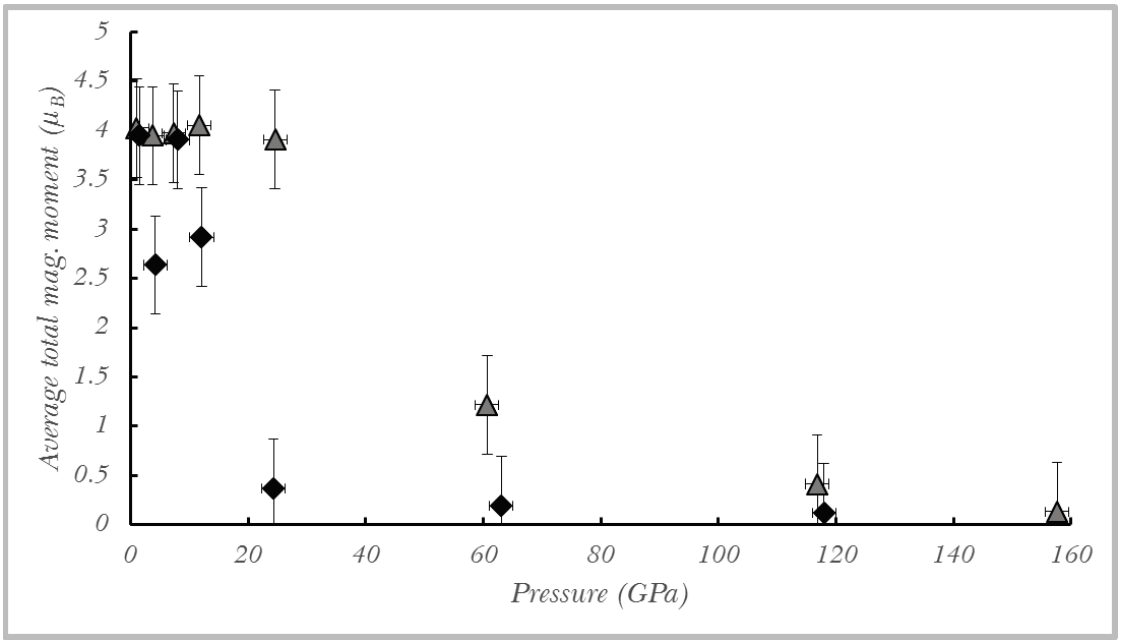

Figure 33 Triangles represent the average total magnetization for a simulation cell containing 1 Fe atom. The diamonds represent data for simulation cell with 6 Fe atoms, and are normalized to 6 atoms. High Fe concentrations approach an LS state at significantly lower pressures. Error bars represent the standard deviation over the simulation time.

were replaced by 6 atoms of Fe.

To ease comparison, the average total magnetization was divided by the number of Fe atoms present in the cell (Figure 33).

The presence of a higher number of Fe atoms facilitates the transition towards an LS state (Figure 33). The spin crossover is dependent on the Fe content of the melt. A 35GPa difference is found between the two compositions presented here. The same compositional effect is observed in bridgmanite, where increasing Fe content decreases the pressure of transition (Umemoto et al.,2008).

4.3. Fe spin state in enstatite melts

For the case of Fe in enstatite melt, the most Fe-poor composition was studied at two temperatures (3000 & 4000K) and the others at 3000K. These compositions are:

Table 5 Melt compositions, the pressure range through which they were investigated, and their abbreviations

Composition	***Hereafter denoted***	***Pressure range investigated***
$(Fe_1,Mg_{31})Si_{32}O_{96}$	Fe1	4-160 GPa
$(Fe_3,Mg_{29})Si_{32}O_{96}$	Fe3	86-160 GPa
$(Fe_6,Mg_{26})Si_{32}O_{96}$	Fe6	4 – 160 GPa
$(Fe_{16},Mg_{16})Si_{32}O_{96}$	Fe16	87 – 160 GPa

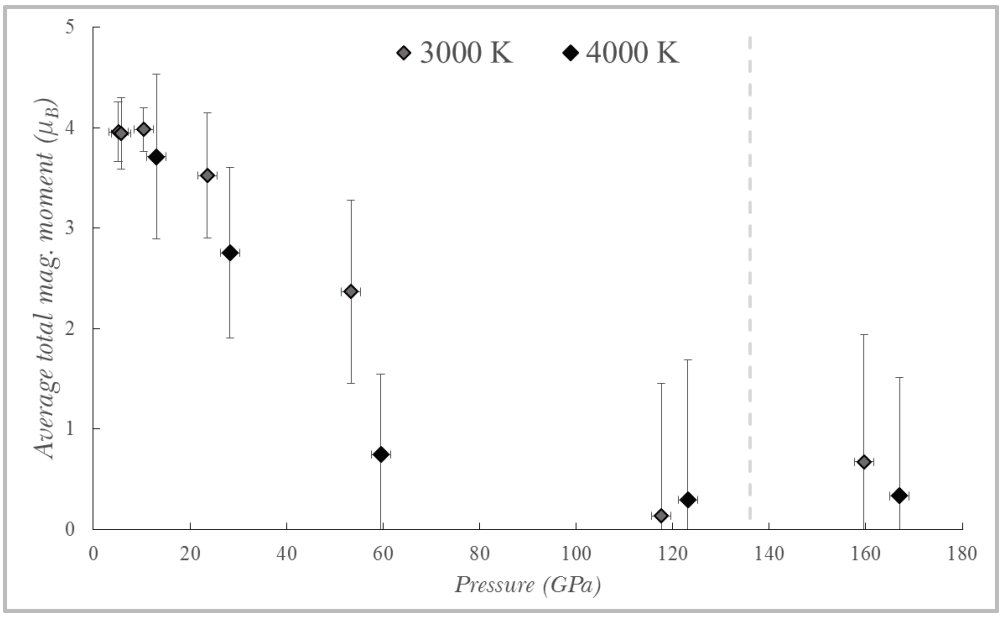

Figure 34 Fe1 total magnetization versus pressure. At 3000K the transition between HS and LS takes place in the D". The dotted line marks the CMB. Error bars represent the standard deviation over the simulation time.

Low concentrations of Fe, such as Fe1, show the transition from HS to LS takes place over a wide pressure range. At lower temperatures (3000K), spin crossover is reached in the D", higher temperatures decrease the pressure of transition (Figure 34). High temperatures reduce the pressure necessary for a spin-crossover.

Fe-rich melts such as Fe6 present an almost identical trend as Fe1. In Figure 35, the average total magnetization per atom is shown, the temperature of the simulations is 3000K. Because of the high computational costs of spin-polarized simulations, iron-rich melts were not simulated at 4000K. On the other hand, $FeSiO_3$ melts might behave differently than the compositions studied here.

No sharp spin crossover is observed at 70 GPa as reported by Nomura et

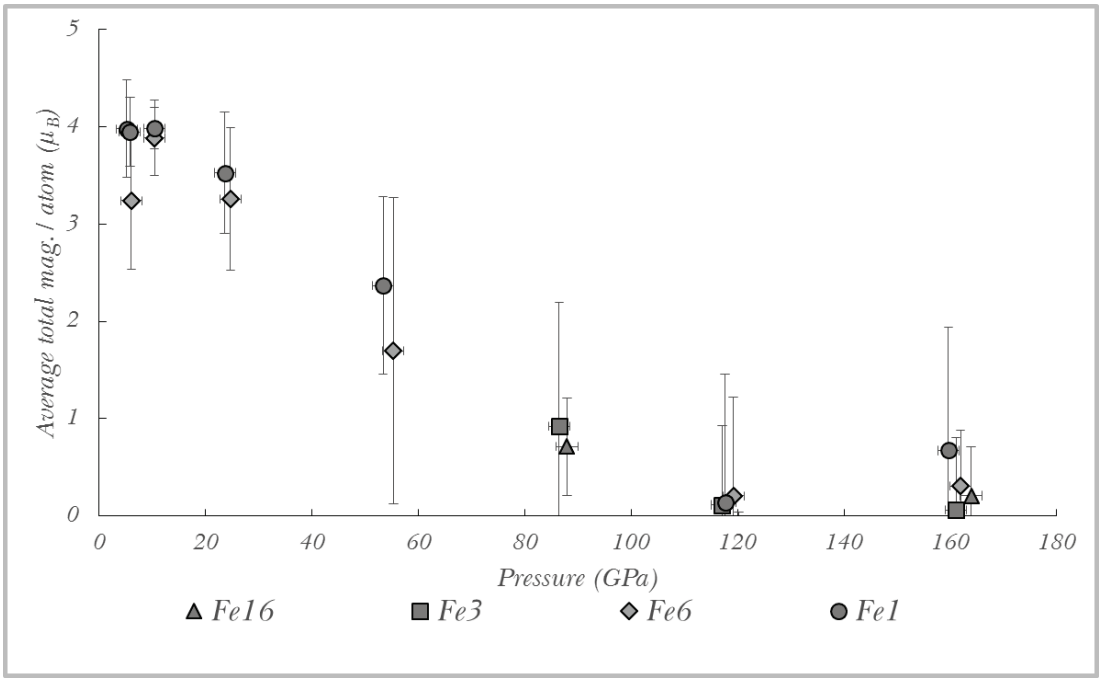

Figure 35 Spin behaviour of Fe in enstatite melts containing different concentrations of iron. For the ease of comparison, M was divided by the number of Fe atoms present in the melt.. No spin cross-over dependence is observed in the errors of the calculations. Y-axis unit of measurement is μ_B. Temperature is 3000K for all simulations. Error bars represent the standard deviation over the simulation time.

al.,2011. Fe, in all concentrations studied here, is in a HS state at that pressure.

Further studies are required to better constrain the pressure of transition. More simulations at volumes corresponding to the pressure range where this study has no data (fig. 34, between 60 and 120 GPa) should improve the pressure dependency of the HS to LS transition.

4.4. Ni spin behaviour in $Ni_{0.06}Mg_2SiO_4$ melt

As previously stated, the simulation box contained only one atom of Ni with the cell composition of $Ni_1Mg_{32}Si_{16}O_{64}$.

Because of the high degree of structural disorder in liquids, M varies during the simulation time (Figure 36). The overall aspect of the variation even without the instances of LS can be described as noisy, with large fluctuations around a mean

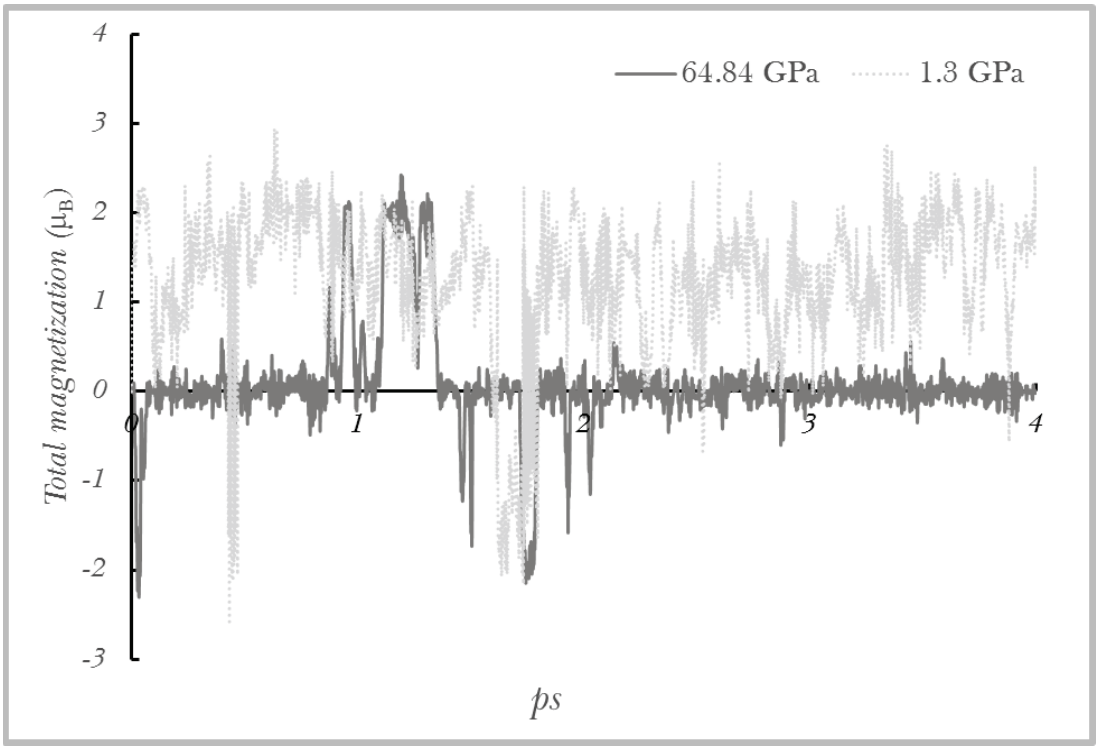

Figure 36 The variation of the total magnetization of Ni bearing forsterite melt at 1.3 and 64.84 GPa, 3000K. At low pressure, for most of the simulation time the spin state of Ni is HS, and only for a few femtoseconds Ni is in LS, with some instances of IS. At higher pressure, the fluctuations are more reduced and only a few moments of HS and LS are present. The LS states are longer lived than the HS ones, indicating that LS states are more stable.

value. For larger pressure (Figure 36), the fluctuations have a smaller amplitude.

The main cause of these fluctuations is the rapid change in the local environment of Ni, with a varying number of oxygen atoms surrounding it. Taking into account these fluctuations in the total magnetization during a run, the average total magnetization can be a more useful tool in assessing the spin state as a function of pressure (Figure 37).

The transition from predominantly HS state to an LS state takes place between 8 to 12 GPa. After this change in the spin state, Ni remains in a predominantly LS

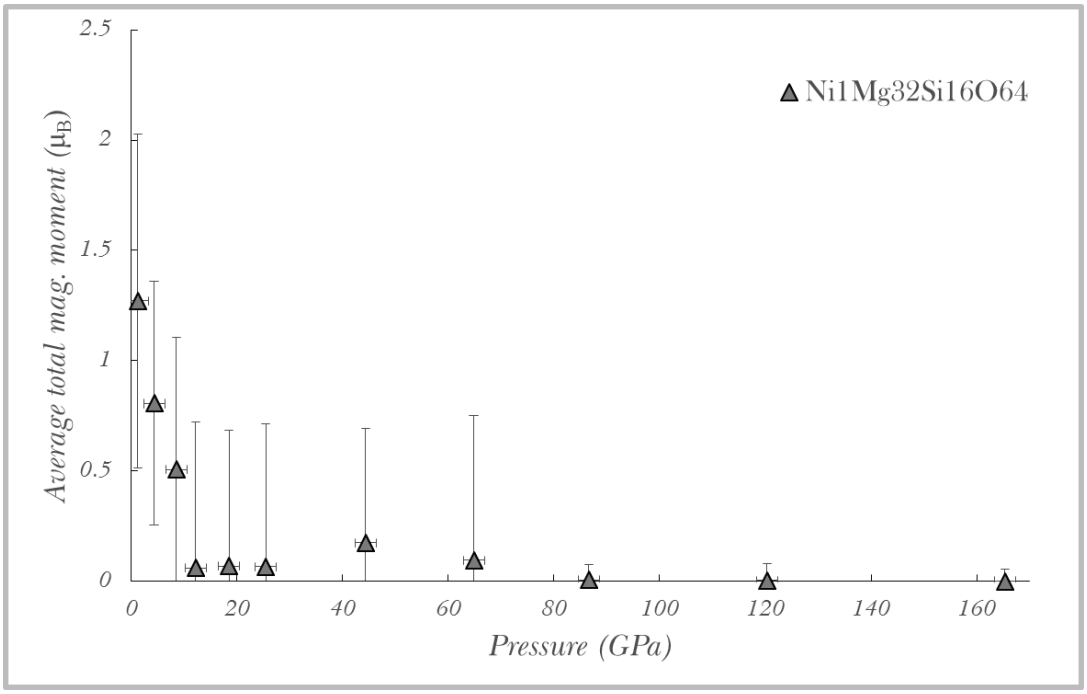

Figure 38 Total average magnetization, in μ_B, versus pressure. In the 0-12 GPa pressure regime the total magnetization drops from values of ~1 to ~0, signifying a change from HS Ni to LS. The LS state of Ni persists beyond the pressure of the Earth's mantle. Error bars represent the standard deviation over the simulation time.

state for the entire pressure regime of the mantle.

The average total magnetization does not offer the full picture of the spin states. From the variation of the total magnetization with time, the abundance of HS and LS can be extracted (Figure 38) by calculating the percentage of time a specific state

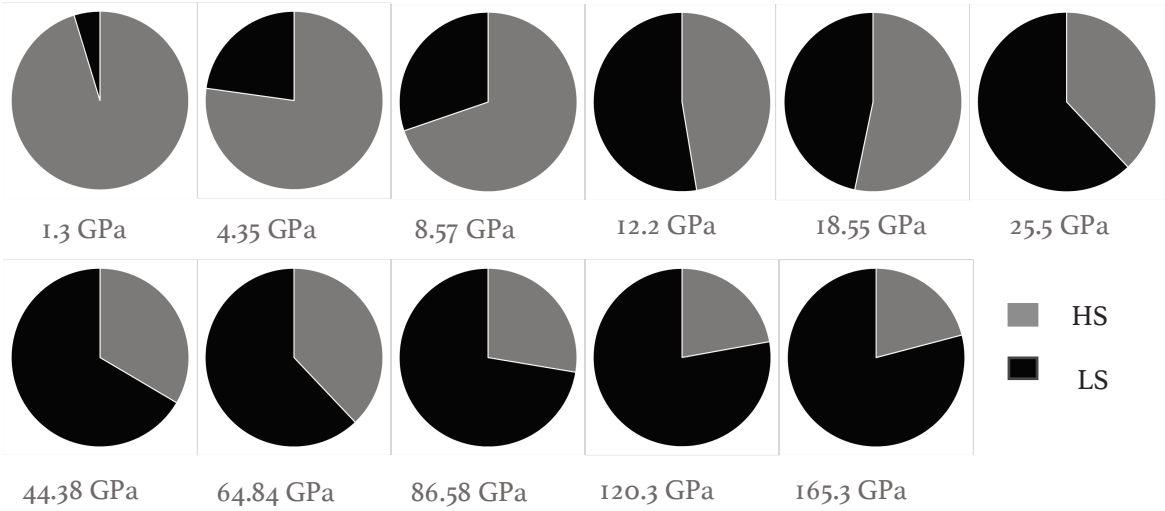

Figure 37 The abundance of the spin states for each run. At very low pressures, Ni is mostly found in HS state, as the pressure increase more LS states appear. In the pressure range 12-18 GPa HS and LS states are equally probable but as the pressure increases, more LS states become stable. Errors estimated at ± 10%.

exists. HS states are defined as those where M has a value greater than 0.10 μ_B.

The transition from HS to LS happens gradually with both states present. LS states increase in abundance up until 25 GPa. Between 12 and 18 GPa a slow rearrangement of states takes place with HS and LS states being almost equal in abundance. After this slow transition, LS state becomes favourable and the abundances of HS decrease. At the bottom of the Earth's mantle LS state makes up 79% of the spin state of Ni.

This ***transition range*** between the stable low-pressure HS and high-pressure LS, is also reflected in the Ni – O coordination (Figure 39).

Melts represent highly dynamical systems, with SO configuration changes that take place over the time of a femtosecond. These rapid changes in the local environment lead to the appearance and disappearance of spin states that are not stable in the respective pressure-temperature conditions. The PDF used to obtain the Ni-O coordination (see Chapter 3) represents such an average over the simulation time.

For a better understanding of the local environment of Ni, Bader analysis of charges and volumes can offer important information. Several snapshot runs, were performed at each volume in order to compute and write the charge of each atom

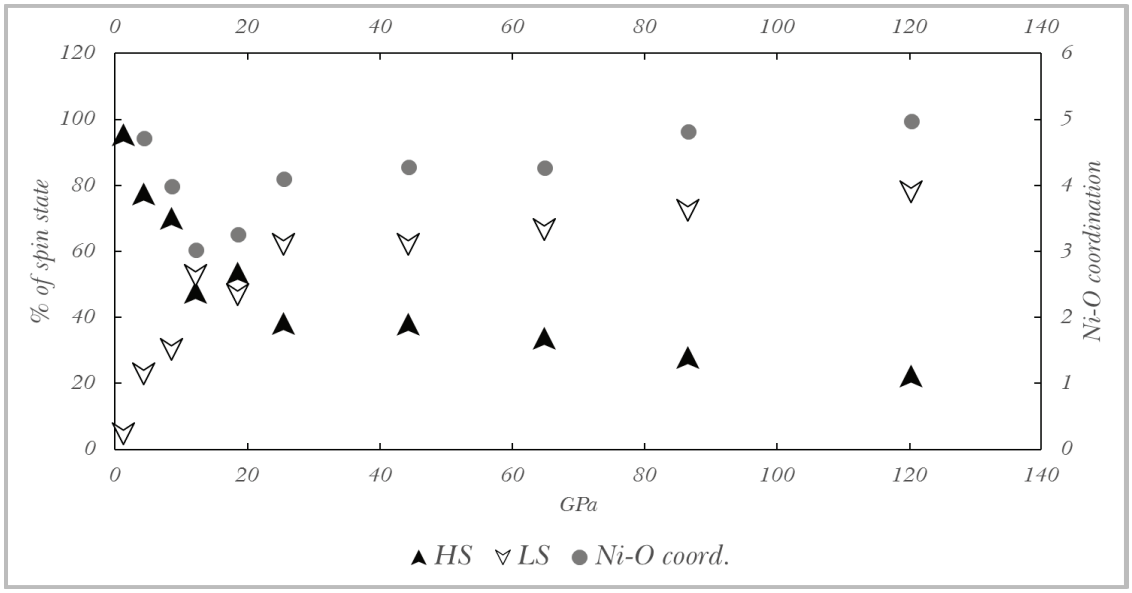

Figure 39 The variation in relative proportions of HS and LS states versus pressure. The period of transition marked by the coexistence of the HS and LS states in equal amounts is reflected in the Ni –O coordination, marked on the secondary Y-axis. This period of electronic rearrangement is reflected in the structural way by unusual Ni-O coordination numbers. Due to the highly fluctuating electronic spin states in the pressure region of the transition the number of oxygens in the proximity of Ni drops. This decrease in the density of oxygen in the 1st coordination sphere might be due to repulsion forces or the inability of the valence electrons to bond.

present in the simulation box.

Figure 40 shows the Bader volume of the Ni atom as a function of pressure. The decrease of the Bader volume is due to two main factors, the compression caused by

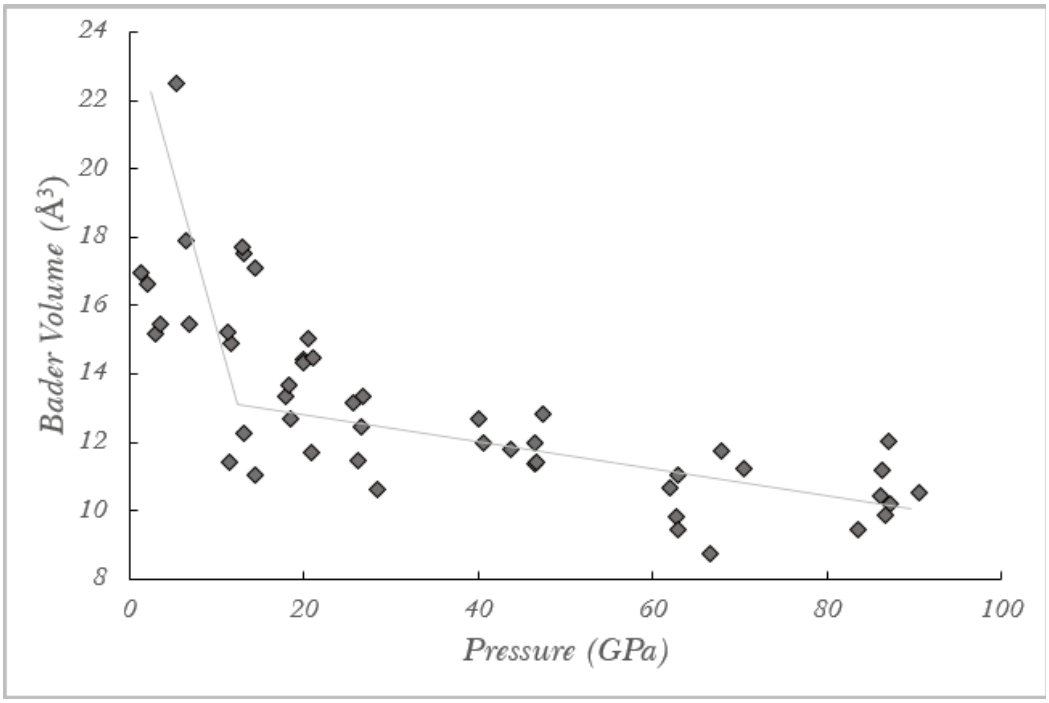

Figure 40 The Bader volume as a function of pressure obtained from snapshots. The Bader volume units of measurement is Å^3. The scatter is due to the relative low number of data points.

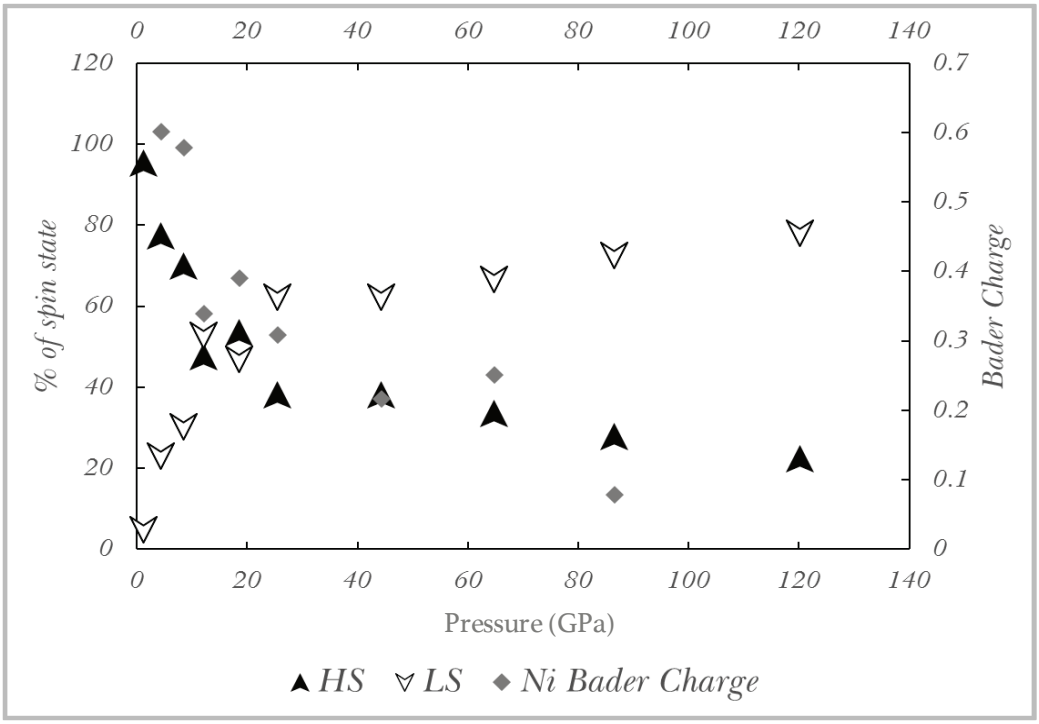

Figure 41 As in the case of Ni-O coordination the Bader charge of Ni correlates well with the change in spin states. It shows fluctuations in the transition period and a general decreasing trend with pressure. The data represent averaged values at compression point of all the snap-shots.

pressure and the change in volume associated with the HS to LS transition. Before the spin transition the average decrease in Bader volume of Ni is 0.2 Å^3/GPa and after the spin crossover is 0.04 Å^3 per GPa.

The two effects are related, and thus a quantitative analysis of the volume change associated to the HS to LS transition of Ni is not possible. Nonetheless, a decrease in volume over the HS to LS states transition is observed.

In Figure 41, the average Bader charge of Ni versus pressure is shown. The Bader charges decrease abruptly at the pressure of spin crossover and increase slightly after the spin transition. The HS to LS transition spans over 10 GPa. The transition pressure, where HS states are as probable as LS states is marked by anomalous charges and SO configurations.

Figure 42, shows the predominant d-orbitals of Ni depending on the value of the total magnetization and pressure. In inset ***c*** of Figure 42, orbital hybridization by oxygen is visible.

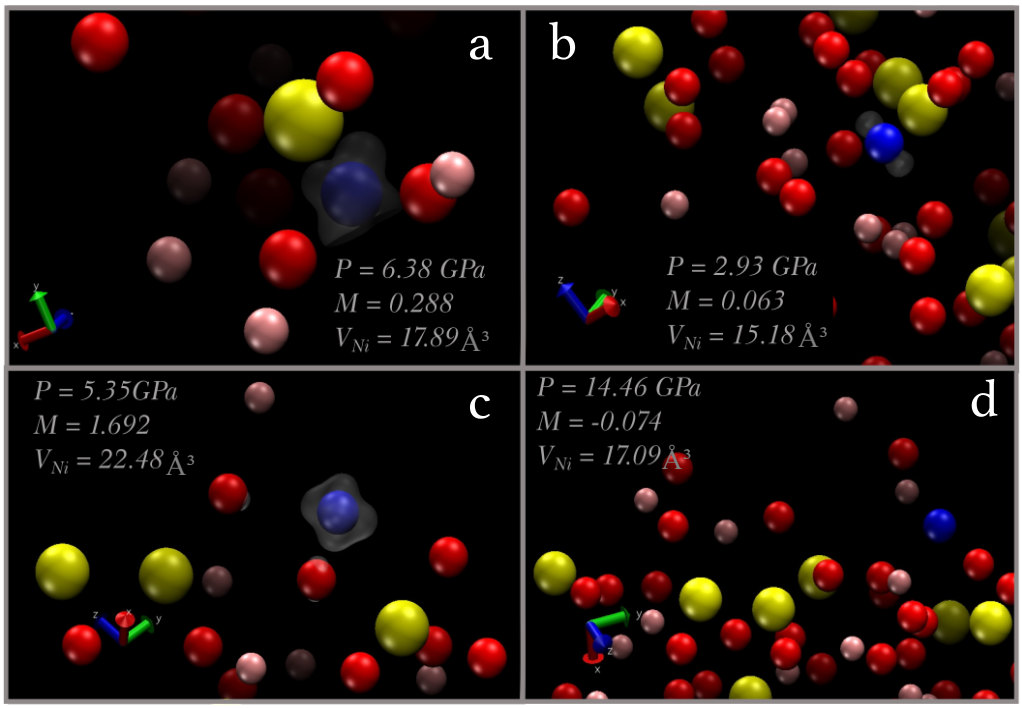

Figure 42 Charge surface plotted around the Ni atoms (blue atoms) in the melt. a) a $d_{x^2-y^2}$ –like orbital is visible. b) d_{z^2} –like orbital with the negative part smaller than the radius of the Ni atom. c) d_{zy} –like orbital. d) no positive surface exists because the Ni atom is in LS and the plotting condition was ↑ - ↓=+x . The pressure, M (μ_B) and the Bader Volume are given.

4.4.1. Spin crossover of Ni in $(Ni_{0.03}Mg_{0.97})_2SiO_4$ melt

The results presented above show the spin behaviour of Ni as a metallic impurity in a forsterite melt. The spin behaviour of Ni as a component of a MgO-SiO-NiO solution were investigated through the same means.

We substituted one Mg atom with one Ni atom in the composition $Mg_{32}Si_{16}O_{96}$. Several volumes, corresponding to similar pressure points presented above were investigated using the composition $Ni_1Mg_{31}Si_{16}O_{64}$. The results are presented in Figure 43.

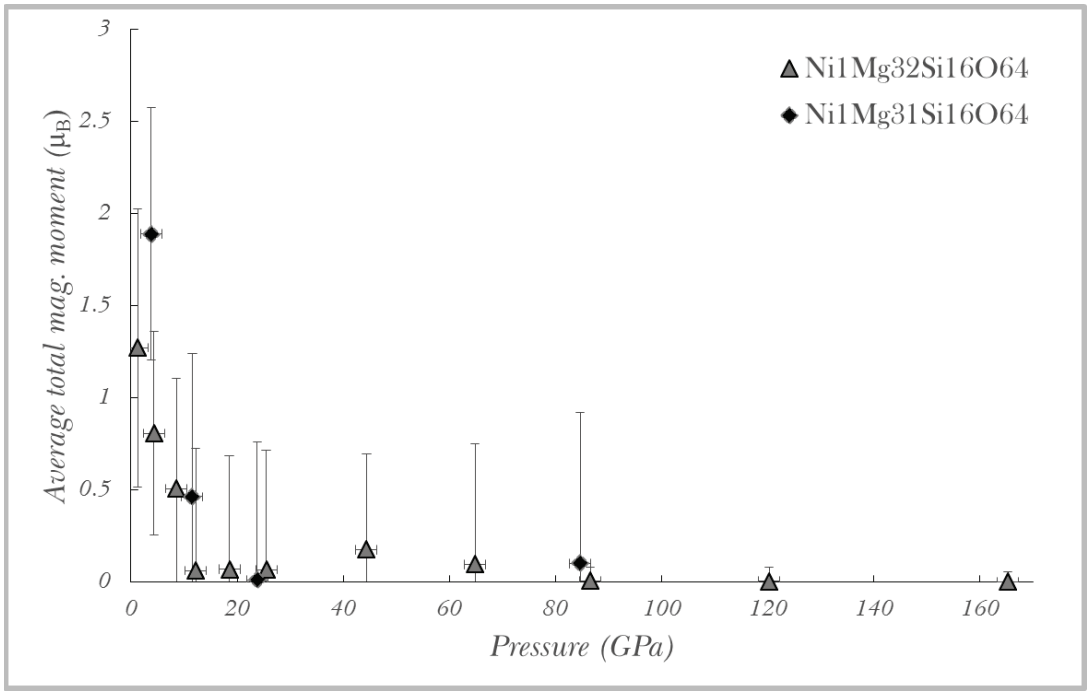

Figure 43 The average total magnetization, in Bohr magnetons, of forterite melts containing Ni^{2+} either as a metallic impurity (triangles) and as an oxide (diamonds). The two compositions show an almost identical behaviour in terms of spin-state change. The High-Spin to Low-Spin transition pressure is the same in both compositions.

The similar spin-state behaviour with pressure in the two forms of Ni is perhaps due to the fact that metallic Ni interacted with the neighbouring oxygen atoms and became ionized (Figure 42). The oxidation of the metallic Ni was possible because of the disordered nature of the silicate melts, where bonds can be broken and re-arranged with more ease than in the solid counterpart.

4.5. Ni spin behaviour in enstatite melt

We study the spin state of Ni in $MgSiO_3$ melts using the same approach as it was described in the case of Mg_2SiO_4 melts. The average total magnetization indicates that Ni has no spin state change across the Earth's mantle (Figure 44).

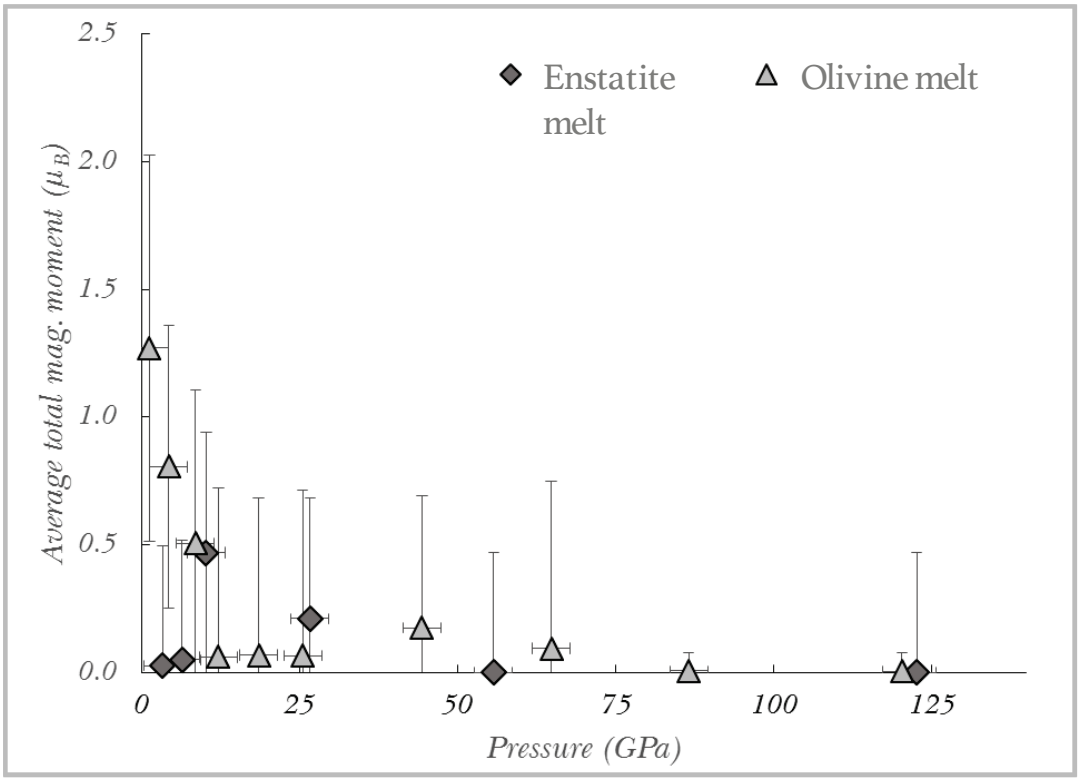

Figure 44 Comparison between the total average magnetization of Ni in Mg_2SiO_4 melt (triangles) and $MgSiO_3$ melt (diamonds). Ni in enstatite melts is in LS throughout the pressure range investigated.. This anomaly may be attributed to local environment changes or the short time of the simulation. The temperature is 3000K for both cases.

The low values of the total magnetization represent an almost constant LS state throughout the pressure range investigated here.

As in the case of crystalline solids, the spin state of a transitional metal is dependent of the local environment. By comparison with Mg_2SiO_4 melts, $MgSiO_3$ are more polymerized and represent a different structural environment for Ni. Based on the data presented here, it is most probable that Ni in enstatite-stoichiometry melts is in LS regardless of pressure effects.

4.6. Co spin state in olivine melt

Co has a higher Δ energy than Ni and it has 7 electrons in the d-orbitals, one less than Ni. These differences are reflected in the spin state behaviour with pressure. As in the case of Ni, a gradual transition from HS to LS is observed in olivine melt. Co reaches a full LS spin state after 26GPa (Figure 45). The transition from a predominantly HS state to a LS is done through the increasing abundance of LS states, while IS maintains a constant presence (Figure 46). Between 13 GPa and 26

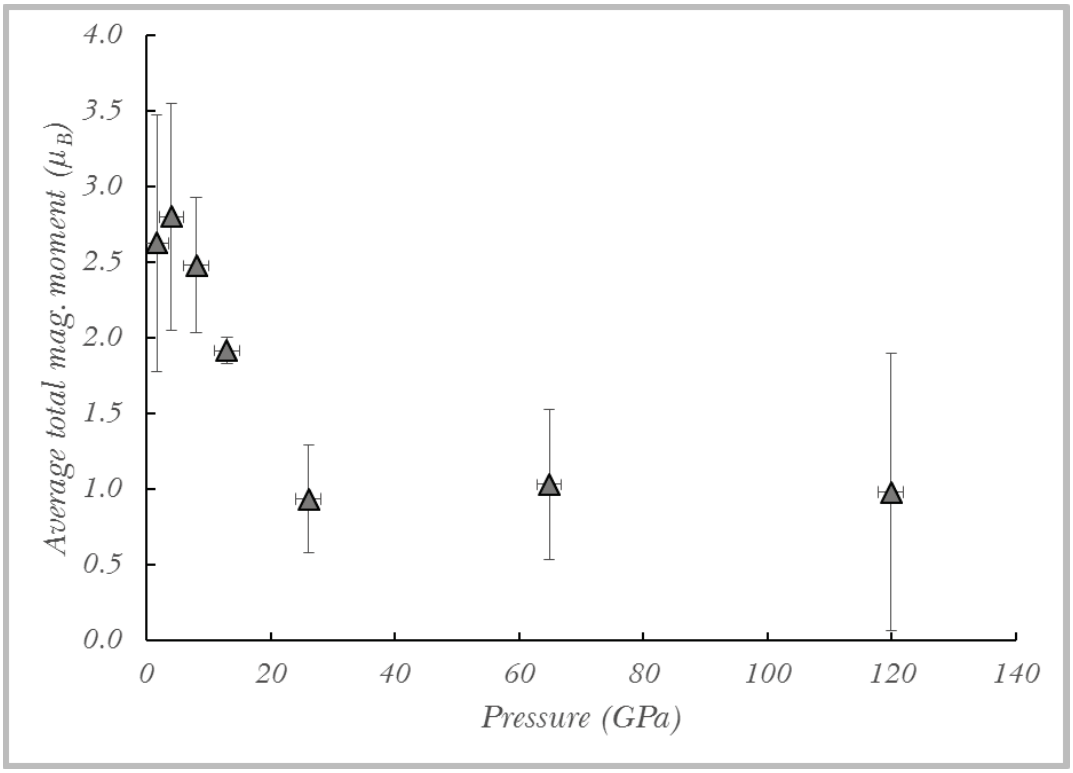

Figure 45 Average total magnetization of Co versus pressure. From 0 to 26GPa the HS states decrease in abundance and after 26 GPa the LS spin state is established and it persists until the bottom of the Earth's mantle. Error bars represent the standard deviation over the simulation time.

GPa, LS states increase in abundance and the IS disappears.

The appearance of LS states in larger number is correlated with the trend of the Bader charge with pressure (Figure 47a). Differently from Ni, the change in the spin state of Co is not reflected in its coordination number by oxygen. The lack of Co-O coordination change (Figure 47b) at the spin crossover pressure might be due to the fact that IS states are possible, and allow for a smooth increase in coordination. As in

the case of Ni, Co presents a spin crossover across a relative narrow pressure range and reaches a predominant LS state below the Transition Zone.

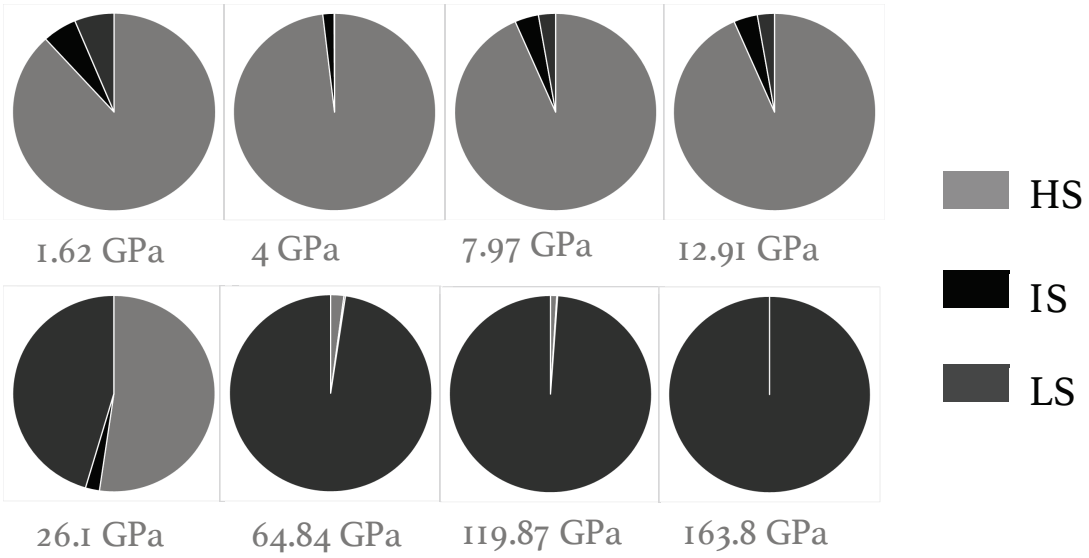

Figure 47 Abundances of the spin states of Co through the Earth's mantle. The transition from HS to LS is achieved after 26 GPa through a transition state where the two extreme states, HS and LS, coexist. After this pressure, LS state is more stable and is the major spin state present. No IS states are found after the transition to LS.

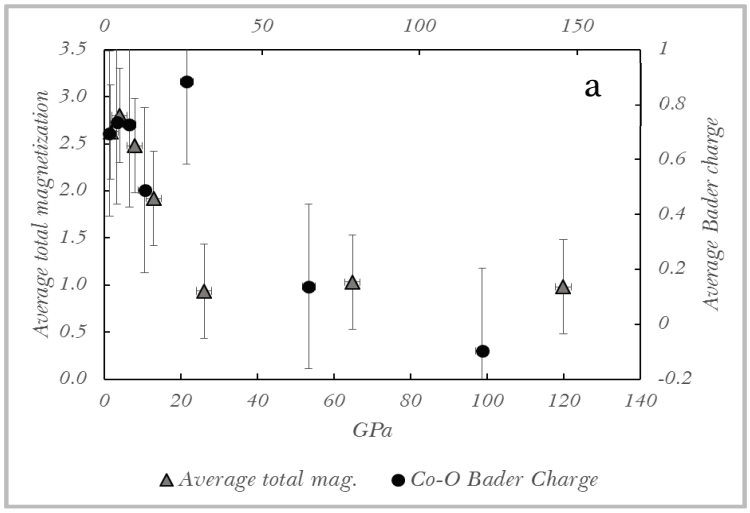

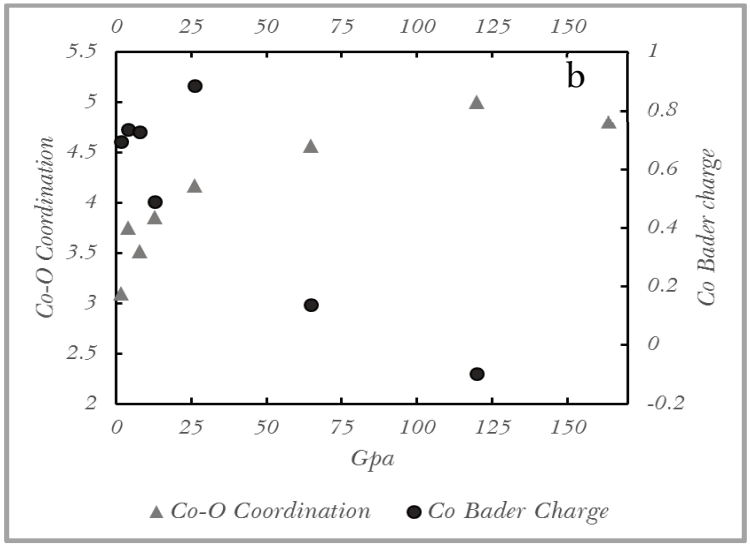

Figure 47 Inset a shows the average total magnetization versus pressure compared with the average Bader charge of Co. The highest value of the Bader charge is reached at 26 GPa corresponding to the pressure where HS and LS states are found in equal amounts. Inset b shows the variation of Co-O coordination with pressure and the Bader charges. No correlation between the Co coordination by oxygen can be seen. For clarity the error bars have been omitted.

4.7. The spin state of Ni and Fe in Ni-Fe-bearing olivine melt

The presence of more than one transitional metal species in a silicate melt, as is the case in nature, might affect the spin-state of all transitional metals present in the melt. We investigate this possible effect in $Ni_1Fe_1Mg_{31}Si_{16}O_{64}$.

We found that the total magnetization (M) of the $Ni_1Fe_1Mg_{31}Si_{16}O_{64}$, at low pressures, is the sum of the M^{Ni} and M^{Fe} melts (Figure 48). For example, at around 0GPa, the value of M for Fe-bearing olivine melt is 4, and 1.2 for Ni-bearing olivine melt. The total magnetization at the same pressure for an olivine melt containing both Ni and Fe, is 5.1. At the pressure of Ni spin crossover (12 GPa), the value of the total magnetization decreases rapidly to a value of 2. Above 12 GPa the value of M increases, and it reflects only the HS states of Fe. Fe reaches a spin-crossover at pressures corresponding to the CMB.

Based on this observation we conclude that Fe and Ni spin-states do not affect each other in olivine melts. In an olivine melt containing both Fe and Ni, the latter will experience a spin crossover close to the Transition Zone pressures, while Fe will have a crossover at much higher pressure.

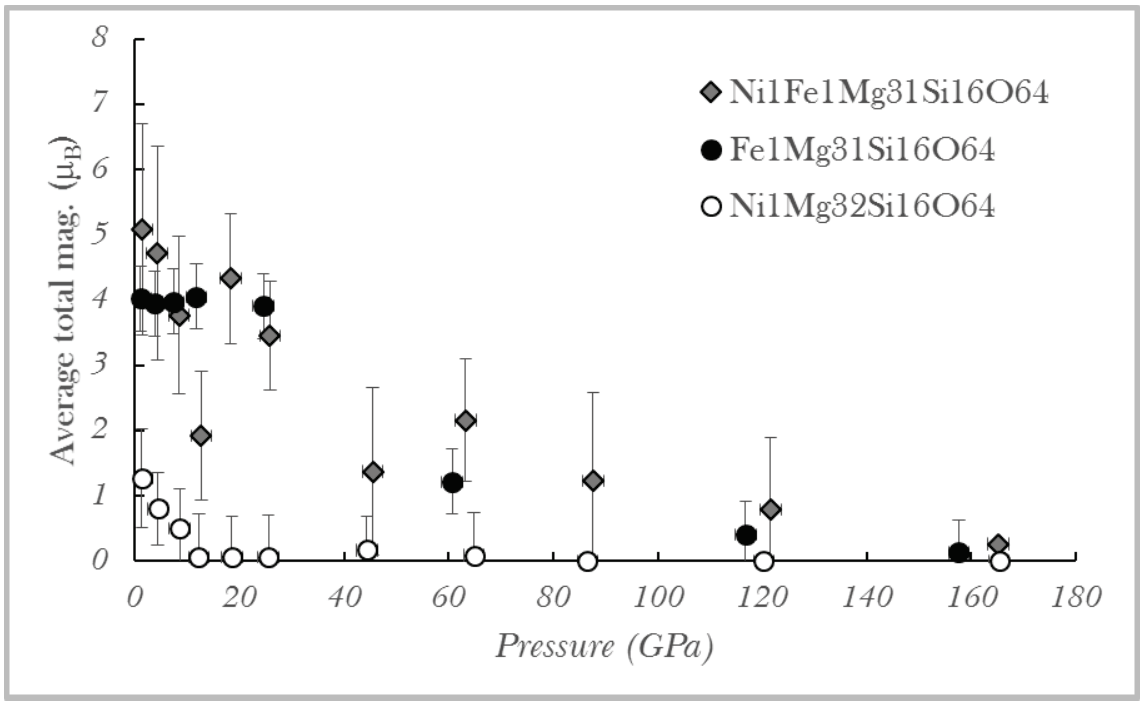

Figure 48 The total magnetization of the simulation cell containing both Fe and Ni is the sum of the total magnetizations of the compositions containing only one transitional metal. The High Spin of Fe decreases slowly across the mantle pressure regime, reaching a Low Spin state at the bottom of the Earth's mantle. The behaviour of Ni is unaffected by the presence of Fe. Error bars have the same meaning as in the previous figures.

4.8. Discussion

We have shown that spin state changes of Ni, Co and Fe, in some silicate melts, can take place in the Earth's mantle pressure range. High temperatures should favour the HS state due to thermal expansion and more space available for the large HS state but we find the opposite effect.

Fe is the most important transitional element studied in the present work. Previous works have either suggested that Fe presents a sharp spin crossover at 70GPa (Nomura et al.,2011) that affects its partitioning behaviour between silicate and metallic melts, or that it does not present any spin crossover in the Earth's mantle (Prescher et al.,2014). Both of these studies were performed on glasses. The usefulness of glass as a melt proxy is debatable, especially when it comes to spin states due to the lack of temperature. Ramo & Stixrude,2014 provide the only study on silicate melts. They argue that in a Fe_2SiO_4 melt, there is no spin crossover in the mantle pressure range.

Ramo & Stixrude,2014 do not investigate the effects of silicate melt composition or Fe amount. This work provides this missing data.

In both types of melts studied here, Fe has a spin crossover within the Earth's mantle pressure range.

In enstatite melts, the spin crossover takes place at D" pressure conditions and it is not affected by the Fe concentration. In olivine melts, the Fe content has a strong effect on the pressure of spin crossover.

Mg_2SiO_4 melts containing only 3.125% Fe, at 3000K, a spin state crossover is observed at ≈60 GPa. If Fe content is increased to 18.75% Fe, the pressure of the spin state change is decreased to ≈20 GPa. In both cases the spin crossover is done gradually, over a wide pressure range.

The pressure at which the Fe spin state changes occur is dependent on the melt composition. Polymerized melts increase the Fe spin crossover substantially.

For $MgSiO_3$ melts, higher temperature seems to have an effect on the pressure of spin state change from HS to LS. The effect observed from 3000 to 4000K is of ≈30 GPa. In both cases the, spin state change seems to happen at the bottom of the lower

mantle. We have not investigated the temperature effect on Fe spin behaviour in Mg_2SiO_4 melts.

Our results do not exclude the findings of Prescher et al.,2014 since the maximum pressure investigated in their study is 84GPa. Contrary to the findings of Ramo & Stixrude,2014, our results suggest that in a $FeSiO_4$ melt, Fe would have a HS to LS transition at low pressures.

In bridgmanite, GGA-PBE zero-temperature simulations show the pressure of transition decrease from 210 GPa for $(Fe_{.05}, Mg_{0.95})SiO_3$ to ≈90 GPa for $FeSiO_3$ (Bengtson et al.,2008). We do not find a Fe-content dependency on the spin crossover pressure in $(Fe,Mg)SiO_3$ melts. The work of Umemoto et al.,2008 on bridgmanite find a spin crossover pressure between 50 to 70 GPa for a $(Fe_{.5},Mg_{.5})SiO_3$. For lower Fe-content the pressure of spin crossover found by Umemoto et al., is similar to our Fe in olivine melt results. The Fe-content increase in olivine melts required for a 1GPa decrease in spin crossover pressure is smaller than in bridgmanite.

Ni shows a spin state crossover in Mg_2SiO_4 melt between 12 and 19 GPa at 3000K. This transition is facilitated by the low Δ energy of Ni and the depolymerized state of the melt. The spin state crossover affects the Bader charge creating a kink in the partial charge trend with pressure. Spin state changes, charge changes, and Ni-O coordination changes happen at the same pressure.

HS to LS transition decrease the atomic volume of Ni (Figure 49), more significantly than pressure effects.

In the case of Ni distribution between a silicate and a metallic melt, the most plausible process is a cation exchange (Wade & Wood,2005; Corgne et al.,2008):

$$Ni + FeO = NiO + Fe \quad (27)$$

Pressure decrease on the molar volumes of both silicate and metallic melts would induce an increasing nickel affinity for silicate melts, but it would not produce the kink (Sanloup et al.,2013; Sanloup et al.,2011; Kegler et al.,2008) in the partition trend.

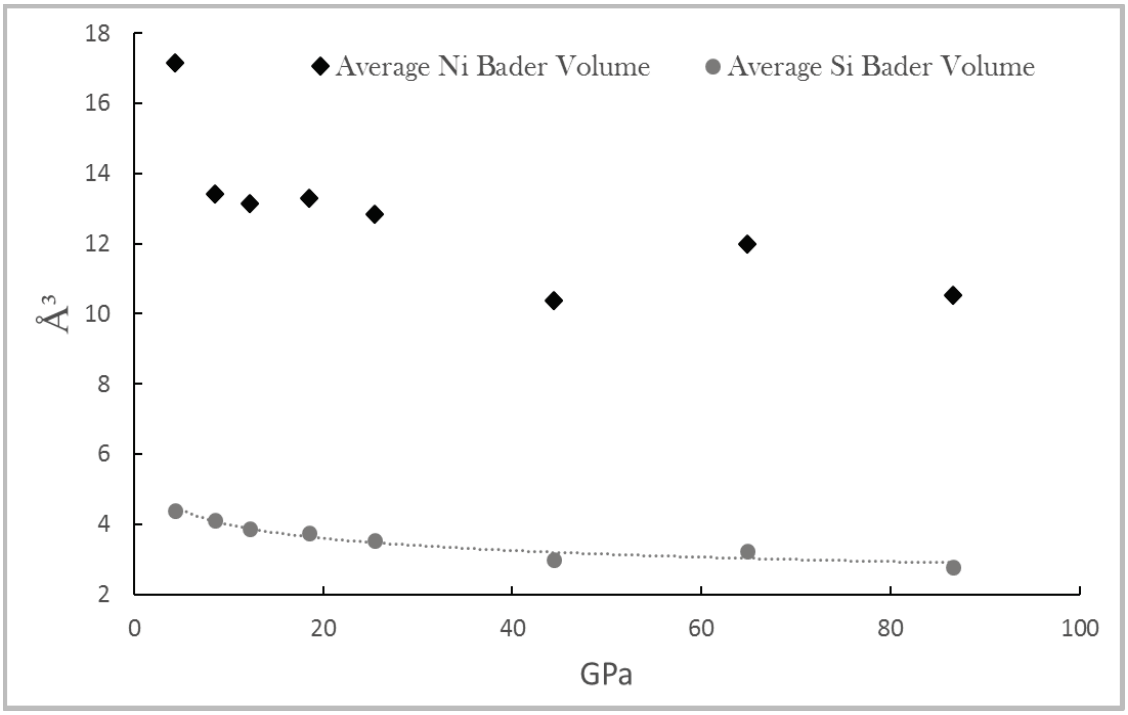

Figure 49 The average Bader volume of Ni in the olivine melt shows a substantial decrease at low pressures. The marked decrease in volume corresponds to the pressure where the LS spin states of Ni become stable. By comparison the Bader volume of Si in the same melt has been plotted. The Bader volume of Si feels only the effects of pressure, and the volume decrease can be fitted very well to an exponential forms.

Since the metallic melt is more insensitive to pressure (Morard et al.,2013) the change that matters happen in the silicate melt.

At low pressure, below 12 GPa, only the HS states would matter:

$$Ni^{HS} + Fe^{HS}O = Fe^{HS} + Ni^{HS}O \quad (28)$$

At pressure above 19 GPa the LS state of Ni is the preferred spin state and in the case of Fe the HS states are still predominant. Thus the exchange equation has changed from two cations of similar volumes and identical charges, into an exchange equation between two cation of different volumes.

$$Ni^{LS} + Fe^{HS}O = Fe^{HS} + Ni^{LS}O \quad (29)$$

The spin-crossover of Ni marks the kink in the partition coefficient trend with pressure (Figure 50). Even though oxygen fugacity has a substantial effect on the

partitioning behavior of Ni, Figure 50 shows that our spin data fits very well with partitioning data at IW-1 (yellow line).

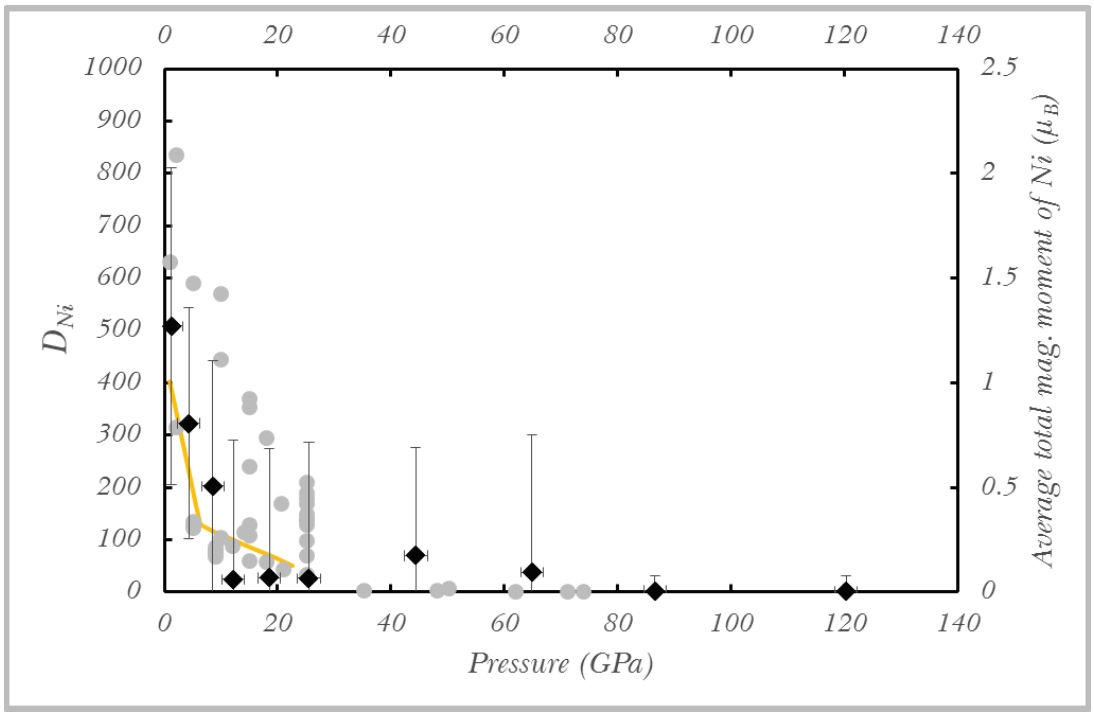

Figure 50 Correlation between the Ni partition coefficient between a silicate and a metallic melt and the Ni spin cross over. Light grey circles represent literature data on the partitioning of Ni and the black diamonds are the total average magnetization of Ni. The HS to LS transition of Ni coincides with the kink the partition coefficient. Partition data from Li & Agee,1996; Fischer et al.,2015; Siebert et al.,2012; Siebert et al.,2011. *The yellow line marks the position of the kink as proposed by (*Sanloup et al.,2011; Kegler et al.,2008*).*

Sanloup et al.,2013 proposed that structural changes in silicate melts (Si-O coordination number) imposed by pressure affect the partitioning coefficient of Ni, but they did not analyse the Ni-O coordination number nor did they study the spin state of any transitional metals present in their samples. We do not agree with the interpretation of Sanloup et al.,2013, because the Si-O coordination reaches the value 6 at substantially higher pressures than the spin crossover.

In Ni-bearing $MgSiO_3$ melt, due to the higher degree of polymerization than in olivine melts the spin crossover does not occur in the Earth's mantle pressure range. Ni remains in a LS state, with minor variations in the abundance of HS and LS states.

An important observation is the effect of silicate melt composition on the spin state of Ni. In depolymerized melts, such as Mg_2SiO_4, Ni presents a spin crossover

while in polymerized melts it does not. The influence of the melt composition is important since the partitioning of Ni is affected by its spin state.

Co presents a spin crossover at around 26GPa. Even though pressure effects could not be distinguished from spin-state induced volume decrease of Co, a volume decrease is expected. As in the case of Ni, the transition is marked by anomalous Bader charge values. In contrast to Ni, the Co-O coordination number does not show major variations from the steady increase with pressure specific to all cations studied here. The presence of LS as well as IS must be translated in an overall

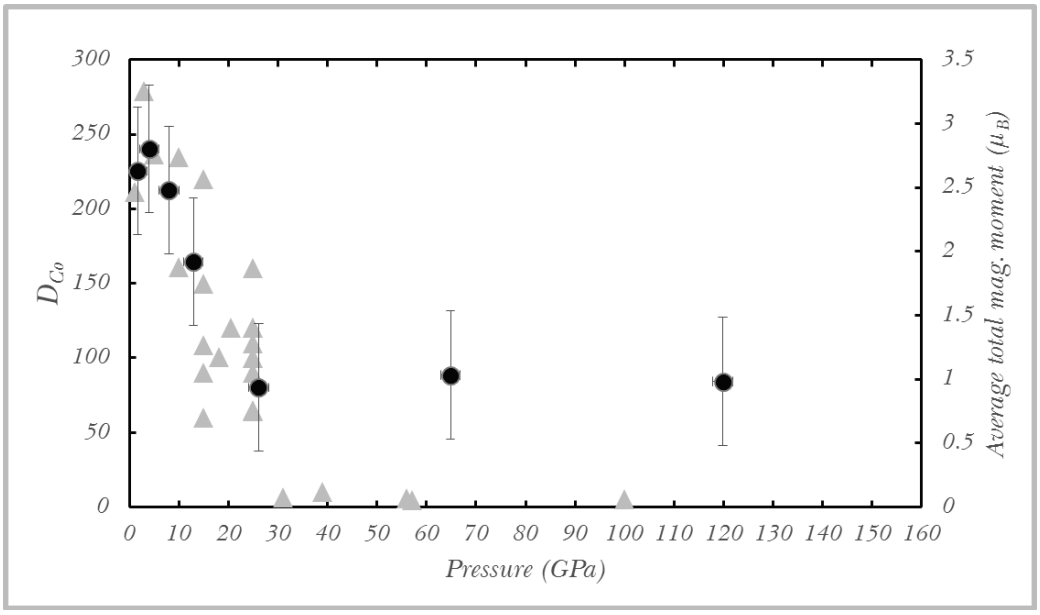

Figure 51 The partitioning coefficient of Co between a silicate and a metallic melt shows a similar kinked pattern as the average total magnetization. Triangles represent partition coefficient data from literature Siebert et al.,2011; Fischer et al.,2015 *and the dots are the average total magnetization of Co. The inset shows a zoomed in view of the low pressure range.*

volume decrease.

Figure 51, shows a comparison between the partitioning coefficient evolution with pressure, taken from literature data, and the average total magnetization. The spin crossover pressure coincides with the kink in the partition coefficient. This suggests that the spin state change of Co, is responsible for its increasing lithophile character with pressure.

To conclude, the spin-state of Ni, Co and Fe in silicate melts is affected by pressure, composition and in a lesser degree by temperature. The transition from one spin state to another is done gradually, through a pressure range where all spin

states possible are present. The spin crossover of Ni and Co might affect their partitioning behavior.

5. *The influence of the melt structure on the partitioning of Ni, Co, and W*

Earth's mantle is depleted in siderophile elements with respect to the chondritic material. This discrepancy can be explained by the siderophile character of these elements and their partitioning into the core during core formation. Nonetheless, the abundances of these elements in the mantle are not those expected after their partitioning into the core. These higher than expected concentrations of Co, Ni and W and other siderophile elements is known as the "***siderophile elements anomaly***" (Kimura et al.,1974; Ringwood,1966). W in particular is of greater interest since it is part of one of the isotopic systems (^{182}Hf – ^{182}W) used to date the core formation events (Halliday et al.,1996).

The partitioning of elements between a silicate melt and a metallic one can be influenced by a wide range of factors such as composition, pressure, temperature, oxygen fugacity, and melt structure (Siebert et al.,2011). This chapter represents our efforts to clarify the influence of structural factors, with a focus on the degree of polymerization, on the partitioning of Co, Ni and W.

A change in the pressure evolution of the partitioning coefficients of Co and Ni has been reported (Kegler et al.,2008; Siebert et al.,2012). This change in slope might be the result of changes in the melt structure (Sanloup et al.,2013). An inconsistency in experimental procedures might also be responsible for the kink in the partitioning coefficient. Most low pressure experiments are performed using mafic melts, while for high pressure ultramafic compositions are used, for example Kegler et al.,2008. It could be argued that different silicate melt compositions change the nature of the system, modifying the degree of polymerization of the silicate melt, thus leading to incomparable partitioning coefficients between low and high pressures.

Changes in the coordination of network-forming cations as silicon, due to increasing pressure, have been attributed as an explanation for the change in slope of

the partitioning of Ni (Sanloup et al.,2013). The change in coordination of Si happens at high pressures, as argued previously in this thesis. Therefore determining the short-order of silicate melts in situ is a difficult process, and it is perhaps beyond the experimental means available nowadays in the case of metal-silicate melt partitioning experiments. Because of this, a chemical approach to quantifying the degree of polymerization is used (NBO/T) (Mills,1993).

There has been considerable debate in the literature about whether the NBO/T affects the partitioning of elements between a silicate melt and a metallic one (Righter,2011a; Palme et al.,2011; Righter,2011b). It can be argued intuitively that a depolymerized melt has a more open framework and thus more room for the elements to partition into it.

If the degree of polymerization does indeed affect the partitioning of some elements between a silicate melt and a metallic melt, then models that predict the evolution of the differentiation of the Earth should take into account this effect (beside pressure, temperature, and oxygen fugacity). Changes in the partitioning behaviour of elements due to the change of the degree of polymerization might lead to an evolving partitioning behaviour during fractional crystallization or melting.

Here we will present multianvil experiments on metal-silicate melts partitioning, at 8GPa and 1950° C, constructed and performed as an attempt to answer the question: ***does the degree of polymerization affect the partitioning of Co, Ni, and W***? We also employ FPMD simulations to explore structural factors affecting the partitioning.

5.1. Experimental set-up

For decades the best approximation for the degree of polymerization of a silicate melt has been the ratio of Non-Bridging Oxygens to Tetrahedral coordinated cations (NBO/T) (Mills,1993).

In most silicate melts, alt low pressures, the major elements cations found in a tetrahedral coordination are Si and Al (and we chose not to include P in our experiments in an attempt to keep the compositions of our silicate melts simple but still relevant to Earth systems).

We perform multianvil experiments to test the effects of NBO/T value of silicate melts on the partitioning of Ni, Co, and W. The starting materials were high purity commercially available oxide powders (with the exception of Ca which was found as carbonate – $CaCO_3$ which was decarbonated). All powders were weighted and heated in order to lose the adsorbed water according to the heating scheme shown in Figure

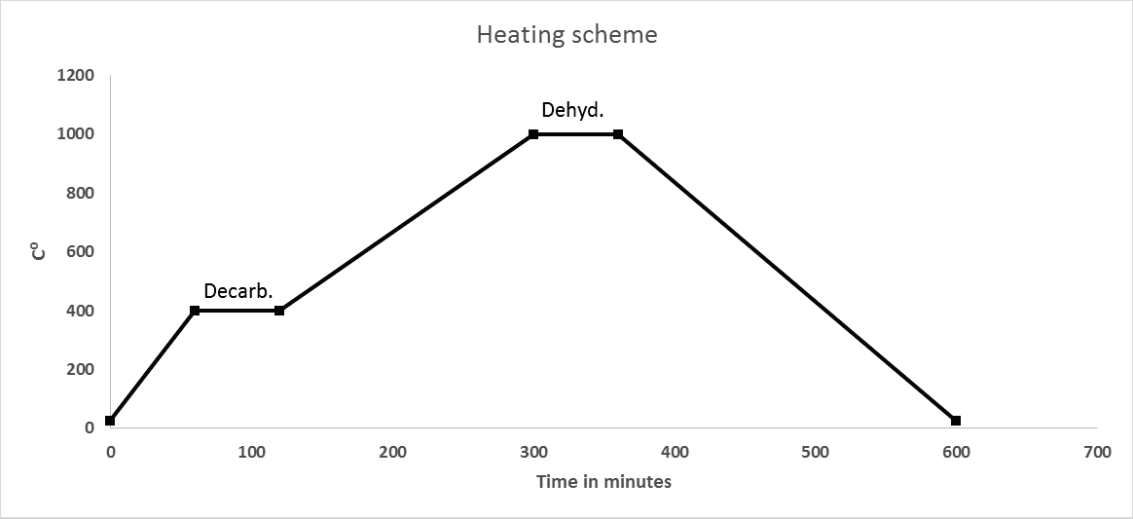

Figure 52 Heating scheme for SiO_2, $CaCO_3$, Al_2O_3, MgO, Fe_2O_3 powders.

52.

The powders were kept at 400°C for 1 hour after which the temperature was increased slowly to 1000°C, and kept constant for another hour. The samples were weighted before and after heating, to ensure the loss of volatiles.

We prepared 6 silicate compositions with various NBO/T values (Table 6).

Table 6 Starting compositions with different NBO/T values, in wt%.

Sample	SiO_2	MgO	Al_2O_3	CaO	Fe_2O_3	NiO	CoO	WO_3	NBO/T
1	57	17	8	6	10	1	1	1	1.22
2	51	23	8	5	10	1	1	1	1.58
3	46	27	7	6	10	1	1	1	2.07
4	37	34	8	8	10	1	1	1	2.95
5	35	35	8	8	10	1	1	1	3.15
6	33	39	7	7	11	1	1	1	3.64

The powders were weighted on a high precision scale and mixtures of 1 gram were made for each sample. Samples were pressed in a pill, set on a platinum cradle and reduced in a gas mixing oven at the IW buffer. The conditions for reduction were: 1200^0 C and $\log fO_2 = -11$. The gas mixture used was a 99% CO_2 and 1% CO mixed gas flow. The samples were held in the gas mixing oven for 24h.

As soon as possible after the reduction of the sample, it was grinded back into a powder. Equal amounts of sample and Fe metal powder were mixed and set in the

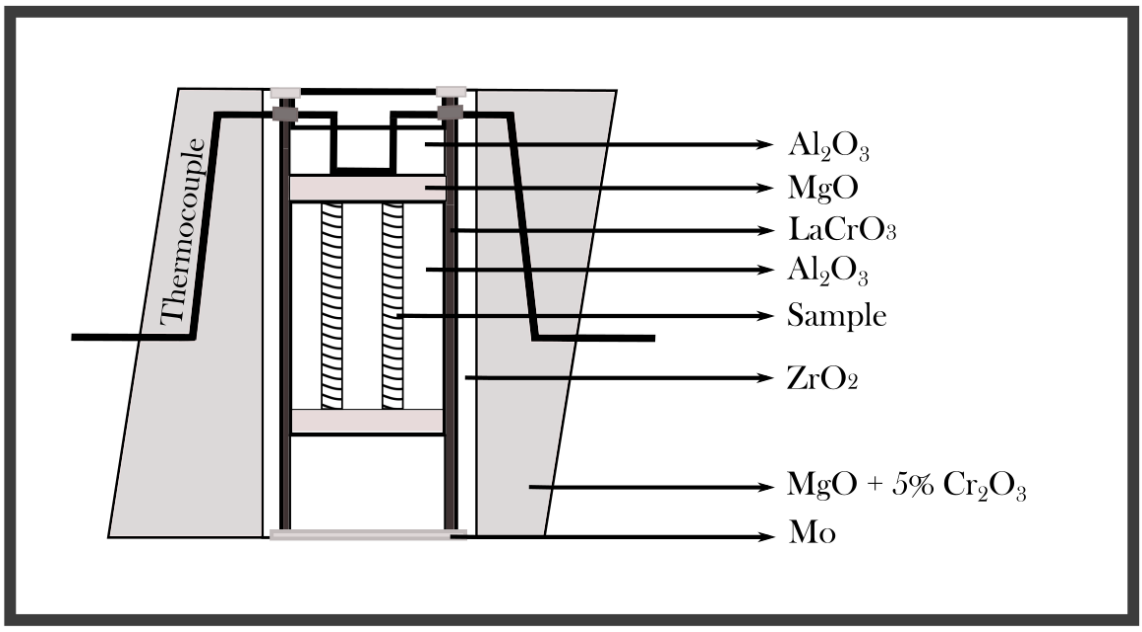

Figure 53 Cross section through the 18/11 assembly showing the first experimental set-up used.

18/11 assembly as shown in Figure 53.

The sample capsule was a high density Al_2O_3 tube with two holes in the centre which acted as sample holders. The reason behind the choice of an Al_2O_3 capsule is

that carbon, a common material for capsules, is soluble in metallic melts and it affects the partitioning of other elements (Siebert et al.,2011). Each experiment carried two separate samples (Figure 53), with two different initial NBO/T.

A MgO micro-polycrystalline octahedron doped with 5% Cr_2O_3 acts as a pressure medium. The $LaCrO_3$ sleeve is a high temperature heater when electric current is passed through it. The electrical circuit is connected to the exterior through a Molybdenum ring on the thermocouple side and a Mo disk on the other side. The thermocouple is isolated from this circuit by two high density Al_2O_3 tubes. Electrical current is passed through the anvils of the press, through the tungsten carbide cubes (the inner anvils) and thus completing the circuit.

The 18/11 assembly is positioned in the centre of 8 tungsten carbide inner anvils separated by gaskets. Insulating tape is used to cover the tungsten cubes so that the electrical flow is directed only through the $LaCrO_3$ heater.

High-pressure was achieved by using the Sumitomo 1200 tonnes press. The

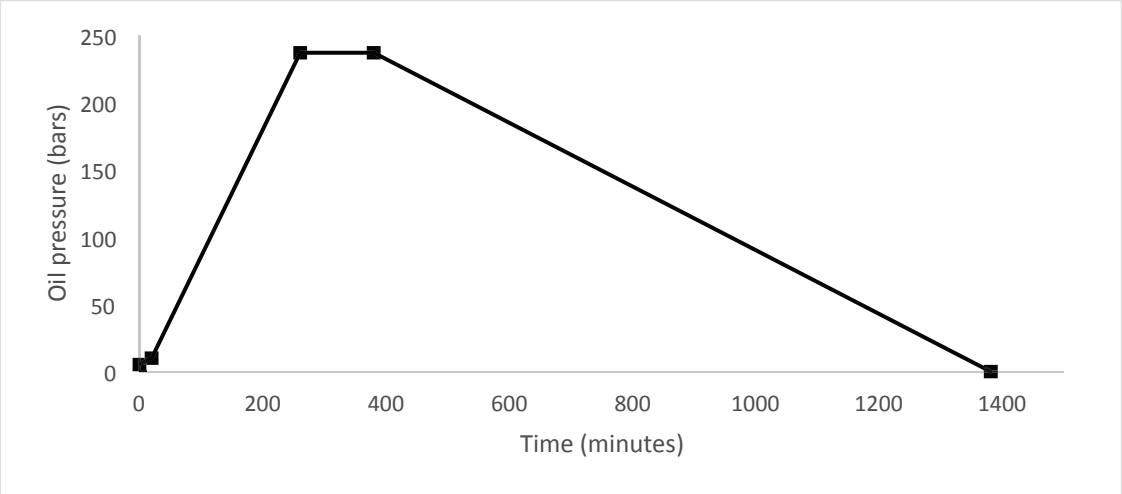

Figure 54 Compression regime, pressure is the oil pressure given as input to the press. Maximum pressure corresponds to the target pressure of 8 GPa.

compression regime is shown in Figure 54.

Pressure calibration indicated that for 18/11 assembly the oil pressure required to reach the target pressure of 8GPa is 237 bars. Once the target pressure was reached the sample was heated relatively fast up to 1950^0 C and was given an equilibration time of 10 or 5 minutes. After that, the sample was quenched by

shutting down the electrical current. After decompression the octahedron was removed from the cube anvils, cut and polished for SEM analysis.

Because the sample capsule was a two-hole alumina thermocouple tubing Al_2O_3 contamination of the silicate melt reduced the final NBO/T ratios of the silicate melts (regardless of the equilibration time). Samples 1 through 6 were affected by this.

In order to obtain various NBO/T silicate melt values we changed the capsule to

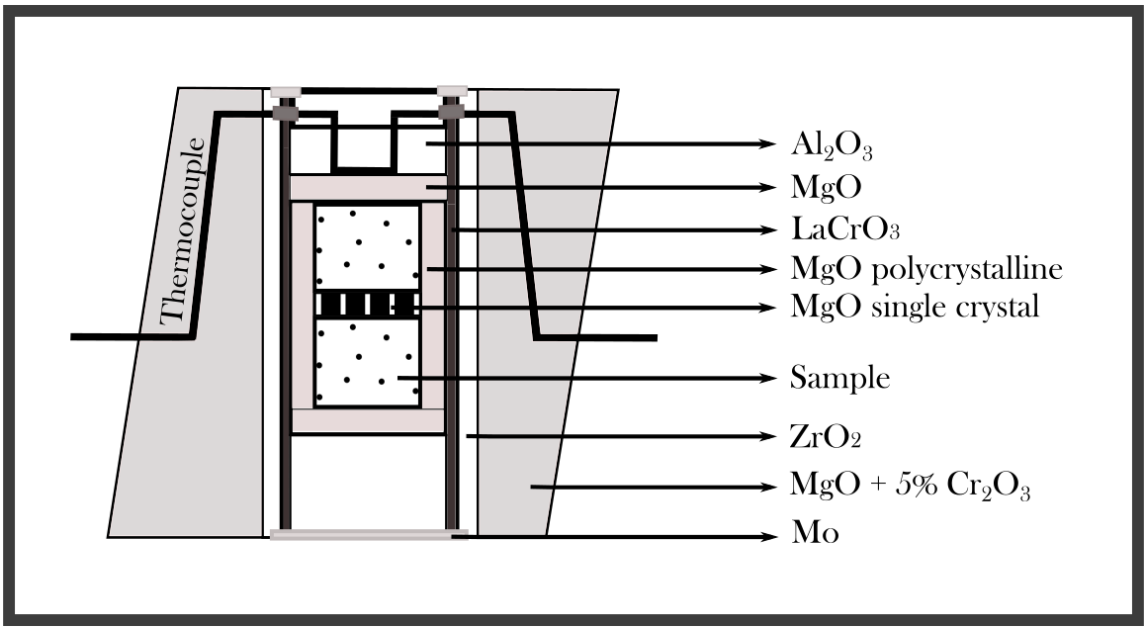

Figure 55 Cross section through the 18/11 assembly showing the second experimental set-up. The two samples are now arranged one on top of the other, and separated by a single crystal MgO disk.

a double MgO capsule, separated by a single crystal MgO disk as shown in Figure 55.

The MgO single crystal separator between the two samples was chosen as to resist the high temperature and minimize the MgO contamination of the silicate melts formed by the melting of the samples. Samples 5x and 6y (from starting material 5 and 6, table 3) were compressed in this type of experimental set-up.

5.2. Sample imaging and compositional measurements

Scanning Electron Microscope Back-Scattered Electrons (SEM –BSE) images were taken of each sample and preliminary SEM – Energy Dispersive X-ray Spectroscopy (EDS) spot analysis were done in order to check the major

compositions of the two quenched phases. This information was also used to assess the success of the experiment. SEM-EDS resolution was considered insufficient and the information obtained has only a qualitative nature. The high resolution images obtained and the chemical information were used to identify the best spots for further, more accurate chemical measurements.

Micro-quench textures were observed alongside the presence of large corundum crystals in the quenched silicate melt. The corundum crystals are the result of

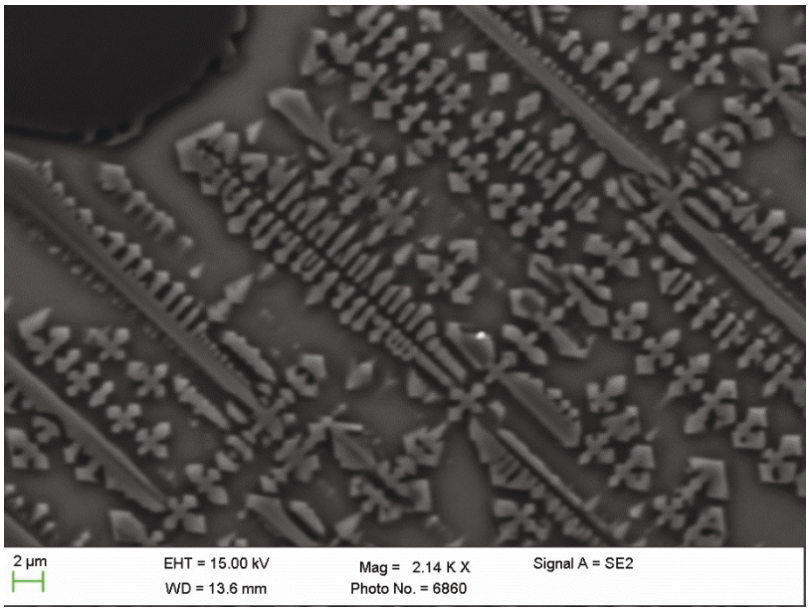

Figure 57 SEM-BSE image of quench textures formed by the crystallization of corundum crystals

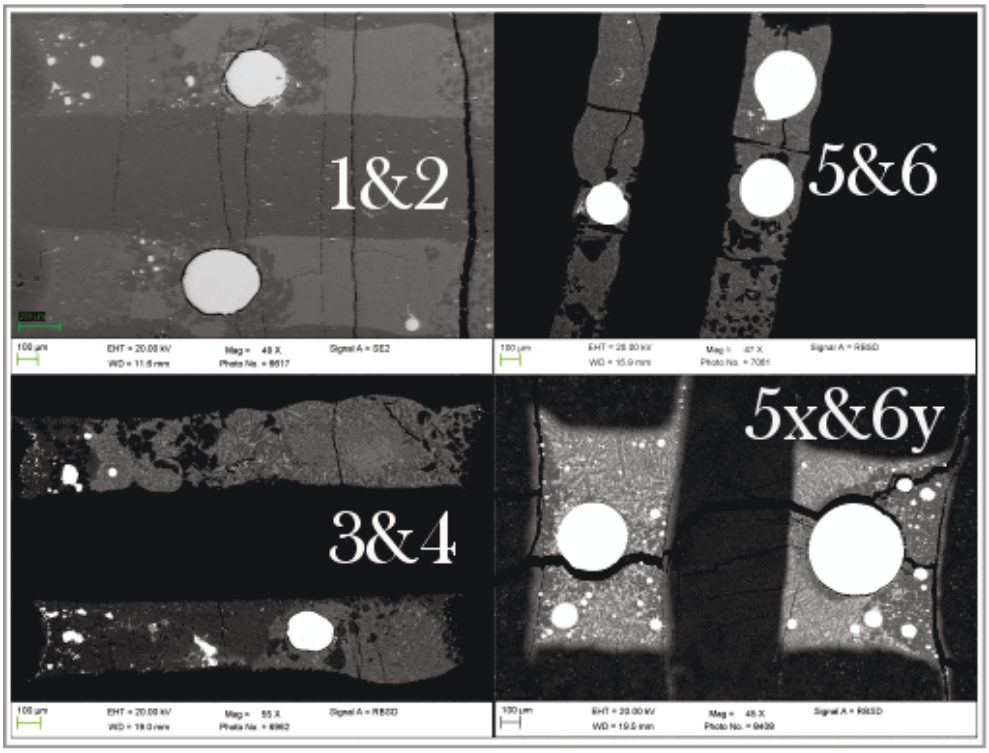

Figure 56 SEM-BSE images showing all the multi-anvil experiments. All experiments were done at 8GPa and 1950^{o} C. The darker phases in the sample are corundum and spinel crystals.

alumina contamination from the Al_2O_3 capsule (Figure 56). SEM-BSE images of all successful experiments are shown in Figure 57.

A Jeol JXA-8200 electron microprobe was used to measure the composition of the quenched metal and silicate melt. Due to the absence of big enough glass pockets and the presence of quench textures, a defocused beam was used to measure the composition of the quenched silicate melt. Since all three trace elements in question, Cobalt, Nickel, and Tungsten are highly siderophile their concentrations in the quenched silicate melt are too small to be measured accurately by electron microprobe in any circumstance. Only the metallic melt composition obtained by electron microprobe was used.

The materials used for calibration, measurement conditions, and element-crystal allocation are listed in table 7 and 8.

Table 7 Electron Microprobe standards. "Met." stands for metallic. By which it means that a pure metal standard was used.

Element	**Si**	**Al**	**Mg**	**Fe**	**Ca**	**Ni**	**Co**	**W**
Standard	Diopside	Spinel	Enstatite	Met. Fe	Diopside	Met. Ni	Met. Co	Met. W

Table 8 Beam characteristics and element-to-crystal distribution set for the microprobe.

Beam size: 20 µm and beam characteristics: 20KeV/50 µA				
TAP	**TAP**	**PET**	**LIF**	**LIF#**
Si	Al	Ca	Fe	Ni
	Mg		W	Co

For the compositional measurement of the quenched silicate melt we used Laser-Ablation Inductively Coupled Plasma Mass Spectrometry (LA-ICP-MS).
Two standards were used for the LA-ICP-MS measurements, the NIST 610 (artificial glass) and BCR2G (natural basalt). The elements measured are: Si, Mg, Al, Fe, Ni, Co, W, Ca, K, Cr, Zr, La and Re. Potassium, chromium, zirconium, lanthanum and rhenium were measured in order to check for possible contamination of the sample, either from the 18/11 assembly components or other possible contaminants.

The measurement protocol was the measurement of both standards before measuring the sample, this ensured a good calibration of the measured compositions.

Spot measurements were taken, with spot sizes of 40, 50, and 70 μm at 5Hz. Acquisition time was 2 minutes and eventual spikes were manually removed before integration, no drift correction was necessary.

5.3. Experimental results

The composition of the metallic quenched melt and the silicate quench was determined by electron micro-probe and LA-ICP-MS respectively. LA-ICP-MS data was preferred for the silicate quenched melt as the accuracy of the measurements is superior to that of the micro-probe, especially for the concentrations of the trace elements Ni, Co and W. No contamination of unwanted elements was detected in any of the phases measured.

The compositions of the silicate quenched melt and the metallic one are reported in Tables 9 and 10. Measured elements not reported were either zero or less than the error of measurement.

Sample 1 presents a silicon contamination of 1% in the metal either due to diffusion of Si from the silicate melt into the metallic one or due the presence of small silicate inclusions. If the diffusion of Si into the metal is responsible for this small contamination then the absence of silicon in the other samples can be explained by the smaller equilibration time. Silicon content of the metallic melt is known to affect the partitioning of elements and thus we decided to ignore this sample in order to maintain the comparability of our experiments.

Differences between the initial compositions and the final ones are due to weighing errors and contamination from the sample capsule with either alumina or MgO, depending on the capsule used. The NBO/T shown in table 9 is the calculated value for the final composition. Even though the aimed-for NBO/T covered a wider range of values, the achieved NBO/T values are sufficient (Figure 58).

Table 9 Metal compositions obtained by Electron Micro-probe, uncertainties are 0.02 wt%.

Sample	Si wt%	Al wt%	Ca wt%	Fe wt%	Ni wt%	Mg wt%	W wt%	Co wt%	Ni ppm	W ppm	Co ppm
2	0.27	0.03	0.00	96.26	1.00	0.03	0.80	1.61	7760.60	6173.07	12470.14
3	0.01	0.00	0.00	94.83	1.68	0.00	1.75	1.72	13063.45	13502.94	13366.54
4	0.04	0.04	0.08	91.92	2.20	0.10	2.99	2.64	14772.38	23036.27	19238.92
5	0.00	0.00	0.00	95.12	1.61	0.00	1.55	1.72	12500.01	11961.44	13368.67
6	0.00	0.00	0.00	95.18	1.54	0.00	1.58	1.70	11979.74	12141.63	13193.91
5x	0.00	0.00	0.00	96.54	1.03	0.00	1.22	1.20	8006.29	9403.78	9288.88
6y	0.00	0.00	0.00	96.70	1.11	0.00	0.99	1.19	8644.16	7635.76	9236.35

Table 10 Silicate melt compositions obtained by LA-ICP-MS, uncertainty is 0.0232 ppm

Sample	MgO wt%	Al2O3 wt%	SiO2 wt%	CaO wt%	FeO wt%	Co ppm	Ni ppm	W ppm	NBO/T
2	14.98	27.59	47.26	2.35	7.82	126.38	26.26	3.19	0.61
3	14.11	26.06	46.15	4.07	9.61	174.34	49.44	27.90	0.67
4	18.60	18.40	46.11	6.92	9.96	338.71	110.43	260.88	0.99
5	32.82	7.54	47.34	6.88	5.42	147.75	44.29	52.38	1.30
6	30.72	9.25	45.76	8.39	5.88	154.74	42.92	103.85	1.50
5x	22.99	19.32	44.98	5.09	7.62	99.23	56.07	94.96	2.90
6y	24.60	18.47	43.10	5.58	8.25	136.51	34.33	150.18	2.45

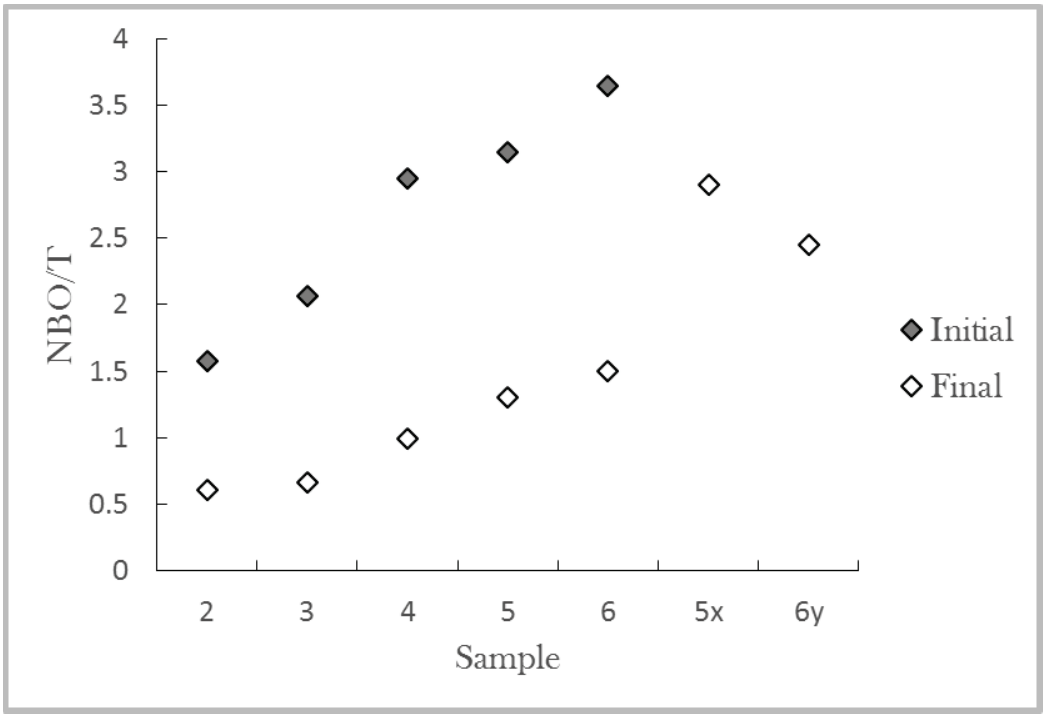

Figure 58 Differences between expected and final NBO/T values. Alumina contamination from the capsules reduced substantially the values of NBO/T. By changing the capsule to a MgO one, for samples 5x and 6y a wider range of NBO/T values could be achieved.

Runs 1 through 6 were done in an alumina capsule so they were affected by a large Al_2O_3 contamination (Figure 59). This reduced the NBO/T values substantially. Equilibration times and initial SiO_2 concentrations are probably responsible for the contamination.

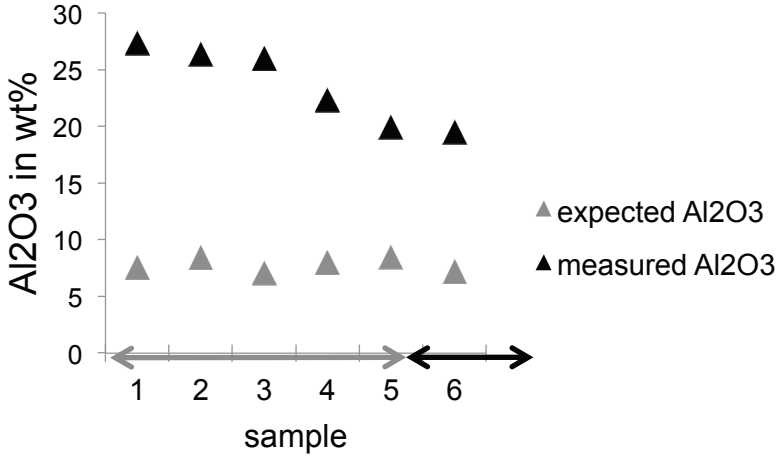

Figure 59 Difference between the expected Al2O3 concentrations in samples 1 to 6 and the concentrations measured after the run. The grey arrow denotes the samples with an equilibration time of 10 minutes and the black one corresponds to an equilibration time of 5 minutes.

The partitioning coefficients (table 11) were calculated as:

$$Di = \frac{C_i^{metal}}{C_i^{silicate}} \tag{30}$$

In order to check that the oxygen fugacity was not affecting the partitioning we also calculated the $D_{Ni/Fe}$ (table 10, Figure 60) (Kegler et al.,2008):

$$D_{\frac{Ni}{Fe}} = \frac{D_{Ni}}{D_{Fe}} \tag{31}$$

Table 11 Partitioning and exchange coefficients and the corresponding NBO/T values of the silicate melts

Sample	D_{Ni}	D_W	D_{Co}	D_{Fe}	D_{Ni}/D_{Fe}	NBO/T
2	295.50	1935.45	98.67	8.45	34.96	0.61
3	264.24	483.90	76.67	6.89	38.34	0.67
4	133.77	88.30	56.80	6.55	20.41	0.99
5	282.23	228.37	90.48	12.43	22.70	1.30
6	279.13	116.91	85.27	11.54	24.20	1.50
5x	142.79	99.03	93.61	8.92	16.01	2.90
6y	251.76	50.84	67.66	8.32	30.26	2.45

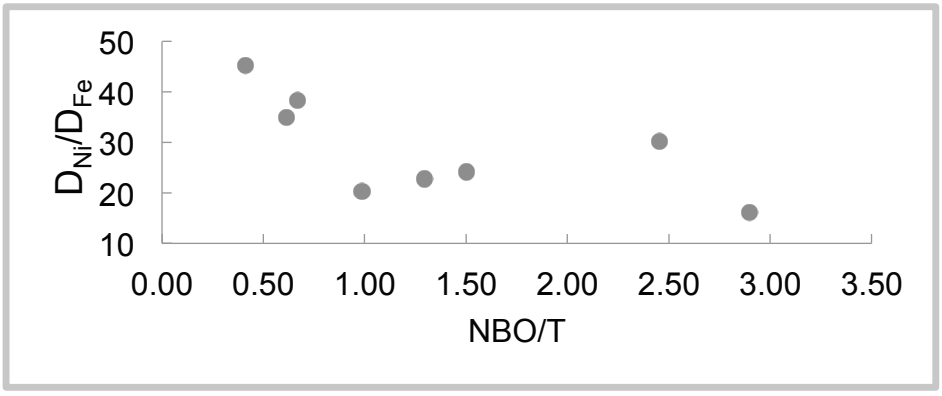

Figure 61 DNi/DFe versus their respective NBO/T silicate melt values

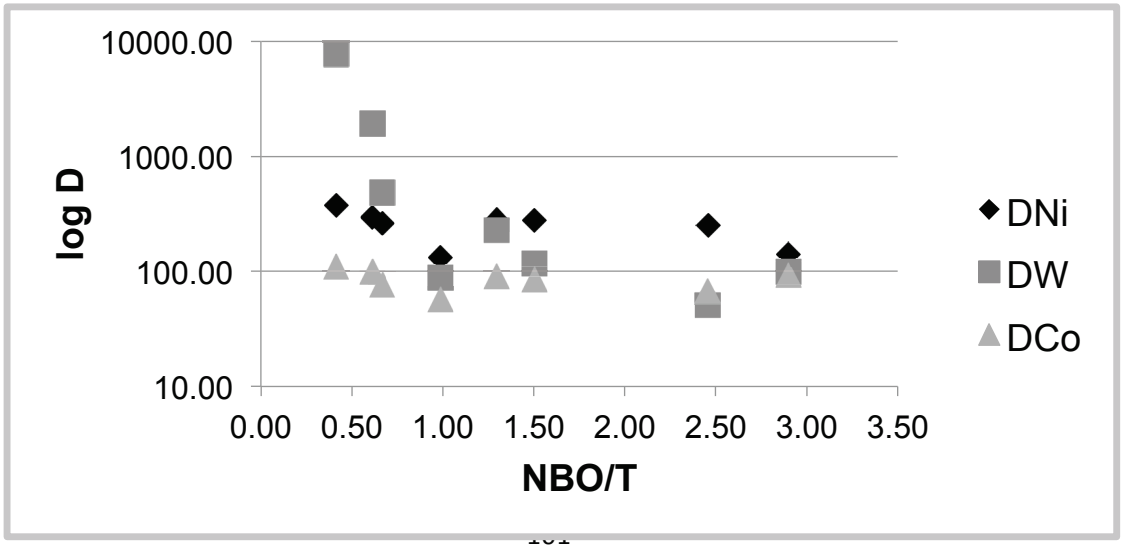

Figure 60 Partitioning coefficients of Ni, Co, and W versus NBO/T

5.4. FPMD study of W and Ca in highly polymerized silicate melts

As it can be observed in Figure 61 there is a general decreasing trend of the partitioning coefficients of W with increasing NBO/T, or decreasing polymerization,

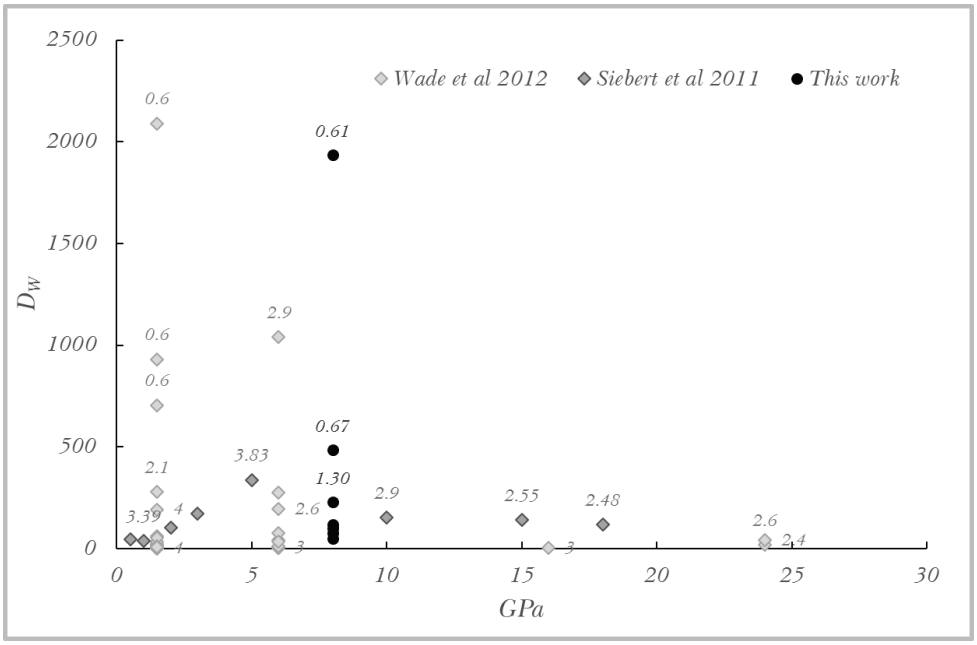

Figure 62 Comparison between the literature data and the results of this work. The numbers on the graph represent the NBO/T values. For the data from Siebert et al.,2011; Wade et al.,2012 *pre-run NBO/T values were reported and shown here. For this work the after-run values are shown. As observed, the data presented here is in good agreement with literature.*

in accordance with previous studies (e.g. Siebert et al.,2011) (Figure 62).

Tungsten's partitioning seems to have a pronounced dependence on the value of NBO/T. In other words, the litophile character of tungsten increases with the decrease in polymerization. Cobalt and Nickel on the other hand, seem to be less affected by the variations in NBO/T values.

W has the biggest atomic radius of all the siderophile elements present in the system. The larger atomic radius of tungsten, approximately 23% bigger than Ni, can explain the apparent aversion for highly polymerized melts. At 8 GPa the Si-O coordination is still predominantly 4 (Chapter 3).

Previous studies (Walter & Thibault,1995; Cottrell et al.,2009; Siebert et al.,2011) have shown that the partitioning coefficient of W has a negative dependence on the NBO/T value of the silicate melt. We observe a similar behaviour (Figure 61).

Siebert et al.,2011 argue that the increased affinity of W for highly depolymerized melts is due to its high charge and the availability of non-bridging oxygens in these melts. The charge variation of W with increasing pressure, or silicate melt composition has not been constrained. O'Neill et al.,2008 have concluded that at ambient pressure the predominant valence state of W in silicate melts is 6+. Cottrell et al.,2009 calculate the regression of valence state with pressure approximating a valence state of 4+ for higher pressures, but their errors become significantly large with increasing pressure. The litophile character of W increases with pressure, regardless of the polyhedral rearrangements of Si with O. The tighter packing of Si by O decreases the available non-bridging oxygens for W to bind with, and thus a behaviour similar to the relationship with the NBO/T can be expected but it is not observed. The slow decrease in the valence state calculated by Cottrell et al.,2009 can not compensate by itself for the increased lithophyle character.

Cottrell et al.,2009 found that the activity of W in silicate melts is similar to that of Mo. They state that the activity of W in the silicate melt should be affected by the Ca/Mg ratio of the melt. If indeed the Ca amount present in silicate melts leads to the stabilization of W in the silicate melt, a correlation with Ca amount should be observed. This correlation should have a significant impact on the partitioning of W between silicate and metallic melts. Our experimental results might show such a

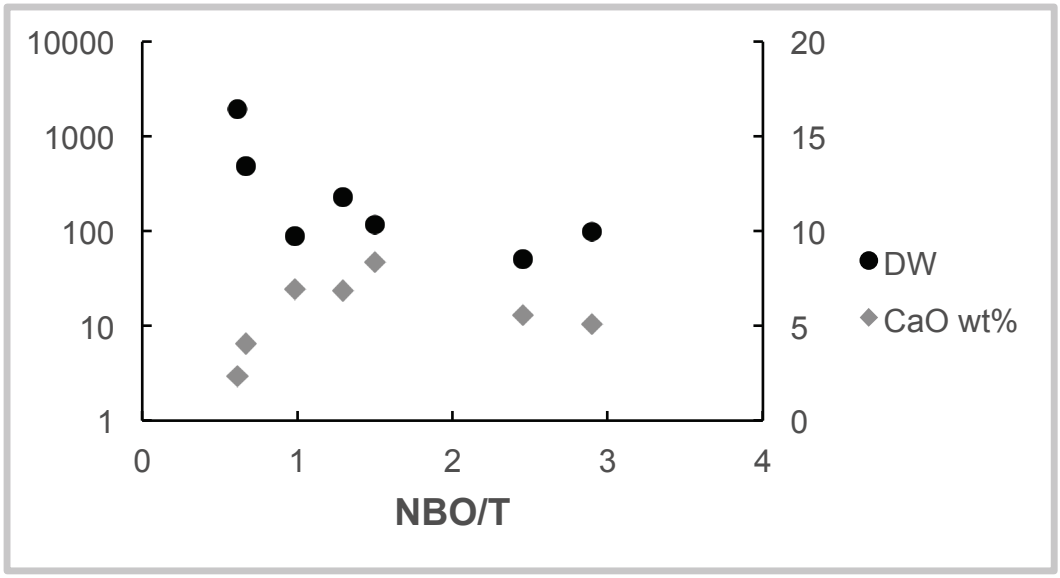

Figure 63 D_W variation compared to CaO present in the silicate melt. An inverse correlation can be observed between W's partitioning coefficient and CaO content of the silicate melt.

correlation (Figure 63).

Another perspective for the similar behavior of Ca and W, despite their different affinities, can be through their large ionic size.

5.4.1. FPMD set-up and results

In order to investigate the atomic behavior of Ca and W in highly polymerized melts we have employed first principles molecular dynamic. A silicate melt with a $Ca_1W_3Mg_{26}Si_{64}O_{161}$ composition was made (Figure 64). It was thermalized at 2000K and 8 (±2) GPa. 14 ps of simulation were performed. At regular time intervals (300 fs), the atomic coordinates were extracted and snapshot runs at the same conditions were performed writing the electronic charges for Bader analysis.

The main run, 14 ps, was used to study the structure of the melt and the self-diffusivities of all the atomic species present.

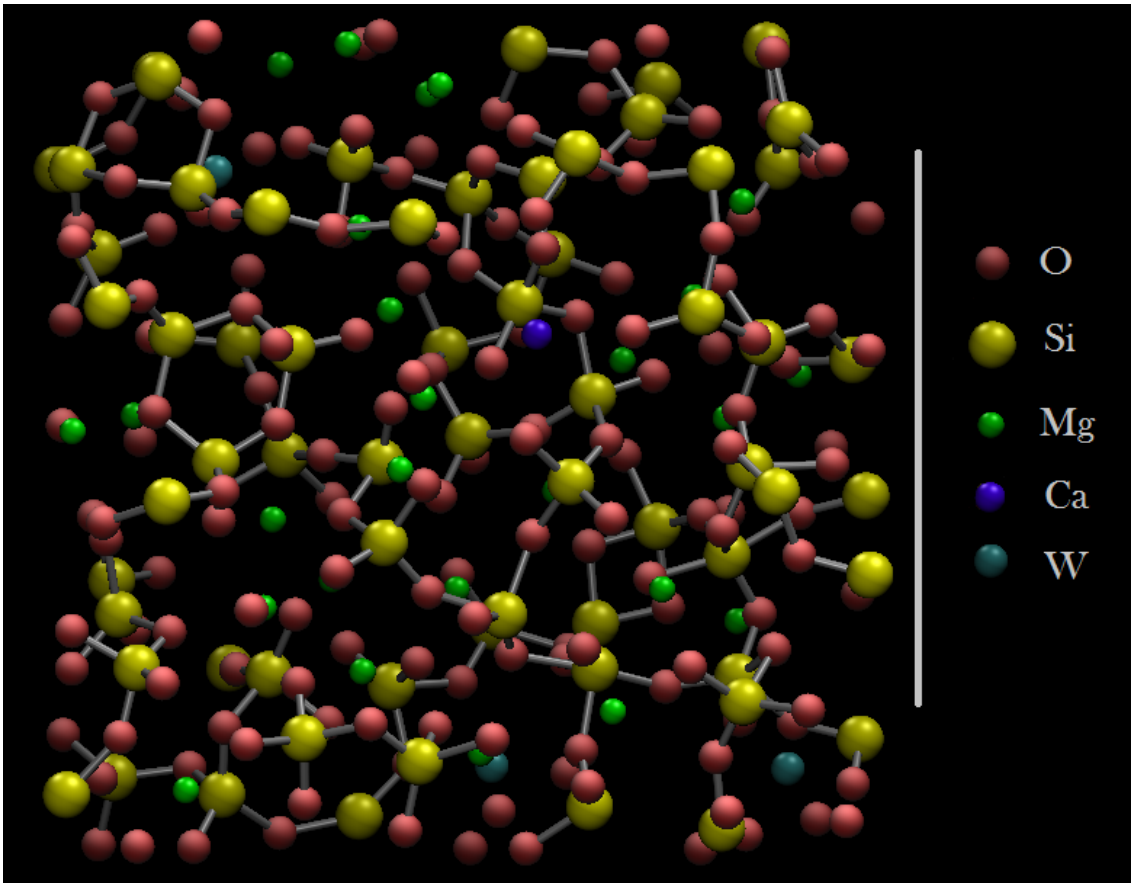

Figure 64 The simulation box containing 255 atoms ($Ca_1W_3Mg_{26}Si_{64}O_{161}$). For clarity only the Si-O bonds have been represented. There are no free-floating Si-O tetrahedral, all Si-O are interconnected. Incompletely linked Si have the corresponding O on the opposite side of the simulation box due to period boundaries conditions.

The W atoms present in the melt are inserted in the 4+ oxidation state. The reason for this choice are the findings of Cottrell et al.,2009, who state that with increasing pressure the valence state of W decreases, reaching 4+ at high pressures. Ca was inserted in its normal oxidation state of 2+.

Figure 65 shows the PDF function for the most relevant atomic pairs. The radial pair distribution function of Mg-O overlaps slightly with the Si-O one. A stronger overlap is present in the case of W-O. The Ca-O g(r) has a more rugged aspect, perhaps due to the fact that Ca is present in the melt as only 1 atom. Ca-O distribution function shows greater Ca-O distances than in the case of W-O. Surprisingly, the average W-O distance extracted from the radial pair distribution function is closer to that of Mg-O despite the charge difference. We also checked the degree of polymerization of our melt by computing the O-Si PDF and calculating the

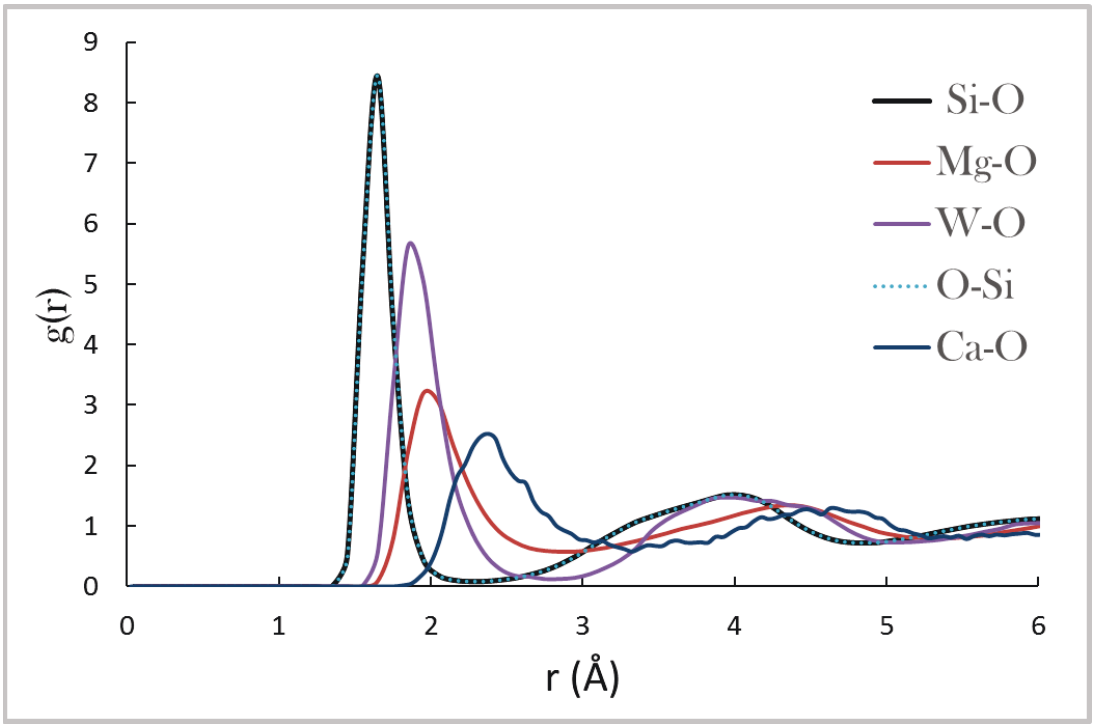

Figure 65 The radial pair distribution function for $Ca_1W_3Mg_{26}Si_{64}O_{161}$ melt. The cutoff radius used is 10 Å, but only the first 6 Å are represented for clarity. The W-O and Ca-O distribution functions are very different and indicate that the average distance between Ca and the O found in the first coordination sphere is greater than in the case of W.

coordination number of O by Si.

The Si-O coordination number is 4 and is in good agreement with the previous results presented in this work and reported data (de Koker et al. 2008; De Koker 2010; Bajgain et al. 2015) on silicate melts despite the temperature difference (Figure

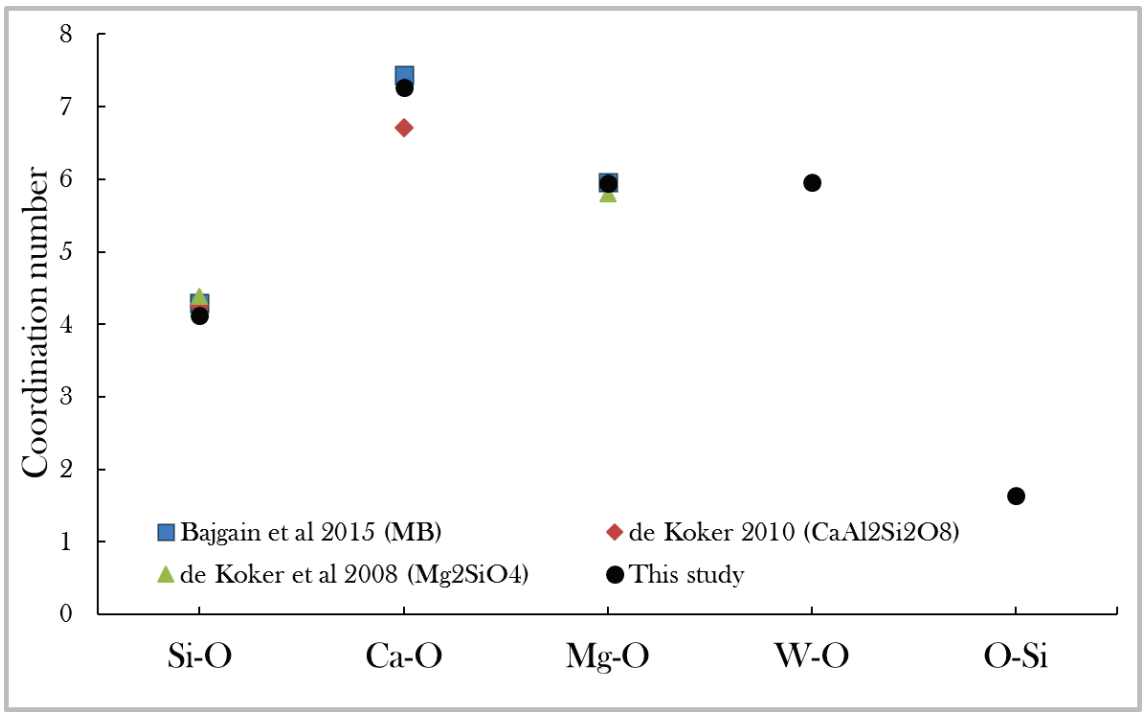

Figure 66 Coordination by O numbers for all the atomic species present in the $Ca_1W_3Mg_{26}Si_{64}O_{161}$ melt. For the atomic species for which there was coordination data Si, Ca, and Mg our results are in good agreement. A slight difference between the results presented here and de Koker 2010 is observed in the case of Ca-O. Both composition, MB and CaAl2Si2O8 contain Al, both our results and MB contain Mg, an element missing in the composition studied by de Koker 2010. It is doubtful that the presence of Mg increases the coordination of Ca. It might be an effect due to the smaller simulation cell used by de Koker, versus the one used here and by Bajgain et al.,2015.

66).

We find a Ca-O coordination number higher than that reported by De Koker,2010 but in good agreement with that of Bajgain et al.,2015 even though both of these studies were performed at higher temperatures, 3000K, but similar pressures. Mg-O coordination number is in good agreement with both De Koker, 2010 and Bajgain et al. 2015. This work is the first to investigate the coordination of W in silicate melts at high pressure and temperature. The coordination number of W by O, at 8 GPa, is 6. The coordination number of O by Si is approximately 1.5 and it shows that the melt is highly polymerized.

The Bader analysis shows that W and Ca have similar Bader volumes, and that their volumes fluctuate greatly with time (Figure 67).

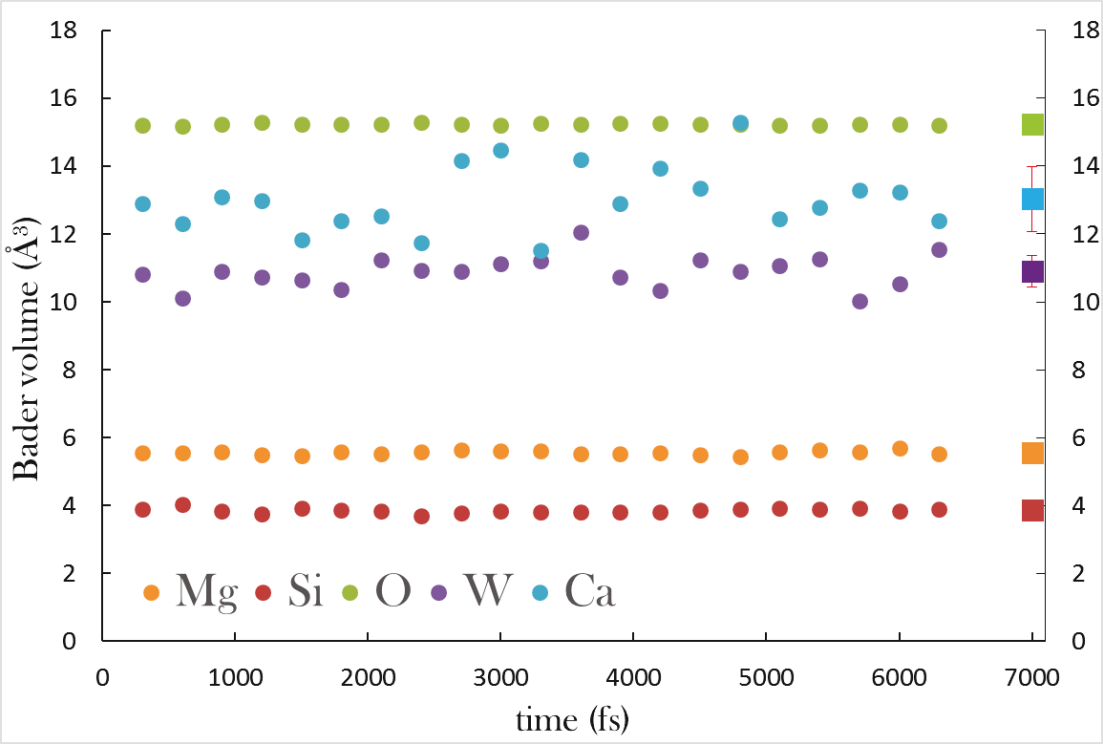

Figure 67 Bader volumes of all the atomic species present in the melt plotted as a function of time. Atomic coordinates at different time steps were extracted from the main simulation, and snapshot simulations were performed in order to write the charges.Ca has the largest Bader volume of the cations and it is very close to that of W. We interpret the fluctuations in Bader volumes of the two species as being the result of their surrounding environments. The squares close to the secondary Y axis mark the average volume values. The error bars represent standard deviations, for O, Si, and Mg they are smaller than the symbols.

We interpret this as the result of a highly variable local environment for both species, by comparison to the other atomic species present. Si and O have strong bonds and form the backbone of the silicate polymerized structure thus they are mostly found in rigid geometries that fluctuate little in time. Mg is a cation, larger than Si but smaller than the SiO tetrahedra and thus it can move freely through the melt structure. The ionic radii of the atoms could not be computed since the Bader volumes are not those of sphere.

Bader partial charges show a small deviation from conventional charges in the case of Mg and Ca, the average values being +1.7 and +1.6 respectively (Figure 68). O has an average Bader charge of -1.5. Si shows a larger deviation from the expected charge, being +3.1. The largest deviation is observed in the case of W, with a Bader charge of +2.5. The large deviation from the initial 4+ might be due to the fact that high pressure has a more pronounced effect on the charge of W, but a more in-

depth study must be done. FPMD simulations of silicate melts of the same composition presented here, containing WO or WO_3 instead of WO_2 can shed light on this matter. Bader charge variation of W and Ca is very small suggesting that the

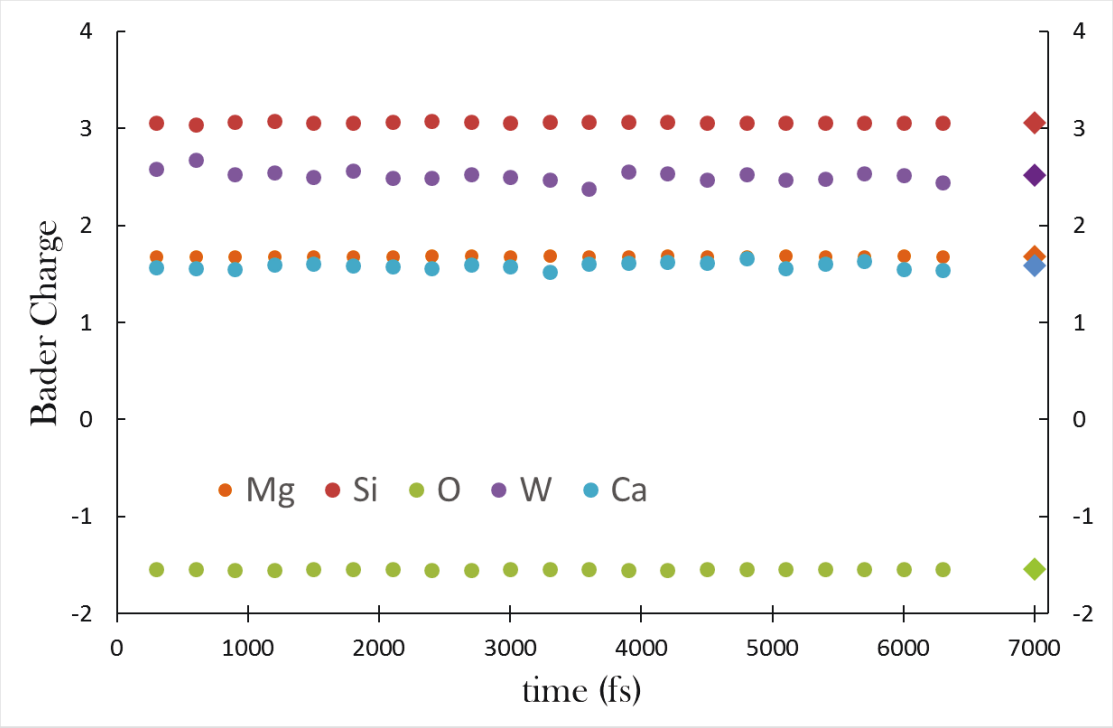

Figure 68 Bader charge variation with simulation time. Ca, Mg, and O show the smallest deviations from the standard, expected charges. Si has charge 0.9 smaller than expected. W has the biggest charge difference between the Bader charge and the expected. This might be an effect of pressure, but it is unclear at this time. The diamonds on the secondary Y axis represent the averaged Bader charges for each species. The error bars are smaller than the symbols.

Bader volume large variation of Ca and W are indeed due to geometry, the ionic volume responding to local environment.

The mean square displacement (MSD) of each atomic species was computed (Figure 69). W is the most mobile species present in the melt despite its large mass, and Ca follows closely. As expected, Si is the least mobile, because it is trapped in the highly polymerized network. The increased mobility of O with respect to Si, is due to the fact that O are exchanges between the Si-O tetrahedra, while Si moves at the same pace with the tetrahedra. Mg is much more mobile than Si and O but less mobile than Ca. The computed diffusivities are in the 10^{-9} order of magnitude (inset table in Figure 69). We approximate the errors to be in the range of half to one order of magnitude, based on the change of slope in the MSD.

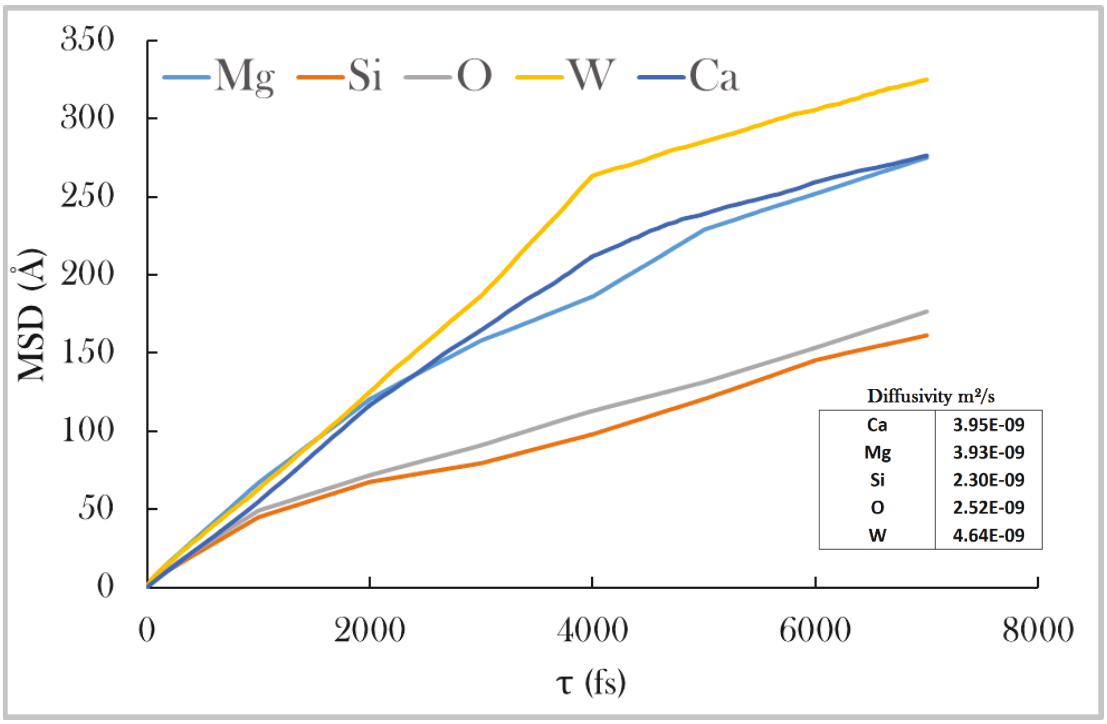

Figure 69 Mean Squared Displacement of all atomic species present in the melt. The MSD was computed on 14ps of simulation. W is by far the most mobile species, followed by Ca which at times have similar MSD. Si and O follow each other closely but Si is always slower. The increased mobility of O is due to its bonding to Mg and Ca & W in a lesser degree. The table shows the calculated self-diffusivities.

As shown by the Bader analysis, Ca has a large volume. If it is present in high amounts in highly polymerized silicate melts, it can distort the polymer structure creating more room for large cations to occupy, as it is the case of W. The Si-O bond is much stronger than the Ca-O bond (Luo,2007), thus it is unlikely that Ca, in small amounts, can turn bridging oxygens into non-bridging oxygens, depolymerizing the melt.

The mean square displacement indicates that W and Ca are the most mobile species in the silicate melt. The coordination number, MSD, and the Bader analysis, show similarities between the two atomic species in highly polymerized silicate melts.

5.5. Discussion

The NBO/T dependence of W, Co, and Ni partitioning between a silicate and metallic melt has been investigated experimentally.

We interpret the W affinity for depolymerized silicate melts as being the result of mainly space availability. The presence of Ca in silicate melts creates more open spaces in the polymer-network for W to get trapped into. Our interpretation completes the explanation of Siebert et al.,2011 since if charge were to be the only factor, no W should be found in highly polymerized silicate melts after silicate-metal equilibration.

Co and Ni have similar sizes to Fe and are much less affected by the NBO/T variations. The small charge of Co and Ni, 2+, compared to W (4+ or 6+), might also play a role in their indifference to the degree of polymerization of the silicate melt.

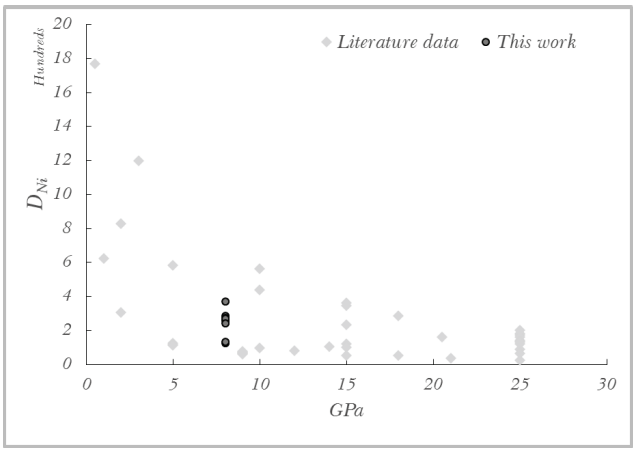

Figure 70 Ni metal-silicate melt partition coefficients obtained in this work compared to published values. Literature data is a compilation from (Siebert et al.,2011; Fischer et al.,2015; Li & Agee,1996; Siebert et al.,2012*).*

Both Co and Ni partitioning results are in good agreement with published literature data (Figure 70 & Figure 71). Even though it is debatable if NBO/T maintains its validity at high pressures as an approximation of the degree of polymerization (see Chapter 3), the partitioning of Co and Ni is not influenced by the value of NBO/T.

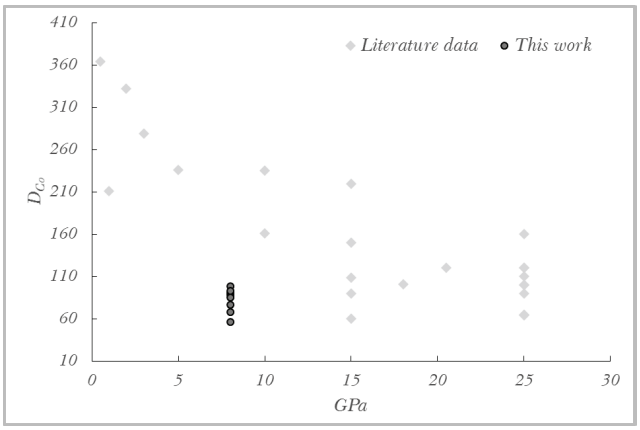

*Figure 71 Co metal-silicate melt partition coefficients obtained in this work compared to published values. Literature data is a compilation from (*Siebert et al.,2011; Fischer et al.,2015*).*

The structural differences between highly polymerized silicate melt and less polymerized ones are responsible for the anomalous behaviour of W. Tungsten has no room in highly polymerized melts. Ca facilitates the incorporation of W in highly polymerized melts by distorting the polymer structure.

6. The chemical and mineralogical composition of the Ultra-Low Velocity zones

In 1995 observations on the large differential travel times of SPdKS-SKS and S2KS-SKS[5] phases with regards to PREM, lead Garnero & Helmberger,1995 to propose the existence of a small low-velocity layer at the top of CMB. Due to the difficulty in resolving the signals, the exact wave velocity reduction and the size of this layer could not be determined at that time.

One year later, Williams & Garnero,1996 published a new study and provided a more constrained model for these seismic anomalies. In their paper, Williams and Garnero, argue that the layer has a sharp boundary, and a thickness of no more than 40 Km. They offer a constraint on the Vp[6] reduction of 10% lower than PREM. They argue, among chemical discontinuity and new undiscovered phase transition, that the presence of melt can be responsible for the high reduction in Vp.

Thorne & Garnero,2004 use broadband SKS and SPdKS waveforms to investigate globally the possible existence of ULVZs. An important part of the total number of waveforms analysed in their study were classified as 'Probable Ultra-Low Velocity Zones' meaning that the existence of a <5 Km ULVZ layer covering the entire CMB is probable. If ULVZs cover the entire lower part of the D", and their low wave velocities are due to the existence of partial melt, then partial might exist on top of the CMB as in the case of the Moon (see Chapter 1).

The multitude of waveforms used to study the ULVZs has generated ranges of Vs[7], Vp and density values. Some of the differences in Vp and Vs values might arise from the errors carried by different methods, but more likely they reflect the diversity of the ULVZs.

[5] SKS are waves that go through the core, starting as S waves in the mantle, turning into P waves in the outer core, and back to S waves as they exit the outer core. S2KS, are reflected once inside the core by the CMB. SPdKS waves start as S waves in the mantle, travel as diffracted P waves at the entrance into the core for a time, then become P waves traveling through the outer-core, and become S waves after exiting it.

[6] Vp, is the velocity of the P-waves (P stands for primary). P-waves are compressional waveforms.
[7] Vs is the velocity of the S-waves, (S stands for secondary or shear). S-waves are shear waves.

Since their discovery, a series of models and explanations were proposed for the mineralogical composition of the ULVZs.

Wicks et al.,2010 proposed a solid ULVZ that relies on Fe enrichment of magnesiowüstite. In Wicks's model $(Mg_{0.16}, Fe_{0.84})O$ is mixed with PREM in order to fit the observed Vp, Vs, and density of the ULVZ. They predict a 12% amount of magnesiowüstite present in the ULVZ.

Williams & Garnero,1996 proposed liquid iron percolation from the core as a possible explanation for ULVZs.

Rost et al.,2005 reported a ULVZ of 8.5 km thick and 50 km wide, east of Australia. Through the use of ScP[8] waves they reported a Vp decrease of 8 (± 2.5) % and a Vs of 25 (± 4) % from PREM. They argue that partial melting is responsible for this ULVZ. Their arguments stand on the substantial decrease in shear wave velocity. In terms of density, they report a 10% increase with a margin of error of 5%. In their discussion about the structure of the ULVZ they propose a model that allows for the coexistence of solids and melt, underlying other lower-mantle seismic anomalies (such as Large Low-Shear Velocity Provinces, or mantle plumes). They propose a scenario where dense melt percolates from the overlying mantle downwards into the ULVZ due to its high density. In this scenario a melt crystal cumulate forms on top of the CMB, becoming the ULVZ. The melt volume of such a cumulate is 25%. This is an interesting scenario with major implication in the dynamics and evolution of the mantle.

No matter the models proposed for the origin of the ULVZs, they all have one thing in common Fe-enrichment.

Most of the previous work has been limited due to the lack of density data for Fe-bearing silicate melts. In the study of silicate melts EOS, a series of end-member compositions were previously reported (Thomas et al.,2012; de Koker et al.,2008; Wan et al.,2007). Here we present new data on the EOS of (Mg,Fe)SiO_3 for the entire Earth's mantle pressure regime.

[8] ScP are a type of seismic waves that start traveling through the mantle as S-waves and they reflect as P-waves upon reaching the core.

6.1. Construction of the model

We consider mixtures of perovskite, magnesiowüstite, and Fe-bearing silicate melt that fit the seismic observations for the ULVZs. If data for Fe-bearing perovskite, post-perovskite, and magnesiowüstite are available in the literature, data for the melt are missing. Consequently we use the equations of state of Fe-bearing $MgSiO_3$ and Mg_2SiO_4 melts as a function of iron content, pressure and temperature

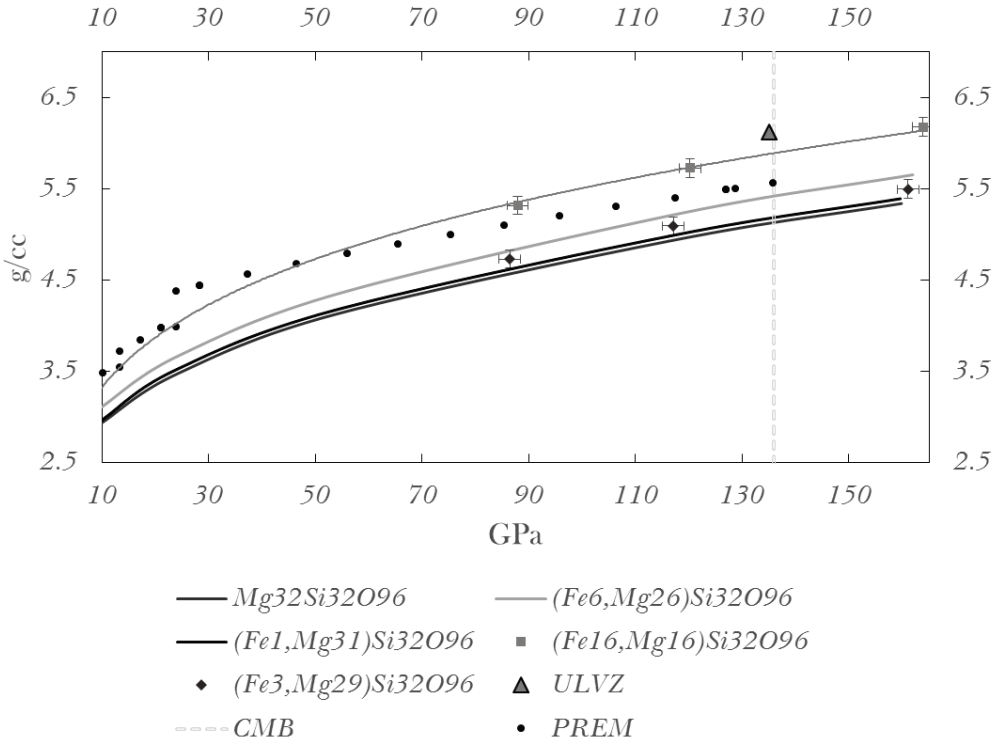

Figure 72 The density variation with pressure for different simulated melts. The triangle shows the density of the ULVZ. For two compositions, marked by diamonds and squares, only 3 points were computed due to the very-expensive nature of FPMD simulation. The black dots represent PREM.

(Figure 72 and Annex 2).

Even though the temperature conditions for our model seem low (3000K), in the Introduction of this thesis we argued that iron rich melted material in the D" does intersect the mantle adiabat.

The purpose of this work is to find the chemical and mineralogical composition of the ULVZs. We want a model that can predict the solid phases present, the amount of melt (if any), and the Fe-content of each phase.

Both Hashin-Shtrikman and Voigt-Reuss are averages of compressional moduli of mixtures as a function of phase proportions. The former is currently available for assemblages of not more than two phases. The second is biased towards the phases with extreme values of moduli, be they very small or very large. In our simulations we found that the bulk modulus of the melts changes weakly with the Fe amounts and stays within the error bars of our EOS (Annex 2). As such, either of the two formulations will be insensitive to the Fe content in the melt. Consequently we opt for an alternative simplified model expressed in terms of velocities and densities rather than moduli.

We consider a mechanical mixture of silicate, magnesiowüstite and melt and we try to fit simultaneously all the seismic observations of the ULVZs: rho, Vs, Vp:

$$\rho_{ULVZ} = x_{melt}\rho_{melt(n^{Fe})} + x_{PV}\rho_{PV(n^{Fe})} + x_{MgW}\rho_{MgW(n^{Fe})} \quad (32)$$

$$Vp_{ULVZ} = x_{melt}Vp_{melt(n^{Fe})} + x_{PV}Vp_{PV(n^{Fe})} + x_{MgW}Vp_{MgW(n^{Fe})} \quad (33)$$

$$Vs_{ULVZ} = x_{melt}Vs_{melt(n^{Fe})} + x_{PV}Vs_{PV(n^{Fe})} + x_{MgW}Vs_{MgW(n^{Fe})} \quad (34)$$

where x is the amount of each phase present, ρ is the density, Vp is the compressional wave velocity, and Vs is the average shear wave velocity. nFe is the iron content which is allowed to vary in each phase present.

To reduce the number of variables and make the problem solvable, we fixed the values of Vp at 10% slower than PREM, and computed results for Vs ranging from 20 to 30% slower than PREM.

The values for the two solid mineral phases come from a compilation of the literature (Caracas & Cohen,2007; Crowhurst et al.,2008; Marton et al.,2000; R. Oganov et al.,2001) (see Annex 1). The density and the bulk modulus, K, of the melt come from EOS fits to our FPMD calculations. In total we end up having six unknowns for the three equations: the amount of melt, of magnesiowüstite, and of bridgmanite, and the amount of iron in magnesiowüstite, in bridgmanite, and in the melt. Based on the equation of states of the enstatite melts (Annex 2) we solve this system of equations considering various amounts of melts in the ULVZs. Figure 73 illustrates that our approach works and generates results. The shortcomings are that

within the ranges of possible melt compositions and amounts[9] we find a multitude of solutions that need to be further constrained.

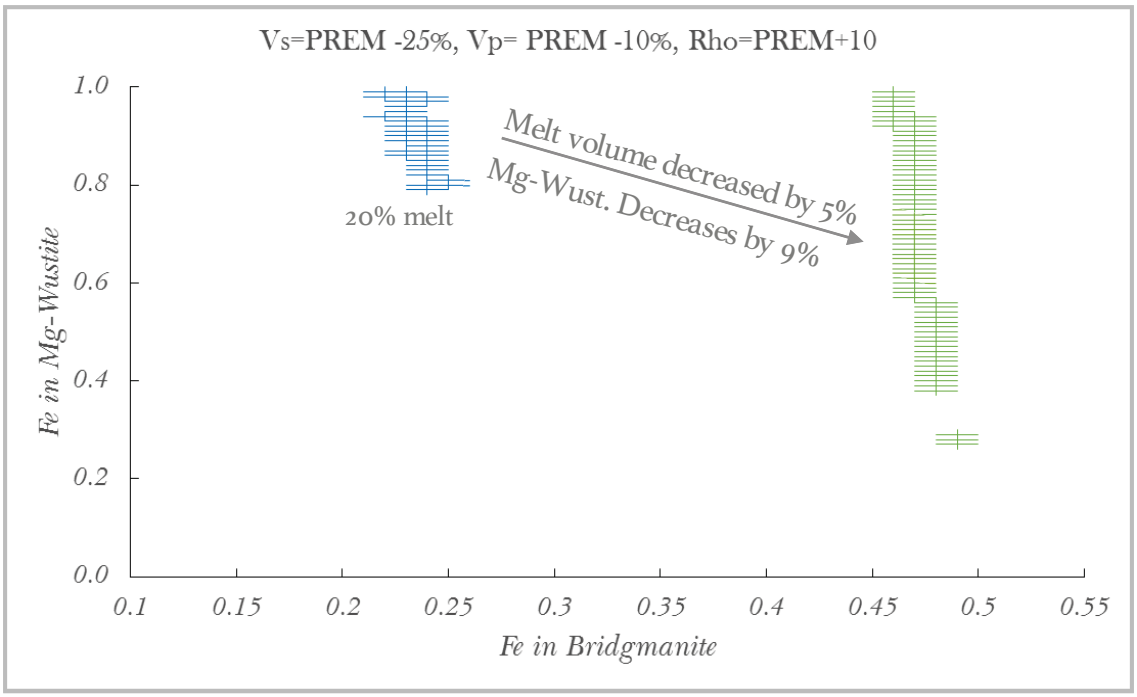

Figure 73 Model results for two melt amounts of the same composition ($Mg_{0.5}Fe_{0.5}$)SiO_3. We chose to show this example out of the multitude of results to illustrate that our model finds results for a melt-bearing ULVZ. The results are shown in the chemical space of the two solids present in this mixture. Blue area denotes the results and the extent of the error bars for 20% melt present in the mixture. The green area represents the totality of solutions for a mixture containing 15% melt. The average magnesiowüstite content of the mixture containing 20% melt (blue) is 12%, and it decreases to 3% as the melt volume is decreased to 15%.

In the case presented in Figure 73, the melt in both scenarios has the same composition, ($Mg_{.5}$,$Fe_{.5}$)SiO_3, only the amount of melt in the mixture was varied. An increase in melt amount leads to a decrease in the Fe-content of bridgmanite and a reduction of Fe-content possibilities for magnesiowüstite, restricting it to high-Fe values.

[9] ***The model generate zero solutions for melt amounts lower than 15%.***

Also, such an increase in melt quantity leads to an increase in the average magnesiowüstite amount present, from 3% to 12%. Increasing the Fe content of the

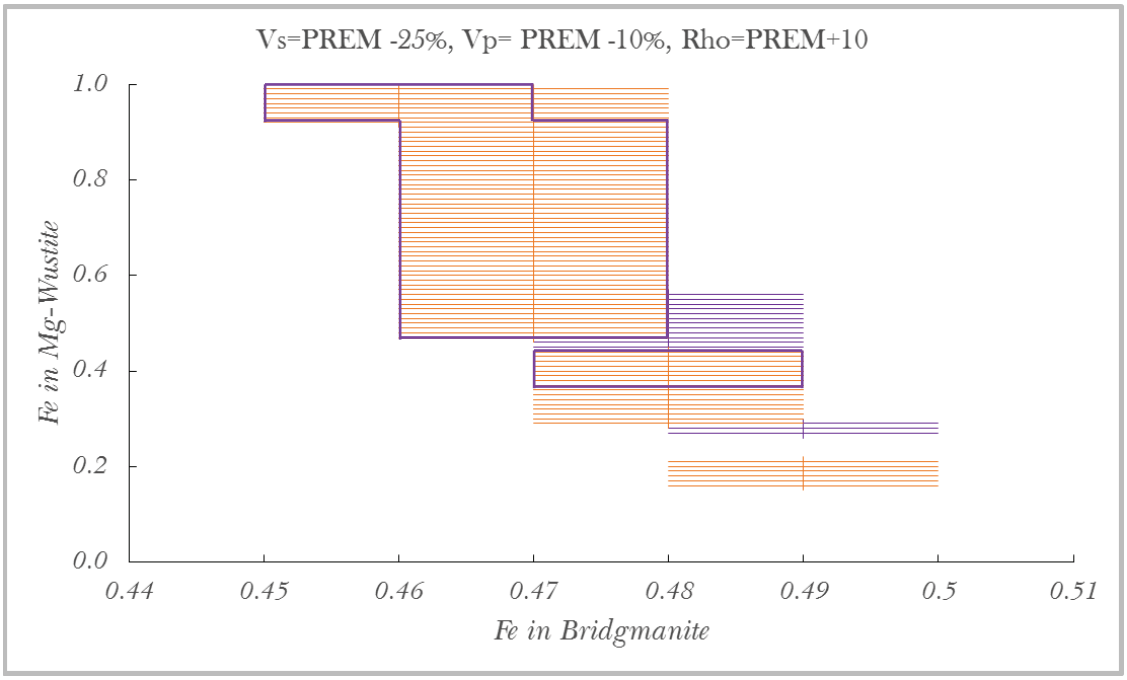

Figure 74 The variations imposed on the compositional space of the solids by a 6% Fe increase in the melt. The Fe difference between the two melts chosen here was arbitrary. The red area represents the chemical compositions of the solids found in a mixture with a melt containing 0.56Fe, while the purple area is for a mixture with a melt containing 0.5Fe. The purple lines show the overlap between the two spaces. The amount of melt present in both mixtures is 15%.

melt, leads to a decrease in the Fe-content of magnesiowüstite and a slight increase in the Fe-content of bridgmanite (Figure 74). The Fe content of the solids changes because of the density redistribution between solids and melt.

A denser melt imposes less dense solids, so the overall density is maintained at ULVZ values.

Any mixture of post-perovskite, magnesiowüstite, and melt was not able to fit the seismic observations. Mixtures of post-perovskite and magnesiowüstite without melt, were also unable to produce results that fit the seismic observations. The elastic constants of post-perovskite at high temperature have not been well constrained. The Fe-dependence of elastic constants at high temperature, is also poorly constrained. We do not exclude the possibility that the above stated reasons are the cause of the inability of our model to generate results, in mixtures with post-perovskite.

6.2. Model results considering equilibrium between the melt and bridgmanite

We have constrained further our model by considering a local equilibrium between the solids and the melt. Such an equilibrium can be quantified by the Fe-Mg exchange coefficient between bridgmanite and melt. There is disagreement in the literature on what is the value of Fe partition coefficient between bridgmanite and melt at lower mantle conditions. Some authors report Fe partition coefficients between Al-bearing bridgmanite of up to 0.6 at 35GPa an decreasing down to 0.47 at 110 GPa (Andrault et al.,2012). Such values of the partitioning coefficients might be due to the presence of Al, which helps retain Fe in the solid (Andrault et al.,2012). Another study, dealing with Al-free compositions finds a much lower Fe partitioning coefficient value, 0.10 (Nomura et al.,2011). The melts studied in this thesis are all Al-free, for this reason we have chosen for the ULVZ model Al-free bridgmanite. Thus we apply to our results the partitioning coefficient of Nomura et al.,2011. Our extrapolation to the ULVZ conditions is in good agreement with that of Boukare et al.,2015.

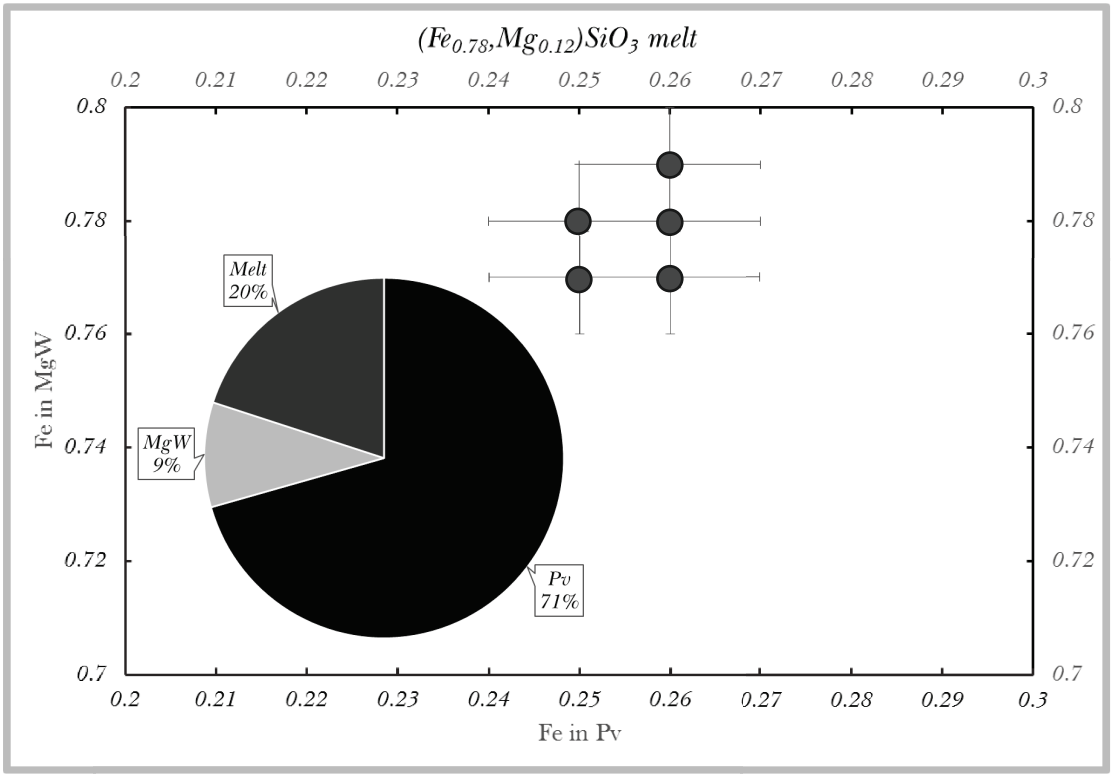

Figure 75 74 Chemical composition and phase proportions of our model results for an ULVZ 10% denser than PREM. The title specifies the melt composition. The amount of each phase present in the mixture is shown in the pie-chart, and it doesn't vary from one solution point to another.

For a density increase of 10% from PREM, our model generates a narrow range of solutions, each very similar in terms of the solid chemical composition, and identical in the melt composition and phase proportions (Figure 75).

No other solutions are possible within the limits of our model. Also, our final model generates a ULVZ with a Vs decrease of 25% from PREM which is in-between the expected value range of 20-30%. The amount of magnesiowüstite is similar to that of the expected lower mantle and close to that predicted by previous models (Wicks et al.,2010). All phases present in the ULVZ are strongly enriched in iron, with an iron content of bridgmanite almost three times that of the expected value for the lower mantle. A high Fe content of the ULVZ was one of the first proposed explanations for their high densities and low velocities (Williams & Garnero,1996), and a trait that all previous models share.

We also performed this exercise again, but considering a 5% density increase of ULVZs with respect to PREM (Figure 76). For this new ULVZ density, we find an even narrower compositional range for a mixture of bridgemanite, magnesiowüstite and melt, at Vp=PREM-10%, Vs=PREM-25, and the same melt composition as the previously discussed results.

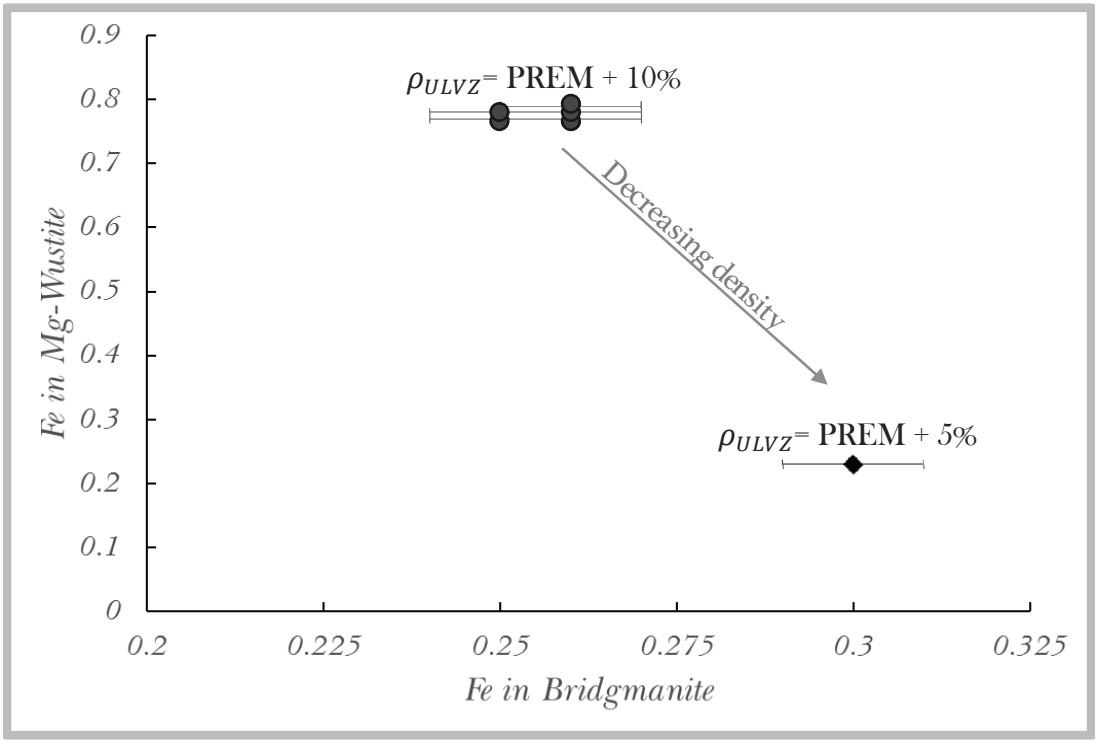

Figure 76 Fe content compositional space of magnesiowüstite and bridgmanite showing the solid compositions for the two densities of the ULVZ mixture. Melt composition is the same as in the previous figure. The vertical error bars are smaller than the symbols.

The increase in the iron content of bridgmanite of the less dense ULVZ (PREM-5%) compared to the denser ULVZ is a natural result of decreasing the mixture target density and maintaining the chemical equilibrium imposed by the partitioning coefficients. The density of magnesiowüstite increases much more rapidly with Fe-content (Figure 77) than bridgmanite. A less dense ULVZ will require a smaller amount of magnesiowüstite containing less Fe.

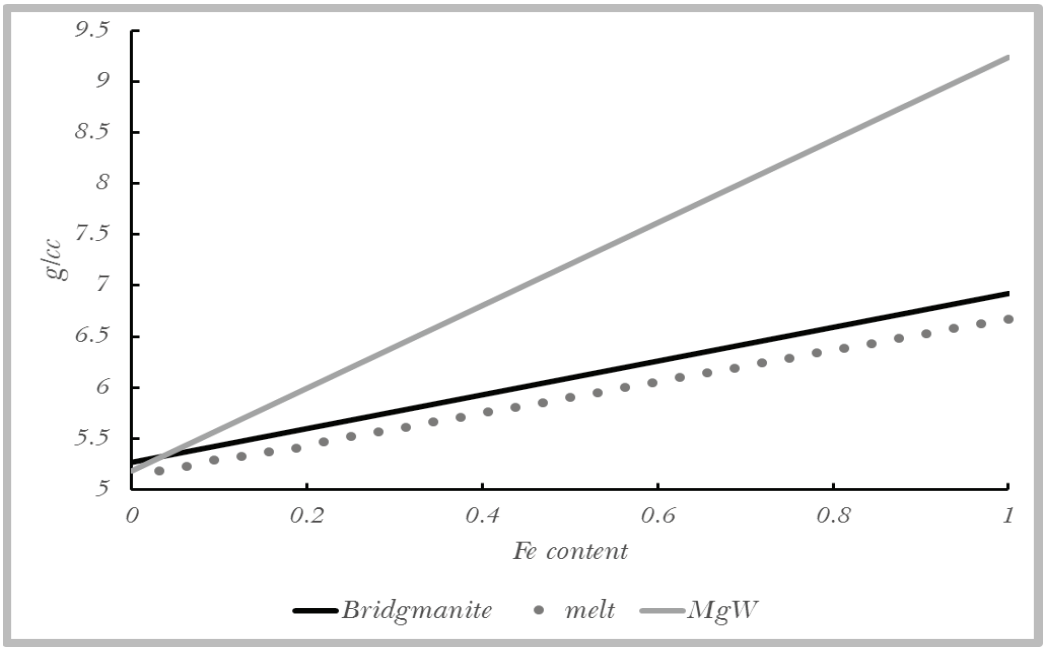

Figure 77 Density as a function of Fe content for the three phases present in our mixture. Magnesiowüstite has a steeper increase in density than the other phases involved. The data for the solids were taken from (Caracas & Cohen, 2007; Crowhurst, Brown, Goncharov, & Jacobsen, 2008; Marton, Ita, & Cohen, 2000; Oganov, Brodholt, & Price, 2001). For more details see Annex 1.

The amount of phases present in the less dense ULVZ is: 6% magnesiowüstite, 74% bridgmanite and 20% $(Fe_{0.78}, Mg_{0.12})SiO_3$ melt.

Because in both ULVZ density cases the melt composition is the same, the variation of solid-phases compositions can be established, imagining a transition between a less dense ULVZ to a denser one. All the compositions on this line satisfy the bridgmanite-melt chemical equilibrium condition imposed by the partitioning coefficient of Fe (Nomura et al.,2011).

6.3. Discussion

Our model results for a ULVZ 10% denser than PREM yields results similar to the model envisioned by Rost et al.,2005. In their model the melt found in the ULVZ is 'near 25%'. Our model fits an ULVZ with a Vp decrease from PREM slightly higher than that reported by Rost et al., 2005 (8%) and predicts 20% melt present in the ULVZ. Also in their model, they assume that an Fe-rich melt would be negatively buoyant and can percolate downwards and pool on the top of the CMB to form the ULVZ. In our mixture, the melt is negatively buoyant (Figure 78).

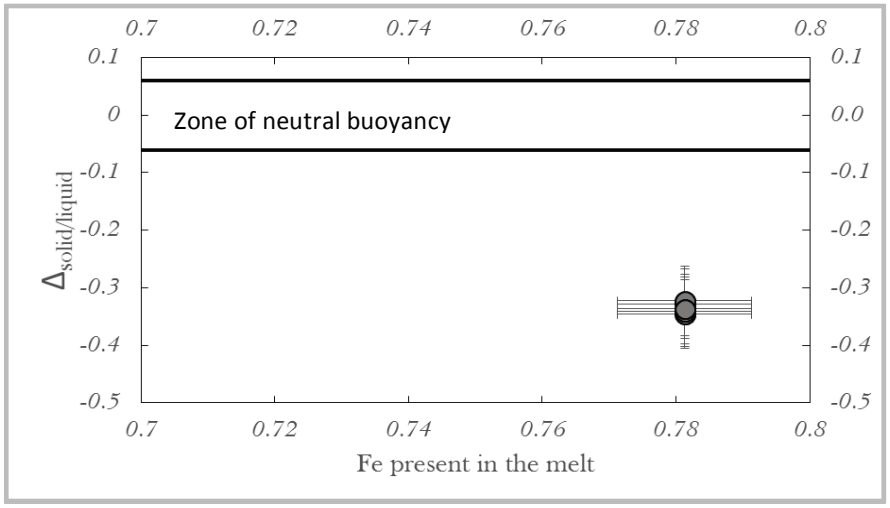

Figure 78 Buoyancy assessment of the mixtures for a ULVZ 10% denser than PREM. Symbols correspond to the solutions presented in Figure 74. Values below the black lines represent mixtures in which the melt is negatively buoyant. The zone of neutral buoyancy represents a density difference between the solids and the melt of 1%, which is the

The amounts of solid phases present in our ULVZ mixtures are close to lower mantle mineral abundancies, and in good agreement with previous models (Wicks et al.,2010). The high Fe-content of

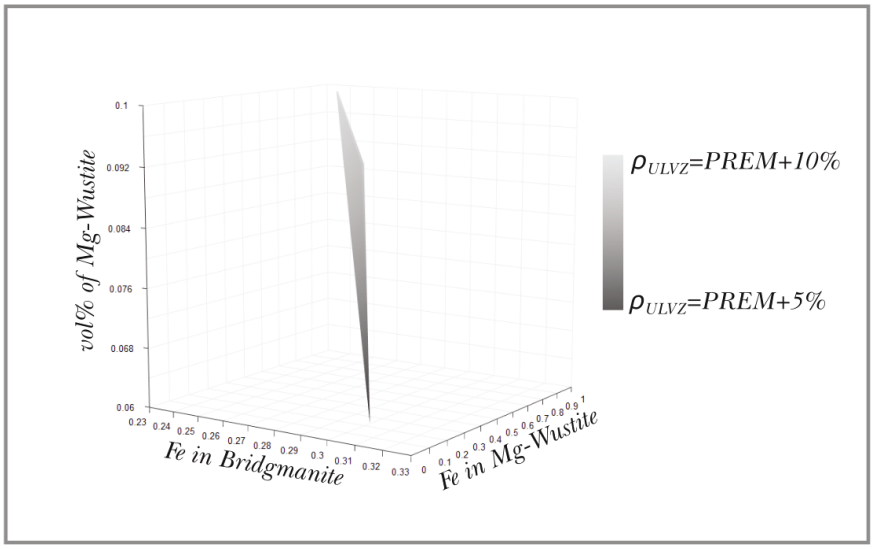

Figure 79 Compositional space for 10% and 5% denser than PREM ULVZs. The amount of magnesiowüstite present in the mixture is given on the Z axis, 1 representing the total sum of the phases present. The melt composition is constant along the surface $(Fe_{0.78}, Mg_{0.22})SiO_3$, and the melt amount is also constant at 20% (or 0.2 as in the figure notation).

the solids is an expected outcome of the density constraints and equilibrium with the melt. Unlike previous models, our model predicts the full mineralogical and chemical composition of the ULVZ, describing the amounts and composition of all three phases considered.

Figure 79 shows the compositional space of our model results for two possible ULVZs densities. We note that on the compositional surface of bridgmanite and magnesiowüstite that fits the two ULVZ densities considered in the presence of melt, the mixtures are all in chemical equilibrium as expressed by the equilibrium constant $K_{Fe}^{Pv-melt}$.

In both ULVZ density cases, an Fe-enrichment of the solids is necessary. The results of our model are in good agreement with the scenario and the seismic observations of Rost et al.,2005.

In Annex 3 we show that melts with 1:1 Mg:Fe ratio are denser than PREM. If PREM can be used as a proxy for early Earth solids, then Fe-rich silicate melts would be negatively buoyant in the young mantle. A younger mantle means a hotter mantle and thus a less dense one, due to thermal expansion. We approximate the thermal

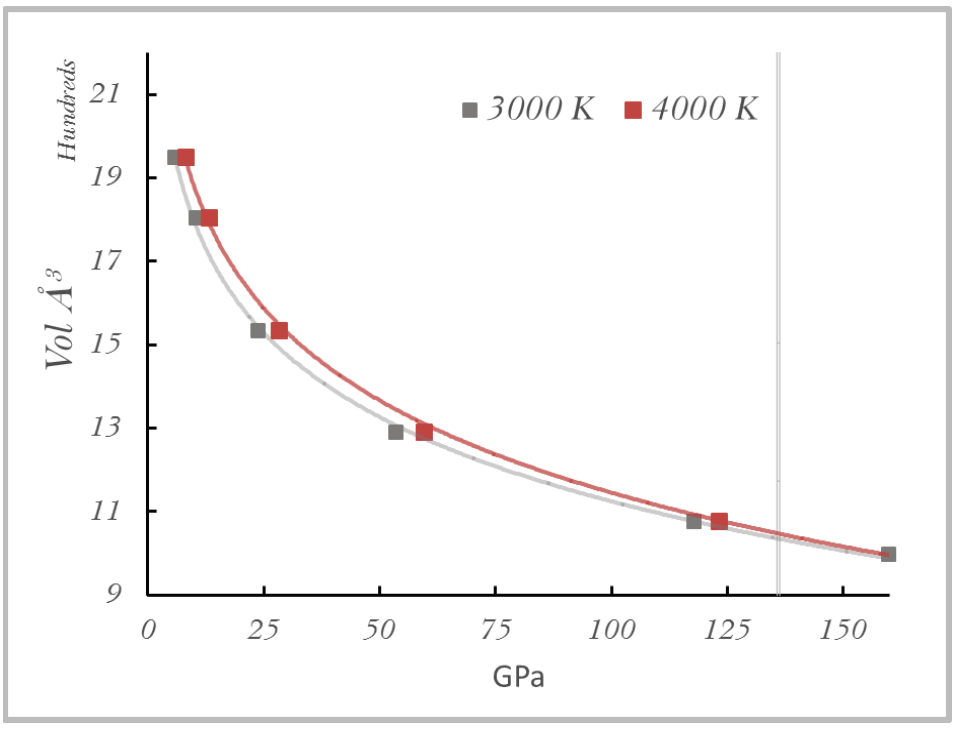

Figure 80 Equation of state of $(Fe_{0.031}, Mg_{0.969})SiO_3$ melt for two isotherms. The squares show the volumes at which FPMD runs were computed. The lines represent the EoS fit. The inset is a zoom in on the D" pressure regime. Very small volumetric differences are observed for a 1000K increase in temperature.

expansion of our enstatite melts to be 10 Å^3 per 1000K (Figure 80 and Annex 2). This thermal expansion will have a -1%/1000K effect on density at D" conditions. From this we assess that a higher temperature will not affect our model results since a density margin error of 1% was included in our model.

Depending on the position and onset of crystallization a scenario involving a basal magma ocean as the one proposed by Labrosse et al.,2007 becomes possible

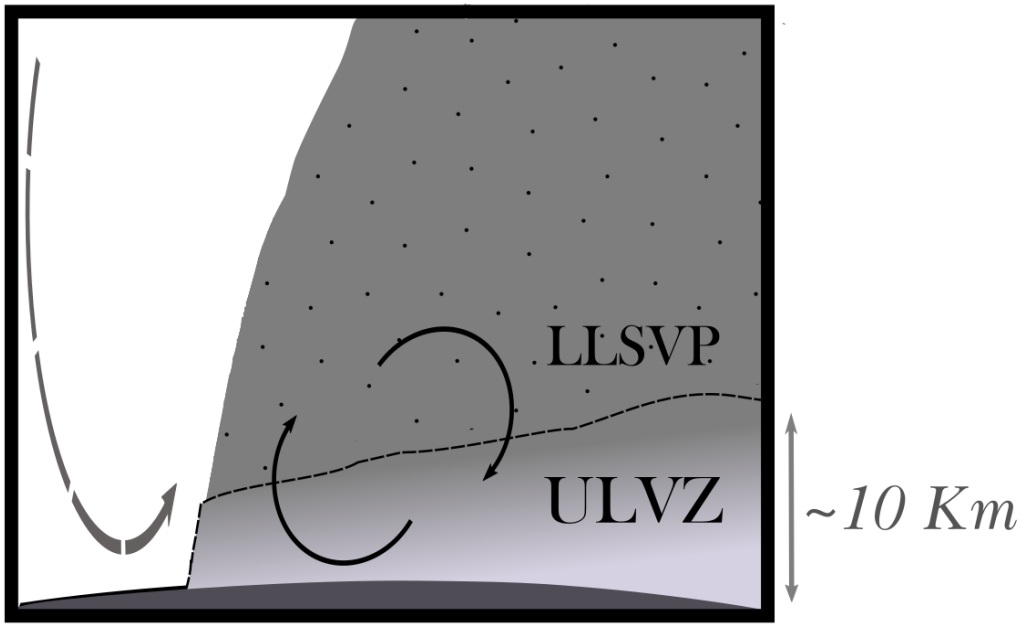

Figure 81 Cartoon depicting the internal steering induced by mantle convection inside the ULVZ. The upwelled parts of the ULVZ freeze and due to density difference descend back into the lowermost part of the D" to be remolten.

(Figure 81). If such a dense liquid as the melt predicted by our model, can be lifted by internal steering induced by mantle convection forces (Figure 81), then it will freeze in the mantle above the ULVZ. The partial crystallization of the melt (with only 10% crystalline fraction formed) would lead to the formation of bridgmanite crystals with similar Vp, Vs, and density as the LLSVP[10]. The problem with this scenario is that it leads inevitably to the extinction of the ULVZ by melt draining. The crystallized bridgmanite would be denser than the surrounding mantle but it would be less dense than the ULVZ, remaining always on top of it. On geological time scale this would mean that ULVZs have a very short lifespan.

[10] Large-Low Shear Velocity Provinces. They represent large scale structures of the lower mantle, extending as much as 1000 Km vertically from the CMB and thousands ok Km wide.

The freezing of the entire melt fraction would result in a solid that is much denser than the surrounding mantle or the overlying LLSVP, and a reworking scenario becomes possible (Figure 81). Such a dense material would sink into the lowermost parts of the D". Because of its high Fe-content it can intersect the mantle adiabat and start melting. This reworking scenario fits both ULVZ densities.

To conclude, we propose a ULVZ formed by the mixture of bridgmanite, magnesiowüstite, and silicate melt. All the phases present are Fe-enriched with regards to the expected Fe-content of the lower mantle. The presence of melt in the lowermost mantle, has, alongside geodynamical implication, also geochemical ones. Such a melt would be not only Fe-rich but also full of incompatible elements, heavy and light, making it an important reservoir for the mantle chemical evolution.

Annex 1: Literature data used in the construction of the ULVZ model

Table 12 List of references of the data compilation used in the ULVZ model.

Reference	**Phase**	**P (GPa)**	**T (K)**	**K (GPa)**	**G (GPa)**	**Rho g/cc**
Crowhurst et al.,2008	(Mg,Fe)O	58.4	300	370	223	4.7
Scanavino et al.,2013	(Mg,Fe)O	134.8	2449	595-660*	-	-
Caracas & Cohen,2005	MgSiO3	120	0	674	343	5.483
Caracas & Cohen,2005	FeSiO3	120	0	715	268	6.789
Marton et al.,2000	MgSiO3	140	3000	-	-	5.28
a R. Oganov et al.,2001	MgSiO3	38-88.1	1500-3500	525.55	226.9	-

We have estimated the temperature, pressure, and Fe-content dependence of K, G, and Rho. We calculated the K, G, and density for bridgmanite and magnesiowüstite at 3000K and D" pressures (130GPa) for their entire Fe compositional range.

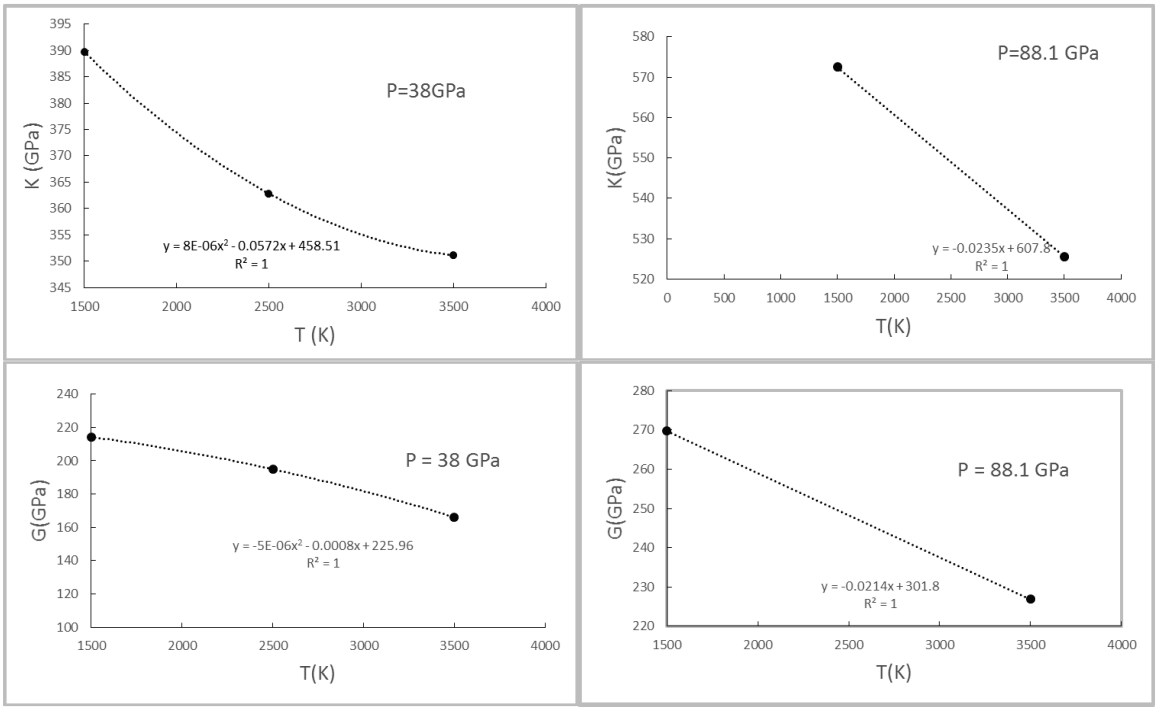

Figure 82 The temperature dependence of bridgmanite was extrapolated from Oganov et al., 2001 based on fits on the reported data at two pressures, shown on the figure.

Bridgmanite compressional moduli dependence on temperature was interpolated at 3000K as shown in Figures 82 for 38 and 88.1 GPa respectively, based on data from Oganov et al., 2001. For thermal expansion, V, was computed the same way. The results obtained from A. R. Oganov et al.,2001 were compared with the results of Caracas & Cohen,2005 adjusted for temperature, and were found

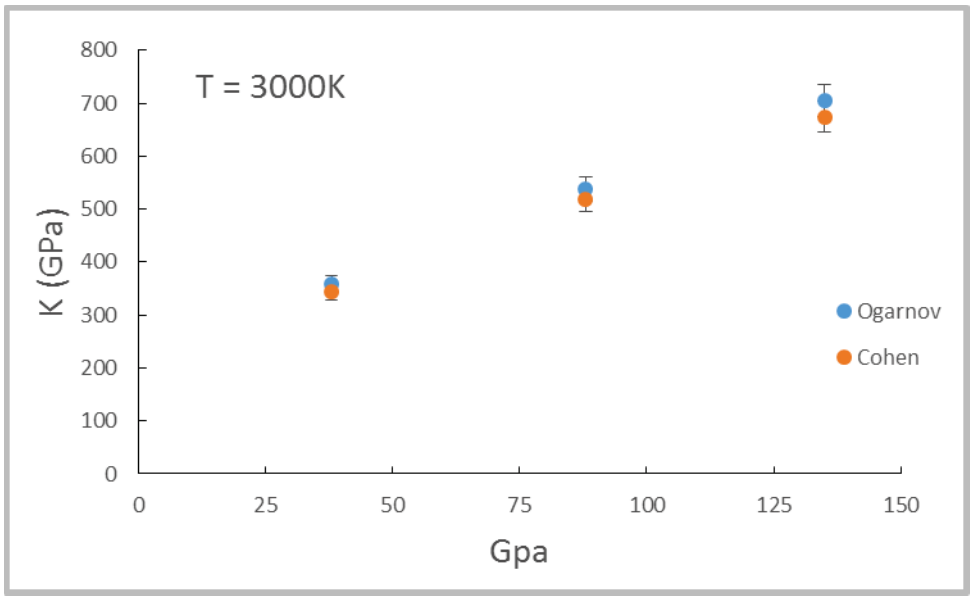

Figure 83 Comparison between bulk moduli at different pressures based on data from Oganov et al., 2001 and Caracas and Cohen, 2005. We used the δT obtained from Oganov et al., 2001 to calculate the values at 3000K.

to be in good agreement (Figure 83).

Based on the data from both authors we computed the pressure effect on K and G.

Caracas & Cohen,2005 study the effect of chemistry, i.e. the effect of Fe on the elastic properties of bridgmanite and from their data reported on $FeSiO_3$ we interpolated the compositional effects.

For magnesiowüstite the same reasoning was applied. Compositional effects were assessed from Scanavino et al.,2013 and δK, δG, and δρ were calculated from Crowhurst et al.,2008 at pressures higher than the spin-crossover. Temperature dependence was assessed based on both sets of data.

Annex 2: Equations of state

The P-V data from first principles molecular dynamics has been fitted to Vinet Equations of State (Table 13).

Table 13 EOS for Fe-free and Fe-bearing silicate melts studied in this thesis.

Melt Chemistry	V_0 Å^3	σV	K_0 GPa	σK_0	K'_0	σK'_0	T K	X^2
$Fe_1Mg_{31}Si_{32}O_{96}$	2313.27	44.31	15.76	0.30	6.63	1.915	3000	3.15
$Fe_6Mg_{26}Si_{32}O_{96}$	2464.4	24.54	11.24	0.09	6.92	0.105	3000	1.78
$Fe_1Mg_{31}Si_{16}O_{64}$	1660.62	31.98	15.67	1.18	6.52	0.03	3000	1.73
$Fe_6Mg_{26}Si_{16}O_{64}$	1673.07	5.15	15.26	0.65	6.55	0.12	3000	0.77
Mg_2SiO_4	1632.1	4.29	16.59	1.14	6.6	0.20	3000	1.50
$Fe_1Mg_{31}Si_{32}O_{96}$	2459.8	8.54	14.04	1.12	6.44	0.22	4000	2.91
$MgSiO_3$	2357.12	37.27	14.78	0.92	6.61	0.03	3000	1.03

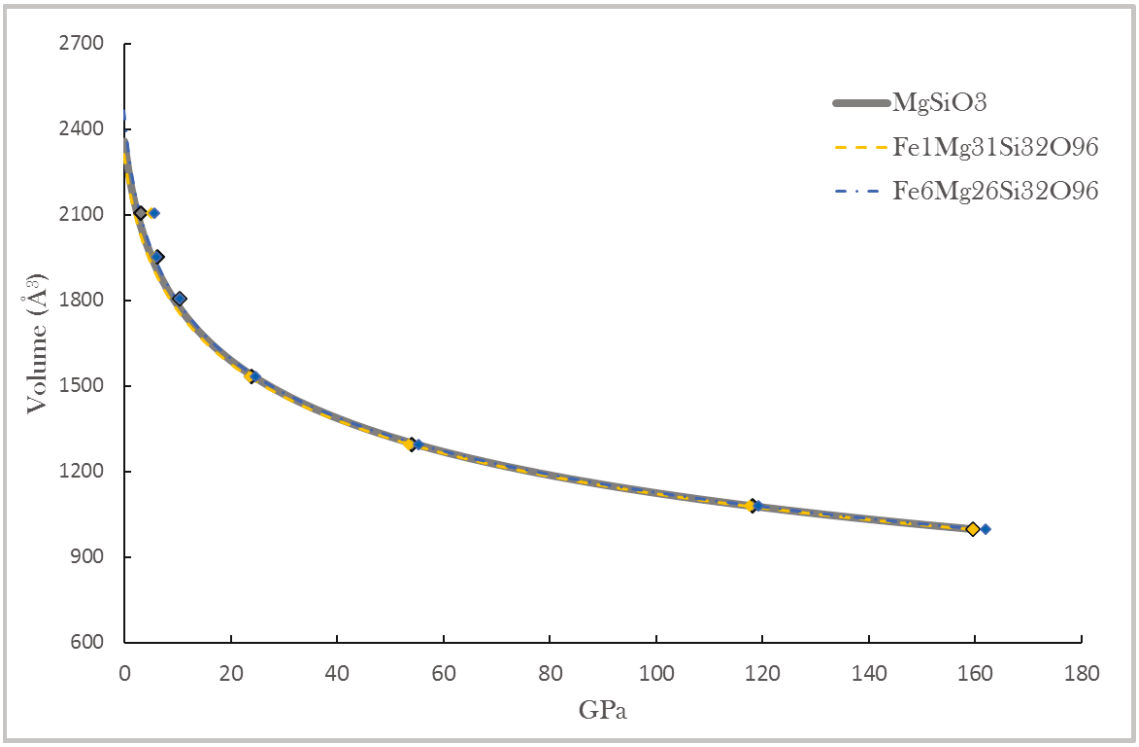

Figure 84 Equation of state of enstatite melts. No discernible effect of Fe is observed as in the case of olivine melts. The lines represent the volume fit to a Vinet form, and the symbols represent the FPMD data. Each colour identifies a composition. At high pressures all 3 compositions have identical volumes.

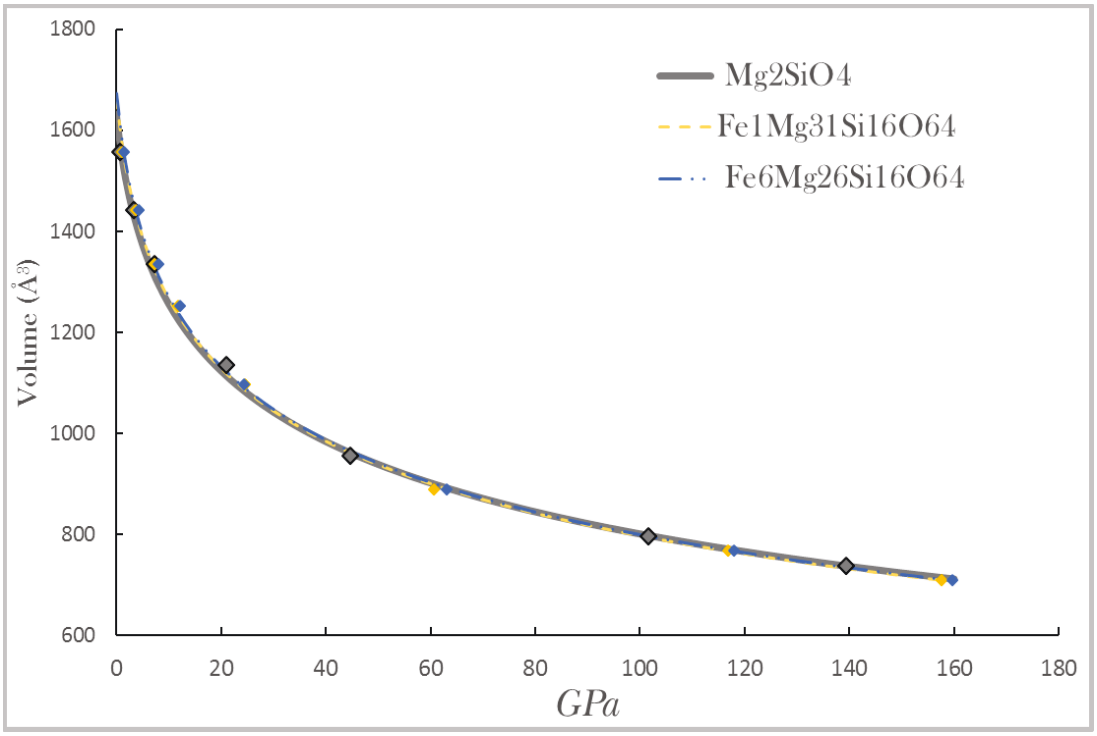

Figure 85 The equation of state of olivine melts. The lines represent the volume fit to a Vinet equation of state, and the symbols represent the FPMD data. Each colour identifies a composition. The addition of Fe has little influence on the volume shift and it is within the equation of state fit error bars. At high pressures all 3 compositions have identical volumes.

Annex 3: The density of Fe bearing silicate melts in the Earth's mantle

Based on the Equations of State presented in the Annex 2 and using the PV data points at high pressure the density variation with Fe content in $(Fe,Mg)SiO_3$ and $(Fe,Mg)_2SiO_4$ melts was calculated. The errors were approximated based on the EoS errors and the pressure errors of the FPMD (see Annex 5). Figure 86 shows the densities for all enstatitic compositions studied, compared to PREM and literature

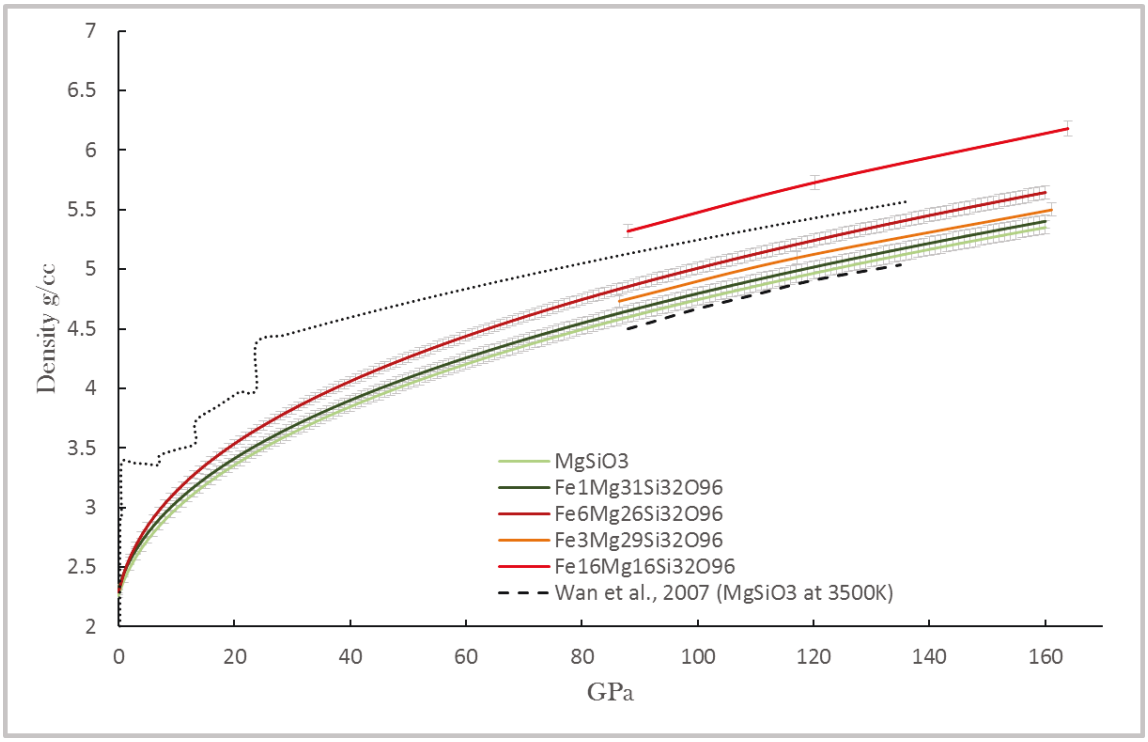

Figure 86 Density versus pressure profile for (Fe,Mg)SiO3 melts at 3000K, covering the Earth's mantle pressure range. The only composition studied here that is denser than PREM (the fine dotted line) is the one containing ght% Fe. Our results are in good agreement with those published by Wang et al., 2007.

data.

Despite the slight temperature difference our results are in good agreement with those published by Wan et al.,2007.

Based on the above results the density space for the whole MgSiO3-FeSiO3 compositional space can be extrapolated (Figure 87).

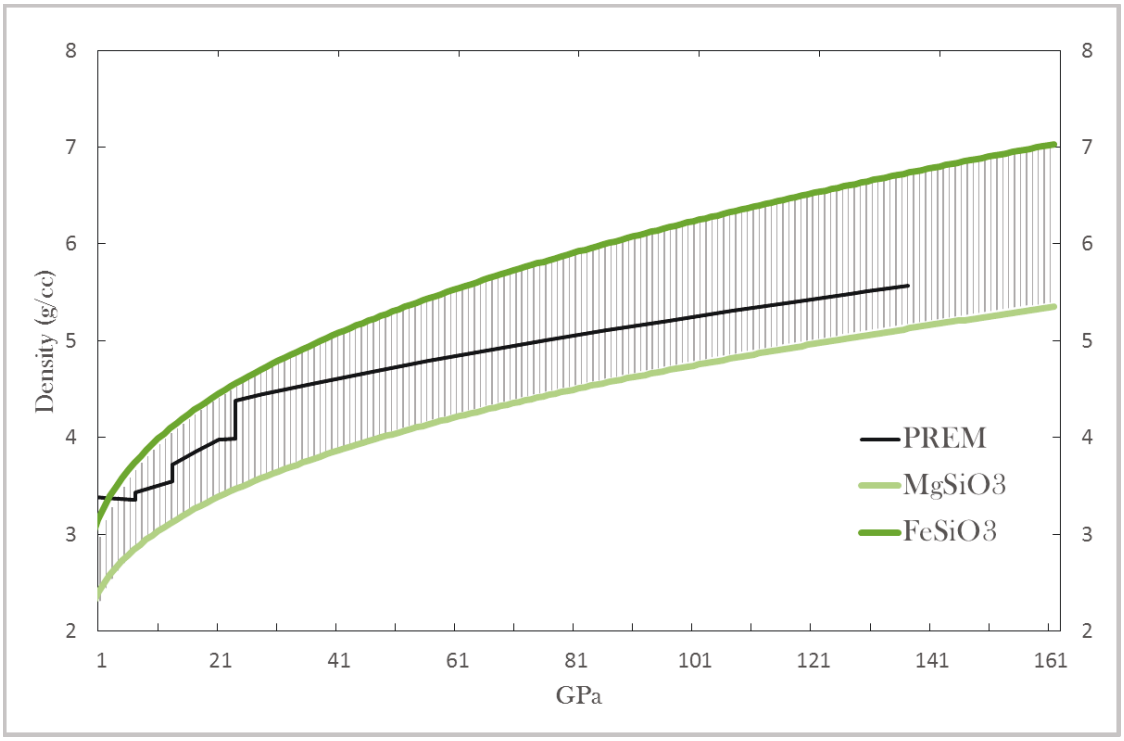

Figure 88 The density of all melts in the compositional range MgSiO3 – FeSiO3 extrapolated based on the results presented in the previous graph (Figure C-1)). Only melts with very high Fe content, more than (Fe.4,Mg.6)SiO3 are denser than PREM at any pressure of the Earth's mantle.

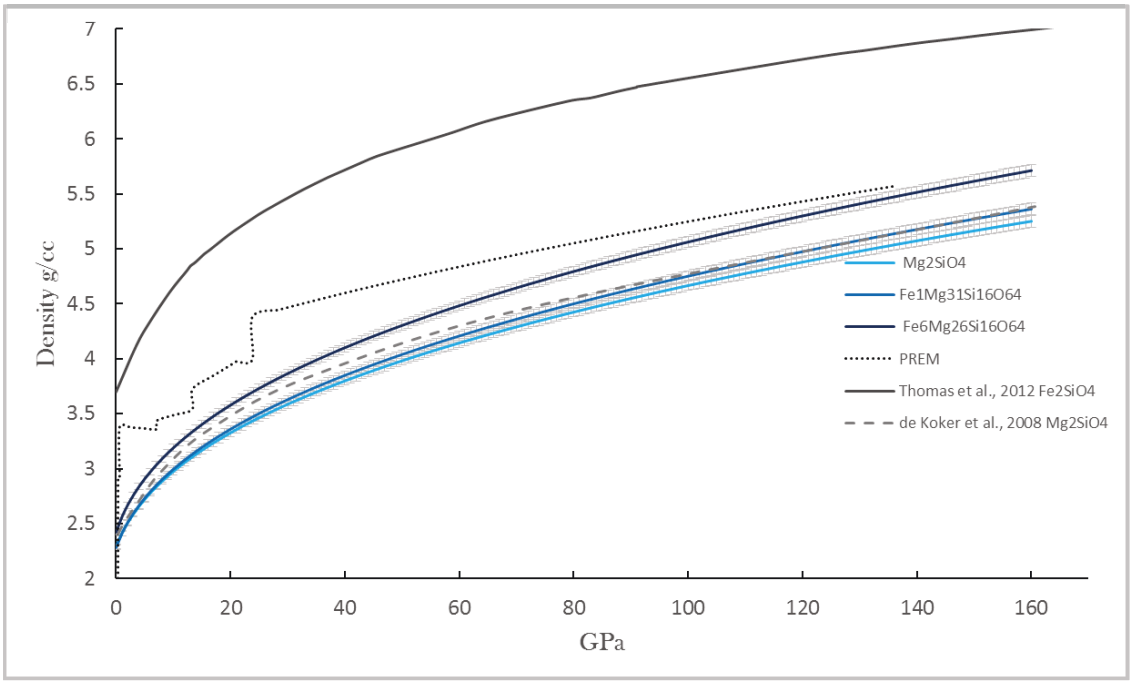

Figure 87 Olivine melt densities across the Earth's mantle. Previously published data, de Koker at al., 2008, are more dense than the results presented here above 8GPa. The difference in density between our results and the one reported by de Koker et al., 2008 might be because of the different pseudopotentials used (GGA-PBE in this study, LDA in the study of de Koker et al., 2008).

The densities of olivine melts are presented in the Figure 88.

In Figure 89 the densities of several melt compositions studied here are plotted alongside previously published results.

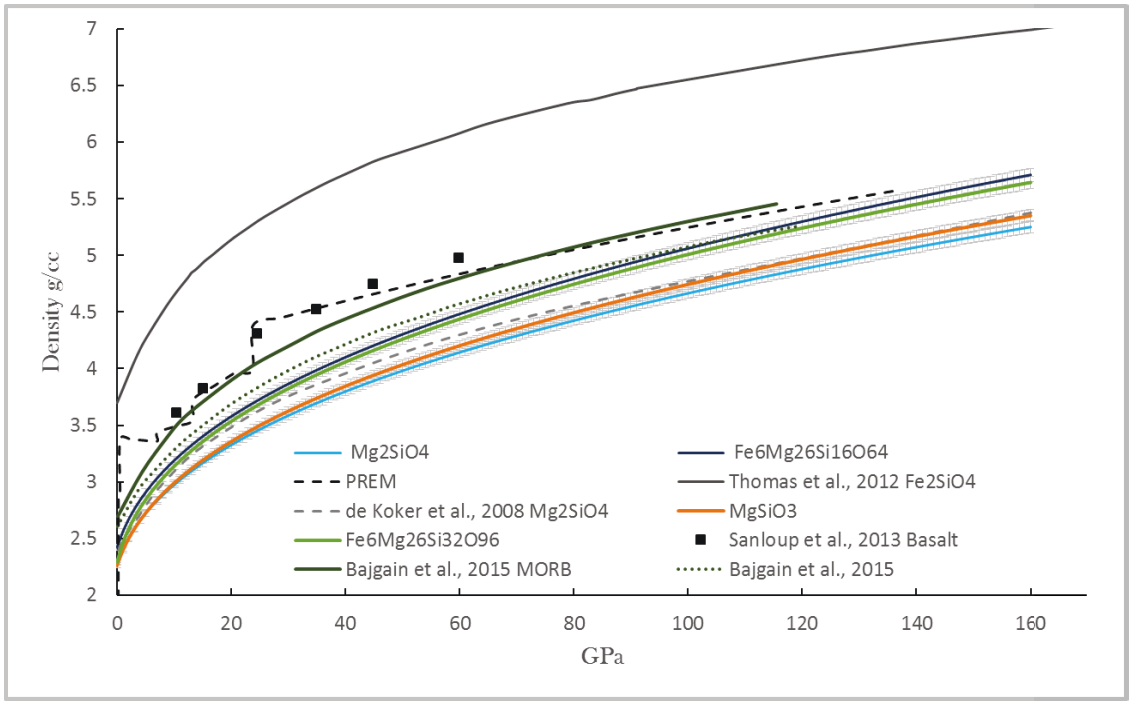

Figure 90 Comparison between the densities of different compositions studied here and published data. For the sake of clarity only the Fe-free compositions and the most Fe-rich composition studied here were plotted. The literature data represented is at 3000K with the exception of Sanloup et al., 2013 and Thomas et al., 2012 which are experimental results. The Sanloup et al., 2013 data is the result of multi-anvil experiments and the temperature varies from data point to data point in the range 2200-3200 increasing with pressure. Thomas et al.,2012 are shock experiments and the temperature is on the Hugoniot.

Figure 90 shows the density difference between two identical compositions but along two isotherms, 3000 and 4000K.

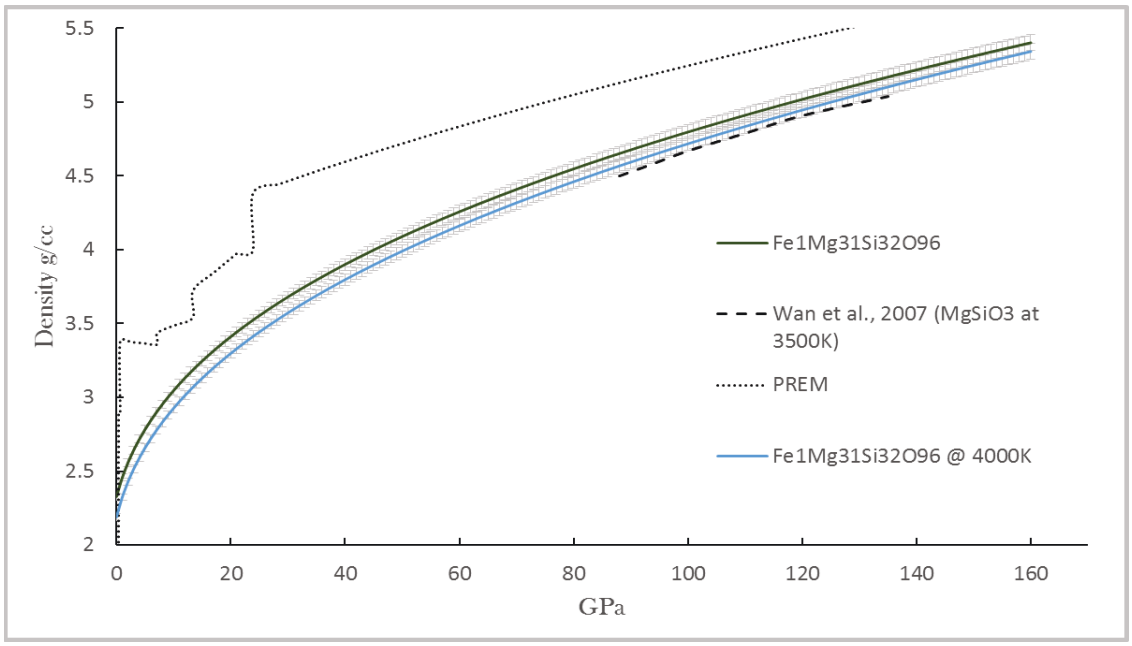

Figure 89 Density comparison between two isotherms, 3000 and 4000K. At pressures higher than 40 GPa the density difference is 1% or less. PREM and data from Wan et al., 2007 for a similar composition have been plotted for comparison.

Annex 4: Integrals over the pair distribution function

As mentioned in the Chapter 2, the integration over the radial pair distribution function must be made in order to obtain the coordination number. The value of the coordination number in the first coordination sphere, is the value of the integral at the first minima of the RPD. In the following graphs, the integral over the PDF

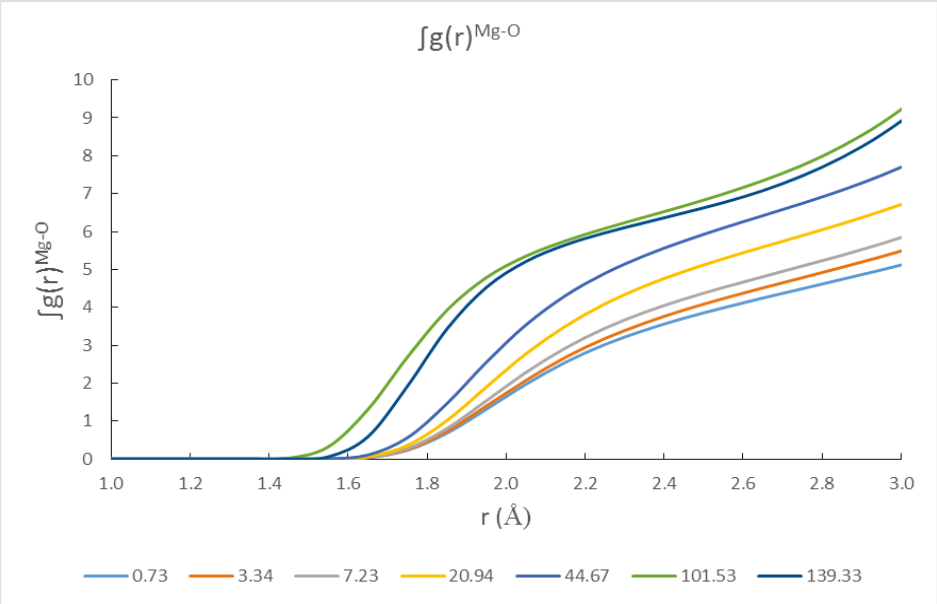

Figure 91 Integrals of the radial pair distribution function of Mg –O plotted versus r. The legend represents the different pressures in GPa.

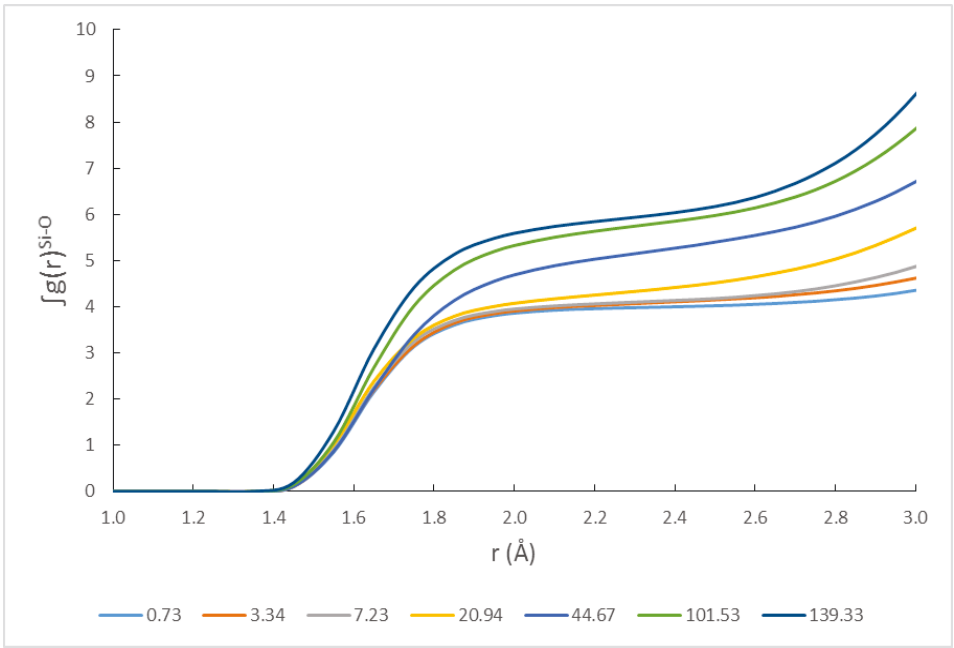

Figure 92 Integrals of the radial pair distribution function of Si –O plotted versus r. The legend represents the different pressures in GPa.

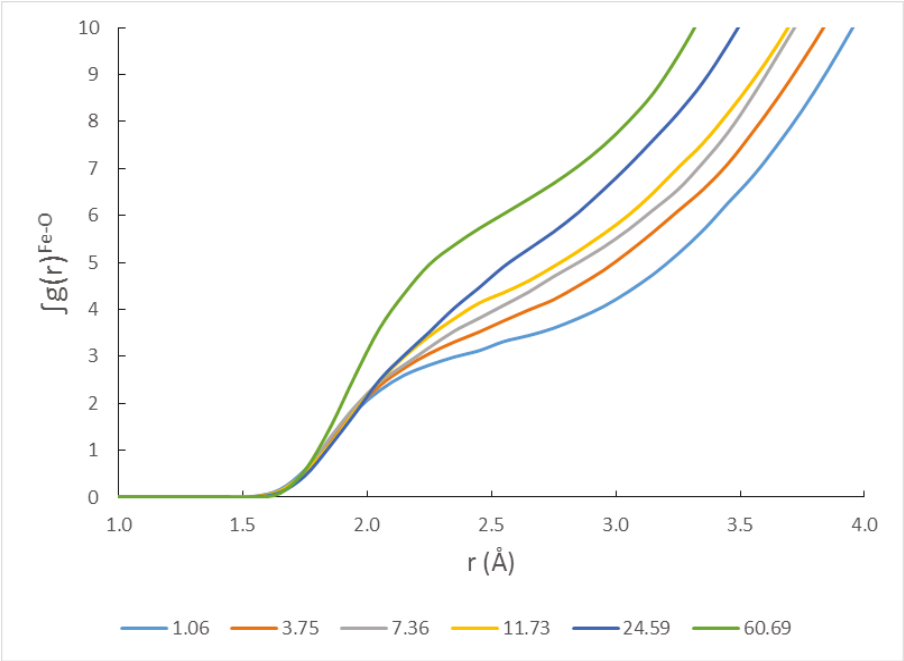

Figure 93 Integrals of the radial pair distribution function of Fe –O plotted versus r. The legend represents the different pressures in GPa.

versus r is shown for the main cations present in olivine melts.

Annex 5: Estimation of errors: FPMD

In Chapter 2, it was stated that the type of first principles molecular dynamics used for the simulations presented here is NVT. This, as mentioned before, means that during the simulation the number of atoms is constant (N), the volume of simulation cell is constant (V), and that temperature is also constant (T). The external pressure can be computed by averaging over the trace of the stress tensors. Temperature is maintained constant by adjusting the kinetic energies of each ion at every simulation step. Because of this the external pressure obtained from the traces of the stress tensors must be corrected for the kinetic contribution. In VASP package versions 5.x.x the kinetic contribution is automatically computed and added to the stress tensors. For the simulations done with older versions the correction was applied as:

$$Kinetic\ contribution\ in\ GPa = \left(\frac{N\ k_B T}{V}\right) 160.2176 \tag{35}$$

where k_B is the Boltzmann constant.

The external pressure varies during the simulation, oscillating around an equilibrium value (Figure 94).

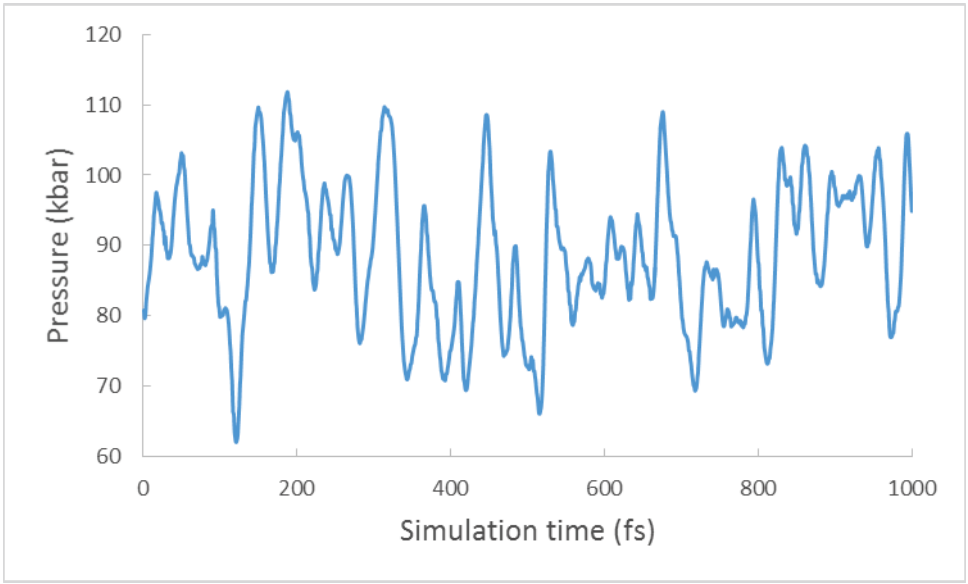

Figure 94 Variation of pressure with simulation time. The simulation is not spin-polarized, the number atoms in the simulation cell is 255, and the temperature is 2000K. The standard deviation of the pressure in this case is 10.245 kbar.

We calculated the standard deviation of pressure for each run at a given volume and we used the average stand deviation to denote the errors in pressure. Another two examples for a different system are shown in Figure 95.

Energy also varies during the simulation. We checked the energy variation during our simulations to check for convergence (Figure 96).

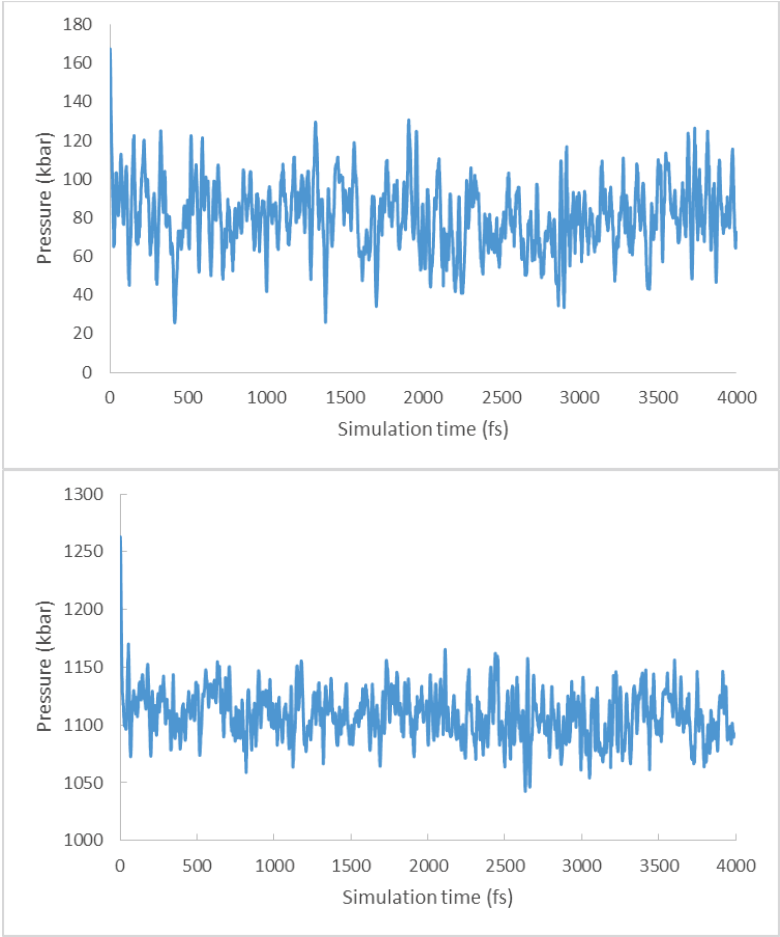

Figure 95 Two spin polarized simulations of the same composition at different volumes. The number of atoms is 112 and the temperature is 3000K. The thermalization time was not removed. In a) the standard deviation is 17.5 kbar, and in b) is 20.41 kbar.

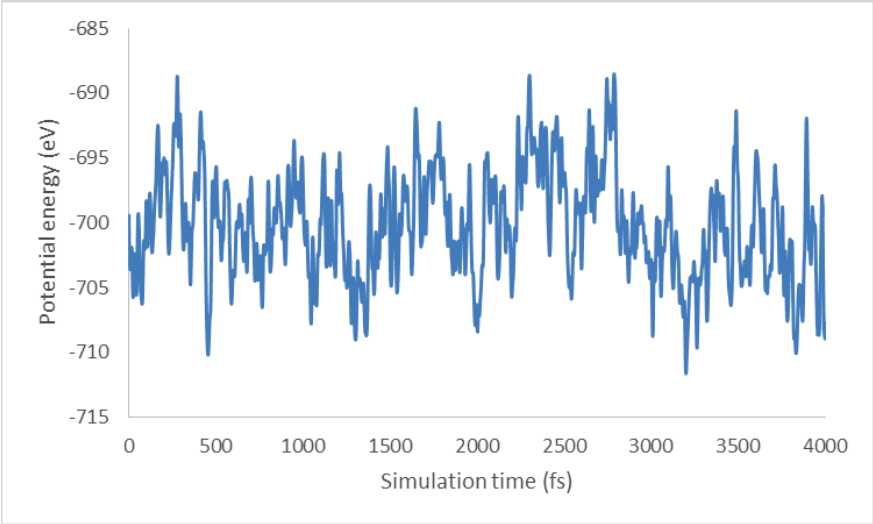

Figure 97 The potential energy of a simulation box containing 112 atoms, spin polarized, at 3000K and ≈8 GPa. The largest variations are 20 eV apart, making the largest energy fluctuations ≈0.18eV/atom.

Conclusions

First principles molecular dynamics have been used to study Fe, Ni, and Co bearing enstatite and olivine melts at pressures covering the Earth's mantle pressure range. We report data on structure, the spin state of the transitional metals, and equations of state.

With the help of multi-anvil experiments we investigate the influence of the polymerization degree of silicate melts on the metal silicate melt partitioning of Co, Ni, and W.

The equations of state obtained for Fe-bearing enstatite melts, alongside published data, have been used to construct a model which aims to provide insight into the chemical and mineralogical composition of the Ultra-Low Velocity Zones.

In this thesis we have explored the structure of Fe, Ni, and Co bearing silicate melts on a 3000K isotherm along the pressure range of the Earth's mantle. The pressure at which Si changes coordination from tetrahedral to octahedral depends on the Si/O ratio of the melt. All cation coordination change with pressure, with the exception of metallic Ni, follows a common trend: a rapid increase in coordination up to 50 GPa (on average), followed by a much slower coordination increase. We also investigate the Bader volume decrease with pressure of Si, Mg, Co, Fe, Ni, and O in olivine melts, and find that O volume decrease is responsible for most of the pressure accommodation. In olivine melts, from 0 to 60 GPa, Si-O coordination number increases with 33.33% (from 4 to 6-fold coordinated), while in the same pressure range the O Bader volume decreases with 50%.

We find discrepancies between the degree of polymerization predicted by NBO/T and the actual O-Si coordination number. We discuss this issue and conclude that NBO/T should not be used as a polymerization proxy at pressures greater than 10GPa.

The pressure induced spin crossover of Fe, Ni, and Co in silicate melts was investigated. We find that all three transitional metals can have a spin crossover in the Earth's mantle pressure range. The spin behaviour of all transitional metals investigated is strongly influenced by melt chemistry. We propose a correlation between the spin crossover of Ni and Co, in olivine melts, and the kink in the pressure evolution of their metal and silicate melts partitioning coefficients.

Using experimental techniques we investigate the effects of silicate melt polymerization on the partitioning of Ni, Co, and W between a silicate and a metallic melt. We find a strong influence in the case of W, as previously reported. We employ FPMD simulations to investigate the coordination, Bader volume, Bader charge, and mobility of Ca and W in highly polymerized silicate melts. Ca and W have high coordination numbers, high mobility and large volumes in the silicate melt studied. We cautiously conclude, that the apparent affinity of W for depolymerized melts is due to its high ionic volume.

From our FPMD runs, we have fitted the EoS of all the melts we have studied up to CMB pressures. We used the compressional coefficients alongside literature data to construct a model that allows us to quantify the composition of the ULVZs. Our model produces independent results in good agreement with previous approaches and expectations. Moreover, our model gives insight into the nature of the phases present in the ULVZ and their chemical compositions. We interpret our model results from a ULVZ origin perspective and propose an Early Earth origin for the ULVZs.

Perspectives

Perhaps this thesis raises more questions than answers, but we hope that it has added a gram of confidence to the idea that silicate liquids are a bit more complex than previously thought.

Future work should continue to look into the spin behaviour of the metals relevant for core and mantle formation at pressures and temperatures of the Earth's mantle. A more extensive investigation on the temperature and compositional effects on the spin state of Ni, Co, and Fe should be done. More detailed simulations can assess the exact volume change associated with HS to LS transitions in silicate melts.

Equations of state for more complex melt compositions can help elucidate the density crossover points within the Earth's mantle. EOS at higher temperatures than those investigated in this thesis can offer invaluable information to Earth and planetary impact and differentiation modelling.

The charge of W in silicate melts relevant to past and present Earth mantle, should be investigated.

A complete understanding of the chemical and physical properties of silicate melts at planetary interiors conditions, would most likely solve the mysteries of planet formation and evolution. Or at least, half of the mystery.

References

Andrault, D. et al., 2014. Melting of subducted basalt at the core-mantle boundary. *Science (New York, N.Y.)*, 344, pp.892–5. Available at: http://www.ncbi.nlm.nih.gov/pubmed/24855266.

Andrault, D. et al., 2012. Solid–liquid iron partitioning in Earth's deep mantle. *Nature*, 487(7407), pp.354–357. Available at: http://dx.doi.org/10.1038/nature11294.

Andrault, D. et al., 2011. Solidus and liquidus profiles of chondritic mantle: Implication for melting of the Earth across its history. *Earth and Planetary Science Letters*, 304(1-2), pp.251–259. Available at: http://linkinghub.elsevier.com/retrieve/pii/S0012821X1100077X.

Bader, R.F.W., 1991. A Quantum Theory of Molecular Structure and Its Appllcatlons. *Chemical reviews*, 91, pp.893–928.

Badro, J. et al., 2004. Electronic transitions in perovskite: possible nonconvecting layers in the lower mantle. *Science (New York, N.Y.)*, 305(5682), pp.383–386.

Badro, J. et al., 2003a. Iron partitioning in Earth's mantle: toward a deep lower mantle discontinuity. *Science (New York, N.Y.)*, 300(5620), pp.789–791. Available at: http://www.ncbi.nlm.nih.gov/pubmed/12677070 [Accessed January 13, 2015].

Badro, J. et al., 2003b. Iron partitioning in Earth's mantle: toward a deep lower mantle discontinuity. *Science (New York, N.Y.)*, 300(5620), pp.789–791. Available at: http://www.ncbi.nlm.nih.gov/pubmed/12677070 [Accessed January 13, 2015].

Badro, J., 2014. Spin Transitions in Mantle Minerals. *Annual Review of Earth and Planetary Sciences*, 42, pp.231–248. Available at: http://www.annualreviews.org/doi/abs/10.1146/annurev-earth-042711-105304.

Bajgain, S., Ghosh, D.B. & Karki, B.B., 2015. Structure and density of basaltic melts at mantle conditions from first-principles simulations. *Nature Communications*, 6, p.8578. Available at: http://www.nature.com/doifinder/10.1038/ncomms9578.

Bengtson, A., Persson, K. & Morgan, D., 2008. Ab initio study of the composition dependence of the pressure- induced spin crossover in perovskite (Mg 1 − x , Fe x) SiO 3. *Earth and Planetary Science Letters*, 265(3-4), pp.535–545. Available at: http://dx.doi.org/10.1016/j.epsl.2007.10.049.

Bennett, V.C., Brandon, A.D. & Nutman, A.P., 2006. Coupled 142Nd - 143Nd Isotopic Evidence for Hadean Mantle Dynamics. *Science*, 318, pp.1907–1910.

Berendsen, H.J.C. et al., 1984. Molecular dynamics with coupling to an external bath. *The Journal of Chemical Physics*, 81(8), pp.3684–3690. Available at: http://link.aip.org/link/JCPSA6/v81/i8/p3684/s1&Agg=doi\npapers2://publication/doi/10.1063/1.448118.

Blochl, P.E., 1994. Projector augmented-wave method. *Physical Review B*, 50(24).

Bouchet, J. et al., 2013. Ab initio equation of state of iron up to 1500 GPa. *Physical Review B - Condensed Matter and Materials Physics*, 87(9), p.094102. Available at: http://link.aps.org/doi/10.1103/PhysRevB.87.094102.

Boukare, C.-E., Ricard, Y. & Fiquet, G., 2015. Thermodynamics of the MgO-FeO-SiO 2 system up to 140 GPa : Application to the crystallization of Earth's magma ocean , vol. 120, 9, *Journal of Geophysical Research*.

Brown, S.P. et al., 2015. A compositional origin to ultralow-velocity zones. Geophysical Research Letters, (2), pp.1039–1045.

Cameron, A.G.W., 1997. The Origin of the Moon and the Single Impact Hypothesis V. *Icarus*, 126(1), pp.126–137. Available at: http://www.sciencedirect.com/science/article/pii/S0019103596956420.

Canup, R.M., 2008. Accretion of the Earth. *Philosophical transactions. Series A, Mathematical, physical, and engineering sciences*, 366(September), pp.4061–4075.

Canup, R.M., 2012. Composition via a Giant Impact. , 338(November), pp.1052–1055.

Canup, R.M., 2004. Simulations of a late lunar-forming impact. *Icarus*, 168(2), pp.433–456.

Canup, R.M. & Asphaug, E., 2001. Origin of the Moon in a giant impact near the end of the Earth's formation. *Nature*, 412(6848), pp.708–712.

Canup, R.M. & Esposito, L.W., 1996. Accretion of the moon from an impact-generated disk. *Icarus*, 119(2), pp.427–446. Available at: <Go to ISI>://A1996TY87000012.

Caracas, R. & Cohen, R.E., 2007. Effect of Chemistry on the Physical Properties of Perovskite and Post-Perovskite , Geophysical Research Letters, vol. 32, pp.115–128.

Caracas, R. & Cohen, R.E., 2005. Effect of chemistry on the stability and elasticity of the perovskite and post-perovskite phases in the MgSiO3-FeSiO3- Al2O3 system and implications for the lowermost mantle. *Geophysical Research Letters*, 32(16), pp.1–4.

Caracas, R., Mainprice, D. & Thomas, C., 2010. Is the spin transition in Fe 2 + - bearing perovskite visible in seismology ? Geophysical Research Letters, vol. 37.

Caro, G. et al., 2005. Trace-element fractionation in Hadean mantle generated by melt segregation from a magma ocean. *Nature*, 436(7048), pp.246–249.

Chen, B. et al., 2012. Spin crossover equation of state and sound velocities of (Mg 0.65 Fe 0.35)O ferropericlase to 140 GPa. *Journal of Geophysical Research*, 117(B8), p.B08208. Available at: http://doi.wiley.com/10.1029/2012JB009162 [Accessed January 13, 2015].

Cohen, R.E., Mazin, I.I. & Isaak, D.G., 1997. Magnetic Collapse in Transition Metal Oxides at High Pressure: Implications for the Earth. *Science*, 275(5300), pp.654–657.

Corgne, A. et al., 2008. Metal–silicate partitioning and constraints on core composition and oxygen fugacity during Earth accretion. *Geochimica et Cosmochimica Acta*, 72(2), pp.574–589. Available at: http://linkinghub.elsevier.com/retrieve/pii/S0016703707005674.

Cottaar, S. & Romanowicz, B., 2012. An unsually large ULVZ at the base of the mantle near Hawaii. *Earth and Planetary Science Letters*, 355-356, pp.213–222. Available at: http://dx.doi.org/10.1016/j.epsl.2012.09.005.

Cottrell, E., Walter, M.J. & Walker, D., 2009. Metal-silicate partitioning of tungsten at high pressure and temperature: Implications for equilibrium core formation in Earth. *Earth and Planetary Science Letters*, 281(3-4), pp.275–287. Available at: http://dx.doi.org/10.1016/j.epsl.2009.02.024.

Crowhurst, J.C. et al., 2008. Elasticity of (Mg,Fe)O through the spin transition of iron in the lower mantle. - supplemetary. *Science (New York, N.Y.)*, 319(5862), pp.451–3. Available at: http://www.ncbi.nlm.nih.gov/pubmed/18218893 [Accessed December 23, 2014].

Cuk, M. & Stewart, S.T., 2012. Making the Moon from a Fast-Spinning Earth : A Giant Impact Followed by Resonant Despinning. , (November), pp.1047–1052.

Delano, J.W., 1986. Abundances of Cobalt, Nickel, and Volatiles in the Silicate Portion of the Moon. *Origin of the Moon*.

Farnan, I. et al., 1992. Quantification of the disorder in network-modified silicate glasses. *Nature*, 358, pp.31–35.

Ferlat, G. et al., 2012. Hidden polymorphs drive vitrification in B2O3. *Nature Materials*, 11(11), pp.925–929. Available at: http://dx.doi.org/10.1038/nmat3416.

Fiquet, G. et al., 2010. Melting of Peridotite to 140 Gigapascals Supplementary. *Science*, 329(5998), pp.1516–1518. Available at: http://www.sciencemag.org/cgi/doi/10.1126/science.1192448.

Fischer, R. a. et al., 2015. High pressure metal–silicate partitioning of Ni, Co, V, Cr, Si, and O. *Geochimica et Cosmochimica Acta*, 167, pp.177–194. Available at: http://linkinghub.elsevier.com/retrieve/pii/S0016703715004093.

Fyfe, W.., 1960. The possibility of d-electron coupling in olivine at high pressures. *Geochimica et Cosmochimica Acta*, 19(2), pp.141–143.

Garnero, E.J. & Helmberger, D. V., 1995. A very slow basal layer underlying large-scale low-velocity anomalies in the lower mantle beneath the Pacific: evidence from core phases. *Physics of the Earth and Planetary Interiors*, 91(1-3), pp.161–176.

Goncharov, a. F. et al., 2010. Effect of composition, structure, and spin state on the thermal conductivity of the Earth's lower mantle. *Physics of the Earth and Planetary Interiors*, 180(3-4), pp.148–153. Available at: http://dx.doi.org/10.1016/j.pepi.2010.02.002.

Goodman, C.H.L., 1975. Strained mixed-cluster model for glass structure. *Nature*, 254, p.620–.

Grove, T.L. & Krawczynski, M.J., 2009. Lunar mare volcanism: Where did the magmas come from? *Elements*, 5(1), pp.29–34.

Gu, C. et al., 2012. Electronic structure of iron in magnesium silicate glasses at high pressure. *Geophysical Research Letters*, 39(24), pp.1–5.

Halliday, A. et al., 1996. Early evolution of the Earth and Moon: new constraints from Hf-W isotope geochemistry. *Earth and Planetary Science Letters*, 142(1-2), pp.75–89.

Henderson, G.S., Calas, G. & Stebbins, J.F., 2006. The Structure of Silicate Glasses and Melts. *Elements*, 2(5), pp.269–273.

Henkelman, G., Arnaldsson, A. & Jónsson, H., 2006. A fast and robust algorithm for Bader decomposition of charge density. *Computational Materials Science*, 36(3), pp.354–360.

Hernlund, J.W., Thomas, C. & Tackley, P.J., 2005. A doubling of the post-perovskite phase boundary and structure of the Earth's lowermost mantle. *Nature*, 434(April).

Herwartz, D. et al., 2014. Identification of the giant impactor Theia in lunar rocks. *Science*,

344(6188).

Hier-Majumder, S., 2008. Influence of contiguity on seismic velocities of partially molten aggregates. *Journal of Geophysical Research*, 113(B12), p.B12205. Available at: http://doi.wiley.com/10.1029/2008JB005662.

Hirose, K. et al., 2004. Trace element partitioning in Earth's lower mantle and implications for geochemical consequences of partial melting at the core-mantle boundary. *Physics of the Earth and Planetary Interiors*, 146, pp.249–260.

Hofmeister, a. M., 1999. Mantle Values of Thermal Conductivity and the Geotherm from Phonon Lifetimes. *Science*, 283(5408), pp.1699–1706.

Hohenberg, P. & Kohn, W., 1964. Inhomogeneous Electron Gas. *Physical Review*, 155(1962).

Hostetler, C.J. & Drake, M.J., 1980. On the early global melting of the terrestrial planets. *Proc. Lunar Planet. Sci. Conf. 11th*, pp.1915–1929.

Ida, S., Canup, R. & Stewart, G., 1997. Lunar accretion from an impact-generated disk. *Nature*, 389(September), pp.353–357. Available at: http://www.nature.com/nature/journal/v389/n6649/abs/389353a0.html.

Jones, J.H. & Delano, J.W., 1989. A three-component model for the bulk composition of the Moon. *Geochimica et Cosmochimica Acta*, 53(i), pp.513–527.

Journaux, B. et al., 2014. Elasticity and dislocations in ice X under pressure. *Physics of the Earth and Planetary Interiors*, 236, pp.10–15. Available at: http://www.sciencedirect.com/science/article/pii/S0031920114001885.

Karki, B., Bhattarai, D. & Stixrude, L., 2006. First-principles calculations of the structural, dynamical, and electronic properties of liquid MgO. *Physical Review B*, 73(17), pp.1–7.

Karki, B., Bohara, B. & Stixrude, L., 2011. First-principles study of diffusion and viscosity of anorthite (CaAl2Si2O8) liquid at high pressure. , 96, pp.744–751. Available at: http://discovery.ucl.ac.uk/1327041/.

Karki, B.B., 2015. First-principles computation of mantle materials in crystalline and amorphous phases. *Physics of the Earth and Planetary Interiors*, 240, pp.43–69. Available at: http://linkinghub.elsevier.com/retrieve/pii/S0031920114002398.

Karki, B.B., 2010. First-Principles Molecular Dynamics Simulations of Silicate Melts: Structural and Dynamical Properties. *Reviews in Mineralogy and Geochemistry*, 71(1), pp.355–389. Available at: http://rimg.geoscienceworld.org/cgi/doi/10.2138/rmg.2010.71.17.

Karki, B.B. & Stixrude, L., 2010. First-principles study of enhancement of transport properties of silica melt by water. *Physical Review Letters*, 104(21), pp.1–4.

Karki, B.B., Zhang, J. & Stixrude, L., 2013a. First principles viscosity and derived models for MgO-SiO2 melt system at high temperature. *Geophysical Research Letters*, 40(1), pp.94–99. Available at: http://doi.wiley.com/10.1029/2012GL054372 [Accessed January 13, 2015].

Karki, B.B., Zhang, J. & Stixrude, L., 2013b. First principles viscosity and derived models for MgO-SiO2 melt system at high temperature. *Geophysical Research Letters*, 40(1), pp.94–99.

Kegler, P. et al., 2008. New Ni and Co metal-silicate partitioning data and their relevance for an early terrestrial magma ocean. *Earth and Planetary Science Letters*, 268(1-2), pp.28–40.

Kimura, K., Lewis, R.S. & Anders, E., 1974. Distribution of gold and rhenium between nickel-iron and silicate melts - Implications for the abundance of siderophile elements on the earth and moon. , 38.

Kohn, W. & Sham, L.J., 1965. Self-Consistent Equations Including Exchange and Correlation Effects. *Physical Review*, 385(1951).

De Koker, N., 2010. Structure, thermodynamics, and diffusion in CaAl2Si2O8 liquid from first-principles molecular dynamics. *Geochimica et Cosmochimica Acta*, 74(19), pp.5657–5671. Available at: http://dx.doi.org/10.1016/j.gca.2010.02.024.

de Koker, N., Karki, B.B. & Stixrude, L., 2013. Thermodynamics of the MgO-SiO2 liquid system in Earth's lowermost mantle from first principles. *Earth and Planetary Science Letters*, 361, pp.58–63. Available at: http://dx.doi.org/10.1016/j.epsl.2012.11.026.

de Koker, N.P., Stixrude, L. & Karki, B.B., 2008. Thermodynamics, structure, dynamics, and freezing of Mg2SiO4 liquid at high pressure. *Geochimica et Cosmochimica Acta*, 72(5), pp.1427–1441.

König, S. et al., 2011. The Earth's tungsten budget during mantle melting and crust formation. *Geochimica et Cosmochimica Acta*, 75(8), pp.2119–2136. Available at: http://linkinghub.elsevier.com/retrieve/pii/S0016703711000482.

Kresse, G., 1995. Ab initio molecular dynamics for liquid metals. *Journal of Non-Crystalline Solids*, 192-193(1), pp.222–229.

Kresse, G., 1996. Efficient iterative schemes for ab initio total-energy calculations using a plane-wave basis set. *Physical Review B*, 54(16), pp.11169–11186.

Kresse, G., 1999. From ultrasoft pseudopotentials to the projector augmented-wave method. *Physical Review B*, 59(3), pp.1758–1775.

Kresse, G. & Furthmüller, J., 1996. Efficiency of ab initio total energy calculations for metals and semiconductors using a plane wave basis set. *Comput. Mat. Sci.*, 6, p.15.

Kresse, G. & Hafner, J., 1994. Ab initio molecular-dynamics simulation of the liquid-metal–amorphous-semiconductor transition in germanium. *Physical Review B*, 49(20), pp.14251–14269.

Kuryaeva, R.G., 2009. The state of magnesium in silicate glasses and melts. *Glass Physics and Chemistry*, 35(4), pp.378–383. Available at: http://link.springer.com/10.1134/S1087659609040051.

Labrosse, S., Hernlund, J.W. & Coltice, N., 2007. A crystallizing dense magma ocean at the base of the Earth's mantle. *Nature*, 450(December), pp.866–869.

Levine, B.G., Stone, J.E. & Kohlmeyer, A., 2011. Fast analysis of molecular dynamics trajectories with graphics processing units-Radial distribution function histogramming. *Journal of Computational Physics*, 230(9), pp.3556–3569. Available at: http://dx.doi.org/10.1016/j.jcp.2011.01.048.

Li, J. & Agee, C.B., 1996. Geochemistry of mantle–core differentiation at high pressure. *Nature*, 381(6584), pp.686–689.

Luo, Y., 2007. *Comprehensive Handbook of Chemical Bond Energies*, CRC Press.

Mao, W.L. et al., 2006. Iron-Rich Post-Perovskite and the Origin of Ultralow-Velocity Zones. , pp.2–4.

Marton, F.C., Ita, J. & Cohen, R.E., 2000. Pressure-volume-temperature equation of state of MgSiO3 perovskite from molecular dynamics and constraints on lower mantle composition. , 106(2000), p.26. Available at: http://arxiv.org/abs/physics/0010083.

Mattsson, A.E., 2002. In Pursuit of the "Divine" Functional. *Science*, 298(October), pp.759–760.

McCammon, C. et al., 2008. Stable intermediate-spin ferrous iron in lower-mantle perovskite. *Nature Geoscience*, 1(October), pp.684–687.

McNamara, A.K., Garnero, E.J. & Rost, S., 2010. Tracking deep mantle reservoirs with ultra-low velocity zones. *Earth and Planetary Science Letters*, 299(1-2), pp.1–9. Available at: http://dx.doi.org/10.1016/j.epsl.2010.07.042.

Mills, K.C., 1993. The Influence of Structure on the Physico-chemical Properties of Slags. *ISIJ International*, 33(1), pp.148–155.

Morard, G. et al., 2013. The Earth's core composition from high pressure density measurements of liquid iron alloys. *Earth and Planetary Science Letters*, 373, pp.169–178. Available at: http://dx.doi.org/10.1016/j.epsl.2013.04.040.

Muir, J.M.R. & Brodholt, J.P., 2015. Elastic properties of ferrous bearing MgSiO3 and their relevance to ULVZs. *Geophysical Journal International*, 201(1), pp.496–504. Available at: http://gji.oxfordjournals.org/cgi/doi/10.1093/gji/ggv045.

Mysen, B.O., Virgo, D. & Seifert, F. a., 1982. *The structure of silicate melts: Implications for chemical and physical properties of natural magma*,

Nakajima, M. & Stevenson, D.J., 2015. Melting and mixing states of the Earth's mantle after the Moon-forming impact. *Earth and Planetary Science Letters*, 427, pp.286–295. Available at: http://www.sciencedirect.com/science/article/pii/S0012821X15003805.

Nomura, R. et al., 2014. Low Core-Mantle Boundary Temperature Inferred from the Solidus of Pyrolite. *Science*, 343(6170), pp.522–525. Available at: http://www.ncbi.nlm.nih.gov/pubmed/24436185.

Nomura, R. et al., 2011. Spin crossover and iron-rich silicate melt in the Earth's deep mantle. *Nature*, 473(7346), pp.199–202. Available at: http://dx.doi.org/10.1038/nature09940.

O'Neill, H.S.C., Berry, A.J. & Eggins, S.M., 2008. The solubility and oxidation state of tungsten in silicate melts: Implications for the comparative chemistry of W and Mo in planetary differentiation processes. *Chemical Geology*, 255(3-4), pp.346–359.

Oganov, a R., Brodholt, J.P. & Price, G.D., 2001. The elastic constants of MgSiO3 perovskite at pressures and temperatures of the Earth's mantle. *Nature*, 411(June), pp.934–937.

Oganov, A.R., Brodholt, J.P. & Price, G.D., 2001. Ab initio elasticity and thermal equation of state of MgSiO3 perovskite. *Earth and Planetary Science Letters*, 184, pp.555–560.

Ohtani, E., 1985. The primodial terrestrial magma ocean and its implication for stratification of the mantle. *Physics of the Earth and Planetary Interiors*, 38(1), pp.70–80.

Palme, H. et al., 2011. Comment on " Prediction of metal – silicate partition coefficients for siderophile elements : An update and assessment of PT conditions for metal – silicate equilibrium during accretion of the Earth " by K . Righter , EPSL 304 (2011) 158 – 167 , 2011. *Earth and Planetary Science Letters*, 312(3-4), pp.516–518. Available at: http://dx.doi.org/10.1016/j.epsl.2011.10.018.

Palme, H. & O'Neill, H.S.C., 2014. *Cosmochemical Estimates of Mantle Composition* 2nd ed., Elsevier Ltd. Available at: http://linkinghub.elsevier.com/retrieve/pii/B9780080959757002011.

Paniello, R.C., Day, J.M.D. & Moynier, F., 2012. Zinc isotopic evidence for the origin of the Moon. *Nature*, 490(7420), pp.376–379. Available at: http://www.ncbi.nlm.nih.gov/pubmed/23075987.

Payne, M. et al., 1986. Molecular Dynamics and ab initio Total Energy Calculations. *Physical Review Letters*, 56(24), pp.2656–2656.

Payne, M.C. et al., 1992. Iterative minimization techniques for ab initio total-energy calculations: molecular dynamics and conjugate gradients. *Reviews of Modern Physics*.

Perdew, J.P. et al., 2005. Prescription for the design and selection of density functional approximations: More constraint satisfaction with fewer fits. *Journal of Chemical Physics*, 123(6).

Perdew, J.P.J., Burke, K. & Ernzerhof, M., 1996. Generalized Gradient Approximation Made Simple. *Physical review letters*, 77(18), pp.3865–3868. Available at: http://www.ncbi.nlm.nih.gov/pubmed/10062328.

Pozzo, M. et al., 2012. Thermal and electrical conductivity of iron at Earth's core conditions. , (0225), pp.10–15. Available at: http://discovery.ucl.ac.uk/1345888/.

Prescher, C. et al., 2014. Iron spin state in silicate glass at high pressure: Implications for melts in the Earth's lower mantle. *Earth and Planetary Science Letters*, 385, pp.130–136. Available at: http://linkinghub.elsevier.com/retrieve/pii/S0012821X13006109 [Accessed December 24, 2014].

Ramo, D.M. & Stixrude, L., 2014. Spin crossover in Fe 2 SiO 4 liquid at high pressure. *Geophysical Research Letters*, 41, pp.4512–4518.

Righter, K., 2011a. Prediction of metal-silicate partition coefficients for siderophile elements: An update and assessment of PT conditions for metal-silicate equilibrium during accretion of the Earth. *Earth and Planetary Science Letters*, 304(1-2), pp.158–167. Available at: http://dx.doi.org/10.1016/j.epsl.2011.01.028.

Righter, K., 2011b. Reply to the Comment by Palme et al. on "Prediction of metal–silicate partition coefficients for siderophile elements: An update and assessment of PT conditions for metal–silicate equilibrium during accretion of the Earth." *Earth and Planetary Science Letters*, 304(1-2), pp.158–167. Available at: http://dx.doi.org/10.1016/j.epsl.2011.10.011.

Ringwood, a. ., 1966. Chemical evolution of the terrestrial planets. *Geochimica et Cosmochimica Acta*, 30(1), pp.41–104.

Ringwood, A.E., 1986. Composition and Origin of the Moon. *Origin of the moon; Proceedings of the Conference, Kona, HI, October 13-16*, pp.673–698.

Rost, S. et al., 2005. Seismological constraints on a possible plume root at the core-mantle boundary. *Nature*, 435(7042), pp.666–669. Available at: http://www.ncbi.nlm.nih.gov/pubmed/15931220 [Accessed January 7, 2015].

Rubie, D.C. et al., 2015. Accretion and differentiation of the terrestrial planets with implications for the compositions of early-formed Solar System bodies and accretion of water. *Icarus*, 248, pp.89–108. Available at: http://www.sciencedirect.com/science/article/pii/S0019103514005545.

Rubie, D.C. et al., 2011. Heterogeneous accretion, composition and core-mantle differentiation of the Earth. *Earth and Planetary Science Letters*, 301(1-2), pp.31–42. Available at: http://dx.doi.org/10.1016/j.epsl.2010.11.030.

Rubie, D.C. et al., 2003. Mechanisms of metal-silicate equilibration in the terrestrial magma ocean. *Earth and Planetary Science Letters*, 205(3-4), pp.239–255.

Rudge, J.F., Kleine, T. & Bourdon, B., 2010. Broad bounds on Earth's accretion and core formation constrained by geochemical models. *Nature Geoscience*, 3(6), pp.439–443. Available at: http://dx.doi.org/10.1038/ngeo872.

Rustad, J.R. & Yin, Q., 2009. Iron isotope fractionation in the Earth ' s lower mantle. *Nature Geoscience*, 2(7), pp.514–518. Available at: http://dx.doi.org/10.1038/ngeo546.

Ryckaert, J.-P., Ciccotti, G. & Berendsen, H.J.., 1977. Numerical integration of the cartesian equations of motion of a system with constraints: molecular dynamics of n-alkanes. *Journal of Computational Physics*, 23(3), pp.327–341. Available at: http://www.sciencedirect.com/science/article/pii/0021999177900985.

Sanloup, C. et al., 2011. Compressibility change in iron-rich melt and implications for core formation models. *Earth and Planetary Science Letters*, 306(1-2), pp.118–122. Available at: http://dx.doi.org/10.1016/j.epsl.2011.03.039.

Sanloup, C. et al., 2013. Structural change in molten basalt at deep mantle conditions. *Nature*, 503, pp.104–107. Available at: http://www.nature.com/nature/journal/v503/n7474/full/nature12668.html\nhttp://www.nature.com/nature/journal/v503/n7474/pdf/nature12668.pdf.

Sanville, E. et al., 2010. Improved Grid-Based Algorithm for Bader Charge Allocation. *Journal of computational chemistry*, 31(16), pp.2967–2970.

Scanavino, I., Prencipe, M. & Mineralogist, A., 2013. Ab-initio determination of high-pressure and high-temperature thermoelastic and thermodynamic properties of low-spin (Mg 1 – x Fe x) O ferropericlase with x in the range [0 . 06 , 0 . 59]. *American Mineralogist*, 98, pp.1270–1278.

Scarfe, C.M., Mysen, B.O. & Virgo, D., 1987. Pressure Dependence of the Viscosity of Silicate Melts. *Special Publication - The Geochemical Society, 1(Magmat. Processes: Physicochem. Princ.)*, (I), pp.59–67.

Shim, S.H. & Catalli, K., 2009. Compositional dependence of structural transition pressures in amorphous phases with mantle-related compositions. *Earth and Planetary Science Letters*, 283(1-4), pp.174–180. Available at: http://dx.doi.org/10.1016/j.epsl.2009.04.018.

Siebert, J. et al., 2012. Metal-silicate partitioning of Ni and Co in a deep magma ocean. *Earth and Planetary Science Letters*, 321-322, pp.189–197. Available at:

http://dx.doi.org/10.1016/j.epsl.2012.01.013.

Siebert, J., Corgne, A. & Ryerson, F.J., 2011. Systematics of metal-silicate partitioning for many siderophile elements applied to Earth's core formation. *Geochimica et Cosmochimica Acta*, 75(6), pp.1451–1489. Available at: http://linkinghub.elsevier.com/retrieve/pii/S0016703710006873 [Accessed January 13, 2015].

Smith, J. V. et al., 1970. Petrologic history of the moon inferred from petrography, mineralogy, and petrogenesis of Apollo 11 rocks. *Proceedings of the Apollo 11 Lunar Science Conference*, 1, pp.897–925. Available at: papers://9813c380-4a5a-426e-ab3b-10e227534cf8/Paper/p137.

Stackhouse, S., Brodholt, J.P. & Price, G.D., 2006. Elastic anisotropy of $FeSiO_3$ end-members of the perovskite and post-perovskite phases. *Geophysical Research Letters*, 33(1), p.n/a–n/a. Available at: http://doi.wiley.com/10.1029/2005GL023887.

Stackhouse, S., Brodholt, J.P. & Price, G.D., 2005. High temperature elastic anisotropy of the perovskite and post-perovskite polymorphs of Al 2 O 3. *Geophysical Research Letters*, 32(13), p.L13305. Available at: http://doi.wiley.com/10.1029/2005GL023163.

Stebbins, J.F., Farnan, I. & Xue, X., 1992. The structure and dynamics of alkali silicate liquids: A view from NMR spectroscopy. *Chemical Geology*, 96(3-4), pp.371–385.

Stixrude, L. et al., 2009. Thermodynamics of silicate liquids in the deep Earth. *Earth and Planetary Science Letters*, 278(3-4), pp.226–232. Available at: http://dx.doi.org/10.1016/j.epsl.2008.12.006.

Suzuki, A. et al., 2010. Pressure and temperature dependence of the viscosity of a NaAlSi2O6 melt. *Physics and Chemistry of Minerals*, 38(1), pp.59–64. Available at: http://link.springer.com/10.1007/s00269-010-0381-4.

Tang, W., Sanville, E. & Henkelman, G., 2009. A grid-based Bader analysis algorithm without lattice bias. *Journal of physics. Condensed matter : an Institute of Physics journal*, 21(8), p.084204.

Taylor, S.R. & Jakes, P., 1974. The geochemical evolution of the moon. *Proceedings of the Fifth Lunar Conference - Geochimica et Cosmochimica Acta*, 2, pp.1287–1305.

Thomas, C.W. et al., 2012. Multi-technique equation of state for Fe2SiO4 melt and the density of Fe-bearing silicate melts from 0 to 161 GPa. *Journal of Geophysical Research: Solid Earth*, 117(10), pp.1–18. Available at: http://doi.wiley.com/10.1029/2012JB009403 [Accessed November 26, 2014].

Thorne, M.S. & Garnero, E.J., 2004. Inferences on ultralow-velocity zone structure from a global analysis of SPdKS waves. *Journal of Geophysical Research*, 109(B8), p.B08301. Available at: http://doi.wiley.com/10.1029/2004JB003010.

Touboul, M. et al., 2007. Late formation and prolonged differentiation of the Moon inferred from W isotopes in lunar metals. *Nature*, 450(7173), pp.1206–1209.

Touboul, M. et al., 2009. Tungsten isotopes in ferroan anorthosites: Implications for the age of the Moon and lifetime of its magma ocean. *Icarus*, 199(2), pp.245–249. Available at: http://dx.doi.org/10.1016/j.icarus.2008.11.018.

Umemoto, K. et al., 2008. Spin transition in (Mg,Fe)SiO3 perovskite under pressure. *Earth*

and Planetary Science Letters, 276(1-2), pp.198–206. Available at: http://dx.doi.org/10.1016/j.epsl.2008.09.025.

Verlet, L., 1967. Computer "experiments" on clssical fluids, I thermodynamical properties of Lennar-Jones potential. *Phys. Rev.*, 165(5), p.201.

Vilella, K. et al., 2015. Spin state transition and partitioning of iron: Effects on mantle dynamics. *Earth and Planetary Science Letters*, 417, pp.57–66. Available at: http://linkinghub.elsevier.com/retrieve/pii/S0012821X15000874.

Wade, J. & Wood, B.J., 2005. Core formation and the oxidation state of the Earth. *Earth and Planetary Science Letters*, 236(1-2), pp.78–95.

Wade, J., Wood, B.J. & Tuff, J., 2012. Metal-silicate partitioning of Mo and W at high pressures and temperatures: Evidence for late accretion of sulphur to the Earth. *Geochimica et Cosmochimica Acta*, 85, pp.58–74. Available at: http://dx.doi.org/10.1016/j.gca.2012.01.010.

Walter, M.J. & Thibault, Y., 1995. Partitioning of Tungsten and Molybdenum Between Metallic Liquid and Silicate Melt. *Science*, 270(5239), pp.1186–1189. Available at: <Go to ISI>://A1995TE90500052.

Wan, J.T.K. et al., 2007. First-principles study of density, viscosity, and diffusion coefficients of liquid MgSiO3 at conditions of the Earth's deep mantle. *Journal of Geophysical Research: Solid Earth*, 112, pp.1–7.

Wang, Y. et al., 2014. Atomistic insight into viscosity and density of silicate melts under pressure. *Nature communications*, 5, p.3241. Available at: http://www.ncbi.nlm.nih.gov/pubmed/24476847.

Wicks, J.K., Jackson, J.M. & Sturhahn, W., 2010. Very low sound velocities in iron-rich (Mg,Fe)O: Implications for the core-mantle boundary region. *Geophysical Research Letters*, 37(June), pp.1–5. Available at: http://doi.wiley.com/10.1029/2010GL043689 [Accessed January 13, 2015].

Wiechert, U. et al., 2001. Oxygen isotopes and the moon-forming giant impact. *Science*, 294(5541), pp.345–8. Available at: http://www.sciencemag.org/content/294/5541/345.

Williams, Q. & Garnero, E.J., 1996. Seismic Evidence for Partial Melt at the Base of Earth's Mantle. *Science*, 273(5281), pp.1528–1530.

Wood, J.A. et al., 1970. Lunar anorthosites and a geophysical model of the moon. *Proceedings of the Apollo 11 Lunar Science Conference*, 1, pp.965–988.

Wu, J. & Stebbins, J.F., 2013. Temperature and modifier cation field strength effects on aluminoborosilicate glass network structure. *Journal of Non-Crystalline Solids*, 362(1), pp.73–81.

Yu, G. & Jacobsen, S.B., 2011. Fast accretion of the Earth with a late Moon-forming giant impact. *Proceedings of the National Academy of Sciences*, 108(43), pp.17604–17609.

Zhang, J. et al., 2012. The proto-Earth as a significant source of lunar material. *Nature Geoscience*, 5(4), pp.251–255. Available at: http://dx.doi.org/10.1038/ngeo1429.

Zhang, W. et al., 2014. Tracking excited-state charge and spin dynamics in iron coordination complexes. *Nature*, 509(7500), pp.345–348. Available at:

http://www.nature.com/doifinder/10.1038/nature13252.

Zhang, Y. et al., 2004. Finite-size effect at both high and low temperatures in molecular dynamics calculations of the self-diffusion coefficient and viscosity of liquid silica. *Journal of Physics: Condensed Matter*, 16(50), pp.9127–9135. Available at: http://stacks.iop.org/0953-8984/16/i=50/a=003?key=crossref.a203c619d111339f829850130b3715a9.

Zhang, Y. & Guo, G., 2009. Partitioning of si and O between liquid iron and silicate melt: a two-phase ab-initio molecular dynamics study. *Geophysical Research Letters*, 36(18), pp.1–5.

Abstract

We explore Fe-bearing Mg-silicate melts through the pressure regime of the Earth's mantle using First Principles Molecular Dynamics (FPMD). The equation of state results we obtained from our simulations are used to create a chemical and mineralogical model for Ultra-Low Velocity Zones (anomalous region on the mantle side of the core-mantle boundary).

Furthermore we study the behaviour of Ni, Co, and Fe in these melts, and asses their spin-crossover dependencies on their concentration, pressure, temperature, and the degree of polymerization of the silicate melts. We show that a decrease in the average spin can be correlated with the previously observed kink in the partitioning coefficient of Ni and Co.

We investigate the melt structure of all the compositions studied as a function of pressure. Our results provide new insight into the coordination of major and trace elements in silicate melts with different degrees of polymerization. We interpret the anomalous Ni-O coordination trend with pressure as the result of the spin state change.

The effect of silicate melt polymerization on the partitioning of Co, Ni, and W between a metal and silicate melt, is investigated at isobaric and isothermic conditions using multi-anvil experiments. We have performed FPMD simulations of melts with similar degrees of polymerization as the experiments in order to explain the increasing lithophile character of W with the decrease in polymerization of the silicate melt. We propose a structural explanation for tungsten's apparent increased affinity for depolymerized silicate melts.

Nous avons étudié des magmas ferrifères silicatés magnésiens à la pression du manteau terrestre en utilisant la dynamique moléculaire (First Principles Molecular Dynamics). Les résultats de l'équation d'état que nous avons obtenus à partir de nos simulations ont été utilisés pour créer un modèle chimique et minéralogique pour les zones de très basse vitesse sismique (ULVZ, anomalies régionales dans le manteau proche de la limite noyau-manteau).

De plus, nous avons étudié le comportement du Ni, du Co et du Fe dans ces magmas et établi la dépendance du spin en fonction de la concentration, de la pression, de la température et du degré de polymérisation du magma silicaté. Nous avons montré qu'une baisse du spin moyen peut être corrélée au changement de pente (kink) observé précédemment pour les coefficients de partage du Ni et du Co.

Nous avons analysé la structure du magma pour toutes les compositions étudiées en fonction de la pression. Nos résultats donnent un nouvel aperçu de la coordination des éléments majeurs et traces dans les magmas silicatés de différents degrés de polymérisation. Nous interprétons l'anomalie de coordination Ni-O en fonction de la pression comme un changement d'état de spin.

L'effet de la polymérisation du magma silicaté sur les coefficients de partage du Co, du Ni et du W entre le métal et le magma silicaté a été étudié par expériences multi-enclumes en conditions isobares et isothermes. Nous avons réalisé des simulations FPMD de magmas à des degrés de polymérisation similaires aux expériences afin d'expliquer le caractère de plus en plus lithophile du W lorsque le degré de polymérisation du magma silicaté diminue. Nous proposons une explication structurale pour expliquer l'affinité décroissante apparente du W dans les magmas silicatés dépolymérisés.